Stochastic modelling of the growth of carbonaceous materials

Gustavo León Cázares

Department of Chemical Engineering and Biotechnology
University of Cambridge

This dissertation is submitted for the degree of
Doctor of Philosophy

Selwyn College   May 2021

I would like to dedicate this thesis to my loving parents and brother. I am extremely grateful for all your support. You have been an inspiration . . .

Declaration

I hereby declare that except where specific reference is made to the work of others, the contents of this dissertation are original and have not been submitted in whole or in part for consideration for any other degree or qualification in this, or any other university. This dissertation is my own work and contains nothing which is the outcome of work done in collaboration with others, except as specified in the text and Acknowledgements. This dissertation contains fewer than 65,000 words including appendices, bibliography, footnotes, tables and equations and has fewer than 50 figures.

Some of the work in this dissertation has been published or submitted for publication:

1. **G. Leon**, N. Eaves, J. Akroyd, S. Mosbach, and M. Kraft. A new methodology to calculate process rates in a Kinetic Monte Carlo model of PAH growth. *Combust. Flame*, 209:133–143, 2019. doi:10.1016/j.combustflame.2019.07.032.

2. **G. Leon**, A. Menon, L. Pascazio, E. J. Bringley, J. Akroyd, and M. Kraft. Kinetic Monte Carlo statistics of curvature integration by HACA growth and bay closure reactions for PAH growth in a counterflow diffusion flame. *Proc. Combust. Inst.*, 38:1449-1457, 2020. doi:10.1016/j.proci.2020.06.352.

3. **G. Leon**, J. W. Martin, E. J. Bringley, J. Akroyd, and M. Kraft. The role of oxygenated species in the growth of graphene, fullerenes and carbonaceous particles. (2021) *Carbon. Submitted for publication*, 2021.

Other collaborative works not presented in this dissertation include:

1. A. Menon, **G. Leon**, J. Akroyd, and M. Kraft. A density functional theory study on the kinetics of seven-member ring formation in polyaromatic hydrocarbons. *Combust. Flame*, 217:152–174, 2020. doi:10.1016/j.combustflame.2020.03.032.

2. A. Menon, J. W. Martin, **G. Leon**, D. Hou, L. Pascazio, X. You, and M. Kraft. Reactive localized π-radicals on rim-based pentagonal rings: Properties and concentration in flames. *Proc. Combust. Inst.*, 38:565-573, 2020. doi:10.1016/j.proci.2020.07.042.

3. E. J. Bringley, M. Y. Manuputty, C. S. Lindberg, **G. Leon**, J. Akroyd and M. Kraft. Radial dependence of TiO_2 nanoparticles synthesised in jet-wall stagnation flames. *Combust. Flame. Submitted for publication*, 2021.

<div align="right">

Gustavo León Cázares
May 2021

</div>

Stochastic modelling of the growth of carbonaceous materials

Gustavo León Cázares

This thesis investigates the processes and morphologies involving key molecules that constitute carbonaceous materials, namely polycyclic aromatic hydrocarbons (PAHs), by applying a detailed particle model solved with a stochastic numerical method. In particular, a Kinetic Monte Carlo (KMC) algorithm is used to study the time-dependent transformations of PAHs in a reactive chemical environment, and thus the model is referred to as a KMC model. Numerical techniques to improve the stochastic simulation of PAHs are proposed. Regarding the PAH transformations, special emphasis is given to processes that integrate or remove curvature, as the morphology of PAHs has direct consequences on the carbonaceous materials they subsequently form.

A new methodology to calculate the process rates in KMC models of PAH growth is developed. The methodology uses a combination of the steady-state and the partial-equilibrium approximation. Comparisons of the results obtained with the new methodology show good agreement with those provided by simulations using a detailed chemical mechanism under conditions relevant to flames (temperatures between 1000 and 2500 K, equivalence ratios between 0.5 and 10). The new methodology is used to calculate the rate of different stochastic processes in KMC simulations of PAH growth of premixed ethylene-oxygen flames. The results of the KMC model with the new methodology are consistent with the concentrations of species calculated using a detailed chemical mechanism for the growth of small PAHs.

An algorithm to efficiently simulate the migration of partially-embedded five-member rings in PAHs is proposed. The algorithm defers the update of the computational carbonaceous structure whilst successive migration processes are sampled and is thus called the deferred update algorithm. The exactness and computational performance of the deferred update algorithm are investigated. A comparison of the algorithm with one in which the structure of the molecule is updated after each process is included. The deferred update algorithm is exact in the sense that it produces the correct sites in the migration of partially-embedded

five-member rings. The computational time saved by the deferred update algorithm is proportional to the number of deferred steps and is, on average, observed to be two orders of magnitude faster than the reference algorithm.

A KMC model that includes processes to integrate curvature due to the formation of five- and seven-member rings is used to simulate PAHs growing in lightly sooting ethylene and acetylene counterflow diffusion flames. New processes to form seven-member rings and to embed five-member rings via hydrogen-abstraction-acetylene-addition and bay closure reactions are included for the first time. The mass spectra of PAHs that are predicted by the model are compared against experimental data, and the distribution of embedded five-member rings and seven-member rings is studied as a function of spatial location, molecule size and frequency of events sampled in the simulation. The number of events and proportion of PAHs containing embedded five-member rings and seven-member rings is analysed at the end of the simulation domain. The formation of seven-member rings and the embedding of five-member rings is shown to be a competitive process. Both types of rings are observed more frequently at longer residence times.

The growth of carbonaceous materials is studied using a KMC model that captures the growth and oxidation of six-member and partially-embedded five-member rings. Circumcoronene molecules are grown at 1500 K and 1 atm in the presence of varying mole fractions of atomic and molecular oxygen and constant mole fractions of hydrogen and acetylene. Four regions of carbon growth associated with different carbonaceous products are identified. Graphene is formed in the presence of high mole fractions of atomic oxygen $\left(10^{-4} < X_O \leq 10^{-2}\right)$. Fullerenes are formed in the presence of low mole fractions of atomic oxygen and high mole fractions of molecular oxygen $\left(X_O \leq 10^{-4} \text{ and } 10^{-2} < X_{O_2} \leq 10^{-1}\right)$. Low mole fractions of both atomic and molecular oxygen $\left(X_O \leq 10^{-4} \text{ and } X_{O_2} \leq 10^{-2}\right)$ result in structures that become curved as simulation time progresses. The highest mole fractions of atomic oxygen $\left(X_O > 10^{-2}\right)$ produce small structures. The production and consumption of partially-embedded five-member rings are suggested to explain the formation of the observed structures. The oxidation of partially-embedded five-member rings produces sites that grow into graphenic structures. Formation and subsequent embedding of partially-embedded five-member rings result in curved structures that resemble fullerenes. These findings suggest that different carbonaceous materials can be synthesised by varying the concentration and type of oxidising species.

Acknowledgements

Table of contents

List of figures

List of tables

Nomenclature

Roman Symbols

A	Arrhenius pre-exponential factor	$\mathrm{m^3\,mol^{-1}\,s^{-1}}$; $\mathrm{s^{-1}}$
a_k	Third connected atom type for carbon atom with index k	
A_i	PAH molecule with i six-member rings	
b_α	Production of species α from non-steady-state species	$\mathrm{mol\,m^{-3}\,s^{-1}}$
b_peq	Vector of production terms of partial-equilibrium species from non-partial-equilibrium species	
b_ss	Vector of production terms of steady-state species from non-steady-state species	
$\mathcal{C}$	Set of carbon atoms in a molecule	
C	Connectivity matrix	
C_k	Gas phase concentration of the k-th species	$\mathrm{mol\,m^{-3}}$
c_k	Carbon atom with index k	
c_peq	Partial-equilibrium vector of concentrations	
c_ss	Steady-state vector of concentrations	
C_s	Carbon atom on primary particle surface	
$\mathscr{D}$	Data structure representing a molecule	
d	Diameter	m
D_f	Fractal dimension	
d_{ij}	Distance between two primary particles with indices i and j	m
E	Edge connectivity matrix	
E_A	Activation energy	$\mathrm{kg\,m^2\,s^{-2}\,mol^{-1}}$
$E_\mathrm{opt\text{-}conv}$	Energy convergence criteria for optimisation	

f_i	Fraction of radical sites for process with index i	
i_m	Initial location of migrating site m	
K	Collision kernel	$\mathrm{m^3\,s^{-1}}$
k_B	Boltzmann constant	$\mathrm{m^2\,kg\,s^{-2}\,K^{-1}}$
k_maj	Majorant rate scaling factor	
k_i	Reaction rate constant for process with index i	$\mathrm{m^3\,mol^{-1}\,s^{-1}\,;\,s^{-1}}$
Kn	Knudsen number	
$\mathcal{L}_\alpha$	Loss term of species α	$\mathrm{s^{-1}}$
L_c	Circular doubly-linked list of edge carbon atoms	
L_s	Circular doubly-linked list of sites	
$\mathfrak{m}$	Mass of a primary particle	kg
M	Molecular weight	$\mathrm{kg\,mol^{-1}}$
M_0	Particle number density	$\mathrm{m^{-3}}$
m_OB	General OpenBabel molecule	
m_j	Molecule with index j	
M_peq	Partial-equilibrium matrix	
M_ss	Steady-state matrix	
$\mathbf{n_R}$	Number of rings vector in a molecule	
$\mathrm{N_A}$	Avogadro constant	$\mathrm{mol^{-1}}$
n	Arrhenius temperature exponent	
$N_\mathrm{opt\text{-}steps}$	Maximum number of optimisation steps	
N_i	Number density of i-th particle	$\mathrm{m^{-3}}$
n_m	Number of steps for migrating site m	
$N_{\mathrm{site},\eta_\mathrm{i}}$	Number of sites for process with index i and site type η	
$n_\mathrm{C,Edge}$	Number of edge carbon atoms in a molecule	
$n_\mathrm{C,Internal}$	Number of internal carbon atoms in a molecule	
$n_\mathrm{C,Mod}$	Number of modified carbon atoms	
$n_\mathrm{C,New}$	Number of new carbon atoms	

n_C	Number of carbon atoms in a molecule	
N_{dens}	Number density	m^{-3}
$n_{H,New}$	Number of new hydrogen atoms	
n_H	Number of hydrogen atoms in a molecule	
n_m	Number of molecules in a primary particle	
N_{peq}	Number of partial-equilibrium species	
N_P	Number of aggregates in the ensemble	
n_p	Number of primary particles in aggregate	
$n_{R5_{emb}}$	Number of embedded five-member rings in a molecule	
n_{R5}	Number of edge five-member rings in a molecule	
n_{R6}	Number of six-member rings in a molecule	
n_{R7}	Number of seven-member rings in a molecule	
N_R	Number of gas phase chemical reactions	
N_{ss}	Number of steady-state species	
n_s	Number of sites in a molecule	
$\mathscr{O}$	Order	
$\mathcal{P}_\alpha$	Production term of species α	$mol\,m^{-3}\,s^{-1}$
$\mathcal{P}_{\alpha,\beta}$	Production of species α from species β	s^{-1}
$\mathcal{P}_{\beta,\eta_r}$	Production of a new site β from site with site type η_r	
P_{stick}	Sticking probability	
p_i	Primary particle with index i	
P_q	Aggregate particle with index q	
Prob	Probability	
K_{ci}	Equilibrium constant for reaction i	$m^3\,mol^{-1}\,s^{-1}\,;\,s^{-1}$
Q	State of the system	
q_i	Rate of progress for reaction i	$mol\,m^{-3}\,s^{-1}$
$R_{\beta\to\alpha}$	Set of reactions that produce species α from species β	
R_{gas}	Gas constant	$kg\,m^2\,s^{-2}\,mol^{-1}\,K^{-1}$

R_{peq}	Subset of partial-equilibrium reactions	
r	Radius	m
$R^{ss\text{--}peq}$	Combined steady-state–partial-equilibrium process rate	s^{-1}
$r^{ss\text{--}peq}_{\alpha_i \to \alpha_j}$	Combined steady-state–partial-equilibrium process rate between two species	s^{-1}
R_i	PAH process rate for process with index i	s^{-1}
R_{cg}	Coagulation rate	s^{-1}
R_g	Radius of gyration	m
$R_{HACA,i}$	HACA growth rate for i-th particle	$m^{-3}s^{-1}$
$R_{Oxid,i}$	Oxidation rate for i-th particle	$m^{-3}s^{-1}$
$\mathfrak{s}$	Surface area of primary particle	m^2
$\mathfrak{s}(p_i, p_j)$	Common surface area between two neighbouring primaries	m^2
$\mathcal{S}$	Set of sites in a molecule	
S_{peq}	Subset of partial-equilibrium species	
S_{ss}	Subset of steady-state species	
S	Surface area of aggregate particle	m^2
s_l	Site with index l	
T	Temperature	K
$\hat{\mathbf{u}}_{New}$	Unitary vector	
$\mathcal{V}_I$	Vector of internal carbon atom spatial coordinates	
V_{smpl}	Sample volume	m^3
V	Volume of aggregate particle	m^3
v	Volume of primary particle	m^3
$v(p_i, p_j)$	Volume of two neighbouring primaries	m^3
w_m	Random walker with index m	
$\mathbf{x}$	Vector of spatial coordinates	

Greek Symbols

α	Fraction of available reactive sites on particle surface	

χ	General gas phase chemical species	
Δ	Change	
$\delta_{\text{c–c}}$	Distance between two carbon atoms	m
$\delta_{\text{c–h}}$	Distance between carbon and hydrogen atoms	m
$\delta_{k,\text{Edge}}$	Binary variable for carbon k being on molecule edge	
η	Principal site type	
$\hat{\varepsilon}_{\alpha}^{\text{ss–peq}}$	Normalised time-integrated error in steady-state–partial-equilibrium approximation of species α	
$\hat{\varepsilon}_{\alpha}^{\text{ss}}$	Normalised time-integrated error in steady-state approximation of species α	
$\varepsilon_{\alpha}^{\text{ss–peq}}$	Time-integrated error in combined steady-state–partial-equilibrium approximation of species α	
$\varepsilon_{\alpha}^{\text{ss}}$	Time-integrated error in steady-state approximation of species α	
λ_{f}	Mean free path of surrounding gas	m
μ	Dynamic viscosity	$\text{kg} \, \text{m}^{-1} \, \text{s}^{-1}$
ν	Stoichiometric reaction coefficient	
$\dot{\omega}_{\alpha}$	Net production rate of species α	$\text{mol} \, \text{m}^{-3} \, \text{s}^{-1}$
ρ	Density	$\text{kg} \, \text{m}^{-3}$
σ	Surface smoothing factor	
τ_{α}	Lifetime of species α	s
$\chi_{\text{C}_{\text{s}}-\text{H}}$	Number density of armchair sites on particle surface	m^{-2}

Superscripts

dens	Density
l	Number of levels in the binary tree used to store the ensemble of particles
neq	Non-partial-equilibrium
peq	Partial-equilibrium
ref	Reference
fm	Free-molecular
sf	Slip-flow
tr	Transition

transf	Transfer

Subscripts

0	Start
AR	Aromatic ring
avg	Average
sph	Sphere
cg	Coagulation
cl	Crosslink
col	Collision
com	Centre of mass
comb	Combined
cutoff	Cutoff
f	Stop
gas	Gas phase species
New	Added to molecule
Int	Internal
k_{first}	Index of first carbon associated with site
k_{last}	Index of last carbon associated with site
lim	Limit
maj	Majorant
mat	Material
max	Maximum
New	New
OB	OpenBabel
opt-conv	Convergence for optimisation
opt-steps	Optimisation steps
pri	Primary
smpl	Sample

tot   Total

Other Symbols

[A]   Concentration of gas phase species A   mol m^{-3}

$\mathscr{C}(p_i, p_j)$ Sintering level between two primaries

$\mathcal{I}_{\text{Edge}}$ Set of edge carbon atom indices for a molecule

$\mathbb{N}$ Natural numbers

$\mathscr{P}$ Pressure   kg m^{-1} s^{-2}

$\mathbb{R}$ Real numbers

$\mathscr{W}$ Set of random walkers

Acronyms / Abbreviations

AALH   Aromatic aliphatically-linked hydrocarbons

ABF   Appel-Bockhorn-Frenklach

ARS   Aromatic Site

ABLH   Aromatic bridged-linked hydrocarbons

HR-AFM   High resolution atomic force microscopy

AMLH   Aromatic multicentre-linked hydrocarbons

APLH   Aromatic penta-linked hydrocarbons

ARLH   Aromatic rim-linked hydrocarbons

SEM   Scanning electron microscopy

AZLH   Aromatic zig-zag-linked hydrocarbons

cPAH   Curved polycyclic aromatic hydrocarbon

cPCAH   Curved pericondesed aromatic hydrocarbons

CVD   Chemical vapour deposition

CHRCR   Clustering of hydrocarbons by radical chain reactions

DFFO   Distance from fuel outlet

DLR   Deutsches Zentrum für Luft- und Raumfahrt

DSA   Direct Simulation Algorithm

fPCAH   Flat pericondesed aromatic hydrocarbons

HACA   Hydrogen-Abstraction–Carbon-Addition

HIM   Helium ion microscopy

HR-TEM High-resolution transmission electron microscopy

CRECK   Chemical Reaction Engineering and Chemical Kinetics

KM   Kaust PAH Mechanism 2

KMC   Kinetic Monte Carlo

LPDA   Linear process deferment algorithm

MMFF94 Merck molecular force field

OB   OpenBabel

ODE   Ordinary differential equation

PAH   Polycyclic aromatic hydrocarbon

PP   Primary particle

Chapter 1

Introduction

1.1 Motivation

Carbonaceous materials have been produced for useful purposes for thousands of years. Different types of soot and charcoal were used in paintings early in human history [132, 289, 338]. Later, carbon black became a major industrial product in polymer reinforcement applications and as covering agent [338]. Although these materials have many applications, they have also been associated with serious human health hazards [335]. The last century saw the appearance of other carbonaceous products like glassy carbon [174] and activated carbons [352] that are still widely used. Recently, novel materials like fullerenes [164] and graphene [233] have been discovered. These materials are currently being studied as it appears they have multiple potential applications, such as energy storage [48], sensors [94, 226] and high-end composite materials [219, 171]. However, the physical and chemical processes that participate in the production of each of these materials are not fully understood.

There are two main motivations for understanding the processes that produce carbonaceous materials. Firstly, carbonaceous particles are known to represent a serious human health hazard as well as being a major contributor to global warming. Secondly, novel carbonaceous materials present promising properties for a variety of applications.

1.1.1 Environmental pollutants

Carbonaceous particles, the most common being soot, are probably the best known carbonaceous material. These particles are typically produced in incomplete (oxygen deficient) combustion processes. The formation of carbonaceous particles is both entropy driven and kinetically favoured [335]. They are assembled in aggregates of primary particles that are widely accepted to consist of mainly polycyclic aromatic hydrocarbons (PAHs).

The production of carbonaceous particles is associated with incomplete combustion. These particles can be produced by industrial and residential sources, as well as by open burning of forests and grasses [18]. Once they are produced, the particles are displaced by convection which takes them to regions where they have negative environmental effects. Carbonaceous particles can interact with clouds, modifying the nucleation mechanisms of liquid or solid droplets [254, 18]. They interact with ice and snow, changing their radiative properties and thus causing a warming effect [110, 158, 195]. The net effects of carbonaceous particles on various climate effects are shown in Figure 1.1 as estimated by Bond et al. [18]. The adverse climate effects of carbonaceous particles makes them one of the main contributors to global warming [260, 284].
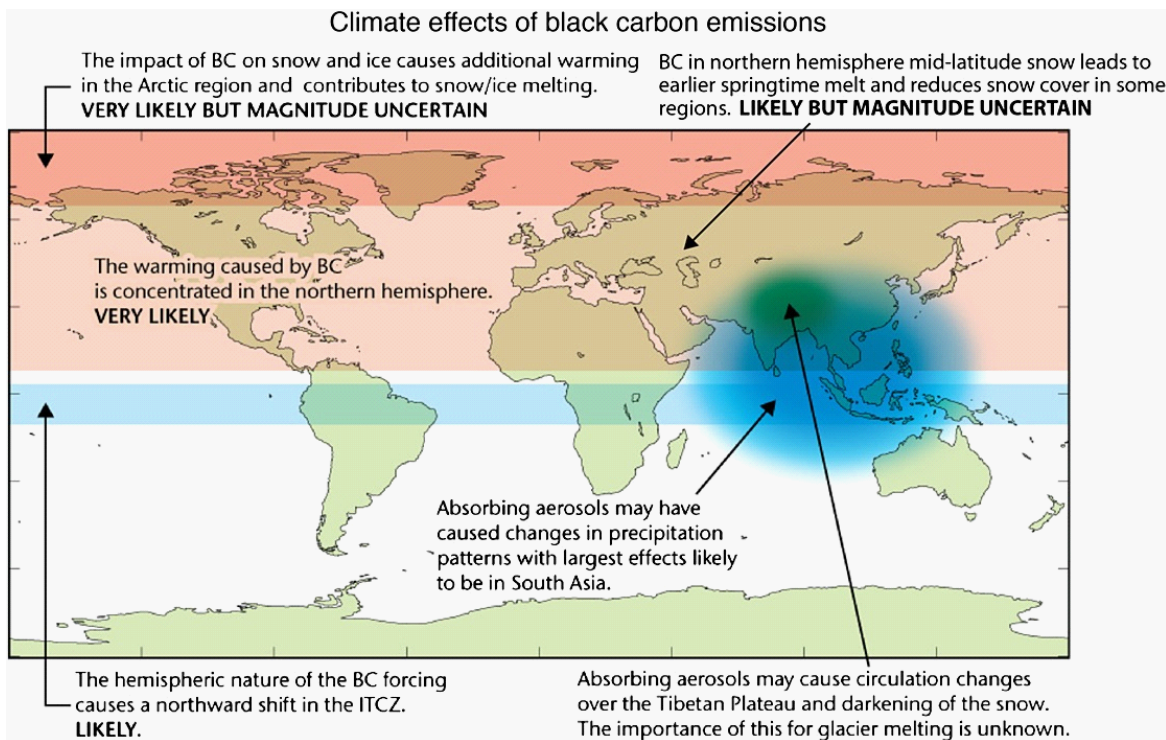
Fig. 1.1 Contribution of carbonaceous particles (black carbon - BC) emissions to various climate effects. Figure reproduced from Bond et al. [18] with permission from John Wiley and Sons ©.

Another serious adverse effect of carbonaceous particles is their impact on human health. Carbonaceous particles are one of the main constituents of particles under 2.5 microns ($PM_{2.5}$) [327]. These particles can be inhaled and the PAHs that constitute them proceed to interact with different tissues in the human body. The negative health effects of these molecules have been widely documented [145, 153, 183, 135] and reducing the contact with this particulate material has been reported to have positive health effects [10].

1.1.2   Novel carbonaceous materials

Other carbonaceous materials have useful properties and are used in different applications. Carbon black, a more compact and carbonised version of carbonaceous particles than soot, is used as reinforcement for polymers as well as a dye for plastics, paints and inks [338]. Activated carbon, a porous carbon material obtained from thermal treatments of particulate carbon, can be used in the filtration of substances for different applications [174, 352]. Recently, two carbonaceous materials have gained increased attention due to their unique properties. These are fullerenes and graphene.

Fullerenes are closed cage molecules that are formed by alternating five- and six-member rings. These molecules have an increased stability due to their closed molecular structure [162] that gives them unique properties and topologies [280]. Several applications have been proposed for fullerenes. They have been studied in the context of fuel cells [48] and have been suggested as possible candidates in the fabrication of electrochemical sensors for their ability to accept electrons [94, 288].

Graphene consists of a large single layer of highly-ordered six-member rings. This material was first obtained by removing a single atom layer from graphite [233] resulting in completely different electric, thermal and mechanical properties for the material [217]. Many applications in a variety of fields have been proposed for graphene including sensors [226, 170], composite materials [217], advanced fabrics [219] and biomedical devices [286] being just a few examples among many others [170]. Although the properties of graphene are highly studied, the production of this material is proving to be challenging [177, 217].

Carbonaceous particles, fullerenes and graphene can be produced in high-temperature reactive environments. The physical and chemical processes that form these materials appear to be related. It is therefore desirable to understand under which conditions each of these materials can be produced.

1.2   Aim

The **purpose of this work** is to model the processes that transform the structure of PAHs in different high-temperature chemical environments by the application of stochastic models. This is to better understand the formation of various carbonaceous materials such as graphene, fullerenes and carbonaceous particles at high temperatures.

1.3   Novel elements of the thesis

This thesis presents the following **novel developments**:

- A methodology to calculate the process rates for a stochastic model of PAH growth. The methodology uses a combination of the steady-state approximation and the partial-equilibrium approximation. The comparison of the time-integrated error of the methodology against that of the steady-state approximation shows that the methodology is more accurate in the region where carbonaceous particles (soot) grow.

- A detailed particle model that is able to capture the transformations of carbonaceous materials. The model is solved stochastically using a Kinetic Monte Carlo (KMC) algorithm. The model includes processes that integrate curvature by forming seven-member rings and by embedding five-member rings. The model also includes processes for the oxidation of six-member rings and partially-embedded five-member rings.

- An algorithm to simulate the migration of partially-embedded five-member rings around the edge of PAHs. The algorithm defers the update of the atomic structure while keeping the reactive sites of the molecule updated. The algorithm is shown to be exact and, on average, to provide computational time savings of two orders of magnitude when compared with the reference algorithm.

- A study of the processes that integrate curvature in PAHs from counterflow diffusion flames. It is shown that curvature is more likely to be integrated at longer residence times and that the formation of embedded five-member rings and seven-member rings is a competitive process as the same sites are necessary to produce both.

- A study of the growth of PAHs in the presence of constant mole fractions of surface growth species (hydrogen and acetylene) and varying mole fractions of oxygenated species. The study identifies four regions of carbon growth associated with different products: graphene, fullerenes, carbonaceous particles and oxidised species. The mole fractions of species necessary to produce each of these products is reported.

- A mechanism that suggests a possible explanation of the formation of graphene, fullerenes and carbonaceous particles. The mechanism is based on the production and consumption of partially-embedded five-member rings. Species that oxidise six-member rings produce short curved structures that are suggested to become fullerenes. Species that oxidise partially-embedded five-member rings result in the formation of large flat structures that are suggested to become graphene. In the absence of oxidising species crosslinking reactions are suggested to form carbonaceous particles.

1.4   Structure of the thesis

The remainder of this thesis is structured as follows.

Chapter 2 provides relevant background information on the formation of carbonaceous particles, fullerenes and graphene in high-temperature reactive environments, with a focus on PAH chemistry.

Chapter 3 contains a description of the detailed particle model used in this thesis. In particular, a brief explanation of the algorithms, rate calculations and processes used in the model can be found in this chapter.

Chapter 4 presents a new methodology to calculate process rates in Kinetic Monte Carlo models of PAH growth. The methodology uses a combination of the steady-state approximation and the partial-equilibrium approximation. The results obtained with the methodology are independently compared to both individual approximations and used in a stochastic simulation of PAH growth of a premixed flame.

Chapter 5 explores the integration of curvature in flame-generated PAHs in counterflow diffusion flames. New processes for the integration of curvature by the embedding of five-member rings and by the formation of seven-member rings via acetylene additions and bay closures are included. The simulated PAHs are compared against previous experimental results. The statistics of processes that integrate curvature and the size and distribution of curved PAHs are studied to improve the understanding of the mechanism by which PAHs become curved.

Chapter 6 studies the growth of PAHs in conditions that have varying levels of oxygenated species but are still suitable for surface growth due to the presence of sufficient hydrogen and acetylene. Four regions of carbon growth are identified and associated with the formation of **graphene**, **fullerenes** and **carbonaceous particles**. Analysis of the processes that integrate curvature into PAHs show that processes that produce and consume partially-embedded five-member rings are important in the formation of the different carbonaceous structures.

Finally, conclusions and avenues for further research regarding stochastic simulations of PAH growth are presented in **Chapter 7**. A bibliography containing all cited references can be found at the end of the thesis.

Chapter 2

Background

This chapter presents a brief background on the high temperature gas phase formation of carbonaceous materials. The processes reviewed focus mostly on the chemistry associated with combustion reactions, although other environments relevant to these materials, such as plasma reactors, are also discussed. The formation of carbonaceous materials is known to be related to the appearance of polycyclic aromatic hydrocarbons (PAHs). These species interact with the chemical environment to grow and form additional aromatic rings. The interaction of two PAHs is widely believed to explain the inception of carbonaceous particles and it has been suggested that it can contribute to the formation of fullerenes. The formation of graphene in plasma reactors is discussed. The mechanism for the production of this material is not well understood. The processes that affect PAHs at high temperatures are thought to be relevant for carbonaceous particles, fullerenes and graphene but determining which processes are relevant to the formation of each unique material is still an open question which forms the basis behind the rest of this thesis.

2.1   Overall formation of carbonaceous particles

Carbonaceous particles are typically produced in incomplete combustion processes. Chemically, carbonaceous particles are constituted of polycyclic aromatic hydrocarbons (PAHs), molecules that gain additional stability in different conditions through the formation of aromatic rings [305]. Although they are associated with high temperature processes, PAHs also represent between the 10-25% of carbon in interstellar medium [196, 319], where low temperature chemistry appears to play a role in their formation and subsequent growth [239]. In oxygen deficient environments, such as flames or pyrolysis reactors, PAHs are a kinetically favoured product that benefit from an entropy decrease in their formation process [335]. Once formed, PAHs self assemble into nascent carbonaceous particles with a stacked nanostructure [335]. Depending on the conditions in which the particles are formed they can have different properties and composition.

The formation of carbonaceous particles occurs as a combination of physical and chemical processes that have different timescales. The main processes involved are shown in Figure 2.1, in which five steps that lead to the formation of carbonaceous particles can be seen from bottom to top. Fuel pyrolysis is the first step in the formation of carbonaceous particles. In this step the fuel is decomposed into small hydrocarbons and hydrocarbon radicals creating a pool of species that become the building blocks for carbonaceous materials. These molecules are typically under 1 nm in size [209]. In the second step, precursor formation, the first aromatic rings are produced from gas phase species [112]. These aromatic rings grow via the addition of small hydrocarbons [76] and form PAHs that contain five-member rings and six-member rings [45]. These species are able to delocalise electrons within their structure gaining additional stability at high temperatures [306, 305] and have sizes between 1 and 10 nm. In the third step, PAHs self assemble and form nanoparticles. These incipient particles [209] have sizes that are comparable to that of the largest precursors (less than 10 nm). This step presents relevant scientific questions in the formation of carbonaceous particles, as the nature of the formation of nanoparticles from the gas phase is not well understood. In the fourth step, the nanoparticles produced in previous steps gain mass by the addition of gas phase species and aromatic precursors. These particles are larger, with sizes over 10 nm [209]. and are constituted by several PAHs. Lastly, carbonaceous primary particles assemble into particle aggregates, larger agglomerates formed by the collision of individual particles with sizes over 100 nm [209].

Some of the physical and chemical processes that contribute to the formation of carbonaceous particles are also important in the synthesis of other materials like fullerenes and graphene. Although these processes are important in different chemical environments, they are discussed in the context of combustion chemistry in the following sections.
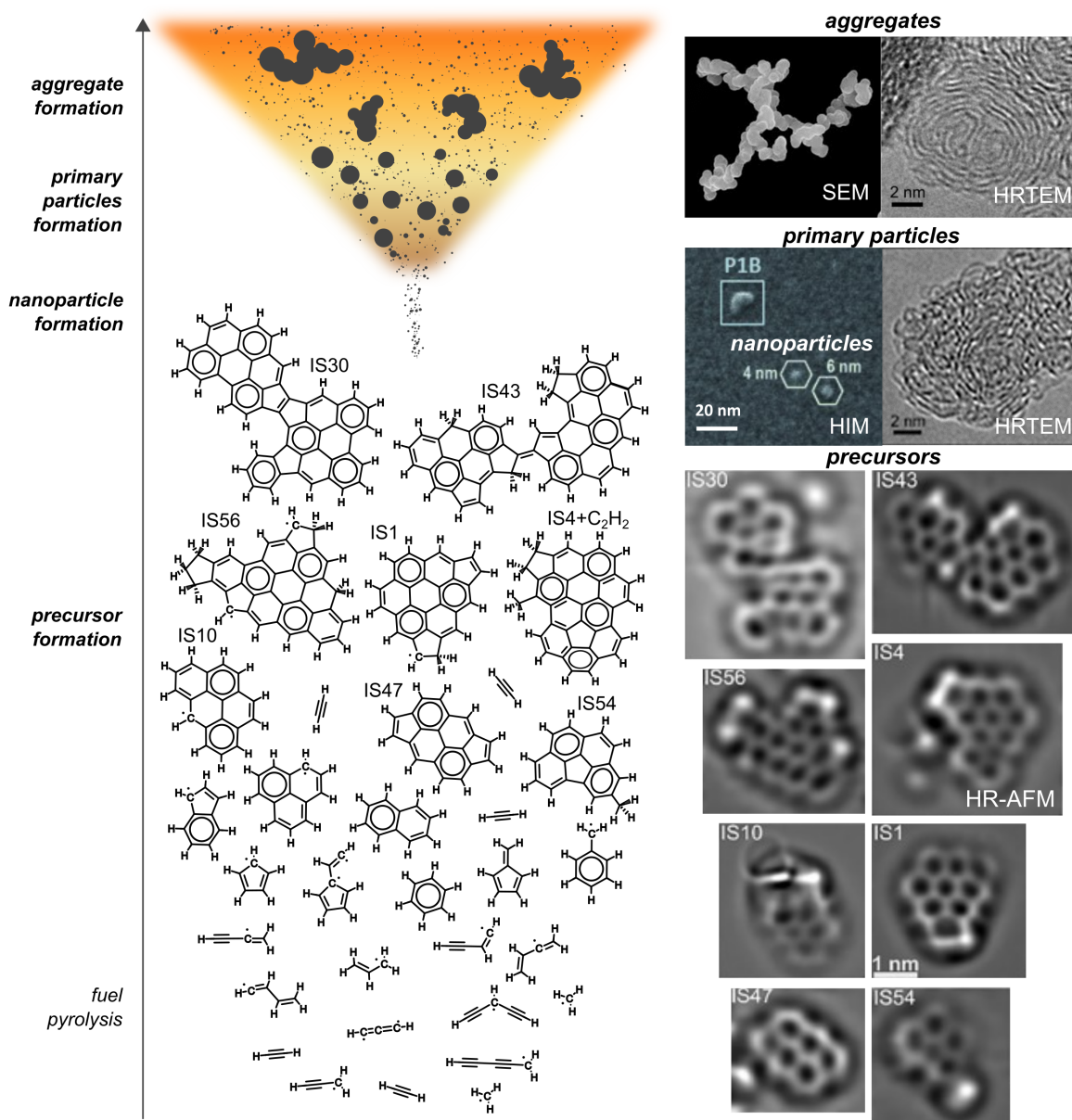
Fig. 2.1 Schematic of the main processes occurring during soot formation in flames. Fuel pyrolysis and single ring species are taken from Hansen et al. [111]; Johansson et al. [139]. The structures and high-resolution atomic force microscopy images of larger PAHs are taken from Commodo et al. [45]. Nanoparticles and primary particles imaged with helium ion microscopy (HIM) are taken from Schenk et al. [278]. HRTEM of primary particles and SEM for a lamp black aggregate particles are taken from [190]. This figure is provided courtesy of Jacob W. Martin © and is used with permission.

2.2 Formation and growth of PAHs

The gas phase formation and growth of PAHs is a crucial step in the formation of carbonaceous materials. PAHs are widely considered to be the main constituents of carbonaceous particles, and have been suggested to play a role in the formation of other materials like fullerenes [121] and graphene [56]. Therefore understanding the processes that affect PAHs is necessary to successfully predict the formation of these materials. In this section the formation of and growth of PAHs are reviewed in the context of combustion environments as this is one of the main fields for the synthesis of carbonaceous materials.

2.2.1 Formation of the first aromatic rings

The first step in the production of carbonaceous materials involves the formation of aromatic molecules. Benzene (C_6H_6), with only one six-member aromatic ring, is one of the simplest aromatic species from which other PAHs are produced. Several works have shown that the most likely pathway towards the formation of benzene involves the self-recombination of propargyl radicals ($C_3H_3{}^\bullet$) [71, 212, 204, 307, 264, 311, 89, 210, 211]:

$$C_3H_3{}^\bullet + C_3H_3{}^\bullet \longrightarrow C_6H_6.$$
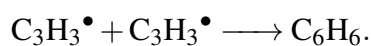
Other pathways that contribute to the formation of benzene involve the combination of propargyl radical with other resonantly stabilised radicals. For example, the combination of propargyl radical with 1-methylallenyl ($C_4H_5{}^\bullet$) [51, 30],

$$C_3H_3{}^\bullet + C_4H_5{}^\bullet \rightleftharpoons C_6H_5CH_2{}^\bullet + H,$$
$$C_6H_5CH_2{}^\bullet + H \rightleftharpoons C_6H_5CH_3,$$
$$C_6H_5CH_3 + H \rightleftharpoons C_6H_6 + CH_3{}^\bullet,$$
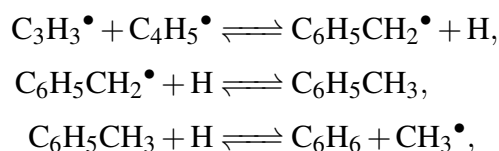
and with allyl radical ($a\text{-}C_3H_5{}^\bullet$) [112]:

$$C_3H_3{}^\bullet + a\text{-}C_3H_5{}^\bullet \rightleftharpoons C_5H_4CH_2 + H + H$$
$$C_5H_4CH_2 + H \rightleftharpoons C_6H_6 + H.$$
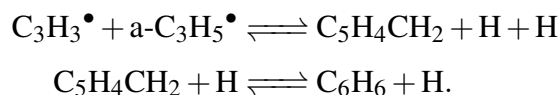
Additionally, the recombination of 1,3-butadienyl radical ($i\text{-}C_4H_5{}^\bullet$) and acetylene has been shown to be a significant contributor to the formation of benzene [43, 51]:

$$i\text{-}C_4H_5{}^\bullet + C_2H_2 \longrightarrow C_6H_6 + H.$$
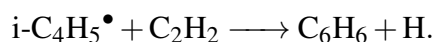
Recently the self-combination 1-buten-3-yne (C_4H_4) has also been proposed as a possible pathway in the formation of phenylacetylene, an acetylene substituted benzene [176]:

$$C_4H_4 + C_4H_4 + H \longrightarrow C_6H_5C_2H + H_2 + H.$$
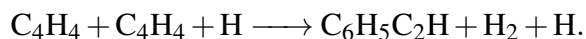
These pathways have been suggested as the most likely to explain the formation of benzene in combustion processes. However, other pathways may be relevant in other reactive environments. For example, the recombination of 1,3-butadiene with ethynyl radical has also been proposed to produce benzene in in non-combustion environments [141].

Another aromatic species that participates in the formation of other PAHs and carbonaceous materials is the cyclopentadienyl radical ($C_5H_5{}^\bullet$). This radical containing a single five-member ring is formed by the oxidation of phenyl radical [265, 310, 52]

$$C_6H_5 + O_2 \rightleftharpoons C_6H_5O + O,$$
$$C_6H_5 + O \rightleftharpoons C_5H_5 + CO,$$
$$C_6H_5O \rightleftharpoons C_5H_5 + CO,$$
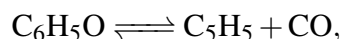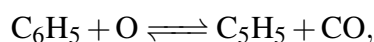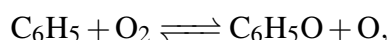
and via the recombination of propargyl radical and ethylene [8, 205]

$$C_3H_3{}^\bullet + C_2H_2 \rightleftharpoons C_5H_5{}^\bullet.$$
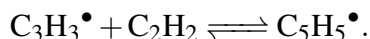
Besides participating in the formation of PAHs, cyclopentadienyl radical also plays a role in the formation of benzene. This has been suggested via the recombination with a methyl radical and a ring enlargement reaction [8, 205]:

$$C_5H_5{}^\bullet + CH_3{}^\bullet \rightleftharpoons C_5H_5CH_3,$$
$$C_5H_5CH_3 \rightleftharpoons C_5H_4CH_2 + H_2,$$
$$C_5H_4CH_2 + H \rightleftharpoons C_6H_6 + H.$$
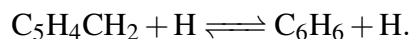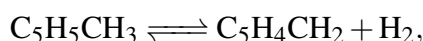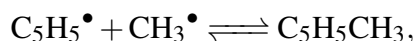
Benzene and cyclopentadienyl radical subsequently participate in processes that produce larger PAHs.

2.2.2   Growth into larger PAHs

HACA

The first aromatic rings can further interact with the pool of chemical species available in the gas phase. This interaction can produce additional aromatic rings resulting in the formation of

PAHs. Although several mechanisms have been proposed to explain the growth of additional rings on aromatic species, none have been as tested as the Hydrogen-Abstraction–Carbon-Addition (HACA) mechanism [337, 76, 74]. This reaction model has been incorporated into modern chemical mechanisms [342, 38, 261, 227] as its predictions reasonably explain the growth of PAHs and carbonaceous particles [269, 203]. The reaction scheme has three main steps: the activation of the PAH via the abstraction of an hydrogen atom (Equation (2.1)), the addition of a first acetylene molecule (Equation (2.2)) and the addition of a second acetylene molecule forming a new ring (Equation (2.3)):

$$A_i + H \xrightleftharpoons[k_{-1}]{k_1} A_i^\bullet + H_2, \tag{2.1}$$

$$A_i^\bullet + C_2H_2 \xrightleftharpoons[k_{-2}]{k_2} A_iC_2H_2, \tag{2.2}$$

$$A_iC_2H_2 + C_2H_2 \xrightarrow{k_3} A_{i+1} + H, \tag{2.3}$$
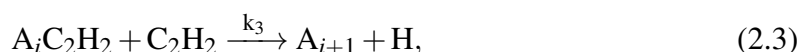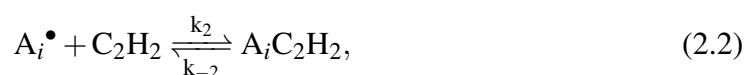
where the notation A_i, defined by Frenklach et al. [83], represents a PAH with i six-member rings, and k represents the rate constant for each reaction. Reaction equations (2.1)–(2.3) provide a simple way to model the growth of arbitrarily sized PAHs. Following these equations, Frenklach [76] demonstrated that the rate of HACA growth of PAHs has the form

$$\frac{\dfrac{k_1[H]}{k_{-1}[H_2]}}{\dfrac{k_{-2}}{k_2k_3[C_2H_2]^2} + \dfrac{1}{k_2[C_2H_2]} + \dfrac{1}{k_{-1}[H_2]}}. \tag{2.4}$$

Equation (2.4) accounts for the different regimes in which HACA growth can be expected. An analogous version of Equations (2.1)–(2.3) can be used to study the surface growth of carbonaceous particles. This model, first proposed by Frenklach and Wang [81], uses the reactions:

$$C_s-H + H \xrightleftharpoons[k_{-1}]{k_1} C_s^\bullet + H_2, \tag{2.5}$$

$$C_s^\bullet + C_2H_2 \xrightarrow{k_2} C_s-H + H, \tag{2.6}$$

$$C_s^\bullet + H \xrightarrow{k_3} C_s-H, \tag{2.7}$$

$$C_s^\bullet + O_2 \xrightarrow{k_4} products, \tag{2.8}$$
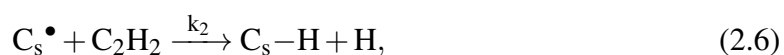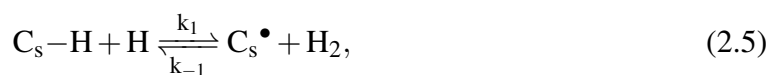
where C_s-H and $C_s^\bullet$ represent the number of reactive sites in a carbonaceous particle and their radicals respectively. The term C_s-H on the right hand side of Equation (2.6) represents

the new site formed after the production of a new ring. Using the steady-state approximation for the radical sites, the HACA growth rate for the i-th particle can be obtained as

$$R_{\text{HACA},i} = \frac{\alpha \, \chi_{\text{C}_\text{s}-\text{H}} \, k_1[\text{H}] \, k_2[\text{C}_2\text{H}_2]}{k_{-1}[\text{H}_2] + k_2[\text{C}_2\text{H}_2] + k_3[\text{H}] + k_4[\text{O}_2]} \mathfrak{s}_\text{i} \, N_i, \tag{2.9}$$

where $R_{\text{HACA},i}$ is the HACA growth rate for the i-th particle, α is a model parameter that represents the fraction of available reactive sites on the surface of a particle, $\chi_{\text{C}_\text{s}-\text{H}}$ is the number density of armchair sites on the surface of a particle ($:= 2.3 \times 10^{15}$ sites/cm^2 [81]), $\mathfrak{s}_\text{i}$ is the surface area of the particle and N_i is the number density of the given particle. This simple reaction model has been used to study the growth of carbonaceous particles in multiple conditions [4, 203, 269].

Although Equations (2.1)–(2.9) provide a good estimation of the growth rate of carbonaceous materials, the reality of the HACA mechanism is more complex as can be seen in Figure 2.2. The three routes for HACA growth from phenyl are those proposed by Bittner and Howard [14] (blue), the original HACA route proposed by Wang and Frenklach [336] (red) and the modified Frenklach route [222] (pink). The studies performed by Mebel and collaborators showed that the three routes can be significant in the growth of naphthalene (A_2) from benzene depending on the gas phase conditions [201, 202].

The potential energy surface for HACA growth of naphthalene has also been investigated by Kislov and collaborators [156, 157] and more recently by Frenklach et al. [86] and by Liu et al. [180]. All of these studies showed that the preferred product for the addition of acetylene to naphthalene is acenaphthylene, which contains a five-member ring. The formation of phenanthrene (A_3) is suggested to be linked to the formation of biphenyl followed by a HACA addition over the crosslink between the aromatic rings. This process, first proposed by Wang and Frenklach [337] and later investigated by Kislov et al. [155], was crucial in assembling chemical mechanisms for the growth of PAHs such as the ABF mechanism [4]. Lastly, the HACA growth of larger PAHs has been studied for different species. Frenklach et al. [86] calculated the potential energy surface for the addition to zig-zag and armchair sites. Raj [255] studied the differences for HACA growth between flat and curved PAHs. The HACA growth reactions implemented in early mechanisms such as the Appel-Bockhorn-Frenklach (ABF) mechanism [4] have been included in a number of modern detailed chemical mechanisms, including the *Deutsches Zentrum für Luft- und Raumfahrt* (DLR) mechanism [297, 298, 38], the Kaust PAH Mechanism 2 (KM2) [341, 342], the Chemical Reaction Engineering and Chemical Kinetics (CRECK) mechanism [262, 261] and the Caltech mechanism [15, 227]. These detailed chemical mechanisms use HACA reactions to explain the growth of larger PAHs.
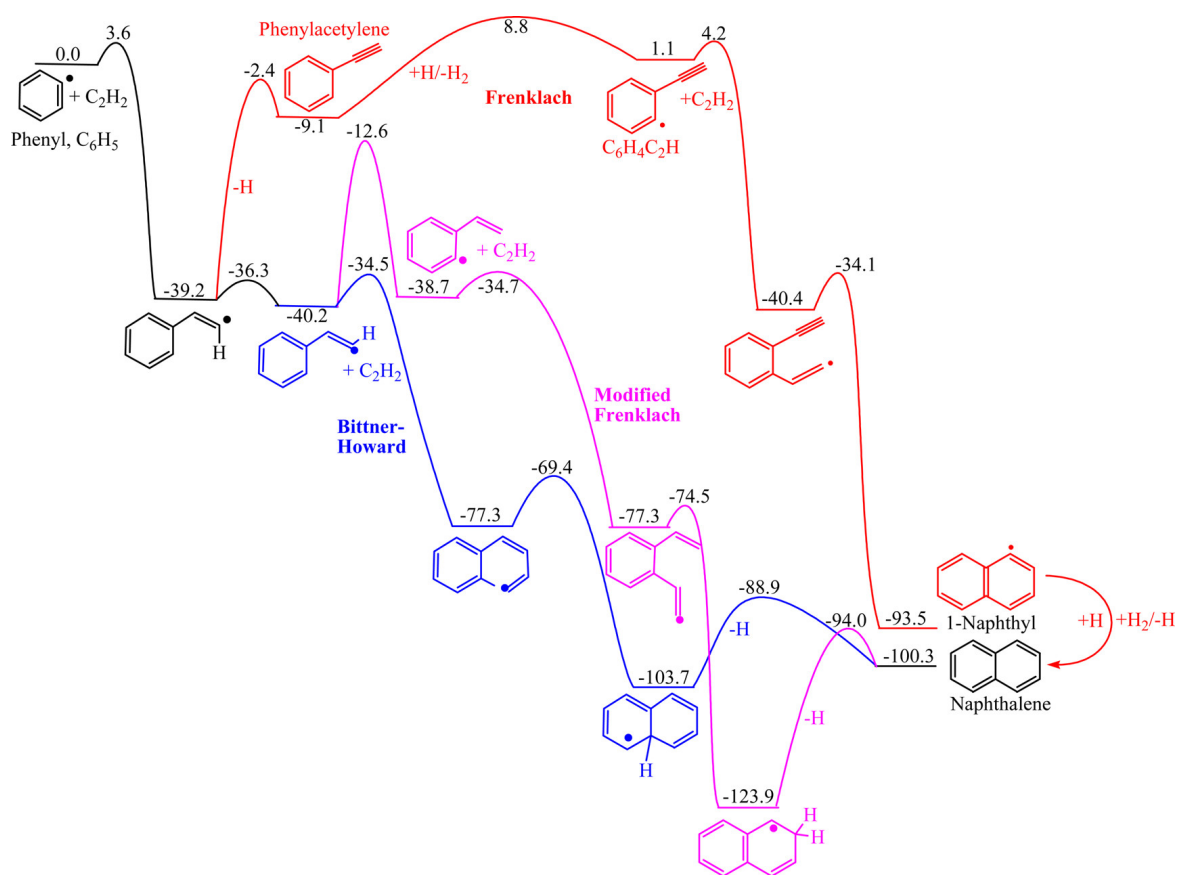
Fig. 2.2 Potential energy surface for various HACA routes. All relative energies are given in kcal/mol. Reprinted from Mebel et al. [202] with permission from the American Chemical Society ©.

Other growth mechanisms

Other growth mechanisms that are important to mention are the recombination of cyclopenta-dienyl radicals, the growth via the addition of other gas phase species and crosslinking and condensation reactions.

Two cyclopentadienyl radicals can recombine in a pathway that explains the fast formation of naphthalene in flame environments [58, 188, 205]. The reaction follows the formation of an hydrogenated fulvalenyl ($C_{10}H_9$)

$$C_5H_5{}^\bullet + C_5H_5{}^\bullet \longrightarrow C_{10}H_{10},$$
$$C_{10}H_{10} \longrightarrow C_{10}H_9 + H,$$
$$C_{10}H_9 \longrightarrow C_{10}H_8 + H.$$
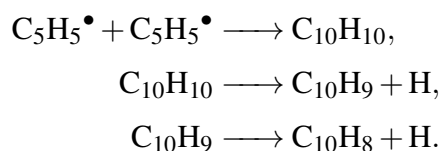
This pathway has been studied in depth by Mebel and collaborators [198, 202], who showed that this recombination also explains the formation of other PAHs such as azulene and fulvalene.

Growth via the addition of other species such as vinylacetylene (C_4H_4), propargyl radical (C_3H_3) and 1,3-butadiene (C_4H_6) has also been studied in the context of naphthalene formation [201, 202]. Ring-enlargement pathways involving the formation of six-member rings from five-member rings have also been proposed via the addition of methyl [200, 201, 8] and acetylene [283].

Lastly, another pathway in which PAHs gain molecular weight consists of crosslink condensation reactions between two PAHs. Density functional theory studies of phenyl, naphthyl and anthracenyl crosslinking on naphthalene and anthracene with the subsequent condensation into additional rings showed that these reactions can be competitive with HACA growth processes [326]. Experimental observations have also provided evidence of crosslinks that rearrange into curved structures containing embedded five-member rings [9, 2, 121]. Crosslinking reactions probably play an important role in the inception of carbonaceous particles as is discussed in Section 2.3.1

2.2.3   Inclusion of curvature

The inclusion of curvature induced during the growth of PAHs has important consequences for carbonaceous materials. In the case of carbonaceous particles, it has been shown that curved PAHs (cPAHs) possess a dipole moment due to the flexoelectric effect [189] that persists at flame temperatures [194]. Curved PAHs have been observed in premixed [3, 102] and non-premixed flames [190], and it has been hypothesised that their dipole moments may influence the formation of the first particles [191, 22].

The curvature arises from five- and seven-member rings that are embedded during the growth of a PAH. Five-member rings surrounded by six-member rings results in positive Gauss curvature, corresponding to a bowl-shaped topology [280]. Seven-member rings surrounded by six-member rings results in negative Gauss curvature, corresponding to a saddle-shaped topology [317].

Five-member rings are found in a variety of carbon materials including nanotubes [175], graphene [267] and fullerenes. Corannulene (the smallest cPAH) has been detected in flame-generated soot [166, 354]. High-resolution transmission electron microscopy (HR-TEM) analysis of soot particles has shown the presence of curved fringes, indicating PAHs containing embedded five-member rings [333, 21]. Partially-embedded five-member rings have been directly observed in PAHs using high-resolution atomic force microscopy (HR-AFM), and may be able to lead to fully embedded five-member rings via an acetylene

addition step, but observing these embedded five-member rings in carbonaceous particles is challenging because the resulting PAHs are no longer planar [45].

The inclusion of curvature in carbonaceous materials has been studied in the context of the formation of five-member rings. Frenklach [75] was the first to propose that PAH growth could be dominated by the HACA growth of five-member rings on the zig-zag edge of a molecule rather than by the growth of six-member rings. In subsequent studies [84, 350], it was shown that edge five-member rings can migrate around zig-zag edges in a reaction facilitated by the addition of an hydrogen atom to the five-member ring forming a localised π-radical. Using Kinetic Monte Carlo (KMC) models, HACA growth reactions in the adjacency of edge five-member rings were suggested to produce partially-embedded five-member rings [75, 84, 348]. Once formed, partially-embedded five-member rings participate in transformation processes that change the morphology of the structure. These are illustrated in Scheme 1. Firstly, partially-embedded five-member rings are able to migrate around the edge of a PAH facilitated by an hydrogen abstraction reaction [351]. Secondly, rings occupying an edge position can become fully-embedded leading to the formation of a cPAH [348, 359, 358].
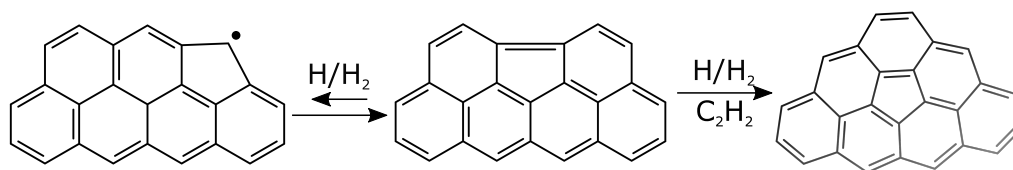
Scheme 1: *Migration and embedding of a partially-embedded five-member ring [351].*

The migration process allows the rings to be positioned on either the edge or the corner of molecules. However, the kinetics of the migration reaction favour the edge position [351]. The rate for this migration process was estimated to be much faster than the rate of formation of additional rings. Therefore, it was concluded that the migration of partially-embedded five-member rings happens several times before other growth reactions. This process follows a one-dimensional random walk around the molecule edge [351]. The migration becomes terminated when the bay-capping reaction [359] (right part of Scheme 1) fully embeds the five-member ring [359]. The number of migration steps, N_{steps}, is [351]

$$N_{steps} \propto \frac{R_{migration}}{R_{termination}}, \tag{2.10}$$

where $R_{migration}$ and $R_{termination}$ are the rates for the migration and termination process respectively.

Seven-member rings are also associated with the inclusion of curvature in carbonaceous materials. Seven-member rings have been observed in non-graphitising carbon [115], nan-

otubes [175], fullerenes [318] and graphene [253].   The Stone-Wales defect, a double pair of five- and seven-member rings, produces local curvature in graphene [248]. Lines of consecutive five- and seven-member rings have been observed in nanoporous carbons [104], and result in different curvatures in different annealed carbons [193]. In graphene, these lines constitute grain boundaries where the orientation of the carbon atoms change [131]. The partially embedded five-member rings observed by Commodo et al. [45] are contained in bays that provide a site for the formation of a seven-member ring next to the five-member ring. HR-TEM analysis of curved fringes also suggests that seven-member rings could be present in soot particles [333, 21].

The formation of seven-member rings in gas phase chemistry has been rarely studied. One exception is Kislov et al. [157], who studied a process to create seven-member rings via two HACA additions on a zig-zag site, but found that it was slow relative to other processes. Other work worth mentioning is the formation of azulene from the recombination of cyclopentadiene radicals as studied by Mebel et al. [201]. In their work they showed that azulene can convert into naphthalene via internal rearrangements of the carbon atoms. Recently, Menon et al. [206] calculated rates for the formation of seven-member rings on bay sites containing five-member rings using density functional theory at the M06-2X/cc-PVTZ//B3LYP/6-311+G(d,p) level of theory. The ring formation mechanisms included hydrogen-abstraction-facilitated, hydrogen-addition-facilitated, carbene formation, and direct cyclisation bay closure processes and closure via HACA growth. The calculated rates showed that the formation of seven-member rings by HACA growth and bay closures proceeded at rates similar to the analogous processes for the formation of five and six-member rings. Scheme 2 shows some of the processes studied for the formation of seven-member rings.
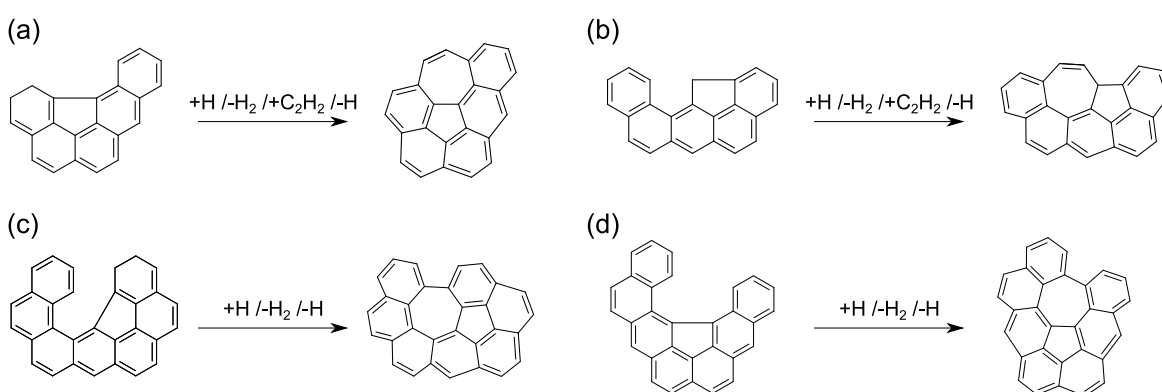
Scheme 2: *Formation of seven-member rings as studied by Menon et al. [206]. (a) and (b) show formation via HACA, (c) and (d) show formation via bay closure reactions.*

2.2.4   Oxidation of PAHs

The interactions between carbonaceous materials and oxygenated species have been extensively studied, most typically in combustion experiments. Early experiments on carbon rods with molecular oxygen (O_2) showed that carbonaceous materials present different types of reactive sites, resulting in the development of the Nagle-Strickland-Constable (NSC) model [332]. This model has been extensively used to study the oxidation of carbonaceous particles such as soot [120, 28, 90] and other materials like glassy carbon [174]. Fenimore and Jones [72] and later Neoh and collaborators [232, 231] showed that the hydroxyl radical (OH) also contributes to the oxidation of carbonaceous particles. They used a two-stage premixed burner where carbonaceous particles and combustion gases from the first stage were mixed with air and burned in the second stage. In these experiments they showed that at low concentrations of molecular oxygen, soot oxidation is dominated by hydroxyl radicals. Using collision theory, Neoh and collaborators [232, 231] showed that the oxidation of carbonaceous particles by hydroxyl radicals has a collision efficiency of 0.13.

Early experiments also showed the capability of atomic oxygen (O) to oxidise carbon filaments [268] and carbonaceous particles [353]. Later, Neoh and collaborators [232, 231] showed that atomic oxygen is unlikely to be a significant oxidiser in typical flame conditions. However, in other conditions such as plasma reactors [138, 312] and plasma assisted combustion experiments [143], atomic oxygen has been detected in significant concentrations. These three species appear to play different roles in the oxidation of carbon materials. Molecular oxygen appears to be responsible for the oxidation of carbonaceous particles from the inside of the particles, while the hydroxyl radical is associated with surface oxidation [103, 91, 230, 228]. Atomic oxygen has been suggested to contribute to the oxidation of resonantly stabilised radicals [85] as well as producing epoxy and ether groups on the basal planes of PAHs [168]. Those oxygenated groups possibly explain the different oxidation rates observed in recent oxidation experiments of carbon black with molecular and atomic oxygen [228].

Different models have been used to study the interaction between oxygenated species and carbonaceous materials. Semi-empirical models such as the NSC model [332] and that of Neoh and collaborators [232, 231] have been extensively used to study the surface growth and oxidation of carbonaceous particles [47, 303, 28, 120, 81]. Other oxidation models such as the one proposed by Lee et al. [173] or the one given by Appel et al. [4] provide a single equation to estimate the oxidation rate of carbonaceous particles by molecular oxygen. Recently Guo et al. [103] and Ghiassi et al. [90] compared model predictions from different oxidation models and determined optimised expressions for the oxidation rate of carbonaceous particles in premixed flames, diffusion flames and flow reactors.

The model proposed by Frenklach and Wang [81] (see Equations (2.5)–(2.8)) for the growth of carbonaceous particles can also be used to model their oxidation. Analogously to Equation (2.9), the oxidation rate for the i-th particle can be obtained as

$$R_{\text{Oxid},i} = \frac{\alpha\,\chi_{\text{C}_s-\text{H}}\,k_1[\text{H}]\,k_4[\text{O}_2]}{k_{-1}[\text{H}_2] + k_2[\text{C}_2\text{H}_2] + k_3[\text{H}] + k_4[\text{O}_2]}\mathfrak{s}_i\,N_i, \qquad (2.11)$$

where $R_{\text{Oxid},i}$ is the oxidation rate of the i-th particle by molecular oxygen. Recently, Frenklach [78] reviewed the implications of this model. In that work the α model parameter was redefined as the ratio of reactive edge carbon atoms to total carbon atoms of a PAH. The reaction model was also expanded to account for the formation of oxygenated intermediate species.

Detailed particle models have also been used to study the interaction of oxygenated species with carbonaceous precursors. Frenklach and collaborators [65, 294, 293] used density functional theory to calculate the oxidation pathways of different sites. They used their rates in a KMC model to study the oxidation of different rings on graphene edges. Their results suggest that molecular oxygen and hydroxyl radical are responsible for the oxidation of six-member rings via the formation and subsequent decomposition of oxyradicals. This reaction produces either a five-member ring or a partially-embedded five-member ring. In a more recent study, Frenklach et al. [85] also showed that atomic oxygen is likely to be responsible for the oxidation of partially-embedded five-member rings. The oxidation of six-member rings and partially-embedded five-member rings by different species is shown in Scheme 3. Other detailed models have focused on the formation of oxygenated groups in molecules that are precursors for carbonaceous particles [339, 340, 274, 69]. These studies suggest that oxygenated species can enhance the growth of carbonaceous materials by creating additional types of ring and types of site in the material.
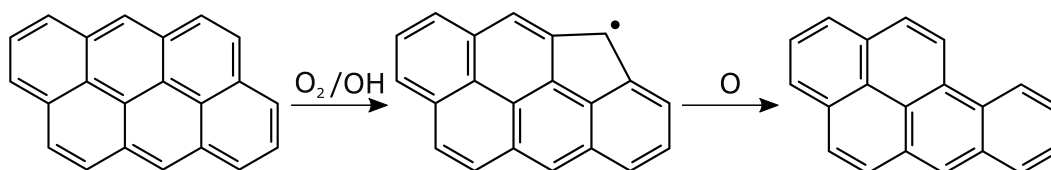
Scheme 3: *Species associated with the oxidation of six-member rings [293] and partially-embedded five-member rings [85].*

2.3 Formation and growth of carbonaceous particles

2.3.1 Particle inception

The transition from gas phase aromatic precursors into the condensed-phase that constitutes incipient particles is the process known as particle inception [209]. There is strong evidence that the interaction of two PAHs leads to the inception of carbonaceous particles, but the identity of these PAHs, and the nature of their interactions, remain elusive [335, 125]. Several mechanisms have been proposed to provide an explanation to the particle inception process. These mechanisms are shown in Figure 2.3 and can be classified in three main categories.

1. Inception via physical interactions, in which dispersion or van der Waals forces keep the PAHs together.

2. Inception via chemical reactions, in which the PAHs stay together by forming bonds between each other.

3. Inception via a combination of physical and chemical interactions between PAHs.

Inception via physical interactions

The irreversible physical dimerisation of flat, small sized PAHs is one of the earliest models for the inception of carbonaceous particles. Based on X-ray diffraction experimental observations, Frenklach and Wang [81] proposed the irreversible dimerisation of two pyrene molecules as the process for particle inception. Throughout the years this model has been applied in several studies with varying levels of accuracy [269, 4, 76, 80]. The irreversible dimerisation of pyrene has arguments both in favour [76, 80, 279, 133] and against [126, 125, 35, 270, 295, 63] it as a possible mechanism for the inception of carbonaceous particles. Recently, Frenklach and Mebel [80] reviewed the different possible mechanisms of particle inception. The formation of pyrene dimers was analysed using rate constants that included reversible processes. It was concluded that the physical dimerisation of pyrene is unlikely to explain particle inception.

Other physical models of particle inception are those that suggest the interaction of ions. The ion-driven particle inception model was first proposed by Calcote [26, 27]. This mechanism relies on the addition of neutral molecules to ions present in the flame. Several works [108, 6, 36] disproved this mechanism on the basis that ions are not present in large enough numbers to sustain particle inception. Recently, the studies performed by Martin and collaborators [189, 194, 190, 191, 22] have suggested that an ionic mechanism would be
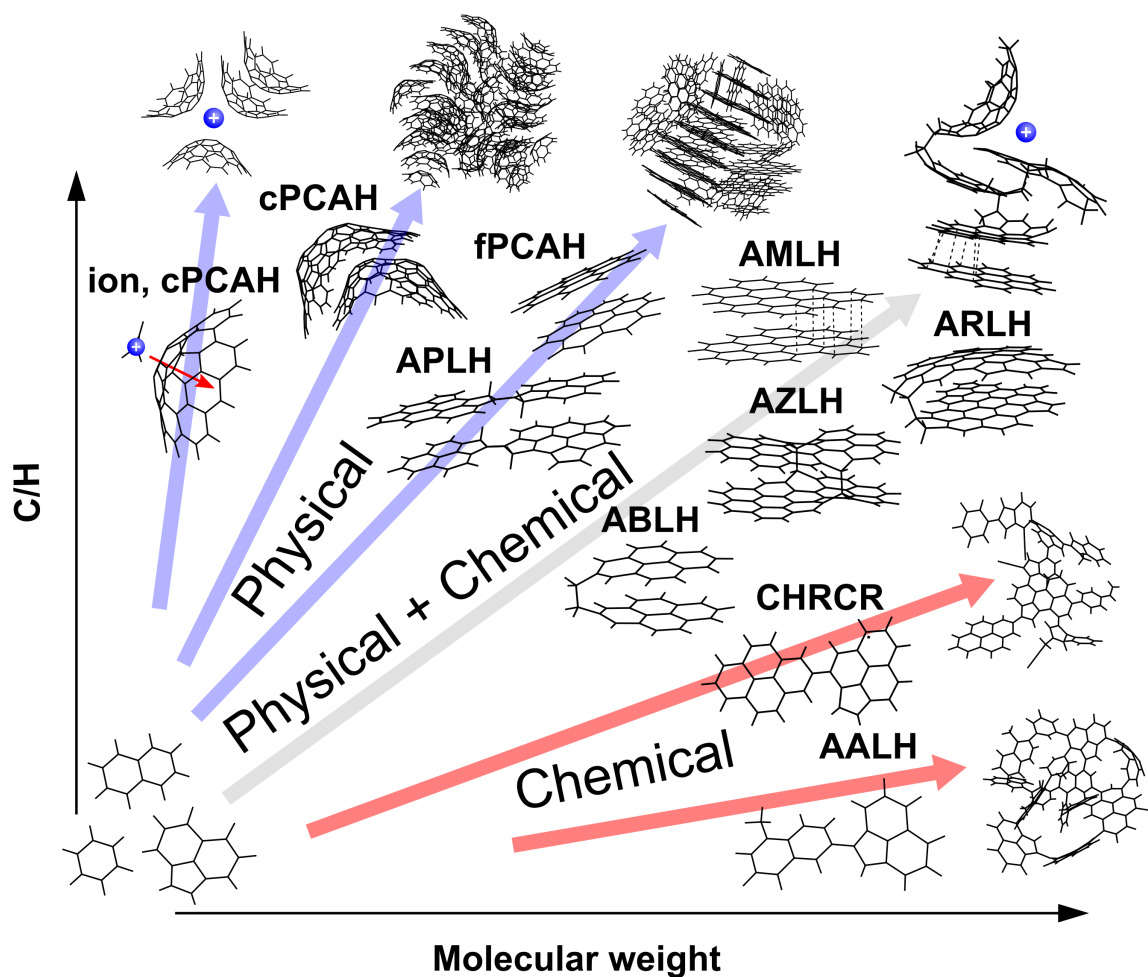
Fig. 2.3 Schematic of various mechanisms for particle inception of carbonaceous nanoparticles arranged as a function of molecular weight and C/H ratio. This figure is provided courtesy of Jacob W. Martin © and is used with permission.

possible around cPAHs. Curved PAHs have a larger dipole moment than that of flat PAHs due to the flexoelectric effect [189]. This dipole moment makes curved PAHs more susceptible to interact with electric fields and ions in flames. A molecular dynamics study of clustering of corannulene, the smallest cPAH, showed that the presence of potassium ions favoured the formation of homogeneous clusters due to interactions between the dipole moment and the ions. This effect was not observed with flat PAHs [22]. These observations suggest that an ionic mechanism for particle inception associated with curved PAHs could be possible. Further investigation of this mechanism is needed.

Inception via chemical interactions

Different chemical mechanisms for particle inception have been suggested to explain the formation of carbonaceous particles. The early works of Homann [121] and Siegmann et al. [290] suggested that a reactive dimerisation mechanism could explain the high concentrations of larger PAHs sampled in flames using mass spectrometry. Homann [121] proposed that a few PAHs could form aliphatic links between peri-condensed PAHs. These aromatic oligomers were called *aromers*. Aromers were suggested to have many five-member rings, to decompose via dehydrogenation reactions and to have varying sizes as a function of the flame fuel and conditions. Aromers were suggested to explain the formation of fullerenes via a *zipper mechanism* in which an aromer consisting of two crosslinked PAHs could form a partially closed cage via dehydrogenation (unimolecular) reactions. Aromers were also suggested as precursors to particle inception. In that case aromers would keep growing via HACA (bimolecular) reactions not allowing the formation of a closed structure. This mechanism initiated the discussion of crosslinking between PAHs but the mechanism for the formation of such bonds is missing.

Following the discussion of crosslinked structures, Violi et al. [331] proposed a mechanism initiated by hydrogen abstraction on one of the six-member rings of a PAH. The newly formed radical proceeded to attack an edge five-member ring on another PAH creating an aliphatic bond. Ring condensation reactions over the aliphatic bond could then form peri-condensed PAHs. This was termed the aromatic-aliphatically-linked-hydrocarbon (AALH) mechanism. In the original work of Violi et al. [331] large crosslinked structures were observed using a kinetic Monte Carlo/molecular dynamics approach. However, the reversibility of the bond formation was not included. Calculations of the stability of bonds on crosslinked PAHs have shown that single aliphatic bonds are quite susceptible to break [335, 80]. To resolve these issues, Frenklach and Mebel [80] suggested modifications to the AALH mechanism. They proposed that instead of repeatedly forming a single aliphatic crosslink, an *E-bridge* or doubly linked structure could be formed. This structure produces two adjoined five-member rings which do not fragment and are more stable and less reversible. Structures with two adjoined five-member ring have also been observed experimentally [81, 45]. However, the formation rate of an E-bridge does not appear to generate sufficient nucleation flux to explain particle inception on its own. To address this issue, Frenklach and Mebel [80] suggested that the formation of internal rotors upon collision could enhance the rate of formation significantly.

Lastly, another chemical mechanism that could explain the inception of carbonaceous particles is the clustering of hydrocarbons by radical chain reactions (CHRCR) mechanism [139]. In this mechanism resonantly-stabilised-radical PAHs act as crosslinking units.

It was proposed that a resonantly-stabilised-radical PAH could react with radicals that come from hydrogen abstraction reactions. This reaction between two radicals is barrierless, and is thus expected to be fast. The crosslinked structure could then have another hydrogen abstraction, creating another resonantly-stabilised-radical PAH that could propagate a chain reaction. This mechanism provides a sensible explanation of the formation of clustered PAHs. However, the rate constants for all the reactions present in this mechanism have not been explored in detail. An assessment of the reversibility of the reactions in the mechanism is also necessary.

Inception via physical and chemical interactions

The final category essentially combines the previous two. In a first step, two colliding PAHs interact physically and stay together due to dispersion forces. In a subsequent step, a thermodynamically stable chemical bond is formed between the PAHs. Some of the mechanisms that have been proposed that follow these two interactions are the aromatic zig-zag linked hydrocarbon (AZLH) mechanism, the aromatic multicentre-linked hydrocarbons (AMLH) mechanism, and the aromatic rim-linked hydrocarbons (ARLH) mechanism.

The aromatic zig-zag linked hydrocarbon mechanism was proposed by Wang [335]. The central species to this mechanism are acenes, linear PAHs that have a diradical character as the PAH becomes longer [308]. Two acenes are proposed to form stacks and then form multiple bonds between their radical sites [335]. However, studies of the thermal stability of acene dimers have shown that their formation at flame conditions is not favoured [360, 216].

The aromatic multicentre-linked hydrocarbons mechanism suggests the formation of *pancake bonds*, bonds formed on the edge of PAHs that are previously stacked [193]. These bonds were associated with π-radicals that are formed on PAHs with an odd number of carbon atoms [223]. For larger non-symmetric aromatic species it was found that the multicentre bond only forms across a few edge carbon atoms [193].

Lastly, the aromatic rim-linked hydrocarbons mechanism was suggested from the recent observations of PAHs containing different five-member ring moieties [45]. This mechanism, suggested by Martin and collaborators [193, 192], proposes the formation of localised π-radicals around edge five-member rings or partially-embedded five-member rings. It was suggested that localised π-radicals formed on edge five-member rings were able to form stable bonds between stacked PAHs. Calculations of the stability of bonded and stacked ARLH dimers showed that these dimers have substantially larger binding energies [192] and equilibrium constants [208] than physically interacting dimers at flame temperatures. A recent study of the kinetics and equilibrium constants of localised π-radicals with different species showed that the reactions of localised π-radicals are as fast as those of other radicals [208].

Although the study showed that crosslinking rates between small PAHs were likely too slow to explain particle inception by itself, the high stability of the formed dimers suggests that this mechanism may be important for larger species. This mechanism is still under investigation.

2.3.2 Aggregate formation

The formation of carbonaceous aggregate particles has been reported since early works in the detection of soot particles in flames [73, 101, 116, 149]. Larger carbonaceous particles are known to be the product of collisions between incipient and smaller particles. Experimental studies showed that initially the particles look spherical and later acquire a fractal shape [117]. Hence, the coagulation of carbonaceous particles has two regimes: coalescent growth and agglomeration into fractal aggregates [76].

Coalescent growth

In this regime particles are usually assumed to be spherical. They collide and coalesce completely, forming new spherical particles [76], which is the reason why these particles have been called liquid-like [209]. The mathematical treatment of this regime is taken from the field of aerosol dynamics [345, 87]. Coalescent growth is described by the Smoluchowski master equations [302], where the collision coefficients are dependent on the sizes of colliding particles. The functional form of this dependence is in itself dependent on the value of the Knudsen number [178] which is the ratio of the mean free path to the particle radius, and hence is a function of pressure (see (3.34)). At low pressures the coagulation is said to be in the free-molecular regime, and at high pressures in the continuum regime [345, 87], while in between, in the transition regime, is assumed to be a function of both (see Equation (3.31)) [252]. The Smoluchowski master equations have asymptotic solutions that result in self-preserving distributions of particle sizes [345, 87, 76]. These asymptotic results are typically used in simplified models of soot formation [77]. Frenklach [76] mentions that experimental evidence [16] and computational results [82] both show that there is a substantial deviation of the particle size distribution function from the self-preserving form in the carbonaceous particles inception zone. This issue is still currently under investigation and, as mentioned earlier, dependent on the uncertainties of particle inception processes.

Particle agglomeration

Larger carbonaceous particles are known to form particle aggregates with a narrow fractal dimension of 1.7-1.8 [76]. Pratsinis and collaborators [67, 66, 148, 328] showed that the fractal dimension of an agglomerate depends mostly on the mechanism that dominates

particle aggregation. In the case of carbonaceous particles, aggregates appear to be formed by diffusion limited aggregation [159] and ballistic cluster-cluster aggregation [144]. The governing regime appears to be a function of the Knudsen number.

Coupled simulations of particle aggregation with surface growth showed that carbonaceous particles are likely to be of roughly equal sizes when they form particle agglomerates [215, 214, 146]. Mitchell and Frenklach [215] showed that carbonaceous agglomerates start to form immediately after the formation of incipient particles. They showed that surface growth of primary particles is an important process that contributes to the sintering of individual particles into the spheroidal shape of a particle agglomerate [215]. A model for the sintering of primary particles in an aggregate has been proposed by Eggersdorfer et al. [67] based on the shared surface area of individual primary particles. This model has been implemented in stochastic models of carbonaceous particle inception and growth [276]. Recently, the sintering of carbonaceous particles has also been experimentally observed [236]. Stochastic models of particle aggregation and growth have confirmed that the combined agglomeration and surface growth of the particles explains the structures of carbonaceous particles [220, 242, 322, 276, 256, 34]. Detailed particle models such as the one proposed by Sander et al. [276], have provided a comprehensive description of the processes that contribute to the formation of carbonaceous particles. These models have been used to study the combined growth of constituting PAHs with the dynamics of particle formation.

2.4   Formation of fullerenes

Fullerenes are a unique type of molecule that are characterised by their closed cage curved structure and the arrangements of its carbon atoms in six-member rings and five-member rings. The curvature of the fullerene structure is such that the three bonds of any carbon atom with its neighbouring atoms are not in a plane [106]. This effect, called pyramidalisation [106], modifies the hybridisation of the atomic orbitals, from the sp^2 hybridisation characteristic of graphene, to an intermediate between sp^2 and sp^3 [105, 218]. Although most fullerenes contain mostly six-member rings and five-member rings, some fullerenes containing seven-member rings have also been found in low pressure acetylene flames [318].

Fullerenes can be produced alongside carbonaceous particles in arc discharges formed between graphite electrodes at low pressures [40]. In this system, first described by Krätschmer et al. [160], single carbon atoms are vaporised from the graphite electrode and rearrange in the gas phase to form fullerenes. The mechanism by which both products are formed is not well understood. Mojica et al. [218] presents different mechanisms that have been suggested to explain the formation of fullerenes in this system. Also worth mentioning are

the mechanism by Kroto and collaborators [361, 163, 49, 161], who suggested the formation of an icospiral molecule by molecular edge growth that could close and form a fullerene, or keep growing and form a quasi-spiral carbonaceous particle as shown in Figure 2.4. This mechanism suggests that fullerenes grow by adding carbon atoms on the molecule edge, a process that appeared to be too slow to explain fullerene formation in arc discharge systems [218, 64, 23]. Instead, there is evidence that fullerenes can add carbon atoms and carbon atom dimers from the gas phase to grow into larger fullerenes [60]. The opposite process has also been suggested as the mechanism that best explains the formation of fullerenes in arc discharges [280]. Large fullerenes are suggested to be formed from the ejection of carbon atom dimers from larger fullerenes [134, 272]. The presence of carbon atom dimers in the laser-ablation of graphite rods [277] suggests that this decomposition pathway is possible [280].
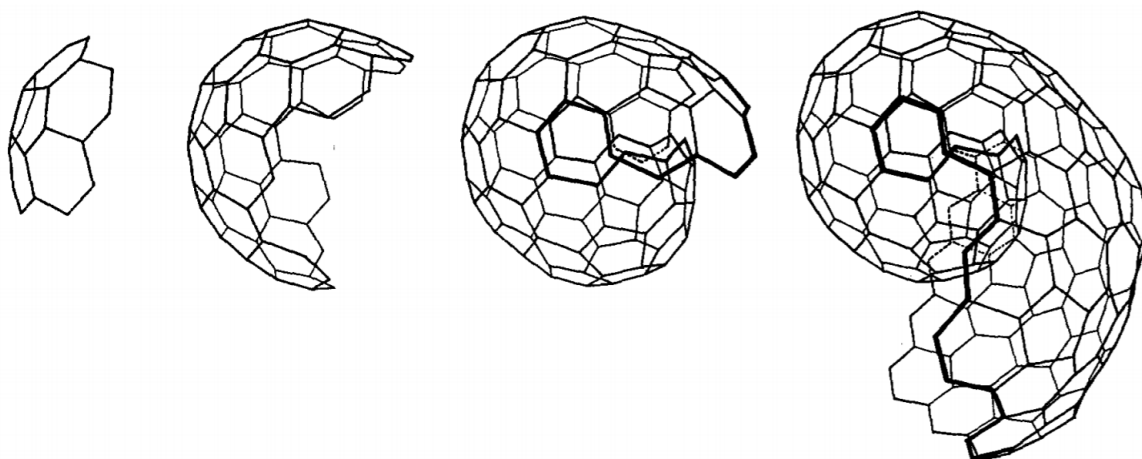
Fig. 2.4 Icospiral mechanism for the formation of fullerenes as described by Kroto [161]. (a) corannulene, (b) growth of curved structure by edge reactions, (c) a structure forming a second shell that can close and form a fullerene, (d) a structure with a second shell that was suggested to form a carbonaceous particle, later disproven by Frenklach and Ebert [79]. Taken from Kroto [161] with permission from Elsevier ©.

Although these pathways seem to be important in the presence of a vapour of carbon atoms, they do not appear to explain the formation of fullerenes in flames. Fullerenes are produced alongside carbonaceous particles in regions of high temperature [121] and in the presence of oxidising species [130, 118] in low pressure benzene [121] and acetylene [344] flames. Several mechanisms have been proposed to explain this phenomena. The addition of carbon atom dimers to smaller fullerenes has been proposed to explain the growth into larger fullerenes [60]. However, the formation of the first fullerene was suggested to be different. Richter and Howard [263] discussed the two main mechanisms that have been suggested to

explain their formation. First, the icospiral mechanism [361] was proposed to explain the formation of both fullerenes and carbonaceous particles in flames. However, coagulation, which is critical in the formation of carbonaceous particles [79], was neglected in the initial analysis. Frenklach and Ebert [79] showed that the HACA mechanism is able to explain the formation of molecules as large as fullerenes in flames without the addition of carbon atom dimers. The presence of corannulene, the smallest cPAH, in both fullerenic [165, 166] and non-fullerenic flames [165] supports this explanation. Using HACA and bay closure reactions as the main growth processes for fullerenes, Pope et al. [249] proposed a chemical mechanism that was able to predict the formation of fullerenes. This mechanism was later extended by Richter et al. [266].

The second mechanism was proposed by Homann [121]. As discussed in Section 2.3.1, it is based on the concept of aromatic oligomers or aromers. Figure 2.5 shows the steps suggested in the formation of curved structures and fullerenes. The figure shows a crosslinked structure forming five-member rings via bay closure (cyclodehydrogenation) reactions and their embedding via HACA growth [359]. The collision of aromers were suggested to explain the formation of fullerenes via the zipper mechanism instead of growing via HACA (bimolecular) reactions [121].
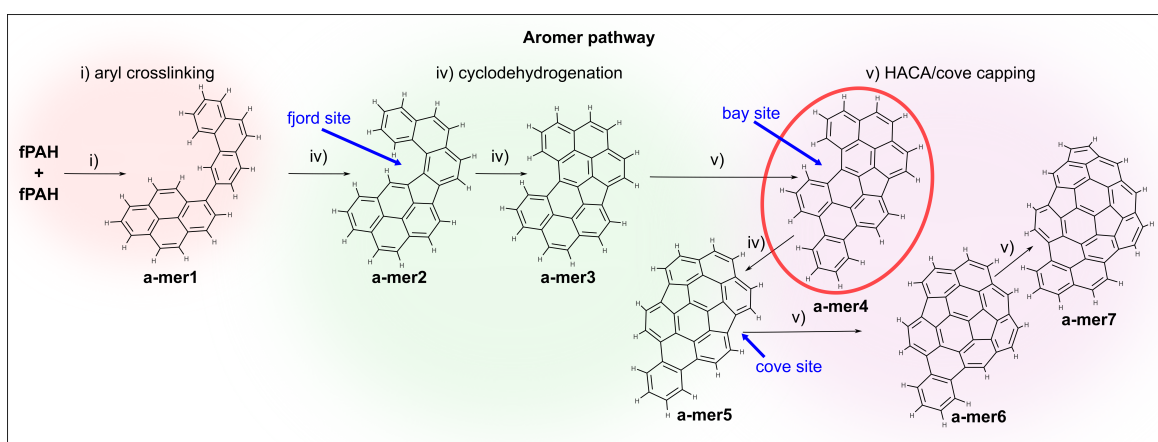
Fig. 2.5 Integration of curvature on aromers as suggested by Homann [121]. The product structure can participate in the formation of carbonaceous particles and fullerenes. The structure circled in red is based on the structure imaged in HR-AFM [45]. This figure is provided courtesy of Jacob W. Martin © and is used with permission.

Other processes have been suggested to be important for the synthesis of fullerenes in hydrocarbon flames. The oxidation of six-member rings has been suggested as a possible pathway to explain the large amount of five-member rings that are present in fullerenes [130, 93]. This observation agrees with the results from Frenklach and collaborators [293, 65, 85, 294], who suggested that molecular oxygen produces five-member rings by oxidising

six-member rings. Also important are the internal rearrangements suggested by Scott and collaborators [281]. Using flash vacuum pyrolysis at high temperatures, they showed that cyclodehydrogenation processes create condensed PAHs via the formation of carbenes. These processes appear to play an important role in the formation of curved structures (see Figure 2.5). Although the combustion synthesis of fullerenes is still not fully understood, it has been suggested to have the largest potential to reach an industrial scale production [281, 309].

2.5 Gas-phase formation of graphene

Graphene can be produced by several methods. For example, Lee et al. [172] and Choi et al. [39] give chemical vapour deposition, thermal annealing of amorphous carbon, unzipping carbon nanotubes, solvothermal synthesis, thermal decomposition of carbides, and different methods for the exfoliation of single layers from graphite as some of the methods to produce graphene. From these methods, chemical vapour deposition (CVD) appears to be the most promising to achieve significant production rates of graphene [172]. The mechanism for the formation of graphene in CVD is heavily dependant in the interaction of carbonaceous species and the substrate, typically a metal like copper or nickel, on which they are deposited [224]. Species adsorbed onto the substrate are dehydrogenated via a catalytic decomposition producing single carbon atoms. These carbon atoms either diffuse into the bulk of the substrate or form dimers that stay on the surface. Eventually diffusion processes arrange the carbon atoms next to each other on the surface of the substrate and nucleate a graphene sheet [224]. Ab initio calculations have shown that these graphene sheets grow by the addition of single carbon atoms and dimers to the different sites on the graphene edge [88]. This process is similar to the growth of PAHs in the gas phase being dependant on the reaction site.

Recently, another method to synthesise graphene in the absence of a substrate has gained attention. Graphene can be produced alongside carbonaceous particles in the gas phase of plasma reactors in a process that was first proposed by Dato et al. [57]. The main setup for this synthesis utilises a generator to create a surface wave induced microwave plasma at atmospheric conditions [315]. The microwave power is provided by a generator with variable input power. The discharge takes place inside a quartz tube which is inserted vertically and perpendicularly to the waveguide wider wall. This tube operates as a plasma reactor where argon and a hydrocarbon are fed under laminar gas flow conditions. Typically the hydrocarbon used for this setup is ethanol that has been previously vaporised, but liquid feeds have also been studied [57, 56, 225]. The reactor flue gases are then passed through a

cooling section that can either be water cooled (as in the design by Tatarova et al. [315]) or not cooled by any additional media (as in the design by Münzer et al. [225]). The produced graphene flakes are then collected in a filter connected to a vacuum pump. Figure 2.6 shows the apparatus for the synthesis of graphene from plasma reactors as per described by Tatarova et al. [315].
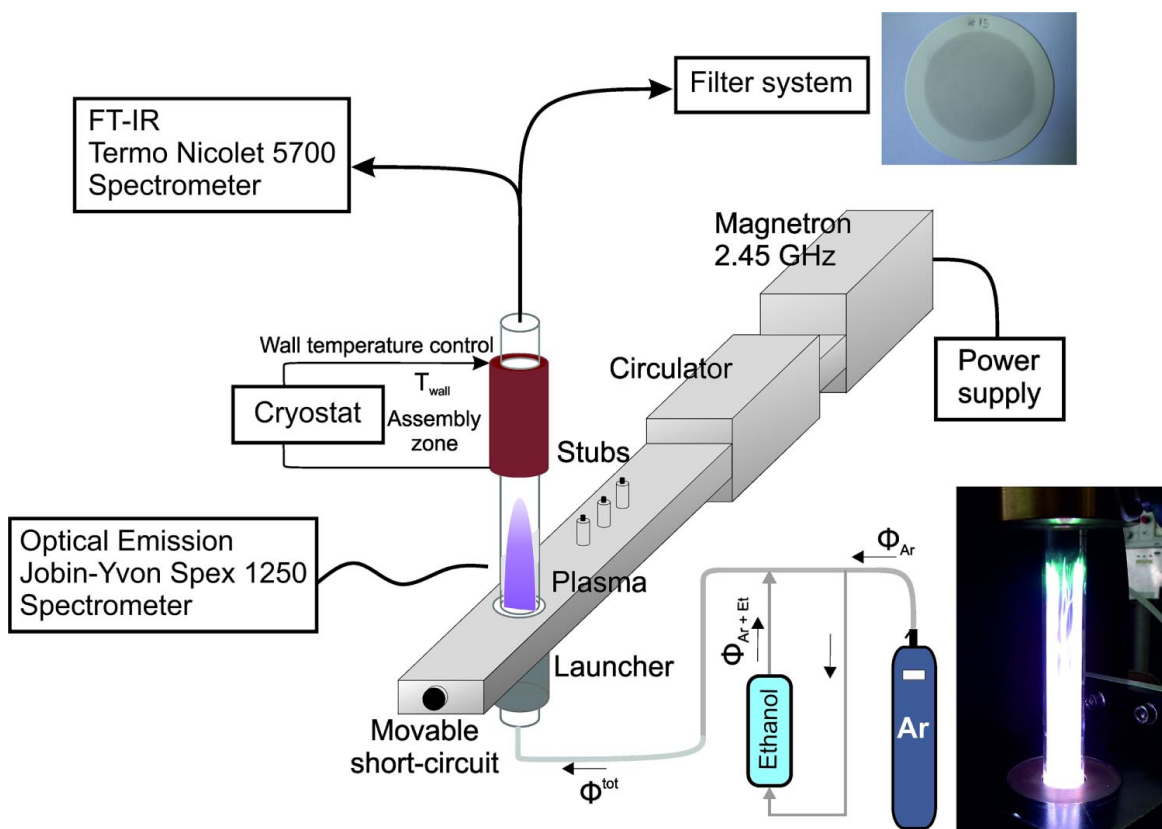
Fig. 2.6 Experimental setup for the plasma assisted synthesis of gas phase graphene. Taken from Tatarova et al. [315] with permission from IOPScience ©.

Different variables have been studied to understand the formation of graphene in the microwave plasma system. Dato and Frenklach [56] studied the effect of replacing ethanol as the main precursor of the synthesis for methanol, isopropyl alcohol and dimethyl ether. They found that ethanol and dimethyl ether produced higher quality graphene while the other precursors produced carbonaceous particles. The effect of varying input power to the plasma reactor has been studied by Dato and Frenklach [56] and Tatarova et al. [315]. Dato and Frenklach [56] did not find structural changes as a function of input power which suggested that the formation and growth of graphene occurs in the afterglow region of the plasma. Tatarova et al. [315] found that reducing the input power from 500 to 400 W resulted in the production of carbonaceous nanoparticles instead of graphene. The effect of different

flow rates of ethanol has been studied by Dato and Frenklach [56] and Tatarova et al. [315]. Both studies found that lower flow rates of precursor to the reactor resulted in the production of graphene, while high flow rates resulted in the production of amorphous carbons. Of particular interest is the observation made by Tatarova and collaborators [315, 314]. In their experiments they found that reducing the temperature in the afterglow region of the plasma resulted in the production of graphene instead of carbonaceous particles. They attributed the formation of carbonaceous particles to the creation of additional solid nuclei at lower temperatures that resulted in agglomeration of the graphene molecules and formation of graphite.

The production of graphene in microwave plasma reactors has been modelled by Tsyganov et al. [323]. They assumed that local thermal equilibrium was present in the high temperatures (2200 K) produced in the plasma. The chemical mechanism first used by Marinov [186] was adapted to this system by adding reactions from different publications [301, 300, 187, 321] to account for the production of species missing in the original mechanism. The model by Tsyganov et al. [323] included heat losses through the plasma reactor walls and their effect over the rate coefficients by calculating a radial averaged rate coefficient over the simulation domain. In their model carbon atoms and carbon atom dimers (C2) were produced in the plasma region. It was assumed that when these species diffused out of the plasma region they crossed a boundary of vaporization that corresponded to reaching the condensation temperature of solid carbon (1800 K). By reaching this temperature it was assumed that solid carbon (graphene) was formed. Subsequent diffusion of carbon atoms and carbon atom dimers from the plasma into the assembly zone contribute to the growth of graphene sheets. The model accounted for the formation of carbonaceous particles on the lower temperature walls of the reactor as well as the formation of the main gas phase products (ethylene, acetylene, carbon monoxide and hydrogen). Figure 2.7 presents the reactions and processes described by Tsyganov et al. [323] for the production of graphene from ethanol in a microwave plasma reactor. Two main channels for the decomposition of the precursor were reported: First, the scission of the C–C bond to form CH_2OH that eventually produces CO, and CH_3 that produces ethylene and acetylene via recombination of two methyl species. Second, the loss of the OH group that produces ethylene and subsequently acetylene. The model proposed by Tsyganov et al. [323] suggested that the growth and formation of carbonaceous materials happens in the afterglow region of the reactor when the temperature is better suited for these processes.

The model by Tsyganov et al. [323] did not account for the formation and growth of PAHs. These species, as discussed in Section 2.1, are critical in the formation of carbonaceous particles and fullerenes. It is not clear if the formation of graphene in the plasma synthesis
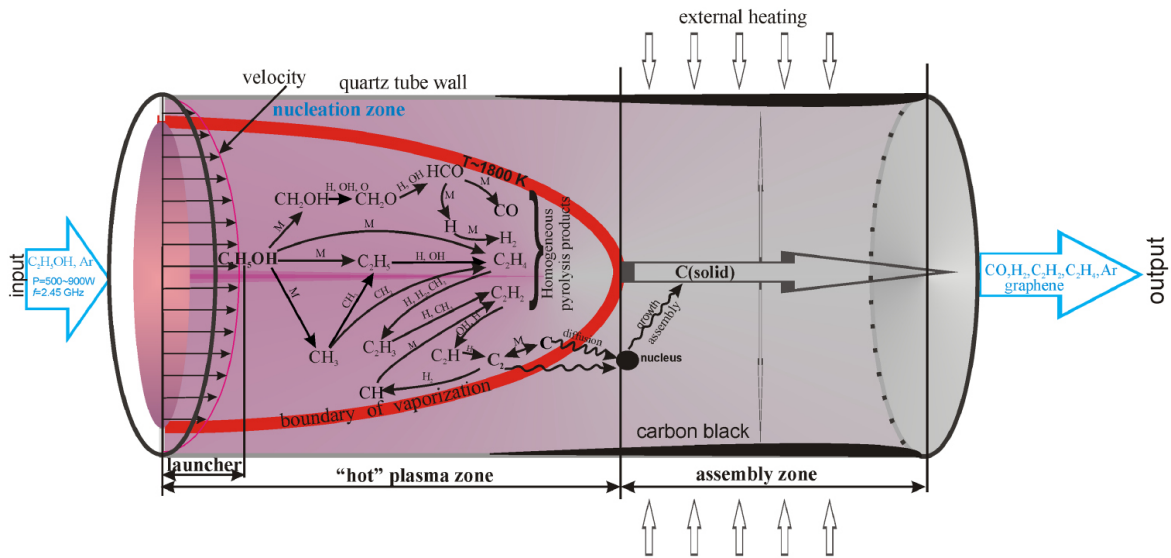
Fig. 2.7 Scheme showing the main reactions and processes in the plasma and assembly regions in the plasma synthesis of graphene as given by Tsyganov et al. [323]. Taken from Tsyganov et al. [323] with permission from IOPScience ©.

discussed here is driven by rearrangement of individual carbon atoms and dimers, as is the case in the synthesis of graphene via CVD, or by a gas phase growth mechanism like the one that controls the growth of carbonaceous particles (HACA, Section 2.2.2). Certainly, the temperatures at which carbon structures are suggested to be formed in the study by Tsyganov et al. [323] agree with temperatures that are suitable for the formation of carbonaceous particles. The plasma used in the decomposition of ethanol is crucial in the formation of graphene. Esarte et al. [70] studied the pyrolysis of ethanol in the presence of nitrogen at temperatures up to 1200 C and reported similar gas phase products but only soot particles as solid products. The temperatures reported for the plasma synthesis are around 2000 K [323]. Besides the temperature of the decomposition, excited gas phase species may contribute to the formation of graphene. For example, large amounts of excited atomic oxygen has been reported in air microwave plasma reactors [312] and air-water mixtures [313]. The presence of oxygen atoms has also been reported in the ethanol decomposition [138] but carbon materials were not synthesised in these experiments. It is not clear if oxygenated species play a role in the formation of graphene but these species certainly trigger other decomposition processes as is well known in the field of plasma assisted combustion [143].

Recently the microwave plasma reactor such as the one shown in Figure 2.6 has been used to produce nitrogen-doped graphene and graphene coated nanoparticles. Nitrogen-doped graphene has been synthesised by adding nitrogen gas to the plasma reactor [316] or by feeding an ethanolic solution of ammonia instead of pure ethanol [24]. In both cases atomic

nitrogen is produced in the plasma which is confirmed by the appearance of CN bands in the plasma emission spectra [316]. The nitrogen atoms produced in the plasma region are integrated to the graphene sheets producing nitrogen-doped graphene. Additionally, the plasma reactor has been used to produce graphene coated metallic composites in a two step process [225, 109, 13, 137] and as a synthesis in the afterglow region of the plasma [54]. The coated materials have been tested for different applications such as water remediation [109] and energy storage [13, 225]. Other possible applications for gas phase synthesised graphene are given by Dato [55]. Examples of such applications include catalysis, lubrication and electrical applications. Overall the quality of the graphene produced via the plasma synthesis method appears to be equivalent to other methods [55].

Other set of plasma experiments that is worth discussing is that of Bundaleska et al. [25] and Singh et al. [292]. The former group used the same setup as the one shown in Figure 2.6 but replaced ethanol as precursor with methane at similar dilution ratios but higher input power (1–1.5 kW). They found that graphene was produced alongside carbonaceous particles. They also found that higher input powers increased the yield of carbonaceous products but at the cost of producing carbonaceous particles instead of graphene. In the experiments performed by Singh et al. [292], hydrogen was added to the methane and argon mixture. Graphene was produced alongside carbonaceous particles but a significant increase in product quality and reduction in the number of carbonaceous particles formed. This contrasts with the observations from Tsyganov et al. [323] and Bundaleska et al. [25] that suggested that additional hydrogen in the gas phase reduced the yield of solid products and increases the presence of sp^3 carbon. It is not clear if the graphene synthesised in the presence of methane and hydrogen follows the same pathways as the decomposition of ethanol. However, the range of temperatures is suitable for the formation of PAHs and carbonaceous particles.

In non-plasma conditions, large molecules that resemble graphene have been detected alongside carbonaceous particles in low pressure acetylene flames [344, 347]. In these experiments large molecules were sampled using time-of-flight mass spectrometry. Large molecules of over 300 carbon atoms were identified with C/H ratios of above 6.0. Homann and collaborators concluded that the large amount of hydrogen sampled in such large molecules was an indication that only few five-member rings were embedded in the atomic structure [344]. Graphene has not been reported in any flame experiment. It appears that flames are suitable for the formation of carbonaceous particles and fullerenes only.

Chapter 3

Detailed particle model

This chapter presents a mathematical description of a detailed population balance model that captures the structure and composition of carbonaceous materials. The model describes particle aggregates that are constituted by their primary particles and the connectivity between these primaries. Each primary in turn is formed by polycyclic aromatic hydrocarbons (PAHs) that describe its chemical composition. In the model, the PAHs are constituted by a series of interconnected carbon atoms and reactive sites susceptible to surface reactions. The implementation of the mathematical model is discussed as are the approximations used to estimate the process rates. The numerical algorithms used to solve the population balance equation are described. A new algorithm to solve the migration of partially-embedded five-member rings is proposed and its exactness and computational performance is studied.

3.1 Introduction

This chapter presents the model to describe carbonaceous materials that is developed in this work. There are two layers in the model. First, the *particle layer* keeps track of the number of particles and their connectivities. Second, the *molecular layer* keeps track of the composition and the internal structure of particles. Although most of the work described in this thesis was performed in the molecular layer of the model, the whole model is shown for completeness. The model is based on the Polycyclic Aromatic Hydrocarbon–Primary Particle (PAH-PP) model [276] and the Kinetic Monte Carlo–ARomatic Site (KMC-ARS) model [256] but draws from other works [33, 32, 31, 257, 258, 37, 358, 357, 123]. The model uses a Kinetic Monte Carlo (KMC) algorithm, commonly known as the Gillespie algorithm [92], to evaluate the transformation of carbonaceous materials.

Early versions of the stochastic model used a two-dimensional representation of PAHs. However, recent studies have shown that the curvature of PAHs is an important characteristic that affects their reactivity [255] and morphology [349]. As demonstrated by Yapp et al. [358], the simplest computational representation of a non-planar PAH consists in storing the reactive edge sites arranged in order, without taking into account the positions of carbon atoms. This *site list* can be used to track the edge of a PAH molecule and study the processes that transform its structure. Morphological information of the carbonaceous material can be inferred from this representation of a molecule. However, as the structure becomes more complicated, this computational representation relies on assumptions that can affect the predictions of such a model (*e.g.* steric hindrance or the internal positions of five-membered rings). For this reason, a model that keeps track of the details of the PAHs that constitute carbonaceous materials is proposed in this work.

The next sections explain the mathematical description of the detailed particle model used in this work and its implementation. Section 3.2 introduces the type space for a detailed particle model of carbonaceous materials. Section 3.3 introduces the state space of the model. Section 3.4 shows the particle and PAH jump processes that modify the state of the particles contained in the model. Section 3.5 discusses the steady-state and partial-equilibrium approximations used in the calculation of PAH jump process rates. Section 3.6 elaborates on the implementation of the model. Section 3.7 details the numerical methods used in the solution of the detailed particle model. Lastly, Section 3.8 provides details for all rates and processes implemented in the model.
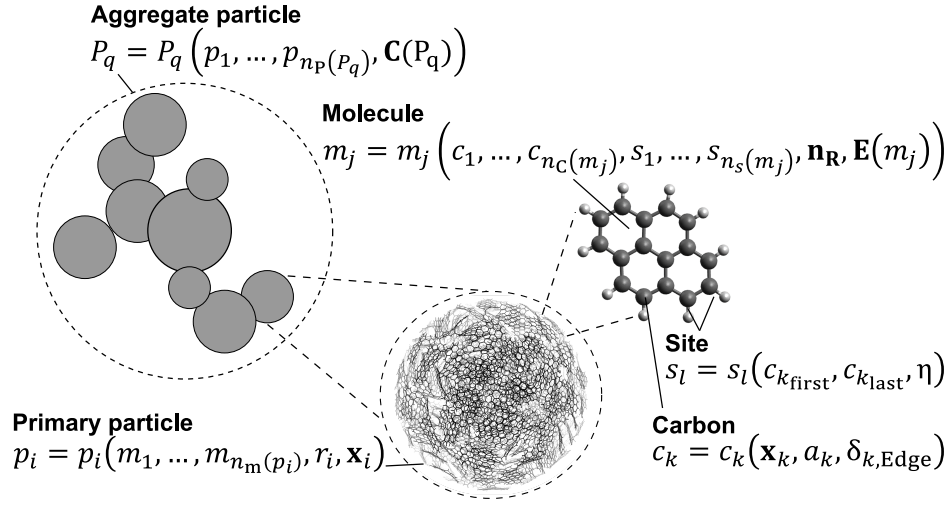
Fig. 3.1 The different levels (aggregate, primary, molecule, carbon and site) of the type space used for representing carbonaceous materials.

3.2 Type space

The type space is the space used for mathematically representing particles. In this work there are different layers of information that are used to represent particles. Figure 3.1 shows briefly the type space hereby used. In a detailed particle type space containing N_P aggregate particles, an aggregate P_q, with $q \in \{1, \ldots, N_P\}$, containing $n_p(P_q)$ primary particles can be represented as

$$P_q = P_q\left(p_1, \ldots, p_{n_p(P_q)}, \mathbf{C}(P_q)\right), \tag{3.1}$$

where $\mathbf{C}$ represents the connectivity of the $n_p(P_q)$ primary particles. $\mathbf{C}$ is a lower diagonal matrix of dimension $n(P_q) \times n(P_q)$ with matrix elements:

$$C_{ij} = \begin{cases} 0, & \text{if } p_i \text{ and } p_j \text{ are not neighbouring;} \\ 1, & \text{if } p_i \text{ and } p_j \text{ are neighbouring.} \end{cases} \tag{3.2}$$

A general primary particle p_i, with $i \in \{1, \ldots, n_p(P_q)\}$, is represented by

$$p_i = p_i\left(m_1, \ldots, m_{n_m(p_i)}, r_i, \mathbf{x}_i\right). \tag{3.3}$$

A primary particle is formed by $n_m(p_i)$ molecules, has a radius r_i and a vector of spatial coordinates $\mathbf{x}_i \in \mathbb{R}^3$ located at the centre of the primary particle assuming it to be spherical. The primary particles in an aggregate can be seen as overlapping spheres such that the

distance, d_{ij}, between two particles p_i and p_j, can be calculated as

$$d_{ij} = |\mathbf{x}_i - \mathbf{x}_j|. \tag{3.4}$$

Equations 3.1 to 3.4 constitute the particle layer of the model. This particle description is not unique to carbonaceous materials and has been used to study other materials, such as titanium dioxide [178, 185]. The molecular layer of the model, which is the main focus of this work, is described below only for carbonaceous materials.

PAHs are the constituting molecules of each primary particle. A general molecule m_j, with $j \in \{1, \ldots, n_{\mathrm{m}}(p_i)\}$, can be represented as

$$m_j = m_j\left(c_1, \ldots, c_{n_{\mathrm{C}}(m_j)}, s_1, \ldots, s_{n_{\mathrm{s}}(m_j)}, \mathbf{n_R}(m_j), \mathbf{E}(m_j)\right). \tag{3.5}$$

In Equation 3.5, each molecule contains $n_{\mathrm{C}}(m_j)$ carbon atoms, $n_{\mathrm{s}}(m_j)$ reactive sites, a vector $\mathbf{n_R}(m_j)$ with the number of rings, and the connectivity of each carbon atom in the edge connectivity matrix $\mathbf{E}(m_j)$. The number of rings vector is defined as:

$$\mathbf{n_R}(m_j) = \begin{bmatrix} n_{\mathrm{R6}}(m_j) \\ n_{\mathrm{R5}}(m_j) \\ n_{\mathrm{R5_{emb}}}(m_j) \\ n_{\mathrm{R7}}(m_j) \end{bmatrix}, \tag{3.6}$$

where $n_{\mathrm{R6}}(m_j)$ is the number of six-member rings, $n_{\mathrm{R5}}(m_j)$ is the number of edge five-member rings, $n_{\mathrm{R5_{emb}}}(m_j)$ is the number of embedded five-member rings, and $n_{\mathrm{R7}}(m_j)$ is the number of seven-member rings, all for molecule m_j. The elements of $\mathbf{n_R}(m_j) \in \mathbb{N}$.

A general carbon atom c_k, with $k \in \{1, \ldots, n_{\mathrm{C}}(m_j)\}$, can be represented as

$$c_k = c_k\left(\mathbf{x}_k, a_k, \delta_{k,\mathrm{Edge}}\right), \qquad \text{where} \tag{3.7}$$

$$\delta_{k,\mathrm{Edge}} = \begin{cases} 1, & \text{if the atom is at the edge;} \\ 0, & \text{otherwise.} \end{cases} \tag{3.8}$$

A carbon atom has a vector of spatial coordinates $\mathbf{x}_k \in \mathbb{R}^3$, a third connected atom type a_k and a binary variable $\delta_{k,\mathrm{Edge}}$ to indicate if the atom is currently on the edge of the molecule. Since there is a distinction between internal and edge carbon atoms, it is useful to split the total number of carbon atoms $n_{\mathrm{C}}(m_j)$ into $n_{\mathrm{C,Internal}}(m_j)$ and $n_{\mathrm{C,Edge}}(m_j)$, the total number of internal and edge carbon atoms, respectively. For the edge atoms, the third connected atom type a_k can either be another carbon atom or a non-carbon atom. In this model, only
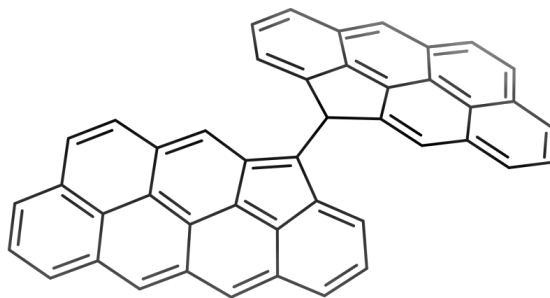
Fig. 3.2 Example of a crosslinked PAH.

carbon and hydrogen atoms are considered, and as such the quantity $n_H(m_j)$ is used to refer to the total number of hydrogen atoms in molecule m_j. The edge connectivity matrix $\mathbf{E}(m_j)$ stores the information about neighbouring edge carbon atoms, with each edge comprising exactly two atoms. It has size $n_{C,Edge}(m_j) \times n_{C,Edge}(m_j)$ and has values E_{k_1,k_2} defined as

$$E_{k_1,k_2} = \begin{cases} 1, & \text{if } c_{k_1} \text{ is a neighbour of } c_{k_2}, \text{with } k_1, k_2 \in \mathcal{I}_{Edge}(m_j), \\ 0, & \text{otherwise,} \end{cases} \tag{3.9}$$

where $\mathcal{I}_{Edge}(m_j)$ represents the set of edge carbon atom indices for molecule m_j. It is important to notice that this representation allows two edge atoms to be connected without this bond being part of a ring. This kind of connection is referred to as a *crosslink* in this work. An example of such a molecule is shown in Figure 3.2.

Lastly, the general reactive *site*, s_l, with $l \in \{1, \ldots, n_s(m_j)\}$ is defined as

$$s_l = s_l \left(c_{k_{first}}, c_{k_{last}}, \eta_l \right), \tag{3.10}$$

where $k_{first}, k_{last} \in \mathscr{I}_{Edge}(m_j)$ and the carbon atoms $c_{k_{first}}$ and $c_{k_{last}}$ both have a third connected atom type different than carbon ($a_{k_{first}}, a_{k_{last}} \neq C$). The site type η, with $\eta \in \{FE, ZZ, \ldots\}$, is determined by the shortest path between the two carbon atoms in the graph defined by $\mathbf{E}$, where all other carbon atoms in the path have an $a_k = C$. Figure 3.3 shows the main available sites in common PAHs. It is useful to define the set of carbon atoms, $\mathcal{C}(m_j)$, and the set of sites, $\mathcal{S}(m_j)$, of molecule m_j to simplify Equation 3.5:

$$\mathcal{C}(m_j) = \{c_1, \ldots, c_{n_C(m_j)}\} \tag{3.11}$$

$$\mathcal{S}(m_j) = \{s_1, \ldots, s_{n_s(m_j)}\} \tag{3.12}$$
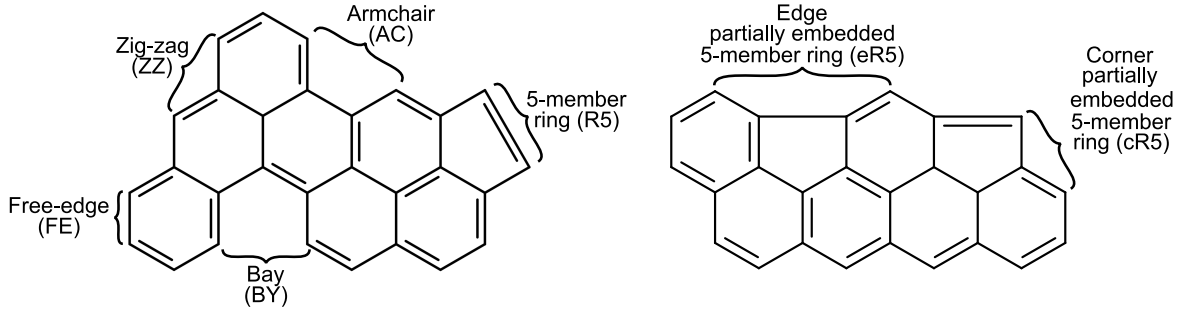
Fig. 3.3 Elementary site types of a PAH.

Derived particle quantities

The following derived quantities correspond to the particle layer of the model and are shown for completeness. The derivation of these quantities can be found in [276, 275, 285, 178]. The derived particle quantities can be obtained in terms of the internal variables of each particle:

Primary particle mass: The mass, $\mathfrak{m}(p_i)$, of a primary particle p_i is calculated in terms of its chemical composition:

$$\mathfrak{m}(p_i) = \left(\sum_{j=1}^{n_\mathrm{m}(p_i)} n_\mathrm{C}(m_j) \times M_\mathrm{C} + \sum_{j=1}^{n_\mathrm{m}(p_i)} n_\mathrm{H}(m_j) \times M_\mathrm{H} \right) / \mathrm{N_A}, \qquad (3.13)$$

where the molecular weights, M, of carbon (C) and hydrogen (H) are 12.01 and 1 g/mol, respectively, and $\mathrm{N_A}$ is the Avogadro constant.

Primary particle volume: The volume, $v(p_i)$, of a primary particle p_i is calculated in terms of its mass and density:

$$v(p_i) = \frac{\mathfrak{m}(p_i)}{\rho_\mathrm{mat}}, \qquad (3.14)$$

where $\rho_\mathrm{mat}(:= 1.8 \text{ g cm}^{-3})$ [37] is the density of the material, assumed to be a constant in this work.

Primary particle diameter: The diameter, $d(p_i)$, of primary particle p_i is calculated by assuming each primary particle to be spherical:

$$d(p_i) = \left(\frac{6v(p_i)}{\pi} \right)^{1/3}. \qquad (3.15)$$

Primary particle surface area: The surface area, $\mathfrak{s}(p_i)$, of primary particle p_i is given by:

$$\mathfrak{s}(p_i) = \pi \left(d(p_i)\right)^2. \tag{3.16}$$

Aggregate volume: The sum of the individual volume of all the primary particles is equal to the volume, $V(P_q)$, of aggregate P_q:

$$V(P_q) = \sum_{i=1}^{n_{\mathrm{p}}(P_q)} v(p_i). \tag{3.17}$$

Aggregate surface area: The surface area, $S(P_q)$, of aggregate P_q is calculated based on the average sintering level of the particle [276]:

$$S(P_q) = \frac{S_{\mathrm{sph}}(P_q)}{\mathscr{C}_{\mathrm{avg}}(P_q)\left(1 - n_{\mathrm{p}}(P_q)^{-1/3}\right) + n_{\mathrm{p}}(P_q)^{-1/3}}, \tag{3.18}$$

where $S_{\mathrm{sph}}(P_q) = 4\pi(3V(P_q)/4\pi)^{2/3}$ is the spherical surface of P_q and $\mathscr{C}_{\mathrm{avg}}(P_q)$ is the average coalescence level of the particle aggregate, defined as:

$$\mathscr{C}_{\mathrm{avg}}(P_q) = \frac{\sum_{i,j=1}^{n_{\mathrm{p}}(P_q)} \mathscr{C}(p_i, p_j)}{n_{\mathrm{p}}(P_q) - 1}. \tag{3.19}$$

$\mathscr{C}(p_i, p_j)$ is the coalescence level between two connected primary particles p_i and p_j and is defined as:

$$\mathscr{C}(p_i, p_j) = \frac{\left(S_{\mathrm{sph}}(p_i, p_j)/\mathfrak{s}(p_i, p_j)\right) - 2^{-1/3}}{1 - 2^{-1/3}}. \tag{3.20}$$

$S_{\mathrm{sph}}(p_i, p_j)$ is the surface area of a sphere with the same volume as those of primaries p_i and p_j:

$$S_{\mathrm{sph}}(p_i, p_j) = 4\pi \left(\frac{3(v(p_i) + v(p_j))}{4\pi}\right)^{2/3}, \tag{3.21}$$

and $\mathfrak{s}(p_i, p_j)$ is the common surface area of two neighbouring primary particles. If these particles are in point contact then:

$$\mathfrak{s}(p_i, p_j) = \mathfrak{s}(p_i) + \mathfrak{s}(p_j). \tag{3.22}$$

After the primaries change in size, the change in common surface area $\Delta\mathfrak{s}(p_i, p_j)$ can be calculated as:

$$\Delta\mathfrak{s}(p_i, p_j) = \Delta v(p_i, p_j)\frac{2}{R_g}, \tag{3.23}$$

where $\Delta v(p_i, p_j)$ is the volume change of the primary particles p_i and p_j, and R_g is the radius of gyration calculated as

$$R_g = \frac{1}{\sum_{i=1}^{n_p(P_q)} \mathfrak{m}_i} \sum_{i=1}^{n_p(P_q)} \mathfrak{m}_i \left| x_i - x_{com} \right|^2, \tag{3.24}$$

where the aggregate centre of mass, x_{com}, is calculated as $\sum_{i=1}^{n_p(P_q)} \mathfrak{m}_i x_i$. Under these definitions, the coalescence level is bound so that $0 \leq \mathscr{C}(p_i, p_j) \leq 1$ for all primary particles. It is assumed that two primaries p_i and p_j are completely sintered if the coalescence level $\mathscr{C}(p_i, p_j)$ is greater than 0.95 [276, 275].

Collision diameter: The collision diameter, $d_{col}(P_q)$, of aggregate P_q is assumed to be [356]:

$$d_{col}(P_q) = d_{avg}(P_q)n_p(P_q)^{1/D_f}, \tag{3.25}$$

where $d_{avg}(P_q)$ is the average primary particle diameter of aggregate P_q and D_f is the fractal dimension of the aggregate. In the case of carbonaceous particles, the fractal dimension is assumed to be constant and equal 1.8.

If P_q consists of a single primary particle then the collision diameter is assumed to be:

$$d_{col}(P_q) = \max\left(\left(\frac{6V(P_q)}{\pi}\right)^{1/3}, d_{AR}\left(\frac{2\sum_{j=1}^{n_m(p_i)} n_C(m_j)}{3}\right)^{1/2}\right), \tag{3.26}$$

where d_{AR} is the size of a single aromatic ring, equal to $1.395 \times 3^{1/2}$ Å.

3.3 State space

The state of the system, Q, at any time consists of three components [285].

1. The first component, Q_1, contains the concentration of the chemical species:

$$Q_1 = \left\{ C_k : k \in \{1, \ldots, N_g\} \right\}, \tag{3.27}$$

where C_k is the gas-phase concentration of the k-th species and N_g is the number of gas-phase species.

2. The second component, Q_2, is the stochastic particle system:

$$Q_2 = \left\{ P_q : q \in \{1, \ldots, N_P\} \right\}, \tag{3.28}$$

where P_q is the q-th particle in the system, Equation 3.1, and N_P is the total number of particles in the system.

3. The third component, Q_3, includes the temperature, T, and pressure, $\mathscr{P}$, of the system:

$$Q_3 = \{T, \mathscr{P}\}. \tag{3.29}$$

3.4 Jump processes

A particle in the type space defined in this work can be modified by jump processes that affect it at different levels. However, the time and length scales of these modifications can be substantially different. Because of this, they are subdivided into two groups, particle jump processes, reviewed in Section 3.4.1, and PAH jump processes, reviewed in Section 3.4.2.

3.4.1 Particle jump processes

Particles can experience four different kinds of transformations that modify their state.

Inception: A particle is formed by the collision of two individual gas-phase PAHs. This transformation can be described as

$$P_q(p_1(m_1), \mathbf{C}(P_q)) + P_r(p_1(m_2), \mathbf{C}(P_r)) \to P_s(p_1(m_1, m_2), \mathbf{C}(P_s)). \tag{3.30}$$
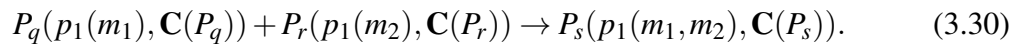
In this description two primary particles, each consisting of a single molecule, form a single primary particle with two molecules. The rate of collision between two particles

P_q and P_r is given by the transition coagulation kernel, $K^{\text{tr}}(P_q, P_r)$, as defined in [252]:

$$K^{\text{tr}}(P_q, P_r) = \frac{K^{\text{fm}}(P_q, P_r) K^{\text{sf}}(P_q, P_r)}{K^{\text{fm}}(P_q, P_r) + K^{\text{sf}}(P_q, P_r)}, \tag{3.31}$$

where the free-molecular collision kernel, $K^{\text{fm}}(P_q, P_r)$, is defined as:

$$K^{\text{fm}}(P_q, P_r) = 2.2 \left(\frac{\pi k_{\text{B}}}{2} \right)^{1/2} \left(T \left(\frac{1}{\mathfrak{m}(P_q)} + \frac{1}{\mathfrak{m}(P_r)} \right) \right)^{1/2} \left(d_{\text{col}}(P_q) + d_{\text{col}}(P_r) \right)^2, \tag{3.32}$$

where k_{B} is the Boltzmann constant. The slip-flow kernel, $K^{\text{sf}}(P_q, P_r)$, is defined as:

$$K^{\text{sf}}(P_q, P_r) = \frac{2 k_{\text{B}} T}{3\mu} \left(\frac{1 + 1.257 \text{Kn}(P_q)}{d_{\text{col}}(P_q)} + \frac{1 + 1.257 \text{Kn}(P_r)}{d_{\text{col}}(P_r)} \right) \left(d_{\text{col}}(P_q) + d_{\text{col}}(P_r) \right), \tag{3.33}$$

where μ is the dynamic viscosity, and $\text{Kn}(P_q)$ together with $\text{Kn}(P_r)$ are the Knudsen numbers of particles P_q and P_r. The Knudsen number, $\text{Kn}(P_q)$, for a particle P_q is defined as [178]:

$$\text{Kn}(P_q) = \frac{2\lambda_{\text{f}}}{d_{\text{col}}(P_q)}, \tag{3.34}$$

where λ_{f} is the mean free path of the surrounding gas. The mean free path and viscosity are approximated as those of air:

$$\lambda_{\text{f}} = 2.371 \times 10^{-5} \frac{T}{\mathscr{P}} \, \text{m} \tag{3.35}$$

$$\mu = 1.458 \times 10^{-6} \frac{T^{1.5}}{T + 110.4} \text{kg} \, \text{m}^{-1} \, \text{s}^{-1}. \tag{3.36}$$

The sticking probability of two molecules is determined by a simple collision efficiency model that compares the number of six-member rings in each collision partner [37]:

$$\text{P}_{\text{stick}} = \begin{cases} 1, & \text{if } n_{\text{R6}}(m_j) \geq n_{\text{R6, cutoff}}; \\ 0, & \text{otherwise.} \end{cases} \tag{3.37}$$

The cutoff number of rings, $n_{\text{R6, cutoff}}$ is assigned as 4 to represent pyrene dimerisation as suggested by Frenklach [76]. Other collision efficiencies models that have been proposed in the literature are those of Raj et al. [258], who suggested that the collision efficiency should be calculated with a probability distribution as a function of PAH diameter, and that of Hou et al. [124], who suggested the collision efficiency to be a function of PAH diameter and temperature.

Particle-particle process: The collision between two particles can lead to a coagulation process if there is enough collision energy or particle-particle affinity. In such an event, two particles P_q and P_r collide and form a larger aggregate particle P_s which contains the primary particles of both, which can be described as

$$P_q(p_1,\ldots,p_{n_p(P_q)},\mathbf{C}(P_q)) + P_r(p_1^*,\ldots,p_{n_p(P_r)}^*,\mathbf{C}(P_r)) \to$$
$$P_s(p_1,\ldots,p_{n_p(P_q)},p_1^*,\ldots,p_{n_p(P_r)}^*,\mathbf{C}(P_s)). \tag{3.38}$$
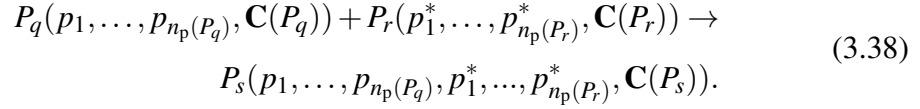
The connectivity of the resulting aggregate particle P_s aggregates can be obtained by different methods. For example, in ballistic cluster-cluster aggregation (see Jullien and Kolb [144]) three random parameters can be used to determine the single-point contact between two primary particles from the different aggregates obtaining a connectivity matrix

$$\mathbf{C}(P_s) = \begin{pmatrix} & & \vdots & & \\ & \mathbf{C}(P_q) & \ldots & 0 & \ldots \\ & \vdots & & \vdots & \\ \ldots & C_{qr} & \ldots & \mathbf{C}(P_r) & \\ & \vdots & & & \end{pmatrix}, \tag{3.39}$$

where $C_{qr} = 1$ represents the new point contact. The rate of collision between particles is calculated using the transition regime coagulation kernel in Equation 3.31.

Heterogeneous processes: Heterogeneous processes can either be condensation events or reactions between particles and gas-phase species. A condensation event can be represented as the addition of a molecule m_{j+1} from the gas-phase to a primary particle p_i within the aggregate P_q as

$$p_i(m_1,\ldots,m_j,\ldots,\mathbf{C}(P_q)) \to$$
$$p_i(m_1,\ldots,m_j,m_{j+1},\ldots,\mathbf{C}(P_q)), \tag{3.40}$$
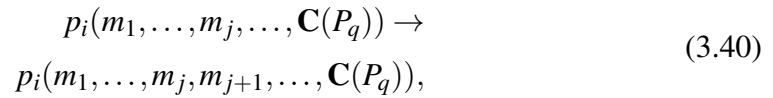
The rate of collision between the additional molecule and particle is calculated using the transition regime coagulation kernel in Equation 3.31 and the collision diameter for the molecule is calculated with Equation (3.26).

Reaction events between particles and gas-phase species can modify the molecules contained inside a primary particle. The details of how these are treated is discussed in Section 3.4.2.

Particle rounding: Particle rounding events are the consequence of heterogeneous additions. When two neighbouring particles increase in radius they can coalesce, where two primary particles p_i and p_j members of P_q form a single particle p_k, such that

$$P_q(p_1, \ldots, p_i, \ldots, p_{j-1}, p_j, p_{j+1}, \ldots, p_{n_p(P_q)}, \mathbf{C}(P_q)) \rightarrow$$
$$P_q^*(p_1, \ldots, p_i^*, \ldots, p_{j-1}, p_{j+1}, p_{n_p(P_q)}, \mathbf{C}(P_q^*)), \tag{3.41}$$

where p_i^* is the product of the coalescence and the star superscript indicates type space elements that are modified.

The change in volume due to heterogeneous additions results in the change in net common surface area of the primary particle p_i with all its neighbouring primaries. This change is described by Sander et al. [276] as

$$\Delta\mathfrak{s}(p_i, p_j) = \left(v(p_i') - v(p_i)\right) \frac{2\sigma}{d_{\text{sph}}(p_i, p_j)}, \tag{3.42}$$

where σ is the surface smoothing factor that can have values $0 \leq \sigma \leq 2$. A smoothing factor of 0 implies instantaneous coalescence, whereas a smoothing factor of 2 corresponds to no rounding. This parameter was studied by Chen et al. [37] and optimised to a value of 1.69 for soot particles from premixed ethylene flames.

Figure 3.4 shows the particle processes discussed in this section for carbonaceous particles as described by Sander et al. [276]

3.4.2   PAH jump processes

The chemical reactions between species in the gas phase and carbonaceous materials can be represented as transformations of the PAHs that constitute them. The reactions directly affect the number of carbon and hydrogen atoms, which are reflected in the mass and volume of primary particles. Several chemical reactions have been reported in the literature for individual PAHs. However, the number of available reactions is excessively large for a program to handle, besides being incomplete: reactions between gas phase species and PAHs are only typically studied for a few PAHs. For these reasons the PAH jump processes need to be grouped into types, each of them affecting one particular reactive site.

A PAH jump process modifies the state of the particle by either adding, removing or modifying carbon atoms, hydrogen atoms and the site where the PAH jump process is performed, as well as its neighbours. This means that, a general reaction between the reactive site s_v of molecule m_j with a gas-phase species A_{gas} creates a product m_j^*. In this

→ Particle inception
‑‑‑► Coagulation
→ Surface growth
⟹ Particle rounding due to surface growth
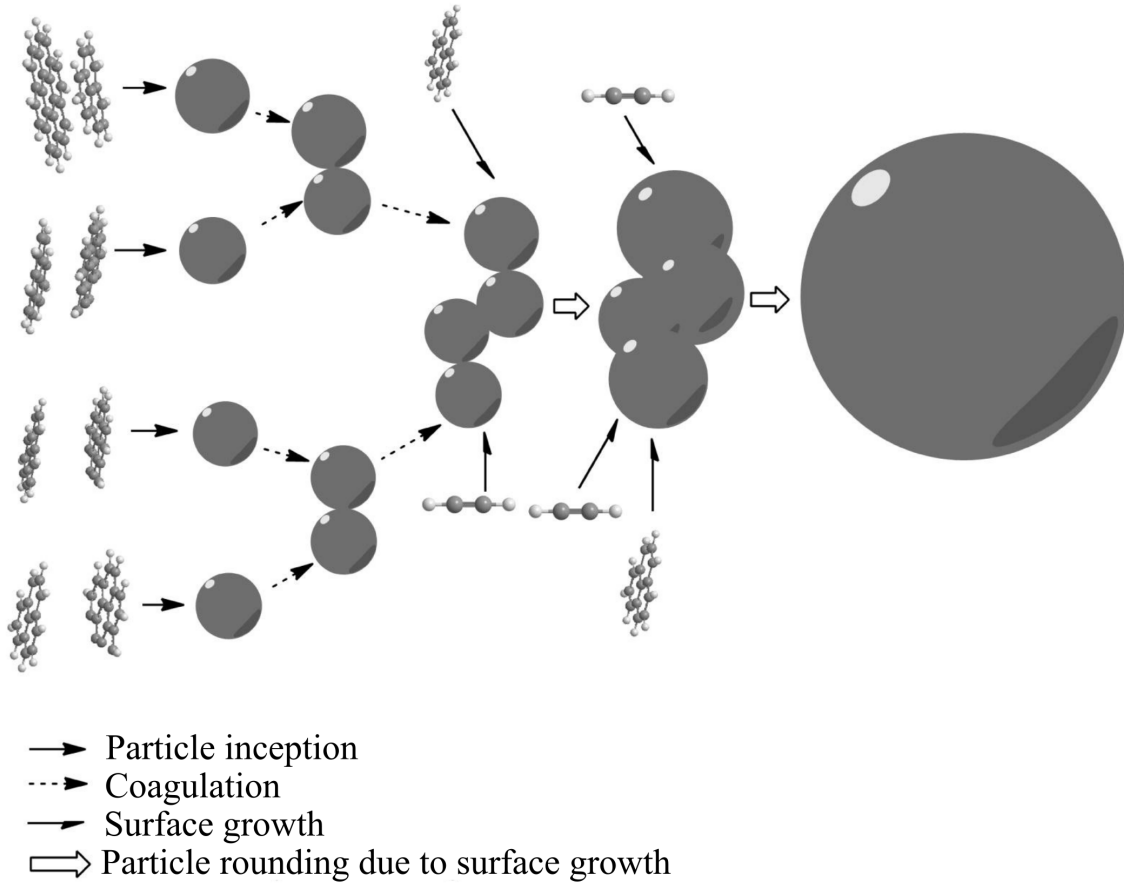
Fig. 3.4 Particle processes included in the detailed particle model. Taken from Sander et al. [276] with permission from Elsevier ©.

process $n_{C,Mod}$ existing carbon atoms are modified, $n_{C,New}$ carbon atoms are added and $n_{H,New}$ hydrogen atoms are added. This can be represented as

$$p_i\left(m_1,\ldots,m_j,\ldots,m_{n_m(p_i)},r_i,\mathbf{x}_i\right)+A_{gas} \rightarrow p_i\left(m_1,\ldots,m_j^*,\ldots,m_{n_m(p_i)},r_i^*,\mathbf{x}_i\right), \quad (3.43)$$

$$m_j\left(\mathcal{C}(m_j),\mathcal{S}(m_j),\mathbf{n_R}(m_j),\mathbf{E}(m_j)\right)+A_{gas} \rightarrow m_j^*\left(\mathcal{C}^*(m_j^*),\mathcal{S}^*(m_j^*),\mathbf{n_R^*}(m_j^*),\mathbf{E}^*(m_j^*)\right),$$
$$(3.44)$$

where the variables denoted with the star superscript are those modified by the gas-phase reaction. The set of carbon atoms, $\mathcal{C}(m_j)$ is modified to:

$$\mathcal{C}(m_j)=\{c_1,\ldots,c_{n_C(m_j)}\} \rightarrow \mathcal{C}^*(m_j^*)=\{c_1,\ldots,c_{n_C(m_j)},c_{1_{New}},\ldots,c_{n_{C,New}}\},$$

and the set of sites, $\mathcal{S}(m_j)$ is modified to:

$$\mathcal{S}(m_j) = \{s_1, \ldots, s_{v-1}, s_v, s_{v+1}, \ldots, s_{n_s(m_j)}\} \rightarrow \mathcal{S}^*(m_j^*) = \{s_1, \ldots, s_{v-1}^*, s_v^*, s_{v+1}^*, s_{n_s(m_j^*)}, \mathcal{S}_{\text{New}}\},$$

$$\mathcal{S}_{\text{New}} = \{s_{1_{\text{New}}}, \ldots, s_{n_{s,\text{New}}}\},$$

where $\mathcal{S}_{\text{New}}$ is the set of new sites added to molecule m_j^*. The modified general site s_v and its neighbours are

$$s_v\left(c_{k_{\text{first}}}, c_{k_{\text{last}}}, \eta_v\right) \rightarrow s_v^*\left(c_{1_{\text{New}}}, c_{n_{\text{C,New}}}, \eta_v^*\right),$$

$$s_{v-1}\left(c_{k_{\text{first, v-1}}}, c_{k_{\text{first}}}, \eta_{v-1}\right) \rightarrow s_{v-1}^*\left(c_{k_{\text{first, v-1}}}, c_{1_{\text{New}}}, \eta_{v-1}^*\right),$$

$$s_{v+1}\left(c_{k_{\text{last}}}, c_{k_{\text{last, v+1}}}, \eta_{v+1}\right) \rightarrow s_{v+1}^*\left(c_{k_{\text{first, v+1}}}, c_{1_{\text{New}}}, \eta_{v+1}^*\right),$$

and the affected carbons c_k are modified as

$$c_k\left(\mathbf{x}_k, a_k, \delta_{k,\text{Edge}}\right) \rightarrow c_k^*\left(\mathbf{x}_k, a_k^*, \delta_{k,\text{Edge}}^*\right), \quad \text{with } k \in \{1_{\text{Mod}}, \ldots, n_{\text{C,Mod}}\}.$$

The PAH processes used in this model are shown later in Section 3.8. However, before discussing the different possible processes, it is necessary to review the assumptions behind the rate equations for PAH jump processes. These can have different forms depending on the gas phase species that participate in the process and the reaction intermediates formed. Typically, the rate equation for the general PAH jump process i has the form

$$R_i = k_i \times f_i \times C_{A_{\text{gas}}} \times N_{\text{site},\eta_i}, \tag{3.45}$$

where k_i is the modified Arrhenius rate constant of the form $AT^n e^{-E_A/R_{\text{gas}}T}$, f_i is the fraction of radical sites, $C_{A_{\text{gas}}}$ is the concentration of the gas-phase species A_{gas}, and N_{site,η_i} is the number of reactive sites of type η_i that are available on the structure. R_i is the rate of jump process i for a single molecule. The summation of R_i over all molecules contained in an ensemble and its product with the particle number density allows an estimation of the volumetric rate for process i. The fraction of radical sites f_i is an important parameter of the rate equation. In previous works [32, 256, 257, 356, 37], this has been calculated using a steady-state approximation of the intermediate species considered to be the most important in the reaction scheme. For example, Figure 3.5 shows the steps along the pathway for the growth of a six-member ring from a free-edge site as defined by Raj et al. [256]. The rate

equation reported for this pathway has the form:

$$R_1 = k_2 \frac{k_1[H]}{k_{-1}[H_2] + k_{-3}[H] + k_2[C_2H_2]}[C_2H_2]N_{FE}, \qquad (3.46)$$

where the square brackets notation represents the concentration of a given species, k_1 the rate constant of a hydrogen abstraction, k_{-1} the reverse rate constant for a hydrogen abstraction, k_2 the rate constant of an acetylene addition, and k_{-3} the rate constant for a hydrogen termination. The site type associated with this process is a free-edge, so N_{FE} represents the number of free-edge sites available in a general molecule and the fraction represents the fraction of radical sites.
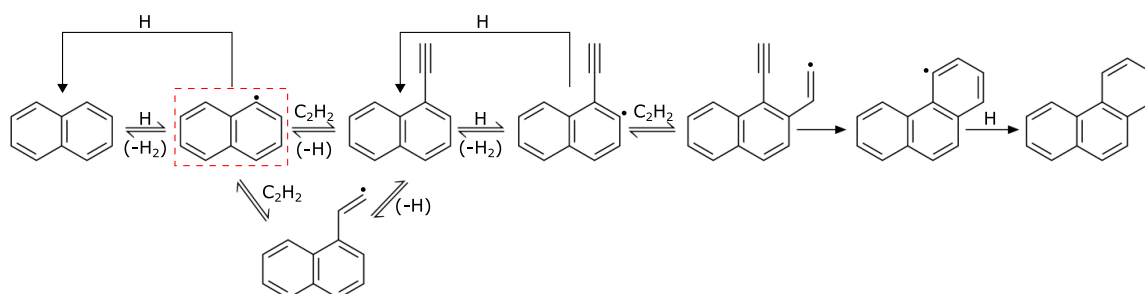
Fig. 3.5 Pathway for free-edge ring growth as described by Raj et al. [256]. The species used for the fraction of radical sites in the process rate equation is shown in the red rectangle.

For this process, the fraction of radical sites is calculated using the steady-state approximation for the concentration of the first radical species, shown in a red rectangle in Figure 3.5. The fraction of radical sites shown has the underlying assumption that the reverse rate constant for the acetylene addition reaction is negligible. The process rate equation suggests that the limiting step of the six-member ring growth resides on the first acetylene addition reaction. Although the process rate equation follows the well documented formulation of PAH growth under the HACA mechanism [76], it does not capture the kinetics of the different intermediates in the ring growth process.

In the case of intermediate species being generated by more than one pathway, or if more than one intermediate species contributes to the net rate of the transformation process (see Figure 4.1), the process rate equation shown in Equation 3.45 becomes ineffective at estimating process rates. In this case, it is necessary to adopt a more general treatment of both the steady-state approximation and the partial-equilibrium approximation, the details of which, as well as the combination of these methodologies, can be found in Section 3.5. The accuracy of both these approximations and their application to stochastic models is discussed in Chapter 4.

3.5   Steady-state and partial-equilibrium model equations

The sections that follow summarise the development of the steady-state and partial-equilibrium model equations used in this work. The bases for these approximations are discussed in the context of a general set of chemical species and reactions before demonstrating its application to PAH jump process rate calculations. The exposition and the production and loss notation closely follows that used in a number of related works [see for example 119, 325, 136, 181, 99].

3.5.1   General reaction equations

A general set of chemical reactions, N_R, can be written in the form

$$\sum_{\alpha=1}^{N_g} v'_{\alpha i} \chi_\alpha \Longrightarrow \sum_{\alpha=1}^{N_g} v''_{\alpha i} \chi_\alpha, \qquad i = 1,\ldots,N_R, \tag{3.47}$$
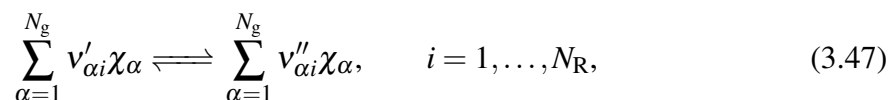
where χ are the chemical species and $v'_{\alpha i}$ and $v''_{\alpha i}$ are the forward and reverse stoichiometric coefficients of species α in reaction i. The rate of progress q_i can be written as

$$q_i = k_i \prod_{j=1}^{N_g} C_j^{v'_{ji}} - \frac{k_i}{K_{ci}} \prod_{j=1}^{N_g} C_j^{v''_{ji}}, \tag{3.48}$$

where k_i is the forward rate constant, K_{ci} is the equilibrium constant of reaction i and C_j is the concentration of species j. The net production rate $\dot{\omega}_\alpha$ of species α is given as

$$\dot{\omega}_\alpha = \sum_{i=1}^{N_R} \left(v''_{\alpha i} - v'_{\alpha i} \right) q_i. \tag{3.49}$$

3.5.2 Production and loss terms

The net production rate $\dot{\omega}_\alpha$ can be manipulated by substituting Equation (3.48) into Equation (3.49) to separate the terms responsible for the production and consumption of species α

$$\dot{\omega}_\alpha = \sum_{i=1}^{N_R} \left(v''_{\alpha i} - v'_{\alpha i} \right) \left(k_i \prod_{j=1}^{N_g} C_j^{v'_{ji}} - \frac{k_i}{K_{ci}} \prod_{j=1}^{N_g} C_j^{v''_{ji}} \right), \tag{3.50}$$

$$= \sum_{i=1}^{N_R} \left(v''_{\alpha i} k_i \prod_{j=1}^{N_g} C_j^{v'_{ji}} + v'_{\alpha i} \frac{k_i}{K_{ci}} \prod_{j=1}^{N_g} C_j^{v''_{ji}} \right)$$

$$- \sum_{i=1}^{N_R} \left(v'_{\alpha i} k_i \prod_{j=1}^{N_g} C_j^{v'_{ji}} + v''_{\alpha i} \frac{k_i}{K_{ci}} \prod_{j=1}^{N_g} C_j^{v''_{ji}} \right). \tag{3.51}$$

Assuming that all reactions are of first order with respect to all species in the forward and reverse reactions, Equation (3.51) can be rearranged to give

$$\dot{\omega}_\alpha = \mathcal{P}_\alpha - \mathcal{L}_\alpha C_\alpha, \tag{3.52}$$

where $\mathcal{P}_\alpha$ and $\mathcal{L}_\alpha$ are the production and loss terms of species α

$$\mathcal{P}_\alpha = \sum_{i=1}^{N_R} \mathcal{P}_\alpha^{(i)}, \qquad \text{where} \qquad \mathcal{P}_\alpha^{(i)} = v''_{\alpha i} k_i \prod_{j=1}^{N_g} C_j^{v'_{ji}} + v'_{\alpha i} \frac{k_i}{K_{ci}} \prod_{j=1}^{N_g} C_j^{v''_{ji}}, \tag{3.53}$$

$$\mathcal{L}_\alpha = \sum_{i=1}^{N_R} \mathcal{L}_\alpha^{(i)}, \qquad \text{where} \qquad \mathcal{L}_\alpha^{(i)} = v'_{\alpha i} k_i \prod_{\substack{j=1 \\ j\neq\alpha}}^{N_g} C_j^{v'_{ji}} + v''_{\alpha i} \frac{k_i}{K_{ci}} \prod_{\substack{j=1 \\ j\neq\alpha}}^{N_g} C_j^{v''_{ji}}. \tag{3.54}$$

In order to assist the analysis in the following sections, it is useful to introduce the terms

$$\mathcal{P}_{\alpha,\beta} = \sum_{i\in R_{\beta\to\alpha}} \mathcal{P}_{\alpha,\beta}^{(i)}, \qquad \text{where} \qquad \mathcal{P}_{\alpha,\beta}^{(i)} = v''_{\alpha i} k_i \prod_{\substack{j=1 \\ j\neq\beta}}^{N_g} C_j^{v'_{ji}} + v'_{\alpha i} \frac{k_i}{K_{ci}} \prod_{\substack{j=1 \\ j\neq\beta}}^{N_g} C_j^{v''_{ji}}. \tag{3.55}$$

$R_{\beta\to\alpha}$ is the set of reactions that produce species α from species β. The term $\mathcal{P}_{\alpha,\beta}$ is a pseudo first-order rate coefficient such that $\mathcal{P}_{\alpha,\beta} C_\beta$ gives the rate of production of species α from species β under the first-order assumption made above and under the provision that species α and β are on different sides of the reaction equation. [1]

---

[1] Under these restrictions, $(v'_{\alpha i}, v'_{\beta i}, v''_{\alpha i}, v''_{\beta i}) = (0,1,1,0)$ or $(1,0,0,1)$.

The loss term is a pseudo first-order rate coefficient and has a connection with the lifetime τ_α of species α

$$\tau_\alpha = \frac{1}{\mathcal{L}_\alpha}, \tag{3.56}$$

which has been shown to be related to the time for which a short-lived species is present in a reaction system [325].

3.5.3   Approximations based on timescale separation

In the analysis that follows, a closed constant-volume isothermal system with N_{g} species and N_{R} chemical reactions is assumed. A material balance over the system yields

$$\frac{\mathrm{d}C_\alpha}{\mathrm{d}t} = \mathcal{P}_\alpha - \mathcal{L}_\alpha C_\alpha, \qquad \alpha = 1, \dots, N, \tag{3.57}$$

where the right hand side describes the net production rate of species α and follows from Equation (3.52), and C is the solution vector containing the molar concentrations of the species.

Steady-state approximation

The steady-state approximation decomposes equation (3.57) into the following equations

$$0 \approx \mathcal{P}_\alpha - \mathcal{L}_\alpha C_\alpha, \qquad \alpha \in \mathrm{S}_{\mathrm{ss}}, \tag{3.58}$$

$$\frac{\mathrm{d}C_\alpha}{\mathrm{d}t} = \mathcal{P}_\alpha - \mathcal{L}_\alpha C_\alpha, \qquad \alpha \notin \mathrm{S}_{\mathrm{ss}}, \tag{3.59}$$

where S_{ss} denotes a subset of species that evolve rapidly relative to the other species in the system. The underlying assumption is that these species reach a local steady-state, such that the left hand side of Equation (3.58) tends to zero over timescales much smaller than those of Equation (3.59). Tikhonov's theorem [320, 324] states that the solution of Equations (3.58) and (3.59) approaches the solution of Equation (3.57) as the left hand side of (3.58) tends to zero.

Equation (3.58) can be written as

$$\mathcal{L}_\alpha C_\alpha - \sum_{\beta \in \mathrm{S}_{\mathrm{ss}}} \mathcal{P}_{\alpha,\beta} C_\beta = \underbrace{\mathcal{P}_\alpha - \sum_{\beta \in \mathrm{S}_{\mathrm{ss}}} \mathcal{P}_{\alpha,\beta} C_\beta}_{=:b_\alpha}, \qquad \alpha \in \mathrm{S}_{\mathrm{ss}}. \tag{3.60}$$

A key insight is that Equation (3.60) is linear in the concentrations of the species in S_{ss} if S_{ss} is chosen such that no more than one species from S_{ss} appears on any side of a reaction. Under the given constraint, $\mathcal{L}_\alpha$ is not a function of C_α (see Equation (3.54)) and $\mathcal{P}_{\alpha,\beta}$ is not a function of C_α or C_β (note that $\mathcal{P}_{\alpha,\beta}$ in Equation (3.55) describes the *production* of species α, such that species α is not a reactant). Furthermore, b_α does not depend on the species in S_{ss} because the second term introduced on the right hand side of Equation (3.60) is designed to exactly subtract those dependencies from $\mathcal{P}_\alpha$.

Under these constraints, Equation (3.60) can be written as a linear system

$$M_{ss}c_{ss} = b_{ss}, \tag{3.61}$$

where c_{ss} is a vector of the molar concentrations of the species in the set S_{ss},

$$M_{ss} = \begin{bmatrix} \mathcal{L}_{\alpha_1} & -\mathcal{P}_{\alpha_1,\alpha_2} & \cdots & -\mathcal{P}_{\alpha_1,\alpha_{N_{ss}}} \\ -\mathcal{P}_{\alpha_2,\alpha_1} & \mathcal{L}_{\alpha_2} & \cdots & -\mathcal{P}_{\alpha_2,\alpha_{N_{ss}}} \\ \vdots & \vdots & \ddots & \vdots \\ -\mathcal{P}_{\alpha_{N_{ss}},\alpha_1} & -\mathcal{P}_{\alpha_{N_{ss}},\alpha_2} & \cdots & \mathcal{L}_{\alpha_{N_{ss}}} \end{bmatrix} \quad \text{and} \quad b_{ss} = \begin{bmatrix} b_{\alpha_1} \\ b_{\alpha_2} \\ \vdots \\ b_{\alpha_{N_{ss}}} \end{bmatrix},$$

where α_i, $i = 1, \ldots, N_{ss}$ is an enumeration of the species in the set S_{ss} and

$$b_\alpha = \mathcal{P}_\alpha - \sum_{\beta \in S_{ss}} \mathcal{P}_{\alpha,\beta} C_\beta. \tag{3.62}$$

Equation (3.61) can be solved for the concentrations of the species in the set S_{ss}. The concentrations of the remaining species must be solved by integrating Equation (3.59). The solutions of these equations must be tightly coupled in order to obtain accurate results. This approach allows the reduction of the dimension of the set of ordinary differential equations (ODEs) from N to $N - N_{ss}$, reducing the computational cost of the problem.

The estimates for the concentrations of fast-forming species can be used to approximate the production rate of a product of interest. For the general slow-forming species α and β that share short-lived intermediates with each other, the production of species β from species α can be approximated by solving Equation (3.61) for the fast-forming species and evaluating their consumption:

$$\mathcal{P}_{\beta,\alpha} \approx \sum_{i=1}^{N_{ss}} \mathcal{P}_{\beta,\alpha_i} C_{\alpha_i,ss}, \tag{3.63}$$

where $C_{\alpha_i,\text{ss}}$ is the steady-state concentration of species in c_{ss}. The solution of Equations (3.61) and (3.63) can be used to estimate the rate of formation of a given product. This is the basis for the calculation of jump process rates using a general treatment of the steady-state approximation.

Several authors have investigated the application of the steady-state approximation to different systems [247, 325, 169, 324]. Its application to slow-forming species can produce significant errors, whereas good results can be achieved given an appropriate selection of fast-forming species. The chemical lifetime of a species seems to be the best predictor to determine whether it can be approximated or not by the steady-state assumption [324].

Partial-equilibrium approximation

The partial-equilibrium approximation decomposes Equation (3.57) into two equations

$$\frac{\mathrm{d}C_\alpha}{\mathrm{d}t} = \mathcal{P}_\alpha - \mathcal{L}_\alpha C_\alpha, \qquad \alpha \in S_{\text{peq}}, \tag{3.64}$$

$$\frac{\mathrm{d}C_\alpha}{\mathrm{d}t} = \mathcal{P}_\alpha - \mathcal{L}_\alpha C_\alpha, \qquad \alpha \notin S_{\text{peq}}, \tag{3.65}$$

where S_{peq} denotes a subset of species whose concentrations are controlled by a set of reactions that rapidly approach equilibrium, R_{peq}. These should be reversible reactions where the forward and reverse rates are large and approximately equal, and where at least one species in the reaction (a reactant, a product or one of each) belongs to S_{peq}.

The terms in Equation (3.64) can be further decomposed

$$\frac{\mathrm{d}C_\alpha}{\mathrm{d}t} = (\mathcal{P}_\alpha^{\text{peq}} + \mathcal{P}_\alpha^{\text{neq}}) - (\mathcal{L}_\alpha^{\text{peq}} + \mathcal{L}_\alpha^{\text{neq}}) C_\alpha, \qquad \alpha \in S_{\text{peq}}, \tag{3.66}$$

where $\mathcal{P}_\alpha^{\text{peq}}$ and $\mathcal{L}_\alpha^{\text{peq}}$ denote the contribution from reactions in R_{peq} (and $\mathcal{P}_\alpha^{\text{neq}}$ and $\mathcal{L}_\alpha^{\text{neq}}$ denote contributions from the remaining reactions) to $\mathcal{P}_\alpha$ and $\mathcal{L}_\alpha$, such that

$$0 \approx \mathcal{P}_\alpha^{\text{peq}} - \mathcal{L}_\alpha^{\text{peq}} C_\alpha, \qquad \alpha \in S_{\text{peq}}. \tag{3.67}$$

Under constraints analogous to those described in relation to Equation (3.60), Equation (3.67) can be used to obtain a linear system for c_{peq}

$$M_{\text{peq}} c_{\text{peq}} = b_{\text{peq}}, \tag{3.68}$$

where c_{peq} is a vector of the molar concentrations of the species in the set S_{peq},

$$
M_{\text{peq}} =
\begin{bmatrix}
\mathcal{L}_{\alpha_1}^{\text{peq}} & -\mathcal{P}_{\alpha_1,\alpha_2}^{\text{peq}} & \cdots & -\mathcal{P}_{\alpha_1,\alpha_{N_{\text{peq}}}}^{\text{peq}} \\
-\mathcal{P}_{\alpha_2,\alpha_1}^{\text{peq}} & \mathcal{L}_{\alpha_2}^{\text{peq}} & \cdots & -\mathcal{P}_{\alpha_2,\alpha_{N_{\text{peq}}}}^{\text{peq}} \\
\vdots & \vdots & \ddots & \vdots \\
-\mathcal{P}_{\alpha_{N_{\text{peq}}},\alpha_1}^{\text{peq}} & -\mathcal{P}_{\alpha_{N_{\text{peq}}},\alpha_2}^{\text{peq}} & \cdots & \mathcal{L}_{\alpha_{N_{\text{peq}}}}^{\text{peq}}
\end{bmatrix}
\quad \text{and} \quad
b_{\text{peq}} =
\begin{bmatrix}
b_{\alpha_1}^{\text{peq}} \\
b_{\alpha_2}^{\text{peq}} \\
\vdots \\
b_{\alpha_{N_{\text{peq}}}}^{\text{peq}}
\end{bmatrix}.
$$

In these equations, α_i, $i = 1, \ldots, N_{\text{peq}}$, is an enumeration of the species in the set S_{peq},

$$
b_\alpha^{\text{peq}} = \mathcal{P}_\alpha^{\text{peq}} - \sum_{\beta \in S_{\text{peq}}} \mathcal{P}_{\alpha,\beta}^{\text{peq}} C_\beta, \tag{3.69}
$$

and $\mathcal{P}_\alpha^{\text{peq}}$, $\mathcal{L}_\alpha^{\text{peq}}$ and $\mathcal{P}_{\alpha,\beta}^{\text{peq}}$ are defined as special cases of Equations (3.53), (3.54) and (3.55)

$$
\mathcal{P}_\alpha^{\text{peq}} = \sum_{i \in R_{\text{peq}}} \mathcal{P}_\alpha^{(i)}, \tag{3.70}
$$

$$
\mathcal{L}_\alpha^{\text{peq}} = \sum_{i \in R_{\text{peq}}} \mathcal{L}_\alpha^{(i)}, \tag{3.71}
$$

and

$$
\mathcal{P}_{\alpha,\beta}^{\text{peq}} = \sum_{i \in R_{\text{peq}} \cap R_{\beta \to \alpha}} \mathcal{P}_{\alpha,\beta}^{(i)}, \tag{3.72}
$$

where the sum over reactions $i \in R_{\text{peq}} \cap R_{\beta \to \alpha}$ should be understood as a sum over the subset of reactions in R_{peq} that produce species α from species β.

Analogous to Equation (3.63), the production term of a slow-forming species β from species α, that share fast-forming intermediates that slowly produce species β, can be approximated by solving Equation (3.68) for the fast-forming species and evaluating the consumption of these species:

$$
\mathcal{P}_{\beta,\alpha} \approx \sum_{i=1}^{N_{\text{peq}}} \mathcal{P}_{\beta,\alpha_i} C_{\alpha_i,\text{peq}}, \tag{3.73}
$$

where $C_{\alpha_i,\text{peq}}$ is the partial-equilibrium concentration of species in c_{peq}. The solution of Equations (3.61) and (3.73) can be used to estimate the rate of formation of a given product. This is the basis for the calculation of jump process rates using a general treatment of the partial-equilibrium approximation.

One important difference between the partial-equilibrium and steady-state approximations is that the terms in the partial-equilibrium Equations (3.70–3.72) are defined in terms of a subset of the reactions. One consequence of this is that the partial-equilibrium equations, (3.65) and (3.67), are less tightly coupled than the steady-state equations, (3.58) and (3.59).

General treatment of non-partial-equilibrium reactions

The partial-equilibrium approximation equations discussed in the previous section operate on the subset of reactions that exclude the formation of the product species (as these are a set of slow reactions). In this case, evaluating the formation of a product species can be done assuming another partial-equilibrium approximation between the product and its fast-forming intermediates.

For a PAH A_i having i six-member rings, where the notation defined by Frenklach et al. [83] is used, the concentration of its radical species, $A_i^\bullet$, is controlled by the reactions

$$A_i + H \xrightleftharpoons[k_{-1}]{k_1} A_i^\bullet + H_2, \qquad \text{(Table 3.3, reaction 1)}$$

$$A_i + OH \xrightleftharpoons[k_{-2}]{k_2} A_i^\bullet + H_2O, \qquad \text{(Table 3.3, reaction 2)}$$

$$A_i^\bullet + H + (M) \xrightarrow{k_3} A_i + (M), \qquad \text{(Table 3.3. reaction 3)}$$

An algebraic relationship between the concentrations C_{A_i} and $C_{A_i^\bullet}$ can be derived by applying a steady-state or partial-equilibrium approximation to each of these sets of reactions (see for example [75]). In this work, a partial-equilibrium approximation is used to derive the following relationship

$$C_{A_i^\bullet} = C_{A_i} \left(\frac{k_1 C_H + k_2 C_{OH}}{k_{-1} C_{H_2} + k_{-2} C_{H_2O} + k_3 C_H} \right). \qquad (3.74)$$

In the case of ODE-based simulations such as those investigated in Sections 4.4.2 and 4.4.3, the concentrations of species in the set $\alpha \notin S_{peq}$ are calculated by solving Equation (3.65). The concentration of a general product, A_{i+1}, can be obtained by using Equation (3.74) and solving an equation of the same form as Equation (3.65) to find the total concentration of each species and its corresponding radical

$$C_{A_i} + C_{A_i^\bullet} \approx \int_0^t \mathcal{P}_{A_i}^{neq} + \mathcal{P}_{A_i^\bullet}^{neq} \, dt, \qquad (3.75)$$

where

$$\mathcal{P}_{A_i}^{neq} = \sum_{i \in R_{neq}} \mathcal{P}_{A_i}^{(i)} \quad \text{and}$$

$$\mathcal{P}_{A_i^\bullet}^{neq} = \sum_{i \in R_{neq}} \mathcal{P}_{A_i^\bullet}^{(i)}$$

are the production terms of each species due to the reactions in the set R_{neq} defined as per Equation (3.53).

3.5.4 Application to process rates

The concentration of multiple intermediate species can be estimated with the application of the steady-state and the partial-equilibrium approximations. In a subsequent step, the estimated concentrations can be used to predict the rate of formation of a desired species. The advantage of both of these approximations is that they allow estimating process rates by solving linear systems of equations.

The process rate of a jump process r can be estimated using either the steady-state or partial-equilibrium approximation. Analogous to Equations (3.61) and (3.68), a linear system of equations can be used to estimate the fraction of intermediate site types that correspond to a given site type, η_r, present on the edge of a molecule. Using the steady-state approximation this can represented as

$$M_{ss}V_{ss} = b_{ss}, \tag{3.76}$$

where V_{ss}, is the steady-state vector of intermediate sites. This vector contains an estimate of the fraction of sites that are in an intermediate site type, such that the product of any element, $V_{\alpha_i,ss}$, with the number of sites with site type η_r, N_{site,η_r} results in the number of intermediate site types in the molecule. It must be noted that while the number of sites for an individual molecule, $n_s(m_j) \in \mathbb{N}$, the intermediate site types in V_{ss} can only have values between $(0,1)$. The matrix M_{ss}, with size $N_{ss} \times N_{ss}$, contains the production and consumption terms between intermediate site types, and the vector b_{ss} contains the production of intermediate site types from species not included in the steady-state approximation.

In a subsequent step, the elements in V_{ss} can be used to estimate the total process rate in a similar manner to that of Equations (3.63) and (3.73)

$$\mathcal{P}_{\beta,\eta_r} \approx N_{site,\eta_r} \sum_{i=1}^{N_{ss}} \mathcal{P}_{\beta,\alpha_i} V_{\alpha_i,ss}, \tag{3.77}$$

where $\mathcal{P}_{\beta,\eta_r}$ is the production of a new site β from a site with site type η_r, and the product $\mathcal{P}_{\beta,\alpha_i} V_{\alpha_i,\mathrm{ss}} N_{\mathrm{site},\eta_r}$ represents the production of site β from the intermediate site types estimated from Equation (3.76).

Equations analogous to (3.76) and (3.77) can be obtained for the partial-equilibrium approximation. Table 3.4 indicates PAH jump processes that use a general treatment of the steady-state approximation (processes S22–S29) to calculate the process rate. The table also shows what intermediate site types are assumed in each process rate calculation. The individual reactions associated with each principal site type and intermediate site types that are used in the linear system of equations are shown in Table 3.3. The partial-equilibrium approximation is only used combined with the steady-state approximation (process S1).

Combined steady-state–partial-equilibrium approximation

The combined steady-state–partial-equilibrium approximation method is discussed in detail in Chapter 4 and is only introduced here briefly. The method uses the following steps:

1. Use the steady-state approximation to evaluate the rate of each jump process.

2. Use the partial-equilibrium approximation to evaluate the rate of each jump process.

3. Determine the combined steady-state–partial-equilibrium approximation rates

$$
R_{\alpha\to\beta}^{\mathrm{ss\text{-}peq}} = \begin{cases} R_{\alpha\to\beta}^{\mathrm{peq}} & \text{if } \lambda\, R_{\alpha\to\beta}^{\mathrm{peq}} > R_{\beta\to\alpha}, \\ R_{\alpha\to\beta}^{\mathrm{ss}} & \text{otherwise,} \end{cases} \tag{3.78}
$$

where $R_{\alpha\to\beta}$ denotes the rate of a jump process associated with site type α that produces a site type β, and λ is a positive real number acting as a multiplier (defined as := 1.0 in this work). The model compares the partial-equilibrium approximation rate with the reverse rate, $R_{\beta\to\alpha}$. If the reverse rate is large, the assumptions behind the steady-state approximation are better suited to calculate the process rate. If the reverse rate is smaller than the forward process rate, the partial-equilibrium approximation is preferred. More details in the combined method are discussed in Chapter 4. Process S1 in Table 3.4 uses the combined steady-state–partial-equilibrium approximation.

3.6 Model Implementation

This section discusses the implementation of the detailed particle model described in the previous sections. The data structure used in the implementation of the particle layer is

discussed briefly and is followed by a deeper discussion on the implementation of the data structures for the molecular layer.

Particle ensemble

The population balance model uses a variable size particle ensemble with a predefined maximum number of computational particles N_{max}. The particle ensemble represents a real population of particles surrounded by a gas phase that are both contained in a sample volume

$$V_{smpl} = \frac{N_P}{M_0}, \tag{3.79}$$

where M_0 represents the particle number density. The sample volume is initialised by estimating the maximum value of the particle number density over the full course of the simulation, $M_{0,max}$ such that

$$V_{smpl} = \frac{N_{max}}{M_{0,max}}. \tag{3.80}$$

The sample volume can be adjusted during the simulation due to the expansion or contraction of the gas phase, and due to the contraction or the doubling of the ensemble (Section 3.7.2).

3.6.1 Binary tree data structure

Binary tree data structures are used to store information about the stochastic particles contained in the particle ensemble and to represent the connectivity of the primary particles that constitute aggregate particles. Binary trees are used to improve computational efficiency by updating the properties of all modified particles after a transformation process. Figure 3.6 shows an example of the representation of an aggregate particle in a binary tree data structure. Each node in the tree stores the sum of the properties (mass, volume, surface area) of the particles below it. After a transformation process these properties are updated only on the primary particles that are affected. This allows a rapid particle selection and efficient calculation of ensemble statistics that has a cost $\mathcal{O}(\log(N_P))$ [95]. In a binary tree data structure, such as the one shown in Figure 3.6, each non-leaf node is connected to two child nodes below it and a parent node above it (except for the root node). These nodes are illustrated as squares labelled A...E and the connections are shown with solid lines. The leaf nodes, drawn as circles, store the primary particles $p_1...p_6$. Each non-leaf node stores the sum of the properties of the (primary) particles below it, allowing efficient particle selection and updates to particle properties. Consequently, the root node stores the aggregate particle properties. In addition to storing the particle properties, non-leaf nodes also store information
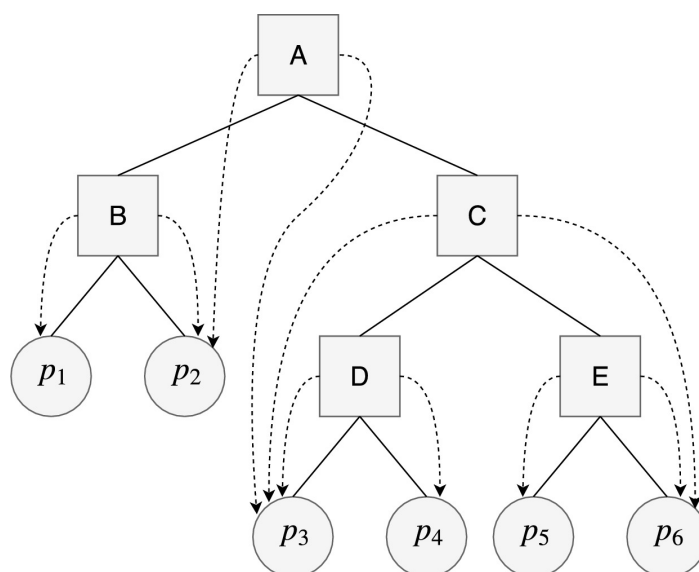
Fig. 3.6 Binary tree data structure used to represent a general aggregate particle. Non-leaf nodes are shown as squares and connections are shown by solid lines. Leaf nodes are shown as circles and represent the primary particles. Dashed lines are used to represent primary particle connectivity. Taken from Lindberg et al. [178] with permission from Elsevier ©.

pertaining to a single connection between two primaries p_i and p_j. In this case, the common surface area $\mathfrak{s}(p_i, p_j)$ is stored and the node points to the two primary particles p_i and p_j. These pointers are represented by the dashed lines in Figure 3.6 [178].

Figure 3.7 shows the aggregate particle that is represented in the binary tree shown in Figure 3.6. The primary particles corresponding to leaf nodes are labelled $p_1 \ldots p_6$ and the connections between particles are indicated in red dots labelled A...E, corresponding to non-leaf nodes. Further details in the implementation of binary tree data structures in the context of particle models, as well as how jump processes affect the binary tree data structure, can be found in [95, 276, 178].

3.6.2   Doubly-linked list data structure

The molecular layer of the type space described in Section 3.2 requires a data structure that avoids storing an excessive amount of information, but that is able to accurately predict properties for individual molecules. Edge carbon atoms, sites and internal carbon atoms are stored in different data structures in this work.

A general carbon atom c_k (Equation (3.7)) can be represented by the vector

$$c_k = \{c_{k-1}, c_{k+1}, c_{k,\mathrm{cl}}, a_k, \mathbf{x}_k\}, \tag{3.81}$$
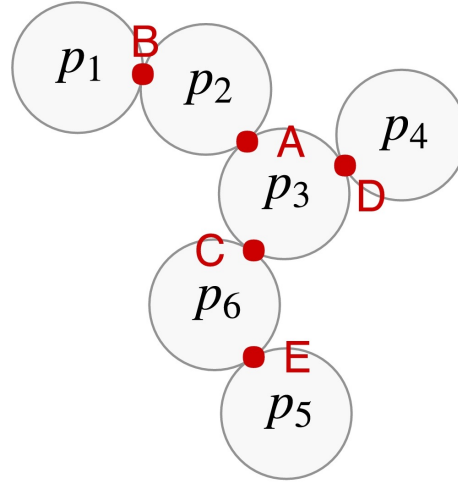
Fig. 3.7 Aggregate particle represented by the binary tree data structure shown in Figure 3.6. The primary particles $p_1 \ldots p_6$ correspond to leaf nodes. The connections A...E correspond to non-leaf nodes. Taken from Lindberg et al. [178] with permission from Elsevier ©.

where c_{k-1} and c_{k+1} are pointers to the predecessor and successor carbon atom vectors neighbouring c_k, and $c_{k,\text{cl}}$ is a pointer to the carbon atom vector crosslinked with c_k. If c_k is not connected to another carbon atom via a crosslink, then $c_{k,\text{cl}}$ will be 0, *i.e.* a null pointer. a_k stores the element type attached to c_k (carbon or hydrogen), and $\mathbf{x}_k \in \mathbb{R}^3$ represents the spatial coordinates of c_k. The matrix $\mathbf{E}(m_j)$ from Equation (3.5) is implemented through the pointers to the different edge carbon atoms.

A general site s_j can be represented by the vector

$$s_j = \{\eta_j, \eta_{\text{comb},j}, c_{\text{first}}, c_{\text{last}}, s_{j-1}, s_{j+1}\}, \tag{3.82}$$

where η_j represents the principal site type, $\eta_{\text{comb},j}$ the combined site type, both for the site with index j, c_{first} and c_{last} are pointers to the first and last carbon atom vectors that form part of a site and have $a_k = \text{H}$, and s_{j-1} and s_{j+1} are pointers to the predecessor and successor sites respectively. The principal site type is used for processes that are performed over one site, while the combined site type is used for processes that require two or more sites as neighbours (see Table 3.2). The predecessor and successor sites are those that have

$$s_{j-1} \rightarrow c_{\text{last}} \equiv s_j \rightarrow c_{\text{first}}, \tag{3.83}$$

$$s_{j+1} \rightarrow c_{\text{first}} \equiv s_j \rightarrow c_{\text{last}}, \tag{3.84}$$

which means that the pointer c_{last} of predecessor site, s_{j-1}, points to the same carbon atom vector as c_{first} for site s_j. Analogously, c_{first} of successor site s_{j+1}, points to the same carbon

atom vector c_{last} for site s_j. The coordinates of a general internal carbon atom, $c_{k,\text{Int}}$, can be represented by the vector

$$c_{k,\text{Int}} = \{\mathbf{x}_{k,\text{Int}}\}, \tag{3.85}$$

where $\mathbf{x}_{k,\text{Int}} \in \mathbb{R}^3$ stores the spatial coordinates of the element. In the implementation of the type space, the connectivity of internal carbon atoms is not stored to avoid computational expenses.

The representations of both edge carbon atoms and sites have pointers towards their immediate neighbours to facilitate their modification without the need of iterators through the whole element list. The data structure of both these classes is a *circular doubly-linked list* L_c and L_s for edge carbon atoms and sites, respectively. The vectors of spatial coordinates corresponding to internal carbon atoms are contained in a vector $\mathscr{V}_{\text{I}}$. The structure of a molecule m_j can then be fully represented by the data structure $\mathscr{D}$.

$$\mathscr{D} = \{L_c, L_s, \mathscr{V}_{\text{I}}\}. \tag{3.86}$$

Figure 3.8 shows a representation of this data structure for phenanthrene as a general molecule m_j. This data structure contains carbon atoms $c_1 \ldots c_{14}$ and sites $s_1 \ldots s_{10}$. The arrows drawn in the data structure show the direction in which the circular doubly-linked list is accessed. It must be noted that since PAHs can rotate in space this direction becomes arbitrary. The inexpensive data structure for internal carbon atoms has both advantages and disadvantages. By only storing the spatial coordinates of these atoms without their connectivity, the model avoids memory expenses pointing to carbon atoms that are assumed non-reactive (the model does not include processes that directly affect them). However, in the case that one of the internal carbon atoms becomes an edge carbon atom, *e.g.* in a migration or oxidation process, the model iterates over the coordinates in $\mathscr{V}_{\text{I}}$, which is an $\mathscr{O}(|\mathscr{V}_{\text{I}}|)$ operation.

Computational sites

The definition of site in the model implementation (Equation (3.82)) differs slightly from the main site types associated with a carbonaceous material (see Figure 3.3). In the model, each site has a defined number of carbons and moieties (*e.g.* five-member rings) that are used to determine what PAH jump processes can be applied to a given structure. The combined site types are used to identify two or more adjacent sites of a certain principal site type. These combined sites are necessary for certain processes. Tables 3.1 and 3.2 show all the site types implemented in the model. In Table 3.1 the site types are classified as families sharing the same structure but with different numbers of carbon atoms. Each of the site types defined in
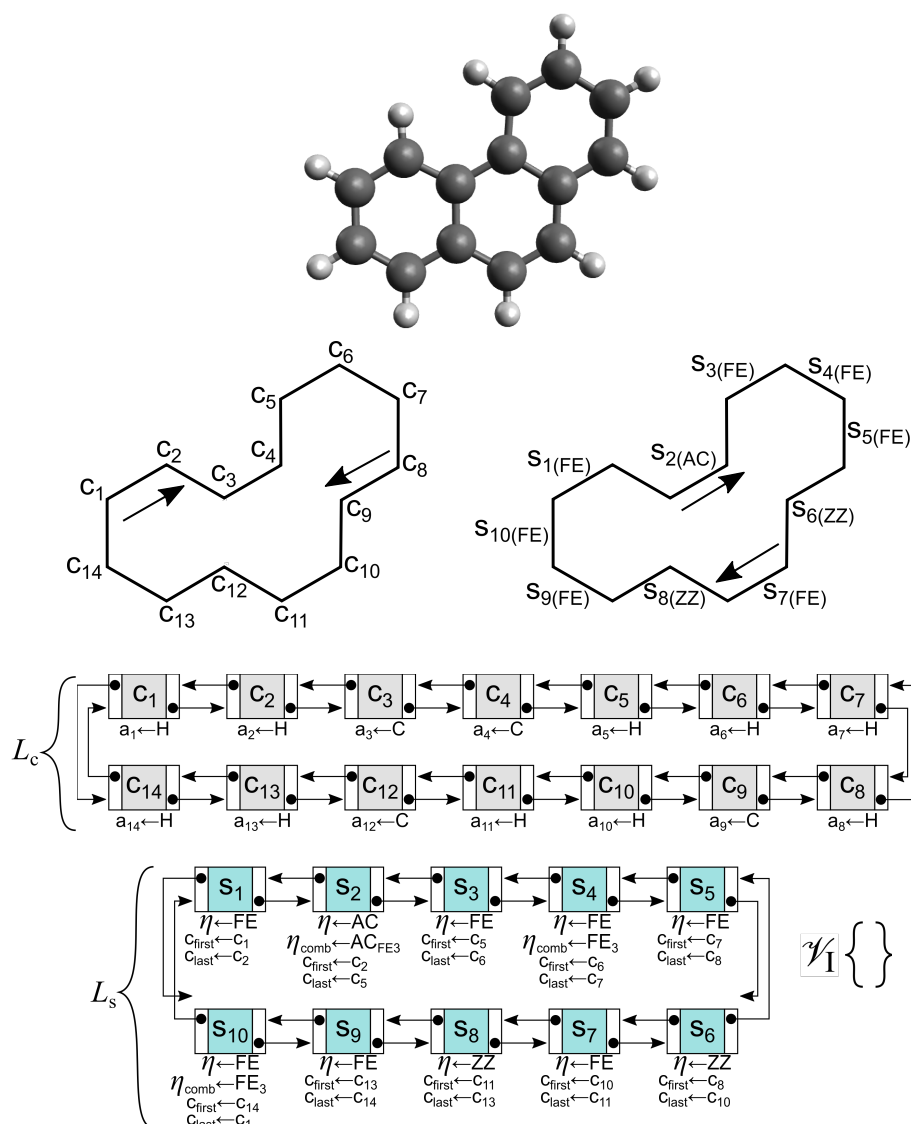
Fig. 3.8 Representation of the data structure for phenanthrene as an example of a general PAH. The molecule can be represented as a circular doubly-linked list of carbon elements, represented as $c_1 \ldots c_{14}$, and site elements, represented as $s_1 \ldots s_{10}$. The arrows represent the way in which the circular doubly-linked list is read.

this table are associated with at least one process from Table 3.4. There are, however, site types that need additional discussion: the *spiral* site type, the missing seven-member bay site types that do not have partially-embedded five-member rings and site types containing seven-member rings.
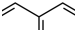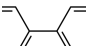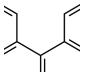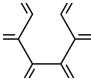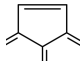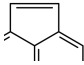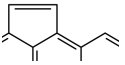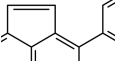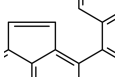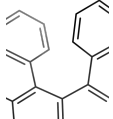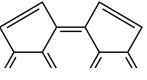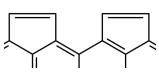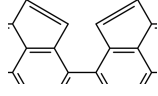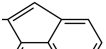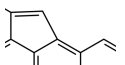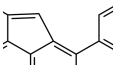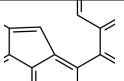
In this work, a spiral site type corresponds to any site with a large number of carbon atoms (≥ 7 for certain families and ≥ 8 for the rest). These sites are characteristic of helicenes [287], a family of PAHs that form spirals and that have been recently synthesised using gas phase
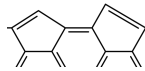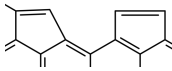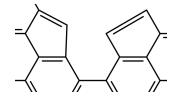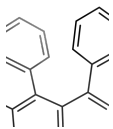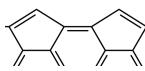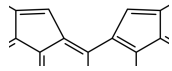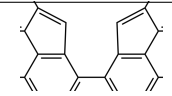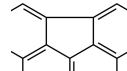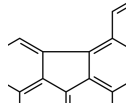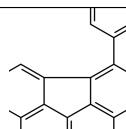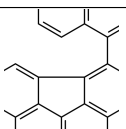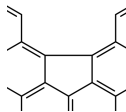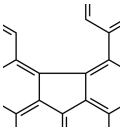
reactions [363]. Spiral sites were first described in stochastic models of PAH growth by Whitesides and Frenklach [348]. In that work, once one of these sites appeared it was not possible to remove them from the structure due to the lack of known processes that can affect them. This behaviour is also included in this work. Once a spiral site is formed it continues to be a spiral. Although this is a model limitation, it is a necessary one to keep the simulation going. Additional work in understanding what processes can affect spiral sites is necessary to better represent carbonaceous structures.

In Table 3.1, the site type families that correspond to six-member rings and any combination of edge five-member rings do not have a seven-member bay site type. This is instead replaced by the spiral site type. The reason for this is that the processes that affect these sites have not been reported in the literature. In the work done by Menon et al. [206], processes that form seven-member rings were investigated always in the presence of partially-embedded five-member rings in either corner or edge positions. In this work, it was assumed that seven-member rings cannot be formed in the absence of partially-embedded five-member rings in their adjacency. This is based on the large amount of experimental evidence reporting that seven-member rings are usually found coupled to five-member rings [248, 104, 193, 131, 253]. Additional work regarding the formation of seven-member rings in the absence of five-member rings is needed.

Lastly, it must be noted that in Table 3.1 there are no principal site types containing seven-member rings. There are three reasons for this. First, only few processes that affect seven-member rings have been reported in the literature. Second, structures containing seven-member rings appear infrequently (as compared with five- or six-member rings, see Chapter 5). Third, the computational expense of having site types with different rings is significant. For every site included in the model an additional site constituted by a seven-member ring could be defined. The new site types would require additional rate equations and process transformations. This approach would probably provide insights into how these rings behave inside a carbonaceous material, but as it was said above, the infrequent appearance of seven-member rings means that there would not be much change in how the molecules are formed. In this work, it was assumed that the site types of six-member rings are also used for seven-member rings. Processes that are associated with a parent site containing six-member rings can also affect seven-member rings. The only difference in the transformation processes shown in Table 3.5 is that whenever this is the case, a seven-member ring is consumed instead of a six-member ring (processes S3, S28 and S29), and the processes that form five-member rings instead form a six-member ring (processes S28 and S29).

Table 3.1 Principal sites implemented in the model.

	Number of carbon atoms					
	2	3	4	5	6	7
Six-member rings (R6s)	Free-edge (FE)	Zig-zag (ZZ)	Armchair (AC)	5-member bay (BY5)	6-member bay (BY6)	
Edge five-member rings (R5s)	5-member ring (R5)	Free-edge R5 (RFE)	Zig-zag R5 (RZZ)	Armchair R5 (RAC)	5-member bay R5 (RBY5)	Spiral (SP)
Two edge five-member rings (R5–R5)			R5–Free-edge R5 (RFER)	R5–Zig-zag R5 (RZZR)	R5–Armchair R5 (RACR)	
Corner partially-embedded five-member rings (cR5)		cR5 Free-edge (cR5)	cR5 Zig-zag (cRZZ)	cR5 Armchair (cRAC)	cR5 5-member bay (cRBY5)	

	Number of carbon atoms					
	2	3	4	5	6	7
Edge five-member ring & corner partially-embedded five-member rings (R5–cR5)			cR5 Free-edge R5 (cRFER)	cR5 Zig-zag R5 (cRZZR)	cR5 Armchair R5 (cRACR)	
Two corner partially-embedded five-member rings (cR5–cR5)			cR5 Free-edge cR5 (cRFEcR)	cR5 Zig-zag cR5 (cRZZcR)	cR5 Armchair cR5 (cRACcR)	Spiral (SP)
Edge partially-embedded five-member rings (eR5)			eR5 Armchair (eR)	eR5 5-member bay (BY5$_{eR}$)	eR5 6-member bay-1 (BY6$_{eR-1}$) / eR5 6-member bay-2 (BY6$_{eR-2}$)	eR5 7-member bay-1 (BY7$_{eR-1}$) / eR5 7-member bay-2 (BY7$_{eR-2}$)
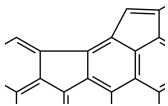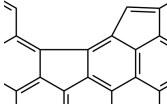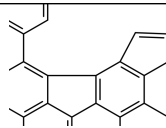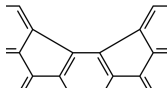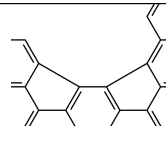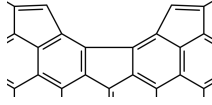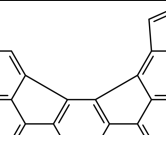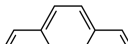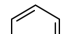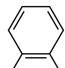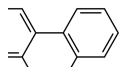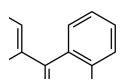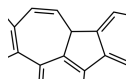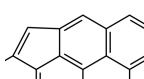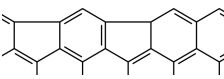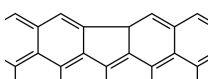
	Number of carbon atoms					
	2	3	4	5	6	7
Edge & corner partially-embedded five-member rings (eR5–cR5)				cR5 Armchair eR5 ($cRAC_{eR}$)	cR5 5-member bay eR5 ($cRBY5_{eR}$)	cR5 6-member bay eR5 ($cRBY6_{eR}$)
Two edge partially-embedded five-member rings (2eR5)					2eR5 6-member bay ($BY6_{2eR}$)	2eR5 7-member bay ($BY7_{2eR}$)
Three partially-embedded five-member rings (3eR5)					3eR5 6-member bay ($BY6_{3eR}$)	3eR5 7-member bay ($BY7_{3eR}$)

Table 3.2 Combined sites implemented in the model.

Combined sites	
Free-edge adjacent to non-free-edges (FE$_{HACA}$)	
Two adjacent free-edges (FE2)	
Three adjacent free-edges (FE3)	
Armchair adjacent to three free-edges (AC$_{FE3}$)	
5-member bay adjacent to three free-edges (BY5$_{FE3}$)	
Seven-member ring adjacent to partially-embedded five-member ring (R5R7)	
Corner partially-embedded five-member ring adjacent to non-R5 site (cR5$_{MIGR}$)	
Edge partially-embedded five-member ring adjacent to one non-R5 site (eR5$_{MIGR}$)	
Edge partially-embedded five-member ring adjacent to two non-R5 site (eR5$_{MIGR2}$)	

3.6.3 Molecule computational jump processes

A jump process uses the computational advantages of the doubly-linked lists defined in the previous sections. This data structure allows the insertion of new nodes between existing list elements by updating the pointers to previous and successive memory allocations. This avoids searching elements in a connectivity matrix and its associated memory cost. Figures 3.9 and 3.10 show a representation of changes to the data structure when a jump process is performed. In this case a six-member ring grows in an armchair site which represents the following transformations in the data structure: (1) two elements that become internal carbon atoms, c_3 and c_4, are removed from L_c. This means that their coordinates are moved to $\mathcal{V}_I$. At this point, elements c_2 and c_5 are connected in L_c. (2) A new element c_{15} is added after c_2. This updates the pointers of neighbouring elements in the list. (3) A second element c_{16} is inserted after c_{15}. At this point, the addition operations of nodes are finalised. (4) The properties of elements c_2 and c_5 are modified. This finalises the operations that affect L_c. (5) The affected element of L_s, s_2, has its properties and pointers modified. It is important to notice that the armchair ring growth process does not add or consume sites. If a process does add or remove sites, then steps analogous to (1)–element removal, or (2)–element insertion can be applied to L_s. The benefit of updating s_2 without adding or removing elements is the computational saving in avoiding these operations. This is not allowed in L_c, in which elements are always added and removed. (6) The properties of the predecessor and successor sites are modified. (7) The combined site type of the affected site and its neighbours are modified if necessary. It is important to note that depending on the process, the combined site type of one or more neighbour sites may be affected.

The circular doubly-linked list of edge carbon atoms stores both the connectivity and the spatial positions of the elements that constitute the edge of a molecule. However, the spatial positions of these atoms are modified as the state of the molecule is transformed by jump processes. It is desirable that these modified spatial positions provide good estimates of the actual morphology of the molecule. To ensure this it is useful to define the distance between any two carbon atoms in L_c

$$\delta_{i,j} = |\mathbf{x}_i - \mathbf{x}_j|, \tag{3.87}$$

where $\delta_{i,j}$ represents the distance between edge carbon atoms i and j. The distance between adjacent edge carbon atoms can be represented as $\delta_{i,i+1}$ or between second neighbours as $\delta_{i,i+2}$. The distances between atoms and their current spatial positions can be used to determine the positions of new carbon atoms by defining a set of model equations. In this
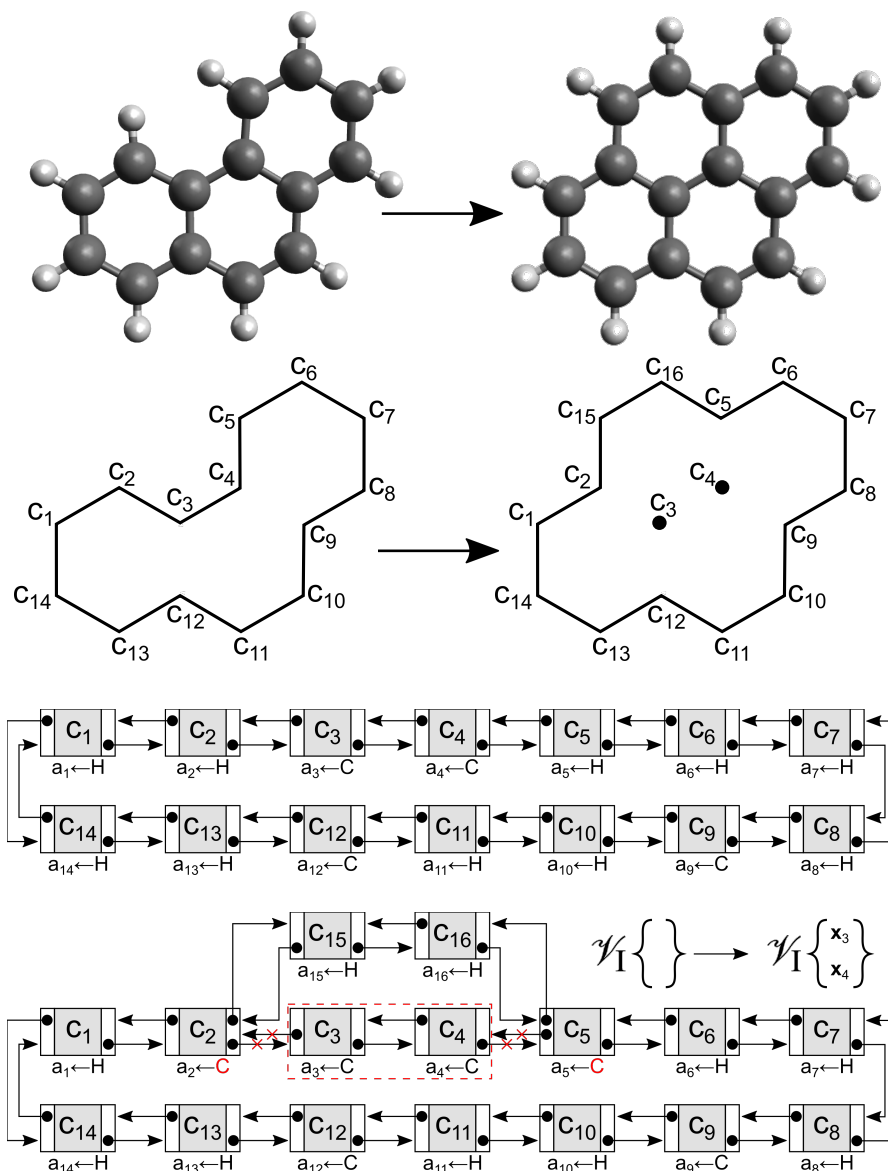
Fig. 3.9 Armchair ring growth of phenanthrene as an example of jump process modifying the data structure (Part 1). The edge carbon list, L_c, before the process is shown in the middle and after the process at the bottom of the figure. Moved pointers are shown with red crosses. Modified connected atoms are shown in red. Edge carbon atom vectors deleted are shown in red rectangle. Coordinates added to $\mathscr{V}_I$ are shown.

case the model equations for the addition of carbon atoms are:

$$\mathbf{x}_{New} = \mathbf{x}_k + \hat{\mathbf{u}}_{New}\, \delta_{c-c}, \qquad \text{and} \qquad (3.88)$$

$$\mathbf{x}_{New,2} = \mathbf{x}_{New} + \hat{\mathbf{u}}_{New,2}\, \delta_{c-c}, \qquad (3.89)$$
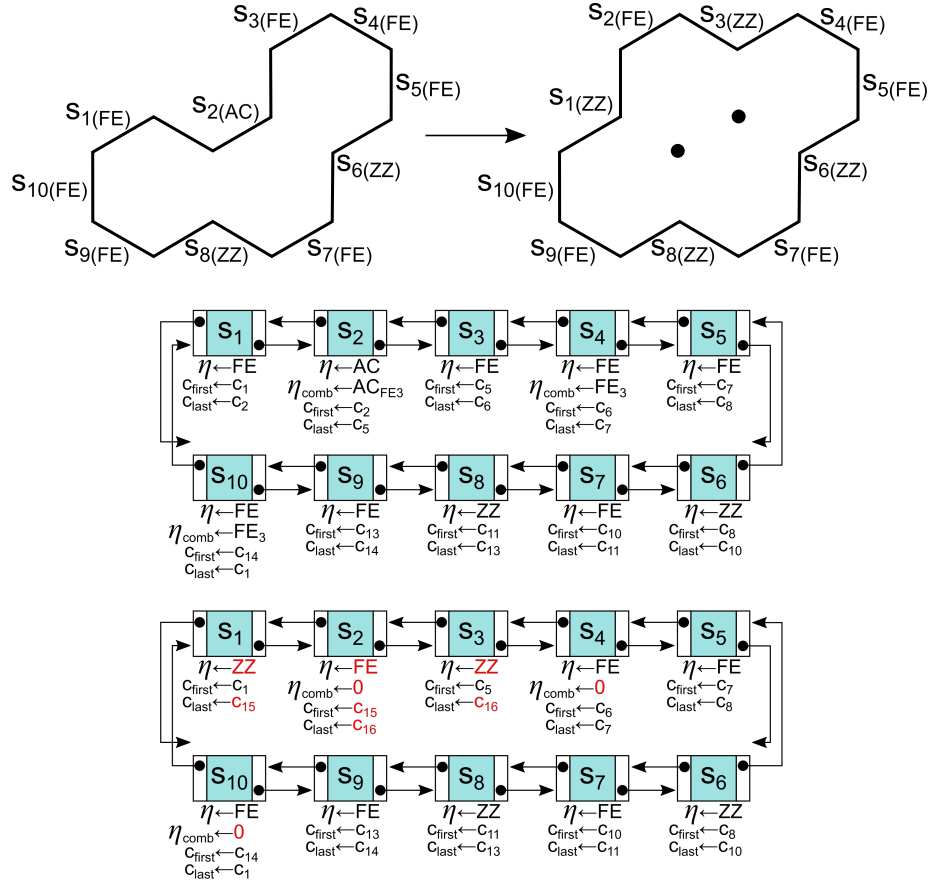
Fig. 3.10 Armchair ring growth of phenanthrene as an example of jump process modifying the data structure (Part 2). The site list, L_s, before the process is shown in the middle and after the process at the bottom of the figure. Modifications to principal site types, combined site types and pointers to new carbon atoms are shown in red.

where $\hat{\mathbf{u}}_{\text{New}}$ is the unitary vector from the position of element c_k, $\mathbf{x}_k$, towards the estimate of the new carbon atom position, $\mathbf{x}_{\text{New}}$. $\hat{\mathbf{u}}_{\text{New},2}$ is the unitary vector from $\mathbf{x}_{\text{New}}$, towards the estimate of the second new carbon atom position, $\mathbf{x}_{\text{New},2}$. $\delta_{\text{c–c}}$ represents the expected distance between two carbon atoms in the model (:=1.4 Å, the aromatic bond distance). The unitary vectors can be calculated with different equations depending on the properties of carbon atom c_k:

$$\hat{\mathbf{u}}_{\text{New}} = \begin{cases} \left(\dfrac{\mathbf{x}_k - \mathbf{x}_{k-1}}{\delta_{k,k-1}} + \dfrac{\mathbf{x}_{k+1} - \mathbf{x}_k}{\delta_{k+1,k}} \right) \Big/ \left| \dfrac{\mathbf{x}_k - \mathbf{x}_{k-1}}{\delta_{k,k-1}} + \dfrac{\mathbf{x}_{k+1} - \mathbf{x}_k}{\delta_{k+1,k}} \right|, & \text{if } a_k = \text{H}, \\ \left(\dfrac{\mathbf{x}_{k-1} - \mathbf{x}_k}{\delta_{k-1,k}} + \dfrac{\mathbf{x}_{k+1} - \mathbf{x}_k}{\delta_{k+1,k}} \right) \Big/ \left| \dfrac{\mathbf{x}_{k-1} - \mathbf{x}_k}{\delta_{k-1,k}} + \dfrac{\mathbf{x}_{k+1} - \mathbf{x}_k}{\delta_{k+1,k}} \right|, & \text{if } a_k = \text{C}, \end{cases} \tag{3.90}$$

$$\hat{\mathbf{u}}_{\text{New},2} = \left(\dfrac{\mathbf{x}_k - \mathbf{x}_{k-1}}{\delta_{k,k-1}} + \dfrac{\mathbf{x}_{k+2} - \mathbf{x}_{k+1}}{\delta_{k+2,k+1}} \right) \Big/ \left| \dfrac{\mathbf{x}_k - \mathbf{x}_{k-1}}{\delta_{k,k-1}} + \dfrac{\mathbf{x}_{k+2} - \mathbf{x}_{k+1}}{\delta_{k+2,k+1}} \right| \tag{3.91}$$

Analogous to Equation (3.88), if a carbon atom that is currently an internal carbon atom needs to be added to L_c, the new position is estimated as

$$\mathbf{x}_{New} = \mathbf{x}_k - \hat{\mathbf{u}}_{New}\, \delta_{c-c}. \tag{3.92}$$

The model then calculates the Euclidean distance between position $\mathbf{x}_{New}$ and every position in $\mathscr{V}_I$ until one distance is less than $\delta_{cutoff-Internal}(:= 0.5\ \text{Å})$, a model parameter. After this element in $\mathscr{V}_I$ is found, it is assigned to the spatial position of the new added edge carbon atom.

Equations (3.88)–(3.92) represent the formation of a new unitary vector from the addition of two existing ones. Figure 3.11 shows the way in which the model determines the addition of new carbon atom elements. It must be noted that $\hat{\mathbf{u}}_{New,2}$ only has one definition. This is because processes that add carbon atoms from elements with $a_k = C$ only add one new element at a time. In Figure 3.11(c), it can be noticed that when a carbon atom is added from an atom with $a_k = C$ a new six-member ring is formed but the structure does not recover the correct shape for this ring. In this case the model uses an structure optimisation to recover a better estimate of the locations of all carbon atom elements, edge and internal.

Structure optimisation

The implementation of the model uses the routines implemented in OpenBabel [234, 235] (OB) to optimise the molecular structure. The implementation of the model uses the OB routines as external auxiliary functions. This means that the data structure that describes carbonaceous materials is not contained in any OB data structure. The model passes information from L_c and $\mathscr{V}_I$ to OB that is returned to the model. The following steps are used to optimise carbonaceous structures:

1. A general molecule m_{OB} is initialised in OB. This general molecule is used in OB to perform the structure optimisation. This general molecule has a data structure and functions that can be found elsewhere [234, 235]

2. The spatial coordinates of every edge carbon atom is passed to OB. For every element in L_c a carbon atom is added to m_{OB} with the same spatial coordinates. For every element in L_c that has $a_k = H$, an additional hydrogen atom is initialised in OB with coordinates calculated as

$$\mathbf{x}_H = \mathbf{x}_k + \hat{\mathbf{u}}_{New}\, \delta_{c-h}, \tag{3.93}$$
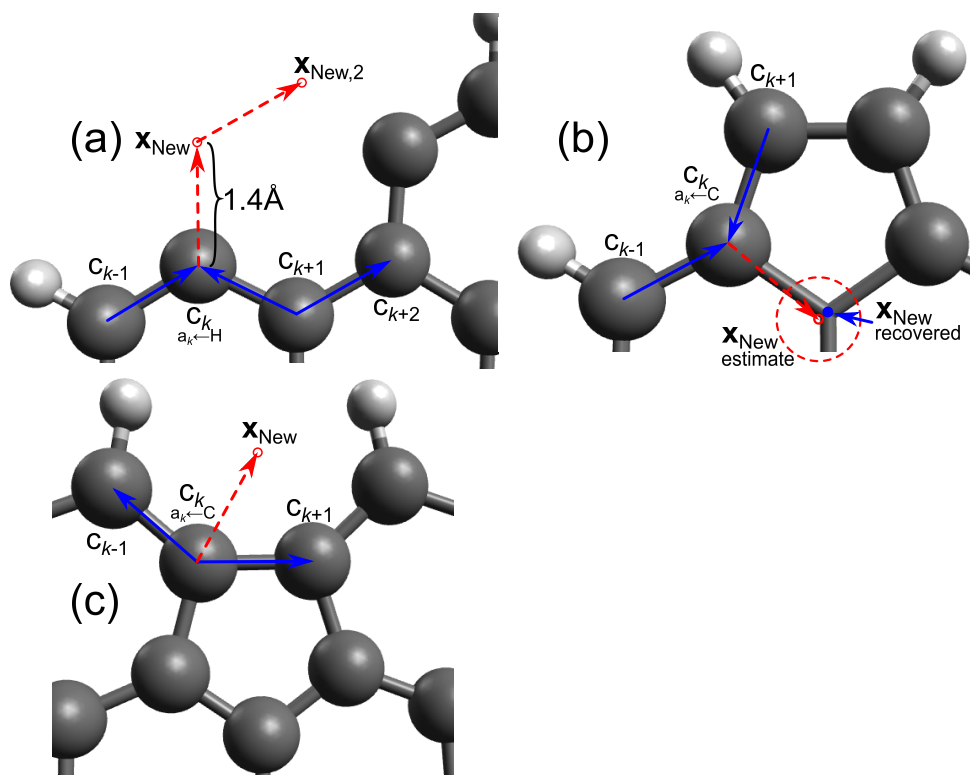
Fig. 3.11 Representation of the carbon additions in the model. Blue arrows show vectors calculated by current positions in the model. Red arrows show vector that estimate the new atom positions. (a) the addition of two carbon atoms starting from $a_k = $ H. (b) the recovery of an internal carbon atom by estimating the probable position addition of two carbon atoms starting from $a_k = $ C, and (c) the addition of a carbon atom starting from $a_k = $ C. This last addition does not recover the shape of a six-member ring properly.

where $\mathbf{x}_H$ is an estimate of the spatial position of the associated hydrogen atom, $\hat{\mathbf{u}}_{New}$ is calculated using Equation (3.89), and $\delta_{c-h}(:= 1.085 \text{ Å})$ is the distance between carbon and hydrogen atoms defined by the model. The connectivity between the new hydrogen atom is added at this point: A bond is declared in m_{OB} between the new initialised hydrogen atom and the previous declared carbon atom.

3. The spatial coordinates for every internal carbon atom is passed to OB. For every element in $\mathcal{V}_I$ a carbon atom is added to m_{OB} with the same spatial coordinates. Note that in m_{OB} there are no differences between carbon atoms. At this point, all atomic information in the model data structure has been passed to OB.

4. The existing bond detection routines from OB are used to connect the atoms added to m_{OB} in the previous points. It is important to mention that these routines do not detect bond order or assume any hybridisation for carbon atoms. These routines use known

experimental atomic radii information and the spatial coordinates to determine which atoms may be bonded to others. After the application of these routines each carbon atom can end bonded to one, two or three other carbon atoms.

5. The connectivity of the elements in L_c is revised in the corresponding atoms from m_{OB}. The different cases in which the connectivity of carbon atoms can be fixed before optimising the structure are shown in Figure 3.12. If there is no bond between two atoms in m_{OB} that should be connected, one is added by the model. If a bond between two atoms in m_{OB} exists (the spatial coordinates of two atoms were too close) and the corresponding elements of L_c are not connected, the bond is removed. This is shown in Figure 3.12(a). This approach has the possibility of leaving unconnected carbon atoms. This is addressed in the next point.

6. To solve a wrong connectivity between carbon atoms in m_{OB}, two lists are obtained: One that contains atoms with only two other atoms bonded (sp hybridisation), and one that contains atoms with four carbon atoms bonded (sp^3 hybridisation). These lists are used to add and remove bonds with the following logic: First, for each carbon atom with sp hybridisation, the nearest neighbour that also has sp hybridisation is found. If the Euclidean distance between these two atoms is less than a parameter $\delta_{\text{cutoff--sp}}$ ($:= 7.5$ Å), a bond between the two atoms is added and both atoms are removed from the first list (Figure 3.12(b)). Second, for each carbon atom with sp^3 hybridisation, it is checked if any of its four neighbouring carbon atoms also have sp^3 hybridisation (are connected to each other incorrectly). If this is the case, the bond between the two carbon atoms is deleted and both of them are removed from the second list (Figure 3.12(c)). Third, for each carbon atom remaining in the first list, the closest carbon atom from the second list is identified. If these two carbon atoms are connected, then a third carbon atom that is connected to the second carbon atom (sp^3) and is closest to the first atom (sp) is selected. A bond between the first atom (sp) and the selected carbon atom is added while the bond between the second carbon atom (sp^3) and the selected carbon atom is removed (Figure 3.12(d)). Lastly, if the two carbons (one from each list) are not connected, a third carbon atom that is closest to the first atom (sp) and connected to the second atom (sp^3) is selected. A bond between the first atom (sp) and the third selected atom is added while the bond between the second atom (sp^3) and the third atom is removed (Figure 3.12(e)). These four cases to fix wrong connectivity between carbon atoms are shown in Figure 3.12(b)–(e).

7. The structure optimisation is performed once the connectivity and spatial coordinates of all the atoms in m_{OB} have been revised. The optimisation is performed using the
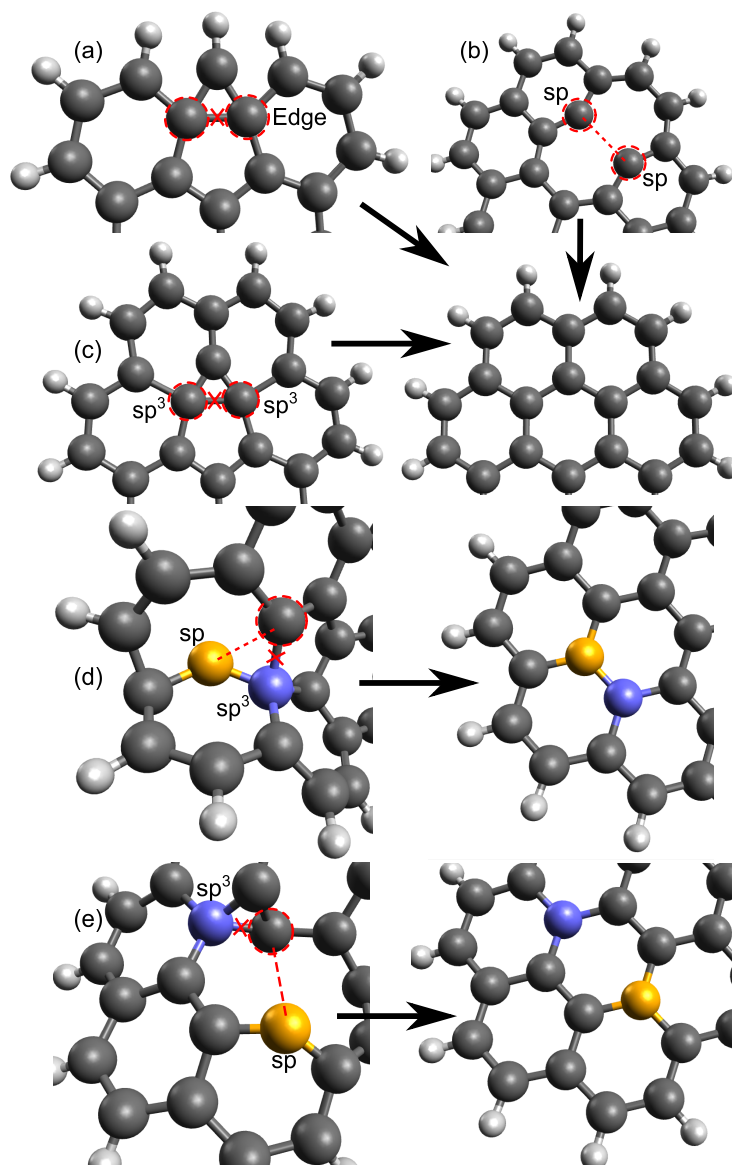
Fig. 3.12 Connectivity issues resolved in the implementation of the model before a structure optimisation. (a) the removal of a bond between edge atoms. (b) the addition of a bond between two atoms that are missing a bond. (c) the removal of a bond between two atoms that have an additional bond. (d) the connectivity fix when an atom that has one missing bond is connected to an atom with an additional bond. A third close atom is selected to add and remove one bond. (e) the connectivity fix when an atom that has one missing bond is close to an atom with an additional bond. A third connected atom is selected to add and remove one bond. Added bonds are shown in red dashed lines. Removed bonds are shown with red crosses. The correct structures (after optimisation) are shown to the right.

MMFF94 forcefield [107] with its standard parameters. The optimisation is performed using the steepest descent method [150] as implemented in OB. Two stopping criteria

are used for the optimisation: First, an energy convergence criteria $E_{\text{opt-conv}}(:= 10^{-6})$ is used. The optimisation is considered converged if the absolute value of the difference in energy between two consecutive forcefield energy calculations is lower than this value. Second, if the optimisation performs $N_{\text{opt-steps}}(:= 4000)$ steps the optimisation is stopped. Both $E_{\text{opt-conv}}$ and $N_{\text{opt-steps}}$ are model parameters.

8. The spatial coordinates of all carbon atoms contained in m_{OB} are passed back to the data structures in the detailed particle model L_{c} and $\mathcal{V}_{\text{I}}$. This is accomplished simply by iterating through all atoms in m_{OB} and only passing back the spatial coordinates of carbon atoms.

The optimisation of the molecular structure is a necessary operation to accurately resolve the structure of carbonaceous structures, although it is a computationally expensive process. For this reason, it is used only when necessary. The structure optimisation can be performed at different points in a transformation process. It can be performed before the jump process to obtain better estimates for the locations of added carbon atoms. Additionally, if the resulting structure is not accurate after a transformation process, a structure optimisation is used. Lastly, some processes need a structure optimisation every time they are sampled to resolve a three-dimensional transformation of the structure, *e.g.* curvature integration and bay closure reactions. The details for optimisations and the transformation processes are shown in Table 3.5.

3.7 Stochastic numerical method

In this thesis, a Direct Simulation Algorithm (DSA) [5] is used as the main numerical method. The algorithm approximates a real system by simulating an ensemble of N_{P} equally weighted stochastic particles contained in a sample volume V_{smpl}. The evolution of the particle ensemble is treated as a Poisson process with an exponentially distributed waiting time τ between events [95]

$$\text{Prob}(\tau \geq t) = e^{-R_{\text{tot}}t}, \tag{3.94}$$

where R_{tot} is the total rate of processes. The probability of a process j being selected for an event is dependent on its relative rate

$$\text{Prob}(j) \propto R_j/R_{\text{tot}}. \tag{3.95}$$

3.7.1   Decoupling of gas phase chemistry and particle processes

The processes discussed in Section 3.4 show the intricate dependence of the particle processes and the gas phase species available in the particle surroundings. This dependence is even more evident for the PAH jump processes. The solution of a gas phase chemistry model coupled to a stochastic model such as the one detailed in this work is a complicated task. Typically, an operator splitting algorithm such as the predictor-corrector algorithm used by Celnik et al. [33] or the Strang splitting algorithm [31] are necessary. These algorithms have been successfully applied to the study of Titania with particle models that only include the particle layer [185, 178, 17]. However, the use of these algorithms in a multidimensional model such as the one used in this work remains too complicated to be practically used.

In this work, the post-processing methodology used in multiple works [291, 37, 356, 358, 357] is employed. The methodology consists of first solving the gas-phase chemistry together with a simplified population balance model. The solution of this system of equations accounts for the production and consumption of gas phase species and provides reasonable estimates for the temperature and gas phase species concentrations. Both the temperature and gas phase species concentrations are used as an input to the detailed population balance model (more details can be found in the work by Chen et al. [37]). In this methodology, a gas phase species is selected as a *transfer* species, A^{transf}, between the gas phase species solution and the detailed population balance model. The number density of this species in the particle ensemble will be forced to follow the gas phase number density supplied as an input to the model. The number density of the transfer species in the ensemble, $N_{\text{dens}}^{\text{transf}}$, is defined as

$$N_{\text{dens}}^{\text{transf}} = \frac{N_{\text{P}}^{\text{transf}}}{N_{\text{P}}\, V_{\text{smpl}}}, \tag{3.96}$$

where $N_{\text{P}}^{\text{transf}}$ is the number of particles in the ensemble that have the same mass and molecule than the transfer species. The number of transfer species molecules in the gas phase for the same sample volume as that of the ensemble, $N_{\text{gas}}^{\text{transf}}$, can be calculated as

$$N_{\text{gas}}^{\text{transf}} = C_{A^{\text{transf}}} N_A V_{\text{smpl}}. \tag{3.97}$$

By comparing these two quantities the model adds or removes molecules from the ensemble such that the transfer species is kept constant in both:

$$\text{If} \begin{cases} N_{\text{P}}^{\text{transf}} < N_{\text{gas}}^{\text{transf}}, & \text{Add } N_{\text{gas}}^{\text{transf}} - N_{\text{P}}^{\text{transf}} \text{ transfer species particles,} \\ N_{\text{P}}^{\text{transf}} > N_{\text{gas}}^{\text{transf}}, & \text{Remove } N_{\text{P}}^{\text{transf}} - N_{\text{gas}}^{\text{transf}} \text{ transfer species particles.} \end{cases} \tag{3.98}$$

According to this inequality, the model adds or removes as many particles as necessary to make Equation (3.98) an equality. It must be noted that the volume should be adjusted after adding or removing particles to the ensemble as discussed in Section 3.7.2.

Recent works that focus on the precursors to carbonaceous particles have omitted the solution of the simplified population balance equation [339, 296, 167, 274, 340]. In these, the solution of the gas phase chemistry model is also used as an input to a stochastic model that only handles the growth of PAHs. Although missing a particle model induces an error in the concentrations of gas phase chemical species, the processes, pathways and structures sampled provide a useful insight into the processes that affect PAH growth.

3.7.2   Ensemble contraction and particle doubling algorithms

In the DSA, if particle-particle processes are included, the number of stochastic particles in the ensemble is not conserved due to the formation of aggregates or the addition of new particles from the gas phase. This can lead to two difficulties: First, the addition of a stochastic particle when the system has reached the maximum possible number of particles. Second, the removal of a stochastic particle until no particles remain. Both of these problems have been studied in depth in the context of stochastic reactor models. In this work, these issues are resolved by using an ensemble contraction algorithm and a particle doubling algorithm.

The ensemble contraction algorithm is used once the number of stochastic particles in the ensemble has reached the maximum possible number of stochastic particles, N_{max}. If this is the case, the algorithm removes a uniformly selected particle from the ensemble before adding the new stochastic particle [285]. The sample volume is then reduced proportionally by a factor of $N/(N+1)$. Although this algorithm handles the addition of stochastic particles, there is an inherent loss of information (by removing a particle that has already sampled jump processes) that may affect the observations of such a simulation. It is therefore advisable that the maximum possible number of stochastic particles, N_{max}, be kept reasonably high to include all particles included in the simulation at all times.

The particle doubling algorithm [271] is activated the first time the number of stochastic particles in the ensemble exceeds 75% of N_{max}. After the doubling algorithm is activated it keeps track of the number of stochastic particles in the ensemble. If this number falls below the doubling limit, N_{lim}, the stochastic particles are duplicated and the sample volume is doubled. This keeps a constant particle number density throughout the doubling event. The assumption of this algorithm is that an equivalent ensemble of stochastic particles can be included in the scope of the simulation to keep a computationally tractable number of particles.

The ensemble contraction algorithm and the particle doubling algorithm bound the number of stochastic particles in the ensemble in the range $[N_{\text{lim}}, N_{\text{max}}]$ after the first time the particle doubling algorithm is activated. The doubling limit is defined in terms of the number of levels in the binary tree, N_{lvl}, that is used to store the ensemble of stochastic particles [95]:

$$N_{\text{lim}} = \begin{cases} \frac{N_{\text{max}}}{2} - 2^{N_{\text{lvl}}-5} & , \quad N_{\text{lvl}} - 5 > 0, \\ \frac{N_{\text{max}}}{2} - 2^0 & , \quad N_{\text{lvl}} - 5 \leq 0, \end{cases} \tag{3.99}$$

where N_{lvl} is defined as $N_{\text{lvl}} = \log(N_{\text{max}})/\log(2)$.

3.7.3 Majorant kernels and fictitious jumps

The total coagulation rate, R_{cg}, requires a summation over every pair of particles

$$R_{\text{cg}} = \frac{1}{2} \sum_{q \neq r}^{N_{\text{P}}} K(P_q, P_r). \tag{3.100}$$

The evaluation of this rate incurs a computational expense of $\mathcal{O}(N_{\text{P}}^2)$ which can become prohibitive for large N_{P}. To address this, the methodology by Eibeck and Wagner [68] and Goodson and Kraft [95] is followed. Eibeck and Wagner [68] introduced a majorant kernel, $\hat{K}$, such that

$$\hat{K} \geq K, \tag{3.101}$$

for which it is computationally efficient to calculate

$$\hat{R}_{\text{cg}} = \frac{1}{2} \sum_{q \neq r}^{N_{\text{P}}} \hat{K}(P_q, P_r). \tag{3.102}$$

Goodson and Kraft [95] proposed a majorant kernel for the free-molecular regime (Equation (3.32)) of the form

$$\hat{K}^{\text{fm}}(P_q, P_r) = 2.2 k_{\text{maj}} \left(\frac{\pi k_B T}{2} \right)^{1/2} \left(\frac{1}{\mathfrak{m}(P_q)^{1/2}} + \frac{1}{\mathfrak{m}(P_r)^{1/2}} \right) \left(d_{\text{col}}(P_q)^2 + d_{\text{col}}(P_r)^2 \right), \tag{3.103}$$

where $k_{\text{maj}}(= 2.0)$ is the majorant rate scaling factor necessary to satisfy the inequality in Equation (3.101) [95, 68]. Patterson et al. [241] extended the approach to the transition regime, defining the majorant rate

$$\hat{R}_{\text{cg}}^{\text{tr}} = \min \left(\hat{R}_{\text{cg}}^{\text{fm}}, \hat{R}_{\text{cg}}^{\text{sf}} \right). \tag{3.104}$$

Due to its simpler form, the slip-flow kernel does not require a majorant. The correct coagulation rate is then recovered by performing *fictitious* coagulation jump processes. This means advancing the simulation time after rejecting coagulation events between two particles P_q and P_r with probability [241, 68]:

$$1 - \frac{K(P_q, P_r)}{\hat{K}(P_q, P_r)}. \tag{3.105}$$

This approach takes advantage of the binary tree data structure, which stores and efficiently updates pre-calculated sums of particle properties.

3.7.4   Linear process deferment algorithm

The linear process deferment algorithm (LPDA) was first proposed by Patterson et al. [243]. This algorithm is designed to solve population balance equations where particle-particle processes cannot be neglected, but the total process rate is dominated by linear processes. In this context, linear refers to processes that involve a single particle at a time, *i.e.* surface growth or condensation processes.

In such cases, the LPDA has been shown to reduce computational times while capturing the non-linear particle interactions. The rationale behind the LPDA is the same as the approximations discussed in Section 3.5. Linear processes are usually faster than non-linear processes. This allows them to be deferred as their rates can be calculated on their own without affecting the physics of slow processes. In the LPDA, the linear processes are deferred and are performed on a pair of particles only once the particle pair is selected for a particle-particle interaction (inception, coagulation or condensation). After all non-linear processes are sampled, the particles that did not interact in these are updated only with linear processes.

In this model, all PAH jump processes are considered linear processes and are performed only after all particle interactions have been sampled. In the case that no particle interactions are considered (as in Chapter 4, Chapter 5 and Chapter 6), the model performs the linear processes for all molecules sequentially, as it makes no difference to select one molecule over another if they are not interacting. The numerical algorithms described in Sections 3.7.1–3.7.4 are shown in Algorithms 1 and 2.

Algorithm 1: Direct simulation algorithm with particle doubling.

Input: State of the system Q_0 at time t_0, Stop time t_f, Transfer species A^{transf}

Output: State of the system Q_f at stop time t_f.

$t_i \longleftarrow t_0$, $Q_i \longleftarrow Q_0$

while $t_i < t_f$ **do**

    Calculate the number of transfer species molecules from the gas phase:

$$N_{gas}^{transf} = \lfloor C_{A^{transf}} N_A V_{sampl} \rfloor$$

    while $N_P^{transf} \neq N_{gas}^{transf}$ **do** /* Compare with transfer species in the ensemble */

        if $N_P^{transf} < N_{gas}^{transf}$ **then**

            Add transfer species (as single molecule primary particles) to the ensemble

            if $N_P(Q) > N_{max}$ **then**

                Uniformly remove a particle

                Contract the ensemble

            end

        else

            Remove transfer species from the ensemble

        end

    end

    Calculate total rate of non-deferred processes:

$$R_{tot}^{non\text{-}def}(Q) = \hat{R}_{cg}^{tr}(Q) = \frac{1}{2} \sum_{q \neq r}^{N_P} \hat{K}(P_q, P_r).$$

    Calculate an exponentially distributed waiting time:

$$\tau = \frac{\ln U}{R_{tot}^{non\text{-}def}(Q)},$$

    where U is a uniformly distributed random variable, $U \in [0,1]$

    Select two particles P_q and P_r

    Calculate the majorant kernel for two particles: $\hat{K}_{cg}^{tr}(P_q, P_r)$

    Perform deferred processes for P_q and P_r

    Calculate the true kernel for the two particles: $K_{cg}^{tr}(P_q, P_r)$

    Perform particle-particle process with probability

$$P = \frac{K_{cg}^{tr}(P_q, P_r)}{\hat{K}_{cg}^{tr}(P_q, P_r)},$$

    if $N < N_{lim}$ **then**

        for $i \in \{1, \ldots, N_P(Q)\}$ **do**   /* Double the ensemble */

            Create a new particle $P_{New,i} \longleftarrow P_i$

        end

        Double sampling volume

    end

    $Q \longleftarrow Q_t$

    $t \longleftarrow t + \tau$

end

for $q \in \{1, \ldots, N_P(Q)\}$, $i \in \{1, \ldots, n_p(P_q)\}$, $j \in \{1, \ldots, n_m(p_i)\}$ **do**   /* LPDA */

    Perform deferred (PAH) processes for all molecules in all particles

    (See Algorithm 2)

end

$Q \longleftarrow Q_t$

$t \longleftarrow t_f$

Algorithm 2: Deferred (PAH) processes for a single molecule according to LPDA.

Input: State of molecule Q_0 at t_0, Final time t_f
Output: State of molecule Q_f at t_f
$t \leftarrow t_0, Q \leftarrow Q_0$
while $t < t_f$ **do**

Calculate total rate of surface growth (deferred) processes:
$$R_{\text{tot}}^{\text{def}}(Q) = \sum_j R_j(Q), \qquad \text{where } j \in \{S1, \dots, S30\} \text{ Table 3.4,}$$

Calculate an exponentially distributed waiting time:
$$\tau = \frac{\ln U}{R_{\text{tot}}^{\text{def}}(Q)},$$

where U is a uniformly distributed random variable, $U \in [0,1]$
Select a process j with probability
$$P(j) = \frac{R_j}{R_{\text{tot}}^{\text{def}}}.$$

Uniformly select a site s_k to perform process j, such that η_k or $\eta_{\text{comb},k}$ are the same site type
  as required by the parent site type for process j
/* Perform Jump Process j */
As stated by Process j (Table 3.5):
Optimise the structure if necessary
Add or remove atoms
Add or remove rings
Add or remove sites
Transform existing sites
Optimise the structure if necessary
$Q \leftarrow Q_t$
$t \leftarrow t + \tau$

end
$Q \leftarrow Q_t$
$t \leftarrow t_f$

3.7.5 Deferred update migration algorithm

In this work, the detailed particle model implements, for the first time, an algorithm that defers the update of the carbonaceous structure whilst successive partially-embedded five-member ring migration processes are sampled. The algorithm keeps track of the number and direction of each partially-embedded five-member ring migration step, such that the structure of the molecule can be recovered whenever it is required for other calculations.

The migration algorithm implemented in this work is based on the studies performed by Frenklach and collaborators [348, 351, 350]. In their work, the migration of a partially-embedded five-member ring was accurately described as a one-dimensional random walk along the edge of a molecule, where the random walk is terminated when a process that consumes the *random walker* is observed. The rates of the migration processes favour the edge position over the corner position as described in Figure 3.13.
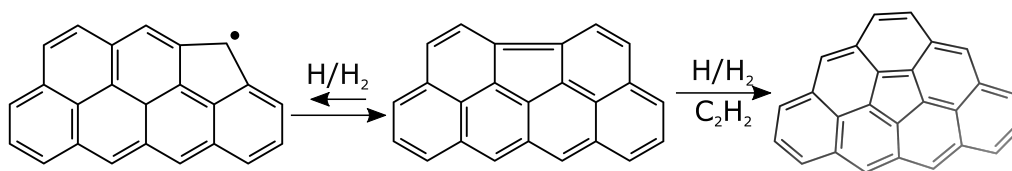
Fig. 3.13 Migration and embedding of partially-embedded five-member rings as studied by Whitesides et al. [351].

In the stochastic model presented in this chapter, two computational structures are modified every time a process is sampled: First, the site list (L_s) is updated to maintain a cache of the types and locations of the sites that exist around the perimeter of the molecule. Second, the structure (L_c and $\mathcal{V}_1$) is updated to record the new locations of the carbon and hydrogen atoms in the molecule. In general, both the site list and the structure of the molecule are required for an accurate simulation of the growth of the molecule. However, in the case of successive migration steps (processes S18 and S19), it is sufficient to update only the site list. It is only necessary to update the structure when a non-migration process is sampled (or when the migration results in certain structural changes, see Section 3.7.5). The rates of the migration processes are such that a partially-embedded five-member ring on a given edge will typically move a number of times before the ring leaves the edge or before a non-migration transformation is sampled, such that updating the structure after each migration process adds significant unnecessary computational cost. The final position of the five-member ring is directly related to the number of steps in the random walk, and thus the probability of finding the five-member ring at any given location is mathematically well defined. During the random walk, it is important that the rates of all processes are accurate to correctly capture

the termination of the five-member ring migration. In this algorithm this is achieved by keeping updated the site list.

The modified algorithm is summarised in Algorithm 3. In the case of random walks of only one step (*i.e.* no deferred migration steps) the modified algorithm reduces to the previous algorithm. The exactness and computational performance of the modified algorithm have been investigated. An algorithm in which both the site list and the structure of the molecule are updated after each process has been selected as a baseline, ensuring accurate resolution of the migration processes. From this point onwards, the modified algorithm is referred to as the *deferred update* algorithm and the previous algorithm as the *reference* algorithm.

Both algorithms were used to simulate the evolution of 163 representative molecules with varying numbers of partially-embedded five-member rings. The representative molecules were taken from the simulation of a counterflow diffusion flame of ethylene such as the one studied in Chapter 5. The simulations used a submechanism that only included migration processes and processes that terminate the migration of partially-embedded five-member rings (Table 3.4, processes S18, S19, S22–S27, S30). The simulations used constant mole fractions of $X_{\mathrm{H}} = 0.01$, $X_{\mathrm{H}_2} = X_{\mathrm{C}_2\mathrm{H}_2} = 0.1$, $X_{\mathrm{O}_2} = X_{\mathrm{O}} = 0.001$ and a constant temperature and pressure of 1500 K and 1 atmosphere. Ten repetitions of each simulation were performed using different numerical seeds.

Exactness

Figure 3.14 shows the net number of steps taken during the migration of partially-embedded five-member rings simulated using the deferred update algorithm (solid lines) and the reference algorithm (open circles) for representative molecules. Both algorithms sampled the same sequence of processes resulting in the same structures at the same point in each simulation. This demonstrates that the deferred update algorithm is exact in the sense that it produces the correct sites in the migration of partially-embedded five-member rings. The same exact agreement was seen for all repetitions of all 163 tested molecules.

Figure 3.14 also shows the distribution of the locations of the partially-embedded rings after different numbers of migration steps. The distributions were calculated using a kernel density estimate (calculated using Scikit-Learn [244] with a Gaussian kernel and bandwidth = 5.0) for 5000 repetitions of the same molecule using the deferred update algorithm. The distributions confirm that the behaviour described by Frenklach and collaborators [351] is maintained: the migration of a partially-embedded five-member ring follows a one-dimensional random walk. As expected, the distributions are approximately Gaussian, centred on the starting position and become wider with successive steps.

Algorithm 3: Deferred (PAH) processes for a single molecule with deferred update migration algorithm.

Input: State of molecule Q_0 at t_0, Final time t_f
Output: State of molecule Q_f at t_f
$Q \leftarrow Q_0$
$t \leftarrow t_0$
deferredMigration $\leftarrow$ *False*
while $t < t_f$ **do**

    Calculate total rate of surface growth (deferred) processes:
$$R_{\text{tot}}^{\text{def}}(Q) = \sum_j R_j(Q), \qquad \text{where } j \in \{S1,\ldots,S30\} \text{ Table 3.4,}$$

    Calculate an exponentially distributed waiting time:
$$\tau = \frac{\ln U}{R_{\text{tot}}^{\text{def}}(Q)},$$

    where U is a uniformly distributed random variable, $U \in [0,1]$
    Select a process j with probability
$$P(j) = \frac{R_j}{R_{\text{tot}}^{\text{def}}}.$$

    Uniformly select a site s_k to perform process j such that η_k corresponds to the principal site type of process j
```
/* Perform Jump Process j                                                        */
```
    if $j \in$ MIGRATION **then**   `/* A migration process */`

        if deferredMigration = *False* **then**   `/* Defer migration process */`
            deferredMigration $\leftarrow$ *True*
            Initialise set of random walkers, $\mathscr{W} = \{w_1, w_2, \ldots, w_{N_w}\}$,   `/* One per migrating site */` where each random walker is represented as a pair $w_m = (i_m, n_m)$ defined by the initial location of the migrating site i_m and the net number of steps taken during the random walk n_m, such that the current location of migrating site k, described by walker $m(k)$, is $k = i_m + n_m$.
        end
        Look up index of migrating site
        $m \leftarrow m(k)$
        Select migration direction
        Select the landing site for the migration, $s_l \in \{s_{k+1}, s_{k-1}\}$.
        $n_m \leftarrow n_m \pm 1$.
        if go around corner **then**   `/* Site moves around the corner */`
            Modify structure – only affected sites
            Add carbon atom to site s_{i_m}.   `/* Site now contains six-member ring */`
            Remove carbon atom from s_l.   `/* Site now contains five-member ring */`
            Remove site next to s_l. Add site next to s_{i_m}.   `/* Update number of sites */`
            Update walker with new migrating site data, $w_m \leftarrow (i_m = l, n_m = 0)$.
        end
        Update sites   `/* Rates are accurate */`
        Update the site type of s_k (remove partially-embedded five-member ring).   `/* Update site list */`
        Update the site type of s_l (add partially-embedded five-member ring).   `/* Update site list */`
        Update neighbouring sites.   `/* Sites affect their neighbours */`
    else   `/* Not a migration process */`
        if deferredMigration **then**
            Modify structure – update the location of all migration sites
            Add carbon atoms and new sites, update site types for all initial sites s_{i_m} in $\mathscr{W}$.
            Remove carbon atoms and neighbour sites, update site types for all final sites $s_{i_m+n_m}$ in $\mathscr{W}$.
            Update neighbouring sites.   `/* Sites affect their neighbours */`
            Optimise structure   `/* After all migration processes */`
            deferredMigration $\leftarrow$ *False*
        end
        Perform non-migration jump process
        $Q \leftarrow Q_t$
    end
    $t \leftarrow t + \tau$
end
$Q \leftarrow Q_t$
$t \leftarrow t_f$
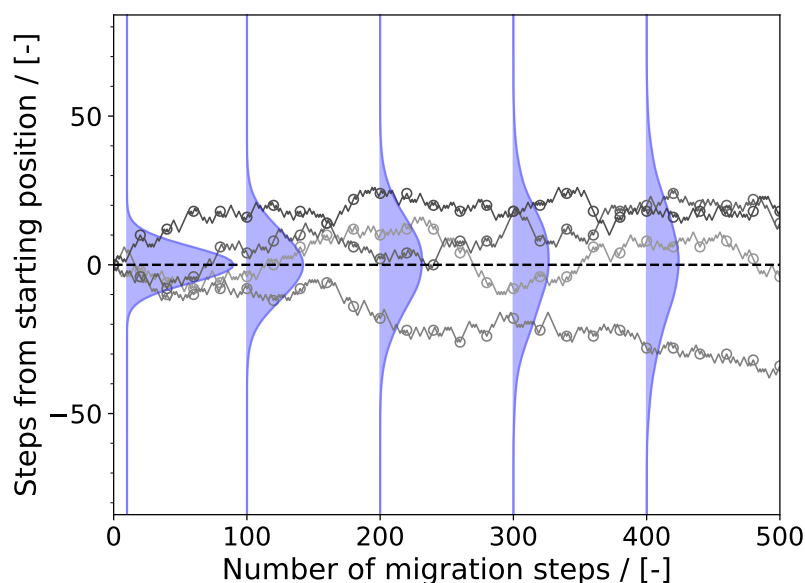
Fig. 3.14 Comparison of the net number of steps taken during the migration of partially-embedded five-member rings simulated using the deferred update algorithm and the reference algorithm. Solid lines show the position of the random walker simulated using the deferred update algorithm. Open circles (○) show the position of the random walker simulated using the reference algorithm (structure updated after every step). The distributions shown after 10, 100, 200, 300 and 400 steps were calculated using 5000 repetitions of the deferred update algorithm.

Computational Performance

Figure 3.15 shows the computational time spent on the simulation of the migration processes using the deferred update algorithm (circles) and the reference algorithm (crosses). The computational time is proportional to the number of migration steps for the reference algorithm. However, the deferred update algorithm shows two groups of points: random walks where there is a weak dependence between the computational time and the number of migration steps, and random walks where the dependence is similar to that of the reference algorithm.

The first group of points corresponds to structures that did not need to be updated until the random walk was finished. The second group of points corresponds to structures that needed to be updated before the end of the random walk. This occurred exclusively in cases where the partially-embedded five-member ring became exposed to the other side of the molecule. This is illustrated in Figure 3.16. The deferred update algorithm identifies this as the creation of an additional random walker on a different edge that could be subject to migration processes. To address this correctly the structure must be updated and optimised
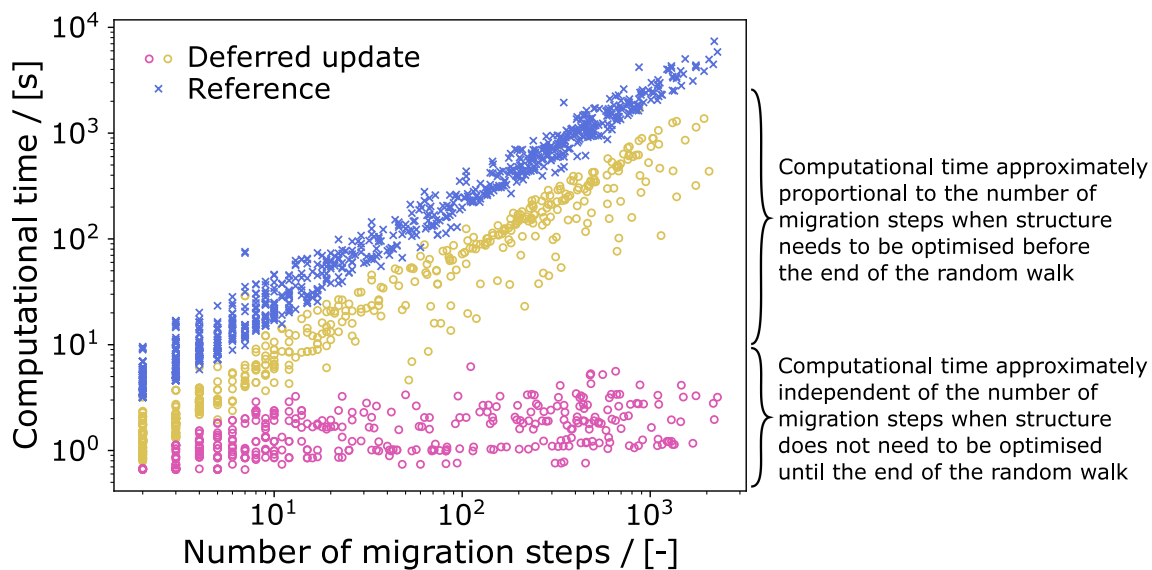
Fig. 3.15 Computational time obtained with the updated deferred algorithm (circles) and with the reference algorithm (crosses). Structures were sampled from the counterflow diffusion flame studied in Chapter 5.

before continuing with the random walk. This shows that there are still several possibilities for further improvements in the simulation of migration processes.

The computational time saved by the deferred update algorithm is proportional to the number of steps that are deferred, such that the computational savings are largest when migration processes dominate. Even though it was still necessary to update the structure of some of the molecules mid-migration (see above), the computational savings obtained are significant. The deferred update algorithm was, on average, observed to be two orders of magnitude faster than the reference algorithm.
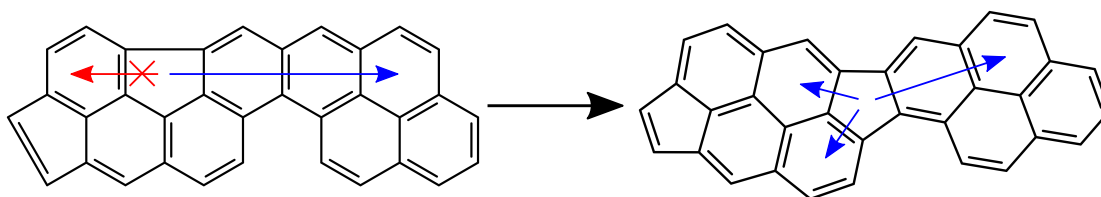
Fig. 3.16 A partially-embedded five-member ring can sometimes become exposed to both sides of a molecule during the simulation of migration processes. Blue arrows show possible directions for the migration.

3.8   List of PAH jump processes and rates

Table 3.3 provides the elementary reaction rate coefficients used for all jump processes implemented in the model. Table 3.4 provides an enumeration of the PAH jump processes included as well as the rate equation for each. Table 3.5 provides the number of atoms and rings that are added or removed, the site transformations and the conditions needed to optimise the structure for each of the PAH jump processes implemented in the model.

<div align="center">Table 3.3 Elementary reaction rate coefficients</div>

No.	Reactions	$k = AT^n \exp(-E_A/\mathrm{R_{gas}}T)$ [a]			References
		A	n	E_A	
	Hydrogen abstraction from six-member rings				
1	$C_sR_6-H + H \rightarrow C_sR_6{}^\bullet + H_2$	4.570×10^{08}	1.880	14.839	[282]
-1	$C_sR_6{}^\bullet + H_2 \rightarrow C_sR_6 + H$	1.690×10^{04}	2.620	4.559	[282]
2	$C_sR_6-H + OH \rightarrow C_sR_6{}^\bullet + H_2O$	5.190×10^{03}	3.040	3.675	[156]
-2	$C_sR_6{}^\bullet + H_2O \rightarrow C_sR_6 + OH$	5.590×10^{00}	3.573	8.659	[156]
3	$C_sR_6{}^\bullet + H \rightarrow C_sR_6-H$	4.170×10^{13}	0.150		[114]
	Hydrogen abstraction from five-member rings				
4	$C_sR_5-H + H \rightarrow C_sR_5{}^\bullet + H_2$	4.890×10^{09}	1.508	19.862	[122]
-4	$C_sR_5{}^\bullet + H_2 \rightarrow C_sR_5 + H$	5.068×10^{04}	2.445	4.520	[122]
5	$C_sR_5-H + OH \rightarrow C_sR_5{}^\bullet + H_2O$	5.190×10^{03}	3.040	3.675	[156]
-5	$C_s{}^\bullet + H_2O \rightarrow C_s + OH$	5.590×10^{00}	3.573	8.659	[156]
6	$C_sR_5{}^\bullet + H \rightarrow C_sR_5-H$	6.080×10^{12}	0.270		[348]
	Hydrogen addition to five-member rings				
7	$C_sR_5H-C_sR_5H + H \rightarrow C_sR_5H_2-C_sR_5H^\bullet$	5.400×10^{11}	0.450	1.820	[348]
-7	$C_sR_5H_2-C_sR_5H^\bullet \rightarrow C_sR_5H-C_sR_5H + H$	3.015×10^{11}	0.450	-33.367	[348]
8	$C_sR_5H_2-C_sR_5H^\bullet + H \rightarrow C_sR_5H-C_sR_5H + H_2$	2.000×10^{12}			[348]
	Armchair growth				
9	$C_sR_6{}^\bullet + C_2H_2 \rightarrow C_sR_6-R_6 + H$	1.190×10^{22}	-2.450	18.890	[86]
10	$C_sR_6{}^\bullet + C_2H_2 \rightarrow C_sR_6-R_6 + H$	1.060×10^{14}	-0.490	8.204	[86]
11	$C_sR_6{}^\bullet + C_2H_2 \rightarrow C_sR_6-C_2H + H$	4.240×10^{14}	0.025	33.080	[86]
12	$C_sR_6{}^\bullet + C_2H_2 \rightarrow C_sR_6-C_2H + H$	7.640×10^{-2}	3.950	16.495	[86]
	Free-edge desorption to produce an armchair				
-9	$C_sR_6-R_6 + H \rightarrow C_sR_6{}^\bullet + C_2H_2$	5.465×10^{30}	-3.657	86.240	[86, 227]
-10	$C_sR_6-R_6 + H \rightarrow C_sR_6{}^\bullet + C_2H_2$	4.868×10^{22}	-1.697	75.550	[86, 227]
	Free-edge ring growth and desorption				
13	$C_sR_6{}^\bullet + C_2H_2 \rightarrow C_sR_6-C_2H_2$	1.910×10^{61}	-14.600	28.610	[201]
-13	$C_sR_6-C_2H_2 \rightarrow C_sR_6{}^\bullet + C_2H_2$	2.499×10^{69}	-16.430	71.290	[201]
14	$C_sR_6{}^\bullet + C_2H_2 \rightarrow C_sR_6-C_2H + H$	1.100×10^{31}	-4.830	26.620	[201]
-14	$C_sR_6-C_2H + H \rightarrow C_sR_6{}^\bullet + C_2H_2$	2.542×10^{37}	-6.213	37.610	[201]
15	$C_sR_6{}^\bullet + C_2H_2 \rightarrow C_sR_6-C_2H_3{}^\bullet$	1.360×10^{75}	-18.400	40.880	[201]

No.	Reactions	$k = AT^n \exp(-E_A/R_{gas}T)$ [a]			References
		A	n	E_A	
-15	$C_sR_6-C_2H_3{}^\bullet \rightarrow C_sR_6{}^\bullet + C_2H_2$	4.055×10^{82}	-20.120	79.400	[201]
16	$C_sR_6{}^\bullet + C_2H_3 \rightarrow C_sR_6-C_2H_3$	6.000×10^{12}			[227]
-16	$C_sR_6-C_2H_3 \rightarrow C_sR_6{}^\bullet + C_2H_2$	8.216×10^{23}	-2.162	119.100	[227]
17	$C_sR_6{}^\bullet + C_2H_4 \rightarrow C_sR_6 + C_2H_3$	9.450×10^{-3}	4.470	4.472	[227]
-17	$C_sR_6 + C_2H_3 \rightarrow C_sR_6{}^\bullet + C_2H_4$	2.316×10^{-2}	4.416	6.709	[227]
18	$C_sR_6{}^\bullet + C_4H_4 \rightarrow C_sR_6-R_6 + H$	1.260×10^{04}	2.610	1.434	[227]
-18	$C_sR_6-R_6 + H \rightarrow C_sR_6{}^\bullet + C_4H_4$	1.130×10^{16}	0.754	66.940	[227]
19	$C_sR_6 + C_2H_3 \rightarrow C_sR_6-C_2H_3 + H$	1.870×10^{07}	1.470	5.533	[227]
-19	$C_sR_6-C_2H_3 + H \rightarrow C_sR_6 + C_2H_3$	2.042×10^{14}	-0.221	10.410	[227]
20	$C_sR_6-C_2H_3 \rightarrow C_sR_6-C_2H_2 + H$	3.010×10^{14}	0.340	111.255	[227]
-20	$C_sR_6-C_2H_2 + H \rightarrow C_sR_6-C_2H_3$	2.184×10^{11}	0.722		[227]
21	$C_sR_6-C_2H_3 + H \rightarrow C_sR_6-C_2H_2 + H_2$	6.350×10^{04}	2.750	11.649	[227]
-21	$C_sR_6-C_2H_2 + H_2 \rightarrow C_sR_6-C_2H_3 + H$	2.509×10^{01}	3.375	3.404	[227]
22	$C_sR_6-C_2H_3 + OH \rightarrow C_sR_6-C_2H_2 + H_2O$	6.550×10^{-2}	4.200	-0.860	[227]
-22	$C_sR_6-C_2H_2 + H_2O \rightarrow C_sR_6-C_2H_3 + OH$	6.705×10^{-4}	4.613	6.162	[227]
23	$C_sR_6-C_2H_2 \rightarrow C_sR_6-C_2H_3{}^\bullet$	2.440×10^{30}	-5.730	32.070	[201]
-23	$C_sR_6-C_2H_3{}^\bullet \rightarrow C_sR_6-C_2H_2$	5.560×10^{29}	-5.620	27.910	[201]
24	$C_sR_6-C_2H_3{}^\bullet + C_2H_2 \rightarrow C_sR_6-R_6 + H$	3.020×10^{10}	0.702	5.530	[201]
-24	$C_sR_6-R_6 + H \rightarrow C_sR_6-C_2H_3{}^\bullet + C_2H_2$	1.387×10^{21}	-0.798	72.450	[201]
25	$C_sR_6-C_2H + H \rightarrow C_sR_6-C_2H_2$	1.590×10^{62}	-14.500	31.760	[201]
-25	$C_sR_6-C_2H_2 \rightarrow C_sR_6-C_2H + H$	9.003×10^{63}	-14.950	63.440	[201]
26	$C_sR_6-C_2H_2 + H \rightarrow C_sR_6-C_2H + H_2$	1.650×10^{11}	0.490	10.630	[227]
-26	$C_sR_6-C_2H + H_2 \rightarrow C_sR_6-C_2H_2 + H$	1.587×10^{09}	1.184	82.650	[227]
27	$C_sR_6-C_2H_2 + OH \rightarrow C_sR_6-C_2H + H_2O$	2.500×10^{12}			[227]
-27	$C_sR_6-C_2H + H_2O \rightarrow C_sR_6-C_2H_2 + OH$	6.230×10^{11}	0.482	87.280	[227]
28	$C_sR_6-C_2H + C_2H_3 \rightarrow C_sR_6-R_6 + H$	3.600×10^{17}	-1.440	15.758	[227]
-28	$C_sR_6-R_6 + H \rightarrow C_sR_6-C_2H + C_2H_3$	1.619×10^{29}	-3.226	74.700	[227]
29	$C_sR_6-C_2H{}^\bullet + C_2H_2 \rightarrow C_sR_6-R_6{}^\bullet$	4.490×10^{82}	-20.000	51.830	[201]
-29	$C_sR_6-R_6{}^\bullet \rightarrow C_sR_6-C_2H{}^\bullet + C_2H_2$	1.338×10^{94}	-21.840	143.500	[201]
30	$C_sR_6-C_2H{}^\bullet + C_2H_2 \rightarrow C_sR_6-R_6{}^\bullet$	1.180×10^{104}	-25.700	76.820	[201]
-30	$C_sR_6-R_6{}^\bullet \rightarrow C_sR_6-C_2H{}^\bullet + C_2H_2$	3.917×10^{115}	-27.550	168.800	[201]
31	$C_sR_6-C_2H{}^\bullet + C_2H_2 \rightarrow C_sR_6-R_6{}^\bullet$	4.490×10^{82}	-20.000	51.830	[201]
-31	$C_sR_6-R_6{}^\bullet \rightarrow C_sR_6-C_2H{}^\bullet + C_2H_2$	1.338×10^{94}	-21.840	143.500	[201]
32	$C_sR_6-C_2H{}^\bullet + C_2H_2 \rightarrow C_sR_6(C_2H)(C_2H_3) + H$	1.760×10^{40}	-7.040	48.210	[201]
-32	$C_sR_6(C_2H)(C_2H_3) + H \rightarrow C_sR_6-C_2H{}^\bullet + C_2H_2$	9.718×10^{46}	-8.438	60.840	[201]
33	$C_sR_6-C_2H{}^\bullet + C_2H_4 \rightarrow C_sR_6-R_6 + H$	3.620×10^{28}	-4.240	23.860	[227]
-33	$C_sR_6-R_6 + H \rightarrow C_sR_6-C_2H{}^\bullet + C_2H_4$	1.583×10^{40}	-6.094	87.580	[227]
34	$C_sR_6-C_2H_2 + C_2H_2 \rightarrow C_sR_6-R_6 + H$	3.570×10^{22}	-2.720	14.470	[201]
-34	$C_sR_6-R_6 + H \rightarrow C_sR_6-C_2H_2 + C_2H_2$	3.736×10^{32}	-4.109	77.230	[201]
35	$C_sR_6(C_2H)(C_2H_3) + H \rightarrow C_sR_6-R_6{}^\bullet$	1.010×10^{86}	-20.600	56.700	[201]
-35	$C_sR_6-R_6{}^\bullet \rightarrow C_sR_6(C_2H)(C_2H_3) + H$	5.450×10^{90}	-21.040	138.800	[201]

No.	Reactions	$k = AT^n \exp(-E_A/\mathrm{R}_{gas}T)$ [a]			References
		A	n	E_A	
36	$C_sR_6(C_2H)(C_2H_3) + H \rightarrow C_sR_6-R_6^\bullet$	6.000×10^{108}	-26.600	83.590	[201]
-36	$C_sR_6-R_6^\bullet \rightarrow C_sR_6(C_2H)(C_2H_3) + H$	3.607×10^{113}	-27.050	162.900	[201]
	Six-member bay closure				
37	$C_sR_6-H + H \rightarrow C_sR_6^\bullet + H_2$	9.240×10^{07}	1.500	9.646	[256]
-37	$C_sR_6^\bullet + H_2 \rightarrow C_sR_6 + H$	9.600×10^{04}	1.960	9.021	[256]
38	$C_sR_6^\bullet \rightarrow C_sR_6-R_6^\bullet$	1.110×10^{11}	0.658	23.990	[256]
39	$C_sR_6^\bullet \rightarrow C_sR_6-R_6^\bullet$	3.490×10^{12}	-0.390	2.440	[256]
	Five-member bay closure				
40	$C_sR_6-H + H \rightarrow C_sR_6^\bullet + H_2$	7.250×10^{07}	1.760	9.69	[330]
-40	$C_sR_6^\bullet + H_2 \rightarrow C_sR_6 + H$	3.400×10^{09}	0.880	7.870	[330]
41	$C_sR_6^\bullet + C_sR_6-H \rightarrow C_sR_6^\bullet-C_sR_6-H$	3.860×10^{11}	0.210	17.700	[330]
	Phenyl addition				
42	$C_sR_6^\bullet + A_1 \rightarrow C_sR_6-A_1 + H$	2.220×10^{83}	-20.790	46.890	[266]
43	$C_sR_6 + A_1^\bullet \rightarrow C_sR_6-A_1 + H$	2.220×10^{83}	-20.790	46.890	[266]
	Five-member ring growth on a zig-zag				
44	$C_sR_6^\bullet + C_2H_2 \rightarrow C_sR_6-R_5 + H$	1.250×10^{27}	-3.950	16.779	[86]
45	$C_sR_6^\bullet + C_2H_2 \rightarrow C_sR_6-R_5 + H$	3.090×10^{20}	-2.780	8.889	[86]
46	$C_sR_6^\bullet + C_2H_2 \rightarrow C_sR_6-C_2H + H$	3.090×10^{25}	-3.110	31.586	[86]
47	$C_sR_6^\bullet + C_2H_2 \rightarrow C_sR_6-C_2H + H$	2.850×10^{7}	1.520	13.190	[86]
	Five-member ring desorption				
48	$C_sR_5^\bullet \rightarrow C_sR_6-C_2H^\bullet$	1.600×10^{14}		42.42	[84]
49	$C_sR_5H_2-C_sR_5H^\bullet \rightarrow C_sR_6^\bullet + C_2H_2$	3.100×10^{11}	0.870	74.323	[348]
50	$C_sR_5H_2-C_sR_5H^\bullet \rightarrow C_sR_6-C_2H + H$	6.700×10^{11}	0.840	70.790	[348]
	Five-member ring migration to a zig-zag site				
51	$C_sR_5H_2-C_sR_5H^\bullet \rightarrow C_sR_5H^\bullet-C_sR_5H_2$	1.300×10^{11}	0.160	45.900	[348]
	Five-member ring migration to an armchair site				
52	$C_sR_5H_2-C_sR_5H^\bullet \rightarrow C_sR_6-C_sR_6 + H$	1.300×10^{11}	0.160	45.900	[348]
	Partially-embedded five-member ring flip reaction				
53	$C_sR_5H^\bullet-CsR_6 \rightarrow CsR_6-C_sR_5H^\bullet$	1.000×10^{11}			[348, 350]
	Five-member ring conversion to six-member ring neighbouring a free-edge site				
54	$C_sR_6^\bullet + C_2H_2 \rightarrow C_sR_6-C_2H_2$	1.100×10^{07}	1.610	3.896	[32]
55	$C_sR_6^\bullet + C_2H_2 \rightarrow C_sR_6-C_2H_2$	3.330×10^{33}	-5.7	25.500	[32, 336]
56	$C_sR_5H_2-C_sR_5H^\bullet + C_s-C_2H \rightarrow C_sR_6$	1.300×10^{11}	0.160	45.900	[348]
	Six-member ring conversion to five-member ring neighbouring an armchair site				
57	$C_sR_6^\bullet \rightarrow C_sR_5H_2-C_sR_5H^\bullet + C_s-C_2H$	1.300×10^{11}	1.080	70.420	[84]
	Six-member ring conversion to five-member ring neighbouring a five-carbon bay site				
58	$C_{s-BY5}-C_sR_6^\bullet \rightarrow CsR_6-C_sR_5-C_sR_5 + H$	2.300×10^{09}	1.603	61.850	[256]
59	$C_{s-BY5}-C_sR_6^\bullet \rightarrow CsR_6-C_sR_5-C_sR_5 + H$	1.230×10^{10}	1.410	85.200	[330]
	Six-member ring desorption neighbouring a five-carbon bay site				
60	$C_{s-BY5}-C_sR_6^\bullet \rightarrow CsR_6-C_sR_6^\bullet + C_2H_2$	2.300×10^{09}	1.603	61.850	[256]

No.	Reactions	$k = AT^n \exp(-E_A/R_{gas}T)$ [a]			References
		A	n	E_A	
	Six-member ring growth on a zig-zag neighbouring a five-member ring				
61	$C_sR_5{}^\bullet + C_2H_2 \rightarrow CsR_5-R_6$	1.235×10^{07}	1.530	9.311	[348]
	Six-member ring growth between two five-member rings				
62	$C_sR_5{}^\bullet + C_2H_2 \rightarrow CsR_5-R_6$	1.235×10^{07}	1.530	9.311	[348]
	Five-member ring conversion to six-member ring neighbouring five-member ring				
63	$C_sR_5{}^\bullet + C_sR_5H \rightarrow CsR_6-R_5$	8.900×10^{05}	2.280	61.489	[348]
	Six-member bay closure containing a partially-embedded five-member ring				
64	$C_sR_6{}^\bullet \rightarrow C_sR_6-R_6{}^\bullet$	1.110×10^{11}	0.658	23.990	[this work]
	Six-member ring growth on a partially-embedded five-member ring armchair				
65	$C_sR_6-H + H \rightarrow C_sR_6{}^\bullet + H_2$	2.540×10^{11}	0.931	16.440	[255]
-65	$C_sR_6{}^\bullet + H_2 \rightarrow C_sR_6 + H$	1.830×10^{12}	0.397	8.815	[255]
66	$C_sR_6{}^\bullet + C_2H_2 \rightarrow C_sR_6-C_2H_2$	1.630×10^{12}	0.409	5.675	[255]
-66	$C_sR_6-C_2H_2 \rightarrow C_sR_6{}^\bullet + C_2H_2$	9.130×10^{11}	0.991	15.990	[255]
67	$C_sR_6-C_2H_2 \rightarrow C_sR_6{}^\bullet-C_2H_3$	6.320×10^{11}	0.166	18.050	[255]
-67	$C_sR_6{}^\bullet-C_2H_3 \rightarrow C_sR_6-C_2H_2$	9.750×10^{10}	0.458	15.830	[255]
68	$C_sR_6{}^\bullet-C_2H_3 \rightarrow C_sR_6H_2-CsR_6H^\bullet$	9.580×10^{11}	−0.064	16.310	[255]
-68	$C_sR_6H_2-CsR_6H^\bullet \rightarrow C_sR_6{}^\bullet-C_2H_3$	9.650×10^{11}	0.501	41.500	[255]
69	$C_sR_6H_2-CsR_6H^\bullet \rightarrow C_sR_6-CsR_6 + H$	3.160×10^{12}	0.787	36.510	[255]
-69	$C_sR_6-CsR_6 + H \rightarrow C_sR_6H_2-CsR_6H^\bullet$	9.710×10^{11}	0.507	4.695	[255]
70	$C_sR_6{}^\bullet-C_2H_3 \rightarrow C_sR_6H-CsR_6$	2.780×10^{11}	0.063	23.870	[255]
-70	$C_sR_6H-CsR_6 \rightarrow C_sR_6{}^\bullet-C_2H_3$	5.470×10^{11}	0.645	32.770	[255]
71	$C_sR_6H-CsR_6 \rightarrow C_sR_6-CsR_6 + H$	8.150×10^{11}	0.563	24.860	[255]
-71	$C_sR_6-CsR_6 + H \rightarrow C_sR_6H-CsR_6$	9.060×10^{11}	0.456	7.286	[255]
	Seven-member ring growth on a five-carbon bay site (partially-embedded five-member ring)				
72	$C_sR_6-H + H \rightarrow C_sR_6{}^\bullet + H_2$	5.897×10^{07}	1.847	17.120	[206]
-72	$C_sR_6{}^\bullet + H_2 \rightarrow C_sR_6 + H$	1.215×10^{05}	2.229	7.720	[206]
73	$C_sR_6{}^\bullet + C_2H_2 \rightarrow C_sR_6-C_2H_2$	1.348×10^{03}	2.573	4.935	[206]
-73	$C_sR_6-C_2H_2 \rightarrow C_sR_6{}^\bullet + C_2H_2$	2.366×10^{12}	0.705	39.670	[206]
74	$C_sR_6-C_2H_2 \rightarrow C_sR_6H-C_sR_6{}^\bullet$	1.958×10^{11}	0.111	25.330	[206]
-74	$C_sR_6H-C_sR_6{}^\bullet \rightarrow C_sR_6-C_2H_2$	3.412×10^{11}	0.625	53.370	[206]
75	$C_sR_6H-C_sR_6{}^\bullet \rightarrow C_sR_6-CsR_6 + H$	1.770×10^{10}	1.094	27.150	[206]
-75	$C_sR_6-CsR_6 + H \rightarrow C_sR_6H-C_sR_6{}^\bullet$	5.321×10^{07}	1.515	7.095	[206]
76	$C_sR_6-H + H \rightarrow C_sR_6{}^\bullet + H_2$	5.315×10^{07}	1.858	16.120	[206]
-76	$C_sR_6{}^\bullet + H_2 \rightarrow C_sR_6 + H$	9.106×10^{04}	2.277	7.007	[206]
77	$C_sR_6{}^\bullet + C_2H_2 \rightarrow C_sR_6-C_2H_2$	3.521×10^{03}	2.598	3.998	[206]
-77	$C_sR_6-C_2H_2 \rightarrow C_sR_6{}^\bullet + C_2H_2$	4.736×10^{12}	0.702	40.800	[206]
78	$C_sR_6-C_2H_2 \rightarrow C_sR_6H-C_sR_6{}^\bullet$	1.125×10^{11}	0.128	30.510	[206]
-78	$C_sR_6H-C_sR_6{}^\bullet \rightarrow C_sR_6-C_2H_2$	2.383×10^{11}	0.596	57.900	[206]
79	$C_sR_6H-C_sR_6{}^\bullet \rightarrow C_sR_6-CsR_6 + H$	1.505×10^{10}	1.076	28.840	[206]
-79	$C_sR_6-CsR_6 + H \rightarrow C_sR_6H-C_sR_6{}^\bullet$	5.841×10^{07}	1.533	7.084	[206]

No.	Reactions	$k = AT^n \exp(-E_A/\mathrm{R_{gas}}T)$ [a]			References
		A	n	E_A	
Seven-member ring growth on a five-carbon bay site (edge five-member ring)					
80	$C_sR_6-H + H \rightarrow C_sR_6^{\bullet} + H_2$	6.586×10^{07}	1.766	14.770	[206]
-80	$C_sR_6^{\bullet} + H_2 \rightarrow C_sR_6 + H$	1.155×10^{05}	2.310	8.819	[206]
81	$C_sR_6^{\bullet} + C_2H_2 \rightarrow C_sR_6-C_2H_2$	3.886×10^{03}	2.592	4.012	[206]
-81	$C_sR_6-C_2H_2 \rightarrow C_sR_6^{\bullet} + C_2H_2$	6.507×10^{12}	0.710	45.050	[206]
82	$C_sR_6-C_2H_2 \rightarrow C_sR_6H-C_sR_6^{\bullet}$	5.755×10^{11}	0.070	2.983	[206]
-82	$C_sR_6H-C_sR_6^{\bullet} \rightarrow C_sR_6-C_2H_2$	1.742×10^{12}	0.419	29.040	[206]
83	$C_sR_6H-C_sR_6^{\bullet} \rightarrow C_sR_6-CsR_6 + H$	3.207×10^{10}	0.958	23.130	[206]
-83	$C_sR_6-CsR_6 + H \rightarrow C_sR_6H-C_sR_6^{\bullet}$	1.293×10^{08}	1.505	7.425	[206]
84	$C_sR_5-H + H \rightarrow C_sR_5^{\bullet} + H_2$	1.479×10^{07}	1.854	17.070	[206]
-84	$C_sR_5^{\bullet} + H_2 \rightarrow C_sR_5 + H$	5.914×10^{04}	2.234	11.870	[206]
85	$C_sR_5^{\bullet} + C_2H_2 \rightarrow C_sR_5-C_2H_2$	1.098×10^{03}	2.581	7.651	[206]
-85	$C_sR_5-C_2H_2 \rightarrow C_sR_5^{\bullet} + C_2H_2$	2.894×10^{12}	0.709	38.300	[206]
86	$C_sR_5-C_2H_2 \rightarrow C_sR_5H-C_sR_6^{\bullet}$	5.097×10^{11}	0.139	19.740	[206]
-86	$C_sR_5H-C_sR_6^{\bullet} \rightarrow C_sR_5-C_2H_2$	9.936×10^{11}	0.410	45.260	[206]
87	$C_sR_5H-C_sR_6^{\bullet} \rightarrow C_sR_5-CsR_6 + H$	3.590×10^{11}	0.604	30.050	[206]
-87	$C_sR_5-CsR_6 + H \rightarrow C_sR_5H-C_sR_6^{\bullet}$	6.258×10^{08}	1.380	24.510	[206]
Seven-member bay closure (H abstraction on site 1)					
88	$C_sR_6-H + H \rightarrow C_sR_6^{\bullet} + H_2$	3.915×10^{07}	1.876	9.421	[206]
-88	$C_sR_6^{\bullet} + H_2 \rightarrow C_sR_6 + H$	5.369×10^{04}	2.275	5.583	[206]
89	$C_sR_6^{\bullet} + C_sR_6-H \rightarrow C_sR_7-C_sR_7-H$	8.513×10^{11}	0.136	4.510	[206]
-89	$C_sR_7-C_sR_7-H \rightarrow C_sR_6^{\bullet} + C_sR_6-H$	3.523×10^{12}	0.293	25.670	[206]
90	$C_sR_7-C_sR_7-H \rightarrow C_sR_7-C_sR_7 + H$	2.033×10^{10}	1.067	31.600	[206]
-90	$C_sR_7-C_sR_7 + H \rightarrow C_sR_7-C_sR_7-H$	1.033×10^{08}	1.495	2.895	[206]
91	$C_sR_6-H + H \rightarrow C_sR_6^{\bullet} + H_2$	3.091×10^{07}	1.891	9.308	[206]
-91	$C_sR_6^{\bullet} + H_2 \rightarrow C_sR_6 + H$	5.144×10^{04}	2.267	7.132	[206]
92	$C_sR_6^{\bullet} + C_sR_6-H \rightarrow C_sR_7-C_sR_7-H$	7.041×10^{11}	0.184	10.340	[206]
-92	$C_sR_7-C_sR_7-H \rightarrow C_sR_6^{\bullet} + C_sR_6-H$	2.944×10^{12}	0.413	28.620	[206]
93	$C_sR_7-C_sR_7-H \rightarrow C_sR_7-C_sR_7 + H$	1.861×10^{10}	1.136	29.570	[206]
-93	$C_sR_7-C_sR_7 + H \rightarrow C_sR_7-C_sR_7-H$	7.712×10^{07}	1.514	2.067	[206]
Seven-member bay closure (Carbene route on site 1)					
94	$C_sR_6-H + C_sR_6-H \rightarrow C_sR_6^{(2\bullet)} + C_sR_6-H_2$	8.031×10^{10}	0.890	95.830	[206]
-94	$C_sR_6^{(2\bullet)} + C_sR_6-H_2 \rightarrow C_sR_6-H + C_sR_6-H$	4.398×10^{11}	0.359	3.385	[206]
95	$C_sR_6^{(2\bullet)} + C_sR_6-H \rightarrow C_sR_7-C_sR_7-H$	8.031×10^{11}	0.010	8.456	[206]
-95	$C_sR_7-C_sR_7-H \rightarrow C_sR_6^{(2\bullet)} + C_sR_6-H$	1.897×10^{12}	0.223	17.790	[206]
96	$C_sR_7-H + C_sR_7 \rightarrow C_sR_7 + C_sR_7-H$	5.759×10^{11}	0.393		[206]
-96	$C_sR_7 + C_sR_7-H \rightarrow C_sR_7-H + C_sR_7$	1.052×10^{11}	0.905	53.500	[206]
97	$C_sR_7-H + C_sR_6-H \rightarrow C_sR_7 + C_sR_6-H_2 + H_2$	8.873×10^{10}	0.639	31.310	[206]
-97	$C_sR_7 + C_sR_6-H_2 \rightarrow C_sR_7-H + C_sR_6-H$	1.728×10^{10}	0.712	60.650	[206]
98	$C_sR_6-H_2 + C_sR_6-H_2 \rightarrow C_sR_6-H + C_sR_6-H + H_2$	3.907×10^{09}	1.273	97.050	[206]
-98	$C_sR_6-H + C_sR_6-H + H_2 \rightarrow C_sR_6-H_2 + C_sR_6-H_2$	2.448×10^{05}	1.999	86.400	[206]

No.	Reactions	$k = AT^n \exp(-E_A/\mathrm{R_{gas}}T)$ [a]			References
		A	n	E_A	
99	$C_sR_6-H + C_sR_6-H \rightarrow C_sR_6^{(2\bullet)} + C_sR_6-H_2$	1.061×10^{11}	0.799	84.260	[206]
-99	$C_sR_6^{(2\bullet)} + C_sR_6-H_2 \rightarrow C_sR_6-H + C_sR_6-H$	5.486×10^{11}	0.335	2.012	[206]
100	$C_sR_6^{(2\bullet)} + C_sR_6-H \rightarrow C_sR_7-C_sR_7-H$	1.000×10^{12}	-0.014	3.568	[206]
-100	$C_sR_7-C_sR_7-H \rightarrow C_sR_6^{(2\bullet)} + C_sR_6-H$	2.167×10^{12}	0.556	59.280	[206]
101	$C_sR_7-H + C_sR_6-H \rightarrow C_sR_7 + C_sR_6-H_2$	3.063×10^{11}	0.824	63.560	[206]
-101	$C_sR_7 + C_sR_6-H_2 \rightarrow C_sR_7-H + C_sR_6-H$	1.514×10^{10}	0.674	50.310	[206]
102	$C_sR_6-H_2 + C_sR_6-H_2 \rightarrow C_sR_6-H + C_sR_6-H + H_2$	4.479×10^{09}	0.714	27.100	[206]
-102	$C_sR_6-H + C_sR_6-H + H_2 \rightarrow C_sR_6-H_2 + C_sR_6-H_2$	2.332×10^{05}	1.742	55.100	[206]
	Seven-member bay closure (H abstraction on site 2)				
103	$C_sR_6-H + H \rightarrow C_sR_6^\bullet + H_2$	2.767×10^{07}	1.913	9.542	[206]
-103	$C_sR_6^\bullet + H_2 \rightarrow C_sR_6 + H$	4.212×10^{04}	2.264	6.878	[206]
104	$C_sR_6^\bullet + C_sR_6-H \rightarrow C_sR_7-C_sR_7-H$	4.703×10^{11}	0.143	4.722	[206]
-104	$C_sR_7-C_sR_7-H \rightarrow C_sR_6^\bullet + C_sR_6-H$	1.476×10^{12}	0.367	27.37	[206]
105	$C_sR_7-C_sR_7-H \rightarrow C_sR_7-C_sR_7 + H$	6.424×10^{09}	1.093	32.16	[206]
-105	$C_sR_7-C_sR_7 + H \rightarrow C_sR_7-C_sR_7-H$	1.693×10^{08}	1.522	1.637	[206]
106	$C_sR_6-H + H \rightarrow C_sR_6^\bullet + H_2$	2.843×10^{07}	1.906	9.533	[206]
-106	$C_sR_6^\bullet + H_2 \rightarrow C_sR_6 + H$	5.338×10^{04}	2.261	7.525	[206]
107	$C_sR_6^\bullet + C_sR_6-H \rightarrow C_sR_7-C_sR_7-H$	6.599×10^{11}	0.082	2.625	[206]
-107	$C_sR_7-C_sR_7-H \rightarrow C_sR_6^\bullet + C_sR_6-H$	5.132×10^{12}	0.340	25.40	[206]
108	$C_sR_7-C_sR_7-H \rightarrow C_sR_7-C_sR_7 + H$	2.006×10^{10}	1.099	32.81	[206]
-108	$C_sR_7-C_sR_7 + H \rightarrow C_sR_7-C_sR_7-H$	1.729×10^{08}	1.489	1.504	[206]
	Seven-member bay closure (Carbene route on site 2)				
109	$C_sR_6-H + C_sR_6-H \rightarrow C_sR_6^{(2\bullet)} + C_sR_6-H_2$	1.603×10^{11}	0.777	83.23	[206]
-109	$C_sR_6^{(2\bullet)} + C_sR_6-H_2 \rightarrow C_sR_6-H + C_sR_6-H$	3.050×10^{11}	0.294		[206]
110	$C_sR_6^{(2\bullet)} + C_sR_6-H \rightarrow C_sR_7-C_sR_7-H$	2.488×10^{11}	0.120	11.62	[206]
-110	$C_sR_7-C_sR_7-H \rightarrow C_sR_6^{(2\bullet)} + C_sR_6-H$	1.472×10^{12}	0.676	45.09	[206]
111	$C_sR_7-H + C_sR_7 \rightarrow C_sR_7 + C_sR_7-H$	1.397×10^{11}	0.581	27.01	[206]
-111	$C_sR_7 + C_sR_7-H \rightarrow C_sR_7-H + C_sR_7$	3.264×10^{10}	0.734	56.81	[206]
112	$C_sR_7-H + C_sR_6-H \rightarrow C_sR_7 + C_sR_6-H_2 + H_2$	5.515×10^{10}	0.849	59.32	[206]
-112	$C_sR_7 + C_sR_6-H_2 \rightarrow C_sR_7-H + C_sR_6-H$	7.566×10^{10}	0.675	38.56	[206]
113	$C_sR_6-H_2 + C_sR_6-H_2 \rightarrow C_sR_6-H + C_sR_6-H + H_2$	6.206×10^{09}	0.848	28.61	[206]
-113	$C_sR_6-H + C_sR_6-H + H_2 \rightarrow C_sR_6-H_2 + C_sR_6-H_2$	2.164×10^{05}	1.798	58.70	[206]
114	$C_sR_6-H + C_sR_6-H \rightarrow C_sR_6^{(2\bullet)} + C_sR_6-H_2$	1.162×10^{11}	0.837	86.01	[206]
-114	$C_sR_6^{(2\bullet)} + C_sR_6-H_2 \rightarrow C_sR_6-H + C_sR_6-H$	4.948×10^{11}	0.331	1.476	[206]
115	$C_sR_6^{(2\bullet)} + C_sR_6-H \rightarrow C_sR_7-C_sR_7-H$	5.744×10^{11}	0.039	8.721	[206]
-115	$C_sR_7-C_sR_7-H \rightarrow C_sR_6^{(2\bullet)} + C_sR_6-H$	2.164×10^{12}	0.292	18.61	[206]
116	$C_sR_7-H + C_sR_6-H \rightarrow C_sR_7 + C_sR_6-H_2$	9.900×10^{11}	0.331	-2.850	[206]
-116	$C_sR_7 + C_sR_6-H_2 \rightarrow C_sR_7-H + C_sR_6-H$	1.025×10^{11}	0.875	57.11	[206]
117	$C_sR_7-H + C_sR_6-H \rightarrow C_sR_7 + C_sR_6-H_2 + H_2$	6.156×10^{10}	0.782	39.25	[206]
-117	$C_sR_7 + C_sR_6-H_2 \rightarrow C_sR_7-H + C_sR_6-H$	9.567×10^{10}	0.696	35.20	[206]
118	$C_sR_6-H_2 + C_sR_6-H_2 \rightarrow C_sR_6-H + C_sR_6-H + H_2$	3.478×10^{09}	1.288	87.43	[206]
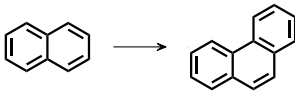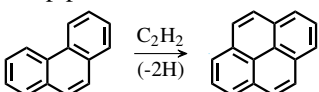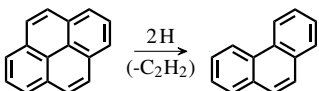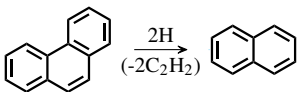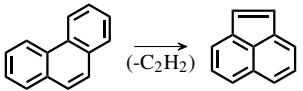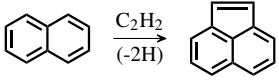
No.	Reactions	$k = AT^n \exp(-E_A/\mathrm{R_{gas}}T)$ [a]			References
		A	n	E_A	
-118	$C_sR_6-H+C_sR_6-H+H_2 \rightarrow C_sR_6-H_2+C_sR_6-H_2$	1.696×10^{05}	2.086	95.63	[206]
	Migration of partially-embedded five-member ring				
119[b]	$C_sR_5-C_sR_5-C_sR_6^\bullet \rightarrow CsR_6^\bullet-C_sR_5-C_sR_5H$	4.960×10^{11}	0.755	50.000	[330]
120[b]	$C_sR_5H-C_sR_5-C_sR_6^\bullet \rightarrow CsR_6^\bullet-C_sR_5-C_sR_5$	4.960×10^{11}	0.755	50.000	[330]
	Reactions above this line are included in Chapters 5 and 6				
	Reactions below this line are included in Chapter 6 only				
	Migration of partially-embedded five-member ring				
119[b]	$C_sR_5-C_sR_5-C_sR_6^\bullet \rightarrow CsR_6^\bullet-C_sR_5-C_sR_5H$	5.188×10^{13}		33.400	[351]
120[b]	$C_sR_5H-C_sR_5-C_sR_6^\bullet \rightarrow CsR_6^\bullet-C_sR_5-C_sR_5$	1.037×10^{14}		33.400	[351]
	Six-member ring oxidation				
121	$C_sR_6^\bullet+O_2 \rightarrow C_sR_6-O^\bullet+O$	3.170×10^{13}		2.021	[294]
122	$C_sR_{6i}-O^\bullet \rightarrow C_sR_5+CO$	1.760×10^{23}	−3.681	48.000	[179]
123	$C_sR_{6j}-O^\bullet \rightarrow C_sR_5+CO$	8.820×10^{09}	−0.063	33.010	[179]
124	$C_sR_6^\bullet+OH \rightarrow C_sR_5+CO$	1.000×10^{14}			[85]
125	$C_sR_6^\bullet+OH \rightarrow C_sR_6-OH$	1.470×10^{14}		1.256	[294]
-125	$C_sR_6-OH \rightarrow C_sR_6^\bullet+OH$	2.140×10^{16}		105.292	[294]
126	$C_sR_6-OH \rightarrow C_sR_6-O^\bullet+H$	2.130×10^{15}		84.064	[294]
-126	$C_sR_6-O^\bullet+H \rightarrow C_sR_6-OH$	4.340×10^{14}		1.955	[294]
127	$C_sR_6-OH+H \rightarrow C_sR_6-O^\bullet+H_2$	5.477×10^{06}	2.147	11.134	[294]
-127	$C_sR_6-O^\bullet+H_2 \rightarrow C_sR_6-OH+H$	1.700×10^{14}		19.146	[294]
128	$C_sR_6-OH+H \rightarrow C_sR_6^\bullet+H_2O$	2.000×10^{14}		5.306	[294]
129	$C_sR_6H+O \rightarrow C_sR_6-O^\bullet+H$	4.000×10^{12}		4.626	[85]
	Partially-embedded five-member ring oxidation				
130	$C_sR_6-C_sR_5H-C_sR_6+O_2 \rightarrow C_sR_6^\bullet-C_sR_6H+CO_2$	3.450×10^{11}		26.670	[85]
131	$C_sR_6-C_sR_5H-C_sR_6+O \rightarrow C_sR_6^\bullet-C_sR_6H+CO$	3.541×10^{11}	0.505	0.608	[85]
	Five- Seven-member ring recombination				
132	$C_sR_7H-C_sR_5+H \rightarrow C_sR_7H_2-C_sR_5$	3.480×10^{08}	1.490	3.440	[206]
-132	$C_sR_7H_2-C_sR_5 \rightarrow C_sR_7H-C_sR_5+H$	2.340×10^{09}	1.180	30.770	[206]
133	$C_sR_7H_2-C_sR_5 \rightarrow C_sR_7H-C_sR_5H$	2.120×10^{10}	0.670	40.320	[206]
-133	$C_sR_7H-C_sR_5H \rightarrow C_sR_7H_2-C_sR_5$	8.390×10^{11}	0.290	18.610	[206]
134	$C_sR_7H-C_sR_5H \rightarrow C_sR_3H-C_sR_3H$	1.030×10^{12}	0.150	9.250	[206]
-134	$C_sR_3H-C_sR_3H \rightarrow C_sR_7H-C_sR_5H$	1.870×10^{12}	0.320	15.040	[206]
135	$C_sR_3H-C_sR_3H \rightarrow C_sR_6H-C_sR_6H$	6.650×10^{12}	−0.130	4.090	[206]
-135	$C_sR_6H-C_sR_6H \rightarrow C_sR_3H-C_sR_3H$	1.520×10^{12}		34.080	[206]
136	$C_sR_6H-C_sR_6H \rightarrow C_sR_6-C_sR_6H+H$	1.130×10^{10}	1.000	15.650	[206]
-136	$C_sR_6-C_sR_6H+H \rightarrow C_sR_6H-C_sR_6H$	2.820×10^{08}	1.360	35.440	[206]
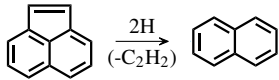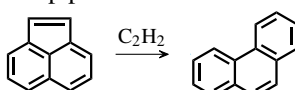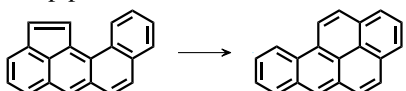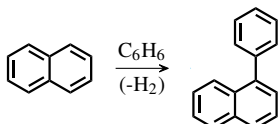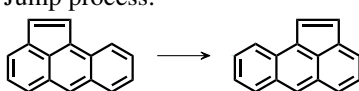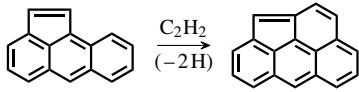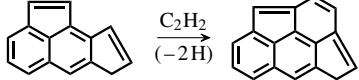
[a] *The units are mole, centimetre, second, and kilocalorie.*
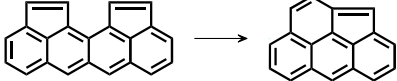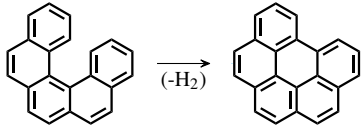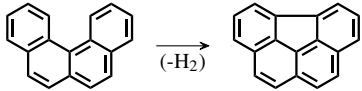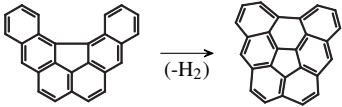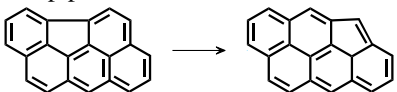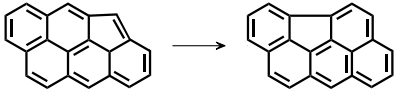
[b] *The value of rate constants for reactions 119 and 120 was changed between Chapters 5 and 6.*
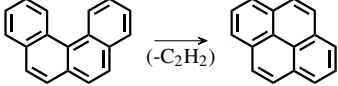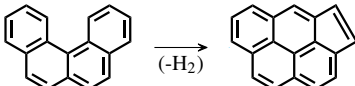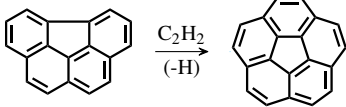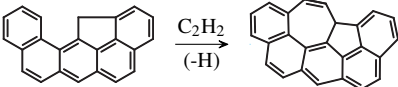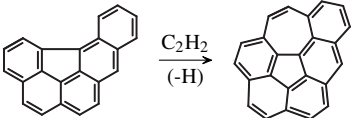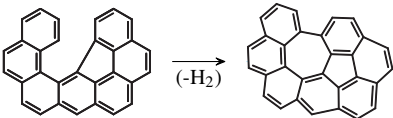
[c] *The reverse rate coefficients were calculated via equilibrium constants.*
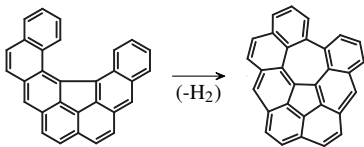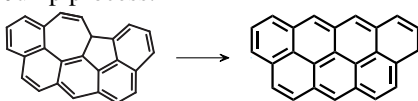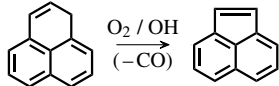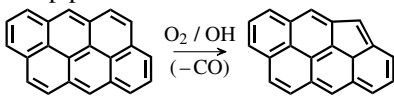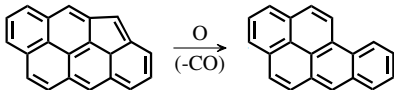
Table 3.4 Kinetic Monte Carlo jump processes.

Process [Reference]	Parent site
S1 Free-edge ring growth [32]	**Free-edge (FE)**

Jump process:

Rate: [a]

$$\left(k_{18}[C_sR_6^\bullet][C_4H_4] + k_{24}[C_sR_6-C_2H_3^\bullet][C_2H_2] + k_{28}[C_sR_6-C_2H][C_2H_3] + \right.$$
$$k_{29}[C_sR_6-C_2H^\bullet][C_2H_2] + k_{30}[C_sR_6-C_2H^\bullet][C_2H_2] + k_{31}[C_sR_6-C_2H^\bullet][C_2H_2] +$$
$$k_{33}[C_sR_6-C_2H^\bullet][C_2H_4] + k_{34}[C_sR_6-C_2H_2][C_2H_2] + k_{35}[C_sR_6(C_2H)(C_2H_3)][H] +$$
$$\left.k_{36}[C_sR_6(C_2H)(C_2H_3)][H]\right)[C_{FE}]$$

S2 Armchair ring growth [32]	**Armchair (AC)**

Jump process:

$$\xrightarrow[(-2H)]{C_2H_2}$$

Rate:

$$(k_9 + k_{10})\left(\frac{k_1[H]+k_2[OH]}{k_{-1}[H_2]+k_3[H]+k_{-2}[H_2O]+(k_9+k_{10}+k_{11}+k_{12})[C_2H_2]}\right)[C_2H_2][C_{AC}]$$

S3 Free-edge desorption to an armchair [86, 227]	**Free-edge adjacent to non-free-edges (FE$_{HACA}$)**

Jump process:

$$\xrightarrow[(-C_2H_2)]{2H}$$

Rate:

$$(k_{-9}+k_{-10})[C_{FE_{HACA}}]$$

S4 Free-edge ring desorption [32]	**Free-edge with two adjacent free-edges (FE3)**

Jump process:

$$\xrightarrow[(-2C_2H_2)]{2H}$$

Rate:

$$\left(k_{-18}+k_{-24}+k_{-28}+k_{-33}+k_{-34}+k_{-35}\right)[H][C_{FE3}] +$$
$$\left(\frac{(k_1[H]+k_2[OH])(k_{-29}+k_{-30}+k_{-31})}{k_{-1}[H_2]+k_3[H]+k_{-2}[H_2O]}\right)[C_{FE3}]$$

S5 6- to 5-member ring conversion at armchair [32]	**Armchair next to FE3 (AC$_{FE3}$)**

Jump process:

$$\xrightarrow[(-C_2H_2)]{}$$

Rate:

$$k_{57}\left(\frac{k_1[H]+k_2[OH]}{k_{-1}[H_2]+k_3[H]+k_{-2}[H_2O]+k_{57}}\right)[C_{AC_{FE3}}]$$

S6 5-member ring addition [32]	**Zig-zag (ZZ)**

Jump process:

$$\xrightarrow[(-2H)]{C_2H_2}$$

Rate:

$$(k_{44}+k_{45})\left(\frac{k_1[H]+k_2[OH]}{k_{-1}[H_2]+k_3[H]+k_{-2}[H_2O]+(k_{44}+k_{45}+k_{46}+k_{47})[C_2H_2]}\right)[C_2H_2][C_{ZZ}]$$

Process [Reference]	Parent site

S7 5-member ring desorption [32] **5-member ring (R5)**

Jump process: Rate:

$$\left(\frac{k_{48}(k_4[H]+k_5[OH])}{k_{-4}[H_2]+k_6[H]+k_{-5}[H_2O]+k_{48}} + \frac{k_7[H](k_{49}+k_{50})}{k_{-7}[H]+k_8[H]+k_{49}+k_{50}}\right)[C_{R5}]$$

S8 5- to 6-member ring conversion at free edge [32] **5-member ring next to free-edge (RFE)**

Jump process: Rate:

$$(k_{54}+k_{55})\left(\frac{k_7[H]}{k_{-7}[H]+k_8[H]+k_{49}+k_{50}+k_{51}+(k_{54}+k_{55})f[C_2H_2]}\right)f[C_2H_2][C_{RFE}],$$
$$\text{where } f = \left(\frac{k_1[H]+k_2[OH]}{k_{-1}[H_2]+k_3[H]+k_{-2}[H_2O]+(k_{54}+k_{55})[C_2H_2]}\right)$$

S9 5- to 6-member ring conversion at armchair [32] **5-member ring next to armchair (RAC)**

Jump process: Rate:

$$k_{52}\left(\frac{k_7[H]}{k_{-7}[H]+k_8[H]+k_{49}+k_{50}+k_{51}+k_{52}}\right)[C_{RAC}]$$

S10 Benzene addition [256] **All site types**

Jump process: Rate:

$$2k_{42}\left(\frac{k_1[H]+k_2[OH]}{k_{-1}[H_2]+k_3[H]+k_{-2}[H_2O]+k_{42}[C_6H_6]}\right)[C_6H_6][C_s]$$

S11 5-member ring migration [256] **5-member ring next to zig-zag (RZZ)**

Jump process: Rate:

$$k_{51}\left(\frac{k_7[H]}{k_{-7}[H]+k_8[H]+k_{49}+k_{50}+k_{51}}\right)[C_{RZZ}]$$

S12 Ring growth next to 5-member ring [348] **5-member ring next to zig-zag (RZZ)**

Jump process: Rate:

$$k_{61}\left(\frac{k_1[H]+k_2[OH]}{k_{-1}[H_2]+k_3[H]+k_{-2}[H_2O]+k_{61}[C_2H_2]} + \frac{k_4[H]+k_5[OH]}{k_{-4}[H_2]+k_6[H]+k_{-5}[H_2O]+k_{61}[C_2H_2]}\right)[C_{RZZ}]$$

S13 Ring growth between 5-member rings [348] **Free-edge between 5-member rings (RFER)**

Jump process: Rate:

$$k_{62}\left(\frac{k_4[H]+k_5[OH]}{k_{-4}[H_2]+k_6[H]+k_{-5}[H_2O]+k_{62}[C_2H_2]}\right)[C_{RFER}]$$

Process [Reference]	Parent site
S14 5-member rings collision [348]	**Zig-zag between 5-member rings (RZZR)**

Jump process: Rate:

$$2k_{63} \left(\frac{k_7[\text{H}]}{k_{-7}[\text{H}]+k_8[\text{H}]+k_{49}+k_{50}+k_{63}} \right) [\text{C}_\text{RZZR}]$$

S15 6-member bay closure [256]	**6-member bay (BY6)**

Jump process: Rate:

$$2(k_{38}+k_{39}) \left(\frac{k_{37}[\text{H}]+k_2[\text{OH}]}{k_{-37}[\text{H}_2]+k_3[\text{H}]+k_{-2}[\text{H}_2\text{O}]+k_{38}+k_{39}} \right) [\text{C}_\text{BY6}]$$

S16 5-member bay closure [256]	**5-member bay (BY5)**

Jump process: Rate:

$$2k_{41} \left(\frac{k_{40}[\text{H}]+k_2[\text{OH}]}{k_{-40}[\text{H}_2]+k_3[\text{H}]+k_{-2}[\text{H}_2\text{O}]+k_{41}} \right) [\text{C}_\text{BY5}]$$

S17 6-member bay closure [256] **(partially-embedded 5-member ring)**	**6-member bay (BY6$_\text{eR5}$)** **with partially-embedded 5-member ring**

Jump process: Rate:

$$2k_{64} \left(\frac{k_{37}[\text{H}]+k_2[\text{OH}]}{k_{-37}[\text{H}_2]+k_3[\text{H}]+k_{-2}[\text{H}_2\text{O}]+k_{64}} \right) [\text{C}_{\text{BY6}_\text{eR5}}]$$

S18 Partially-embedded 5-member ring migration [351] **from edge position**	**Partially-embedded 5-member ring (eR5)** **in edge position**

Jump process: Rate:

$$k_{119} \left(\frac{k_3[\text{H}]+k_2[\text{OH}]}{k_{-1}[\text{H}_2]+k_3[\text{H}]+k_{-2}[\text{H}_2\text{O}]+k_{119}} \right) [\text{C}_\text{eR5}]$$

S19 Partially-embedded 5-member ring migration [351] **from corner position**	**Partially-embedded 5-member ring (cR5)** **in corner position**

Jump process: Rate:

$$k_{120} \left(\frac{k_3[\text{H}]+k_2[\text{OH}]}{k_{-1}[\text{H}_2]+k_3[\text{H}]+k_{-2}[\text{H}_2\text{O}]+k_{120}} \right) [\text{C}_\text{cR5}]$$

Process [Reference]	Parent site
S20 **6-member ring desorption at bay** [257]	**BY5 next to FE3 (BY5$_{FE3}$)**

Jump process: Rate:

$$k_{60}\left(\frac{k_1[\mathrm{H}]+k_2[\mathrm{OH}]}{k_{-1}[\mathrm{H_2}]+k_3[\mathrm{H}]+k_{-2}[\mathrm{H_2O}]+k_{60}}\right)[\mathrm{C_{BY5_{FE3}}}]$$

S21 **6-member ring rearrangement at bay** [257]	**BY5 next to FE3 (BY5$_{FE3}$)**

Jump process: Rate:

$$(k_{58}+k_{59})\left(\frac{k_1[\mathrm{H}]+k_2[\mathrm{OH}]}{k_{-1}[\mathrm{H_2}]+k_3[\mathrm{H}]+k_{-2}[\mathrm{H_2O}]+k_{58}+k_{59}}\right)[\mathrm{C_{BY5_{FE3}}}]$$

S22 **Capping of embedded 5-member ring** [255]	**Partially-embedded 5-member ring (eR5) in edge position**

Jump process: Rate: [b]

$$\left(k_{69}[\mathrm{C}_s\mathrm{R}_6\mathrm{H}_2]_{\mathrm{ss}}+k_{71}[\mathrm{C}_s\mathrm{R}_6\mathrm{H}-\mathrm{C}_s\mathrm{R}_6]_{\mathrm{ss}}\right)[\mathrm{C_{eR5}}]$$

S23 **7-member ring growth** [this work] **(corner partially-embedded five-member ring)**	**Armchair with corner (cRAC) partially-embedded 5-member ring**

Jump process: Rate: [c]

$$\left(k_{83}[\mathrm{C}_s\mathrm{R}_6\mathrm{H}-\mathrm{C}_s\mathrm{R}_6{}^\bullet]_{\mathrm{ss}}+k_{87}[\mathrm{C}_s\mathrm{R}_5\mathrm{H}-\mathrm{C}_s\mathrm{R}_6{}^\bullet]_{\mathrm{ss}}\right)[\mathrm{C_{cRAC}}]$$

S24 **7-member ring growth** [this work] **(partially-embedded 5-member ring)**	**5-member bay (BY5$_{eR5}$) with partially-embedded 5-member ring**

Jump process: Rate: [d]

$$\left(k_{75}[\mathrm{C}_s\mathrm{R}_6\mathrm{H}-\mathrm{C}_s\mathrm{R}_6{}^\bullet]_{\mathrm{ss}}+k_{79}[\mathrm{C}_s\mathrm{R}_6\mathrm{H}-\mathrm{C}_s\mathrm{R}_6{}^\bullet{}_i]_{\mathrm{ss}}\right)[\mathrm{C_{BY5_{eR5}}}]$$

S25 **7-member bay closure** [this work] **(partially-embedded 5-member ring 1)**	**7-member bay site 1(BY7$_{eR5-1}$) with partially-embedded 5-member ring**

Jump process: Rate: [e]

$$\Big(k_{90}[\mathrm{C}_s\mathrm{R}_7-\mathrm{C}_s\mathrm{R}_7-\mathrm{H}]_{\mathrm{ss}}+k_{93}[\mathrm{C}_s\mathrm{R}_7-\mathrm{C}_s\mathrm{R}_7-\mathrm{H}_i]_{\mathrm{ss}}+$$
$$k_{98}[\mathrm{C}_s\mathrm{R}_6\mathrm{H}_2-\mathrm{C}_s\mathrm{R}_6\mathrm{H}_2]_{\mathrm{ss}}+k_{102}[\mathrm{C}_s\mathrm{R}_6\mathrm{H}_2-\mathrm{C}_s\mathrm{R}_6\mathrm{H}_{2i}]_{\mathrm{ss}}\Big)[\mathrm{C_{BY7_{eR5-1}}}]$$

Process [Reference]	Parent site
S26 7-member bay closure [this work] **(partially-embedded 5-member ring 2)**	**7-member bay site 2(BY7$_{eR5-2}$) with partially-embedded 5-member ring**

Jump process:	Rate: ^{f}

$$\left(k_{105}[C_sR_7 - C_sR_7 - H]_{ss} + k_{108}[C_sR_7 - C_sR_7 - H_i]_{ss} + k_{113}[C_sR_6H_2 - C_sR_6H_2]_{ss} + k_{118}[C_sR_6H_2 - C_sR_6H_2i]_{ss} \right)[C_{BY7_{eR5-2}}]$$

Processes above this row were included in Chapters 5 and 6.
Processes below this row were included in Chapter 6 only.

S27 5-7-member ring recombination [this work]	**5-member ring next to 7-member ring (eR5-R7)**

Jump process:	Rate: ^{g}

$$\left(k_{136}[C_sR_6H - C_sR_6H]_{ss} \right)[C_{eR5-R7}]$$

S28 Free-edge oxidation [this work]	**Two adjacent free-edges (FE2)**

Jump process:	Rate: ^{h}

$$\left(k_{122}[C_sR_{6i} - O^\bullet]_{ss} + k_{123}[C_sR_{6j} - O^\bullet]_{ss} \right)[C_{FE2}]$$

S29 Free-edge oxidation [this work]	**Free-edge adjacent to non-free-edges (FE$_{HACA}$)**

Jump process:	Rate: ^{i}

$$2k_{122}[C_sR_6 - O^\bullet]_{ss}[C_{FE_{HACA}}]$$

S30 Partially-embedded 5-member ring oxidation [this work]	**Partially-embedded 5-member ring (cR5) in corner position**

Jump process:	Rate:

$$(k_{130} + k_{131})[C_{cR5}]$$

Notes:

^{a} Steady-state intermediates vector V_{ss} and partial-equilibrium intermediates vector V_{peq} defined as:

$V_{ss} = \{C_sR_6^\bullet, C_sR_6 - C_2H_2, C_sR_6 - C_2H, C_sR_6 - C_2H_3, C_sR_6 - C_2H_3^\bullet, C_sR_6(C_2H)(C_2H_3), C_sR_6 - R_6^\bullet, C_sR_6 - R_6\}$

$V_{peq} = \{C_sR_6^\bullet, C_sR_6 - C_2H_2, C_sR_6 - C_2H, C_sR_6 - C_2H_3, C_sR_6 - C_2H_3^\bullet, C_sR_6(C_2H)(C_2H_3)\}$

Rate calculated using the method described in Section 3.5.4: $\dot{r}_{S1} = \dot{r}_{S1,ss}$ if $\dot{r}_{S1,peq} > \dot{r}_{S3}$, $\dot{r}_{S1} = \dot{r}_{S1,peq}$ o.w.

^{b} Steady-state intermediates vector V_{ss} defined as:

$$V_{ss} = \{C_sR_6{}^\bullet, C_sR_6-C_2H_2, C_sR_6{}^\bullet-C_2H_3, C_sR_6-H_2, C_sR_6H-C_sR_6\}$$

[c] Steady-state intermediates vector V_{ss} defined as:

$$V_{ss} = \{C_sR_6{}^\bullet, C_sR_6-C_2H_2, C_sR_6H-C_sR_6{}^\bullet, C_sR_5{}^\bullet, C_sR_5-C_2H_2, C_sR_5H-C_sR_6{}^\bullet\}$$

[d] Steady-state intermediates vector V_{ss} defined as:

$$V_{ss} = \{C_sR_6{}^\bullet, C_sR_6-C_2H_2, C_sR_6H-C_sR_6{}^\bullet, C_sR_6{}^\bullet{}_i, C_sR_6-C_2H_{2i}, C_sR_6H-C_sR_6{}^\bullet{}_i\}$$

[e] Steady-state intermediates vector V_{ss} defined as:

$$V_{ss} = \{C_sR_6{}^\bullet, C_sR_7-R_7-H, C_sR_6{}^\bullet{}_i, C_sR_7-R_7-H_i, C_sR_6{}^{2\bullet}, C_sR_7H-C_sR_7, C_sR_7H-C_sR_6H, C_sR_6{}^{2\bullet}{}_i,$$
$$C_sR_7H-C_sR_{7i}, C_sR_7H-C_sR_6H_i \}$$

[f] Steady-state intermediates vector V_{ss} defined as:

$$V_{ss} = \{C_sR_6{}^\bullet, C_sR_7-R_7-H, C_sR_6{}^\bullet{}_i, C_sR_7-R_7-H_i, C_sR_6{}^{2\bullet}, C_sR_7H-C_sR_7, C_sR_7H-C_sR_6H, C_sR_6{}^{2\bullet}{}_i,$$
$$C_sR_7H-C_sR_{7i}, C_sR_7H-C_sR_6H_i \}$$

[g] Steady-state intermediates vector V_{ss} defined as:

$$V_{ss} = \{C_sR_7H_2-C_sR_5, C_sR_7H-C_sR_5H, C_sR_3H-C_sR_3H, C_sR_6H-C_sR_6H \}$$
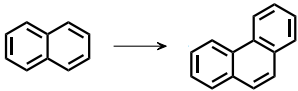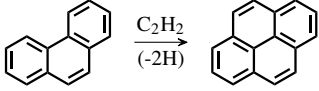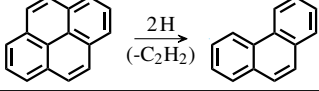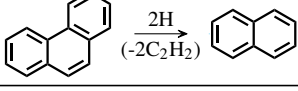
[h] Steady-state intermediates vector V_{ss} defined as:
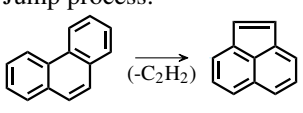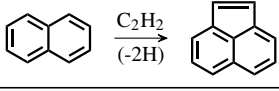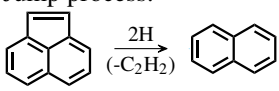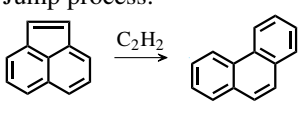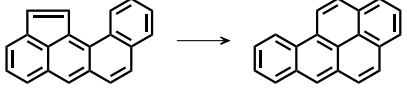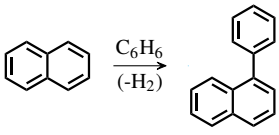
$$V_{ss} = \{C_sR_{6i}{}^\bullet, C_sR_{6j}{}^\bullet, C_sR_{6i}-O^\bullet, C_sR_{6j}-O^\bullet, C_sR_{6i}-OH, C_sR_6j-OH \}$$
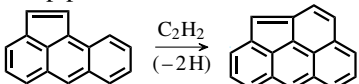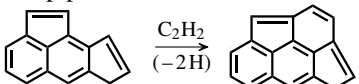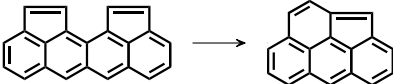
[i] Steady-state intermediates vector V_{ss} defined as:
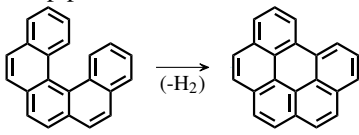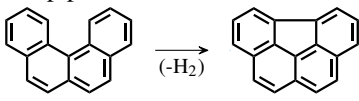
$$V_{ss} = \{C_sR_6{}^\bullet, C_sR_6-O^\bullet, C_sR_6-OH \}$$
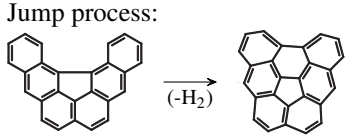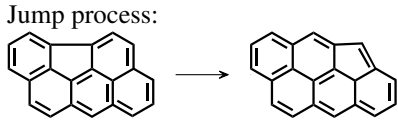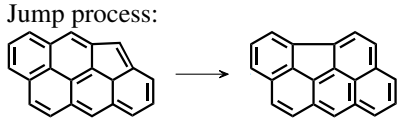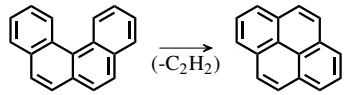
Table 3.5 Transformations for each Kinetic Monte Carlo jump process.
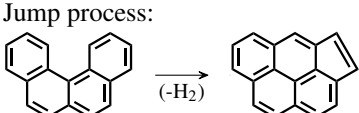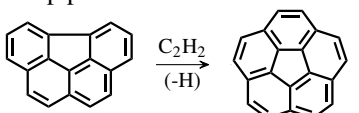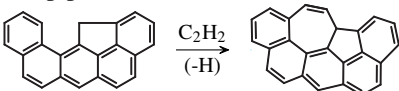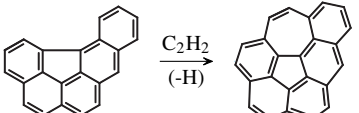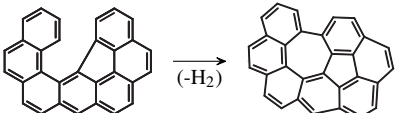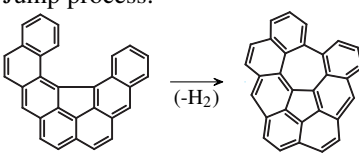
Process	Parent site	Atoms Rings	Sites	Structure optimisation
		Transformation		
S1 Free-edge ring growth				
Jump process:	Free-edge (FE)	+4 C +2 H +1 R6	parent site ← FE +2 Free-edges +1 C to adjacent sites	-
S2 Armchair ring growth				
Jump process:	Armchair (AC)	+2 C +1 R6	parent site ← FE +1 C to adjacent sites	Before: If $\delta_{site} < 2.6$ Å After: If $\delta_{i,i+1} > 1.7$ Å
S3 Free-edge desorption to an armchair				
Jump process:	Free-edge (FE$_{HACA}$) not next to RFE[a]	-2 C -1 R6[b]	parent site ← AC[b] -1 C to adjacent sites	Before: If $\delta_{i,i+1} < 1.2$ Å If $\delta_{i,i+1} > 1.6$ Å
S4 Free-edge ring desorption				
Jump process:	Three adj. free-edges (FE3) non-adjacent to: RFE, cR5, eR5[a]	-4 C -2 H -1 R6	parent site ← FE -2 Free-edges -1 C to adjacent sites	-
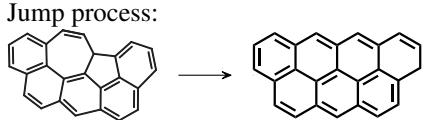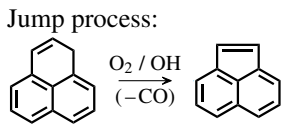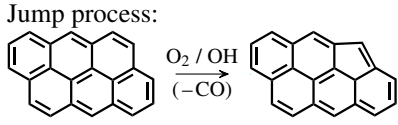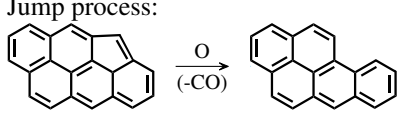
| Process | Parent site | Transformation | | Structure optimisation |
		Atoms Rings	Sites	
S5 6- to 5-member ring conversion at armchair				
Jump process:	Armchair next to FE3 (AC$_{FE3}$) No R5 or eR5 to other side[a] No crosslink	-2 C -2 H -1 R6 +1 R5	parent site ← R5 -3 Free-edges +R5 to adjacent sites -1 C to adjacent sites	After: Every time
S6 5-member ring addition				
Jump process:	Zig-zag (ZZ)	+2 C +1 R5	parent site ← R5 +1 C to adjacent sites +R5 to adjacent sites	Before: If $\delta_{site} < 2.1$ Å After: If $\delta_{i,i+1} > 1.8$ Å
S7 5-member ring desorption				
Jump process:	5-member ring (R5)	-2 C -1 R5	parent site ← ZZ -1 C to adjacent sites -R5 to adjacent sites	-
S8 5- to 6-member ring conversion at free edge				
Jump process:	R5 next to free-edge (RFE)	+2 C +2 H -1 R5 +1 R6	R5 site ← AC -R5 for parent site -R5 for R5 adjacent site -1 C for parent site -1 C for R5 adjacent site +1 C to adjacent site +2 free-edges	-
S9 5- to 6-member ring conversion at armchair				
Jump process:	R5 next to armchair (RAC)	-1 R5 +1 R6	R5 site ← AC parent site ← FE -R5 for R5 adjacent site -1 C for R5 adjacent site +1 C to adjacent site	-
S10 Benzene addition				
Jump process:	All site types Not sites ≥ 5C	+6C +4H +1 R6	+2 C for parent site +2 C to adjacent site +4 FE	-

Process	Parent site	Atoms Rings	Sites	Structure optimisation
			Transformation	

S11 5-member ring migration

Process	Parent site	Atoms Rings	Sites	Structure optimisation
Jump process:	R5 next to zig-zag (RZZ)	-	R5 site ← RZZ parent site ← R5 -R5 for R5 adjacent site -1 C for R5 adjacent site +R5 to adjacent site +1 C to adjacent site	Before: If $\delta_{i,i+2} < 2.0$ After: If $\delta_{i,i+1} > 1.8$ If $\delta_{i,i+2} < 2.4$

S12 Ring growth next to 5-member ring

Process	Parent site	Atoms Rings	Sites	Structure optimisation
Jump process: $\xrightarrow[(-2\mathrm{H})]{C_2H_2}$	R5 next to zig-zag (RZZ) cR5 next to zig-zag (cRZZ)	+2 C +1 R6	parent site ← FE +1 C to adjacent site R5 site ← cR5 R5 adj. site ← cR5 fam. cR5 site ← eR5 fam.	After: If $\delta_{i,i+1} < 2.4$

S13 Ring growth between 5-member rings

Process	Parent site	Atoms Rings	Sites	Structure optimisation
Jump process: $\xrightarrow[(-2\mathrm{H})]{C_2H_2}$	Free-edge next to 2R5s (RFER) Free-edge next to cR5–R5 (cRFER) Free-edge next to 2cR5s (cRFEcR)	+2 C +1 R6	parent site ← FE R5 sites ← cR5 R5 adj. site ← cR5 fam. +1 C for cR5 adj. sites R5 site ← cR5 cR5 site ← eR5 fam. R5 adj. site ← cR5 fam. +1 C to adjacent sites cR5 sites ← eR5 fam. +1 C to adjacent sites	After: If $\delta_{i,i+1} < 2.4$

S14 5-member rings collision

Process	Parent site	Atoms Rings	Sites	Structure optimisation
Jump process:	Zig-zag between R5s (RZZR) Zig-zag between cR5–R5 (cRZZR)	-1 H -1 R5 +1 R6	parent site ← FE R5 site ← ZZ -R5 to R5 adjacent site -1 C for R5 adjacent site R5 adj. site ← cR5 fam. R5 site ← cR5 +1 C to cR5 site cR5 site ← eR5 fam.	After: If $\delta_{i,i+1} < 2.2$

Process	Parent site	Transformation		Structure optimisation
		Atoms Rings	Sites	
S15 6-member bay closure				
Jump process:	6-member bay (BY6)	-2 H +1 R6	Remove parent site Add New site from R6s family with sum of atoms from adjacent sites +R5, +cR5, +eR5 to New site for every R5, cR5, eR5 in adjacent sites Remove adjacent sites	After: If $\delta_{i,i+1} > 1.6$ If at least one eR5 present
			No further changes	
	R5 5-member bay (RBY5)		R5 adj. site ← cR5 fam. New site ← cR5 fam.	
	2R5 armchair (RACR)		R5 adj. site ← cR5 fam. New site ← cR5–cR5 fam.	
	cR5 5-member bay (cRBY5)		R5 adj. site ← cR5 fam. New site ← eR5–cR5 fam.	
	cR5–R5 armchair (cRACR)		New site ← eR5 fam.	
	2cR5 armchair (cRACcR)		New site ← 2eR5 fam.	
S16 5-member bay closure				
Jump process:	5-member bay (BY5) No R5 on sites to other side of site	-2 H +1 R5	Remove parent site Add New site from eR5 family with sum of atoms from adjacent sites +R5 to New site for R5 in adjacent sites +cR5 to New site for cR5 in adjacent sites +eR5 to New site for eR5 in adjacent sites Remove adjacent sites	-

Process	Parent site	Transformation Atoms Rings	Sites	Structure optimisation

S17 6-member bay closure (partially-embedded 5-member ring)

Process	Parent site	Atoms / Rings	Sites	Structure optimisation
Jump process:	eR5 6-member bay-1 (BY6$_{eR-1}$)	-2 H +1 R6 -1 R5 +1 R5$_{emb}$	Remove parent site Add New site from R6s family with sum of atoms from adjacent sites +R5, +cR5, +eR5 to New site for every R5, cR5, eR5 in adjacent sites Remove adjacent sites	After: If $\delta_{i,i+1} > 1.6$ If at least one eR5 present
	eR5 6-member bay-2 (BY6$_{eR-2}$)	-	No further changes	
		-	No further changes	
	cR5–eR5 5-mem. bay (cRBY5$_{eR}$)	-	cR5 adj. site ← eR5 fam. New site ← cR5 fam.	
	2eR5 6-member bay (BY6$_{2eR}$)	-1 R5 +1R5$_{emb}$	No further changes	
	3eR5 6-member bay (BY6$_{3eR}$)	-	cR5 adj. site ← eR5 fam. New site ← 2eR5 fam.	

S18 Partially-embedded 5-member ring migration from edge position

Process	Parent site	Atoms / Rings	Sites	Structure optimisation
Jump process:	Migrating eR5 Armchair (eR5$_{MIGR}$), (eR5$_{MIGR2}$) Non-R5 sites to other side[c]	-	-eR5 to parent site +cR5 to corner (free-edge) sites +eR5 to edge (non-free edge) sites	After: Every time[d]

S19 Partially-embedded 5-member ring migration from corner position

Process	Parent site	Atoms / Rings	Sites	Structure optimisation
Jump process:	Migrating cR5 (cR5$_{MIGR}$) Non-R5 sites to other side[c]	-	-cR5 to parent site +cR5 to corner (free-edge) sites +eR5 to edge (non-free edge) sites	After: Every time[d]

S20 6-member ring desorption at bay

Process	Parent site	Atoms / Rings	Sites	Structure optimisation
Jump process:	5-member bay next to FE3 (BY5$_{FE3}$)	-2 C -2 H	parent site ← FE -3 FE sites +1 C to adjacent sites	After: If $\delta_{i,i+1} < 1.2$ Å If $\delta_{i,i+1} > 1.6$ Å

	Transformation	

Process	Parent site	Atoms Rings	Sites	Structure optimisation
S21 6-member ring rearrangement at bay				
Jump process: $\xrightarrow{(-H_2)}$	5-member bay next to FE3 (BY5$_{FE3}$)	-	parent site ← RFE -2 FE sites adjacent site ← R5 +R5 to R5 adjacent site +1 C to adjacent site +1 C to R5 adjacent site	After: Every time
S22 Capping of embedded 5-member ring				
Jump process: $\xrightarrow[(-H)]{C_2H_2}$	eR5 armchair (eR5)	+2 C +1 R6 -1 R5 +1 R5$_{emb}$	parent site ← FE +1 C to adjacent sites	Before: Every time After: Every time
S23 7-member ring growth (corner partially-embedded five-member ring)				
Jump process: $\xrightarrow[(-H)]{C_2H_2}$	cR5 Armchair (cRAC)	+2 C +1 R7	parent site ← FE +1 C to adjacent sites cR5 site ← eR5 fam.	Before: Every time After: Every time
S24 7-member ring growth (edge partially-embedded 5-member ring)				
Jump process: $\xrightarrow[(-H)]{C_2H_2}$	eR5 5-member bay (BY5$_{eR5}$)	+2 C +1 R7 -1 R5 +1 R5$_{emb}$	parent site ← FE +1 C to adjacent sites	Before: Every time After: Every time
S25 7-member bay closure (partially-embedded 5-member ring 1)				
Jump process: $\xrightarrow{(-H_2)}$	eR5 7-member bay site-1 (BY7$_{eR5-1}$)	-2 H +1 R7 -1 R5 +1 R5$_{emb}$	Remove parent site Add New site from R6s family with sum of atoms from adjacent sites +R5, +cR5, +eR5 to New site for every R5, cR5, eR5 in adjacent sites Remove adjacent sites	Before: Every time After: Every time
S26 7-member bay closure (partially-embedded 5-member ring 2)				
Jump process: $\xrightarrow{(-H_2)}$	eR5 7-member bay site 2 (BY7$_{eR5-2}$)	-2 H +1 R7 -1 R5 +1 R5$_{emb}$	Remove parent site Add New site from R6s family with sum of atoms from adjacent sites +R5, +cR5, +eR5 to New site for every R5, cR5, eR5 in adjacent sites Remove adjacent sites	Before: Every time After: Every time

Process	Parent site	Transformation		Structure optimisation
		Atoms Rings	Sites	

Processes above this row were included in Chapters 5 and 6.
Processes below this row were included in Chapter 6 only.

S27 5-7-member ring recombination

Jump process:	R5 next to R7 (eR5-R7)	-1 R7 -1 R5 +2 R6	+1 C to R7 site eR5 site ← R6 fam. -1 C to previous eR5 site	After: Every time

S28 Free-edge oxidation

Jump process: O_2 / OH $(-CO)$	Two adjacent free-edges (FE2) not next to RFE[c] Not R5 site to other side[c]	-1 C -1 H -1 R6[e] +1 R5[e]	-1 FE site parent site ← R5[f] +R5 to adjacent sites[f]	-

S29 Free-edge oxidation

Jump process: O_2 / OH $(-CO)$	Free-edge (FE$_{HACA}$) not next to RFE[c] Not R5 site to other side[c]	-1 C -1 H -1 R6[e] +1 R5[e]	+cR5 to adjacent sites[g] parent site removed -1 FE site	-

S30 Partially-embedded 5-member ring oxidation

Jump process: O $(-CO)$	All cR5 containing sites	-1 C -1 H -1 R5	-cR5 to adjacent site -cR5 to parent site -1 C to adjacent site -1 C to parent site +1 AC site	Before: If $\delta_{i,i+1} > 1.6$ Å If $\delta_{i,i+1} < 1.2$ Å

General notes:

$\delta_{i,i+1}$ refers to distances between neighbour atoms in L_c (See Equation 3.87),

$\delta_{i,i+2}$ refers to distances between second neighbour atoms in L_c. For both:

$i \in c_{k-1_{first}}, \ldots, c_{k+1_{last}}$, where s_{k-1} is the predecessor site, s_k is the parent site and s_{k+1} is the successor site.

The notation ± 1 C to sites means the site type is moved left or right in the same family in Table 3.1.

The notation Site A ← B family means that Site A is moved to a family B in Table 3.1 in the same column.

Specific notes:

[a] This would create an indene-like site. Not included in the model.

[b] For seven-member ring: -1 R7, parent site ← BY5. If R5$_{emb}$ exposed: -1 R5$_{emb}$, +1 R5.

[c] This would violate the Isolated Pentagon Rule.

[d] Can be deferred in case of successive migration steps. See Section 3.7.5.

[e] For seven-member ring: -1 R7, +1 R6.

[f] For seven-member ring: parent site ← FE. No changes to adjacent sites.

[g] For seven-member ring: No changes to adjacent sites.

Chapter 4

New methodology to calculate process rates in a KMC model of PAH growth

In this chapter, a new methodology to calculate the process rates in Kinetic Monte Carlo (KMC) models of polycyclic aromatic hydrocarbon (PAH) growth is developed. The methodology uses a combination of steady-state and partial-equilibrium approximations. Good agreement with the results from simulations using a detailed chemical mechanism under conditions relevant to flames (temperatures between 1000 and 2500 K, equivalence ratios between 0.5 and 10) is shown. The new methodology was then used to calculate the rates of different stochastic processes in KMC simulations of PAH growth of premixed ethylene-oxygen flames. The results of the KMC model are shown to be consistent with the concentrations of species calculated using a well-established mechanism for the growth of small PAH species.

Collaborative Contributions

The work presented in this chapter has been published in *Combustion and Flame* and is primarily the work of the author. Nick Eaves helped editing the manuscript. Jethro Akroyd helped writing the manuscript. The model implementation, stochastic simulations, figure preparation and manuscript writing were done by the author.

4.1   Introduction

Carbonaceous materials are primarily formed of polycyclic aromatic hydrocarbons (PAHs) that grow in the presence of reactive species. The hydrogen-abstraction, acetylene-addition (often referred to as HACA) mechanism is widely considered the main route to explain the growth of PAH species [76]. This mechanism has been widely investigated [156, 157, 86, 355] and the reactions that it suggests have been included into several detailed mechanisms [337, 4, 297, 298, 38, 341, 342, 262, 261, 15, 227].

It is widely thought that carbonaceous particles are incepted from moderately sized PAHs, of the order of 10–16 rings [213, 1, 20, 19]. It is therefore desirable that simulations of PAH growth are able to describe the evolution of such PAHs. Typically, these simulations solve an ordinary differential equation (ODE) for the concentration of each species. However, the number of possible PAH species far exceeds the number of ODEs that can be solved in practical simulations. For this reason, chemical mechanisms are commonly truncated at PAH sizes much smaller than the sizes relevant to the formation of carbonaceous particles.

Rather than solving an ODE for the concentration of each species, an alternative approach is to use a stochastic numerical method to simulate the evolution of each entity within a given control volume This approach is the basis of kinetic Monte Carlo (KMC) models [92] and is suitable for problems with a very large number of species. One disadvantage of KMC models is that they can spend high computational effort to simulate reversible reactions where the forward and reverse rates are large, but where there is only a small net rate of change. Often this type of problem can be solved by using a timescale separation approximation such as the steady-state and partial-equilibrium approximations (for example [75, 256]).

The purpose of this chapter is to investigate the application of the steady-state and partial-equilibrium approximations in the context of PAH-KMC models [256, 37, 358]. This chapter develops a new methodology to compute the concentrations of PAH reaction intermediates based on a combination of both approximations and also computes a modified rate equation. The methodology is formulated such that is consistent with available gas-phase

mechanisms and such that it is suitable for inclusion in future KMC models of PAH growth and formation of carbonaceous materials.

4.2 Timescale separation approximations in models of PAH growth

Timescale separation approximations often allow a simplified numerical treatment of the processes that control a reaction system. They are based on the separation of *fast* and *slow* processes. Typically a subset of the species concentrations are able to be estimated by solving a linear system of equations (as opposed to coupled ODEs). Examples of such techniques are the steady-state and partial-equilibrium approximations that are studied in this chapter. Both methods are well-documented in the literature [247, 325, 169, 99, 324, 97]. The model equations are summarised in Section 3.5.

A number of related approximations have been used in other applications. For example, the simulation of turbulent combustion [250] and the generation of skeletal mechanisms [251]. Methods worth mentioning are intrinsic lower dimensional manifolds [184, 98], computational singular perturbation [100, 251, 99] and rate-controlled constrained equilibrium [147, 142, 12]. The reader is referred to [247, 169, 324, 97] for a review of these techniques.

Timescale separation approximations can be applied to the reactions that control the growth of PAHs. The HACA mechanism describes the consecutive production of radicals and addition of acetylene molecules. Each intermediate step in the mechanism has a different kinetic behaviour that needs to be analysed to identify possible timescale separations. Figure 4.1 shows an example of the reaction routes that are available for the growth of the most basic PAH, benzene growing to form naphthalene.

In Figure 4.1 reactions are shown as arrows and for simplicity only a single arrow is shown when multiple reaction pathways are involved between two species. The figure not only illustrates some of the main reaction pathways in PAH growth, it also shows the behaviour that can be observed for some of the intermediate species. Some reactions, shown as dashed blue arrows, are typically fast in both the forward and reverse directions, while others, shown as continuous red arrows, are usually fast only in one direction due to the high stabilisation that the formation of a new aromatic ring can provide. This behaviour allows a separation of fast and slow species that can be exploited to model the growth of this type of molecule.

The concentrations of fast-forming intermediates can often be estimated using a steady-state or partial-equilibrium approximation. In such cases, the concentration of these fast-
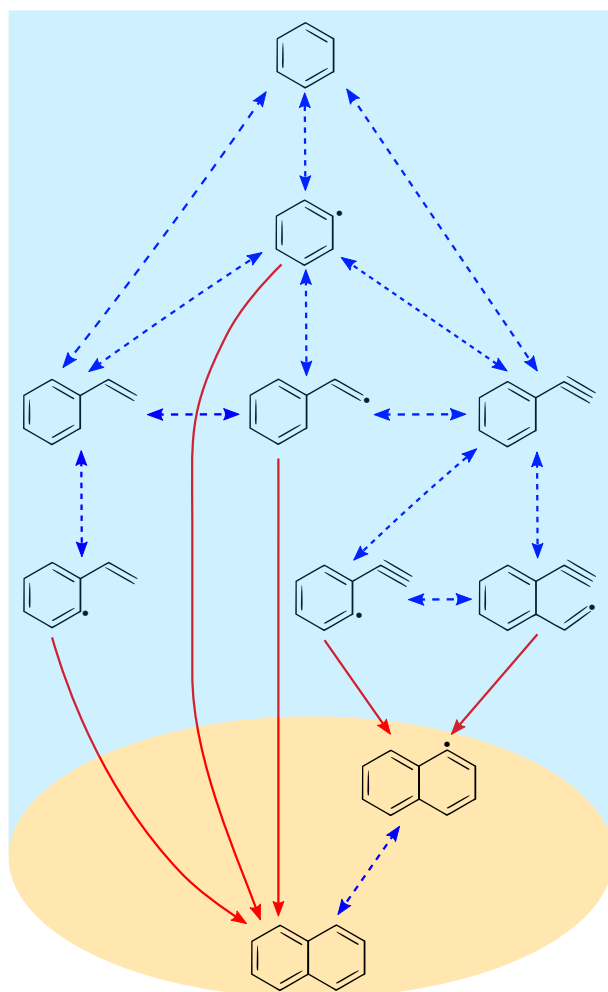
Fig. 4.1 Reaction path flux diagram showing the main reaction pathways between benzene and naphthalene. Dashed blue arrows show reaction fluxes that are similar in magnitude in both directions. Continuous red arrows show reaction fluxes with reverse rates that are at least an order of magnitude smaller than the forward rate at early times under flame conditions.

forming intermediates can be calculated by solving a linear system of the form

$$Mc = b \tag{4.1}$$

where M is an $N_f \times N_f$ matrix and contains pseudo first-order rate constants for the consumption and production of each of the fast species, c is the vector of the N_f concentrations of the fast species, b is a vector that contains the production terms of fast species from slow species and N_f is the number of fast species. The model equations and assumptions behind them are summarised in Section 3.5.

The steady-state approximation has been widely used to analyse PAH chemistry. Early works on the HACA pathways used it to explore the high and low temperature limits of the mechanism [74, 76]. It has also been used to obtain single-step rates for addition reactions [221] and to estimate the concentration of intermediate PAHs that participate in soot inception [304]. Recently, the rate constants for the HACA pathways have been re-examined in different studies in which a steady-state approximation was applied with improved rate coefficients [199, 86], and which concluded that the HACA routes are the main growth pathways in most flame conditions.

The steady-state approximation has also been used to estimate the number of active sites on the surface of soot particles for a simple surface mechanism including five reactions [81]. This approach estimates the number density of the available carbon-hydrogen sites and requires the specification of an α-parameter (see [86] for a discussion of this parameter) as the fraction of sites that will be available to react. Such an approach has been used in multiple studies [62, 269] and has been modified to account for reversibility [44], additional pathways [342] and particle ageing effects [291, 329, 151]. Recently, an alternative approach that expresses the instantaneous value of α in terms of state variables based on consideration of the number of zig-zag and armchair sites has been proposed [78].

The steady-state approximation has been incorporated into a number of KMC models of PAH growth. The fast-lived intermediates that are formed in some HACA reactions have been modelled with this approach in the works of Frenklach and co-workers [75, 348, 349, 294, 293]. This allows the study of PAH growth without the need to spend long computational times simulating highly reversible reactions. KMC models that simulate an ensemble of PAHs have used this approximation to derive simplified rate equations for various reaction sequences [32, 256, 258, 37, 358, 123]. In these studies, the model describes a number of pathways for the addition and desorption of aromatic rings [256]. However, the model makes a number of simplifications including assuming irreversible acetylene addition and irreversible ring closures. A methodology that accounts for the reversibility of these steps and that is valid across a wide range of conditions is still required.

4.3   Methodology

In this chapter the application of the steady-state and partial-equilibrium approximations of the chemical reactions that control the growth of gas-phase PAHs are studied with the purpose to provide simplified rate equations for KMC models. In order to do so, simulations of ethylene-air mixtures in a closed control volume under isothermal and isobaric conditions are considered at a pressure of one atmosphere. The effect of temperature and initial

equivalence ratio was studied. The temperature was varied from 1000 to 2500 K in 100 K intervals. The equivalence ratios considered were 0.5, 1.0, 2.0, 5.0 and 10. All reaction systems were solved until a stationary solution was observed. The model equations for these approximations are summarised in Chapter 3, Section 3.5.

The ABF mechanism [4] was selected as a reference mechanism for this study for the following reasons: Its PAH reaction pathways contain mostly HACA sequences which, although they do not explain all the pathways for the production of some small PAHs, are able to explain the growth of larger molecules and are included in modern mechanisms [297, 15, 259]. It includes ring condensation reactions which have been shown to be important for PAH growth [326]. It includes five-member ring growth and armchair closure reactions, both of which are fast processes that have been shown to affect the shape of larger PAHs [75, 32]. Lastly, by choosing a mechanism that does not contain additional routes that are unique to small PAHs, for example the production of naphthalene from cyclopentadiene or indene, the rates of reaction for analogous processes acting on arbitrarily-sized PAHs can be inferred. For example, by treating the growth rate of naphthalene from benzene (see Figure 4.2) as a proxy for a free-edge ring growth reaction. For all these reasons, the ABF mechanism provides a good candidate for the method development in this work. Note, however, that later mechanisms [for example 297, 15, 259, 261] contain more up to date estimates of the HACA reaction rates as well as more recently investigated reaction processes.
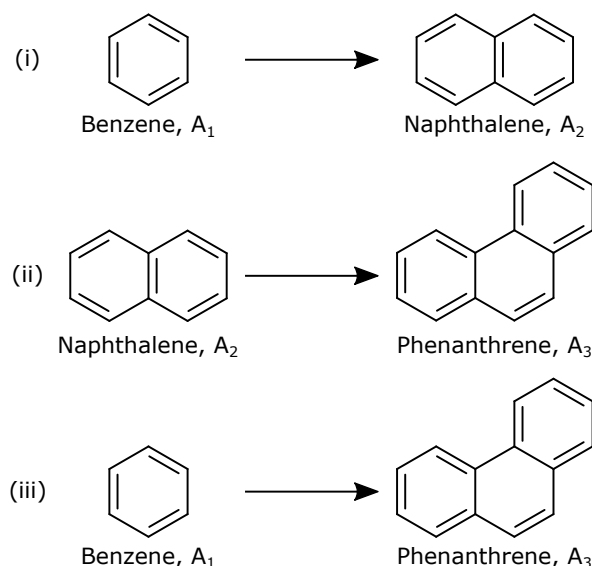
Fig. 4.2 Ring growth processes studied using the steady-state and partial-equilibrium approximations. Notation as defined by Frenklach et al. [83].

New steady-state and partial equilibrium approximations are proposed to calculate the rates of the ring growth processes shown in Figure 4.2. Processes (i) and (ii) follow the HACA pathways starting from different PAHs. Process (iii) corresponds to ring condensation reactions where two benzene intermediates react to form phenanthrene. For each process, a linear system resulting from a steady-state or partial equilibrium approximation is solved for the concentration of key intermediate species. The resulting process rate is then a function of only the concentrations of main gas-phase species and the morphology of the PAH. This procedure can be generalised to obtain the process rates for any arbitrarily-sized PAH in a KMC model.

The steady-state and partial-equilibrium approximations use a different set of species and reactions for each process in Figure 4.2. The species and reactions were selected using a combination of techniques. A time-integrated path flux analysis of the ABF mechanism [4], similar to that performed by Løvas et al. [182], was performed using Kinetics © [42] for all combinations of temperature and equivalence ratio specified above. For each simulation, a 3% cut-off ratio of the maximum carbon flux between benzene and naphthalene (which was found in the benzene to phenyl radical pathway for all conditions) was used to select species and reactions for ring growth process (i). A cut-off ratio of 0.4% (still of the maximum flux between benzene and naphthalene) was used to select species and reactions for ring growth processes (ii) and (iii). Subsequent testing showed that species $A_1C_2H_3^\bullet$ and $A_2(C_2H)_2$ and their associated reactions were also needed to explain the ring growth processes at low temperatures. For this reason, these were also included in the final sets of species and reactions. Reactions that did not contribute significantly were excluded. Likewise, the intermediates that took part in these reactions were also excluded. The full sets of species and reactions used for each process are detailed in Appendix A.

4.4 Results and discussion

In the sections that follow the application of the steady-state and partial-equilibrium approximations in models of PAH growth are studied. In Section 4.4.1 the performance of the steady-state approximation in simulations of a closed isothermal systems at different temperatures and equivalence ratios is critically assessed. In Section 4.4.2 the partial-equilibrium approximation is applied to the same systems and assess its performance versus that of the steady-state approximation. In Section 4.4.3, the performance of a new combined steady-state–partial-equilibrium approximation is introduced and investigated. Finally, in Section 4.4.4, the application of the new combined approximation in a KMC simulation of the PAH chemistry is demonstrated in a premixed burner-stabilised flame.

4.4.1   Steady-state approximation

In this section the case where all PAH species participating in the ring growth reactions, including intermediates and products, are in steady-state with the reactants is studied.

In the case of the formation of naphthalene from benzene, Figure 4.2 process (i), benzene is considered to be a slow species while naphthalene and all its intermediates are included in the steady-state species set. In the case of the formation of phenanthrene from napthalene, Figure 4.2 process (ii), naphthalene is considered to be a slow species while phenanthrene and its intermediates are included in the steady-state species set. The full set of species and reactions used for the steady-state approximation of each process are shown in Tables A.1 and A.2 in Appendix A.The ring condensation, Figure 4.2 process (iii), is not included in the steady-state approximation because it includes a reaction that is non-linear in the sense that it involves the reaction of two PAHs (Table A.3, reaction 17). This cannot be included in a steady-state approximation based on linear equations (*c.f.* Equation (4.1)).

Figure 4.3 shows the concentrations of naphthalene and phenanthrene calculated using the steady-state approximation versus reference solutions calculated using the full ABF mechanism in a closed isothermal system. For simplicity, only one equivalence ratio and four temperatures are shown. The shaded area in the figure shows the range of residence times relevant to the production of PAHs in a typical flame. The figure shows that the state-state approximation closely matches the reference solutions at temperatures above 2000 K. However, at lower temperatures the method shows significant differences from the reference solution at short times. The difference decreases with time (and given long enough, good agreement is seen at all temperatures, see Section A.4).This is a well known feature of the steady-state approximation. The fast species need an *induction time*, a time from the beginning of the reaction system until achieving their steady-state concentrations. This time is a function of the lifetime of the slowest species in the approximation [11, 325].

It is useful to define a metric to measure the quality of the steady-state approximation. However, an instantaneous measurement of the error can be misleading because PAHs are produced and consumed at different times under different conditions. For this reason, a time-integrated metric to provide information about the error over the timescales relevant to the study is introduced.

$$\varepsilon_\alpha^{ss}(\tau;\phi,T) = \log\left(\frac{\int_0^\tau C_\alpha^{ss}(t;\phi,T)\,dt}{\int_0^\tau C_\alpha^{ref}(t;\phi,T)\,dt}\right),$$

$$\hat{\varepsilon}_\alpha^{ss}(\tau;\phi,T) = \frac{|\varepsilon_\alpha^{ss}(\tau;\phi,T)|}{\max\limits_{\phi,T}(\varepsilon_\alpha^{ss})},$$

$$(4.2)$$

Fig. 4.3 Simulations of the reaction of ethylene in a closed isothermal system, initially at an equivalence ratio of 5.0, to form naphthalene (A_2, left panel) and phenanthrene (A_3, right panel). Solid lines show the results of simulations using the full ABF mechanism. Circles show the concentration of each species calculated using the steady-state approximation. The shaded area shows typical flame residence times.

where $\varepsilon_{\alpha}^{\mathrm{ss}}(\tau; \phi, T)$ is the time-integrated error in the steady-state approximation of species α. It is computed as the logarithm of the ratio of the time integrals of C_{α}^{ss}, the concentration of species α calculated using the steady-state approximation, and $C_{\alpha}^{\mathrm{ref}}$, the reference solution calculated using the full ABF mechanism. $\hat{\varepsilon}_{\alpha}^{\mathrm{ss}}(\tau; \phi, T)$ is normalised by the maximum error found over the temperature-equivalence ratio space. It must be noted that in these definitions it is assumed that the steady-state value is larger than the reference solution; a trend that was observed in all simulations but that may not be applicable to other systems.

Figure 4.4 shows a map of $\hat{\varepsilon}_{\alpha}^{\mathrm{ss}}(\tau = 1.0\mathrm{s})$ versus temperature and equivalence ratio. The upper limit of the integral was selected as larger than the typical flame residence times to allow all significant errors to be captured by the time integral. The black lines show the location of a *soot island*, which is a region that is known to be important for soot emissions (in engine applications) [299]. It can be seen that errors accumulate at temperatures under 1700 K and equivalence ratios under 2.0, with some of these conditions being in the region relevant to soot formation.

The concentrations of most intermediates follow the steady-state approximation under a wide range of conditions. However, species involved in the final ring-forming step (Table A.1, reactions 21–25 and Table A.2, reactions 15–16) deviate from this behaviour at the lower end of the temperature space in Figure 4.4. These include $A_1(C_2H)C_2H_2^{\bullet}$, $A_2^{\bullet}$ and A_2 which are involved in the formation of naphthalene, and $A_2(C_2H)C_2H_2^{\bullet}$, $A_3^{\bullet}$ and A_3 which are involved in the formation of phenanthrene.
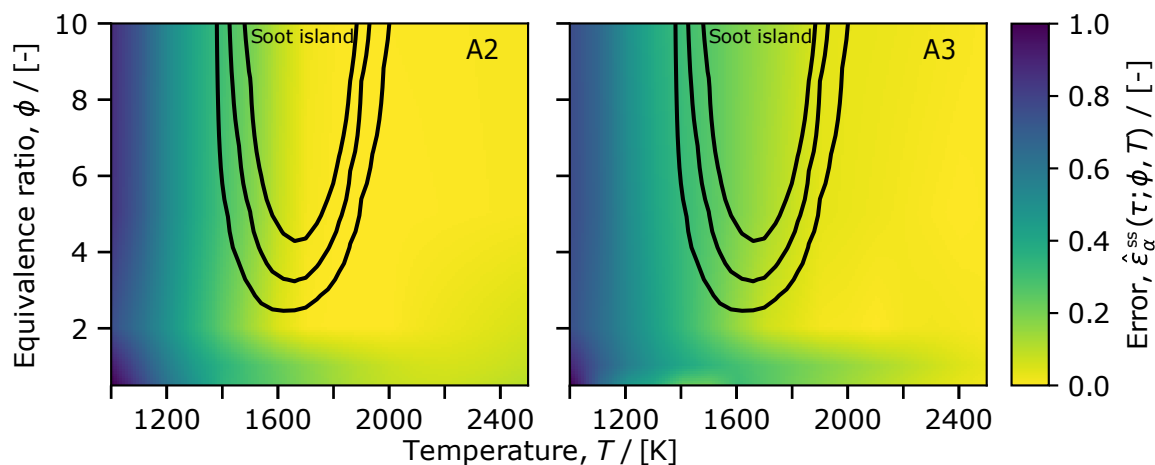
Fig. 4.4 Time-integrated steady-state error $\hat{\varepsilon}_\alpha^{ss}(\tau = 1.0s)$ for the concentration of naphthalene (A_2, left panel) and phenanthrene (A_3, right panel) calculated via simulations of the reaction of ethylene in a closed isothermal system as a function of temperature and initial equivalence ratio and the concentration of each species calculated using the steady-state approximation. The black lines show the region that is most important for soot emissions (in engine applications) [299].

During the induction time, these reactions progress much more quickly in the forward direction than in the reverse direction. The effect of this is that intermediate species are consumed by the forward reactions without being replenished by the reverse reactions. This is inconsistent with the steady-state approximation, which assumes that the rates of the forward and reverse reactions are approximately equal. This is the leading cause of the error shown in Figure 4.4.

4.4.2   Partial-equilibrium approximation

Most species investigated in the previous section are controlled by reactions where the forward and reverse rates are large compared to net rate of conversion to final product. However, some species, notably those responsible for the error shown in Figure 4.4, show a distinct induction period during which the forward (ring-forming) reactions proceed much more quickly than reverse (ring desorption) reactions. This difference in the time scales and the presence of an induction period suggest that the system might be amenable to a partial-equilibrium approximation. In this instance, our primary interest is whether this can improve the behaviour of the model during the induction period.

A set of partial-equilibrium species and reactions is proposed for each process shown in Figure 4.2. In the case of processes (i) and (ii), these are a subset of the steady-state sets. In the case of process (iii), the set excludes the non-linear reaction (Table A.3, reaction 17) that

prevented the use of the steady-state approximation for this process in Section 4.4.1. The full set of species and reactions used for the partial-equilibrium approximation of each process is shown in Tables A.1–A.3.

In each case, the partial-equilibrium approximation excludes the ring-forming reactions responsible for the formation of the final product PAHs A_2 and A_3, and the corresponding radicals $A_2^\bullet$ and $A_3^\bullet$. The concentrations of these species must be computed separately. The set of ODEs governing the concentrations of these species may be written in the form

$$\frac{\mathrm{d}C_\alpha}{\mathrm{d}t} = \mathcal{P}_\alpha - \mathcal{L}_\alpha C_\alpha, \tag{4.3}$$

where $\mathcal{P}_\alpha$ is the rate of production of species α and $\mathcal{L}_\alpha$ is a pseudo-first order rate constant for the loss of species α. During the induction period the rate of production is expected to be much greater than the rate of loss (due to the rates of the ring-forming versus ring desorption reactions). Whilst this condition holds, Equation (4.3) can be approximated as

$$\frac{\mathrm{d}C_\alpha}{\mathrm{d}t} \approx \mathcal{P}_\alpha,$$

and, noting that such that P_α is not a function of C_α,

$$C_\alpha \approx \int_0^t \mathcal{P}_\alpha \, \mathrm{d}t. \tag{4.4}$$

In the simulations that follow, it is assumed that $A_2 + A_2^\bullet$ and $A_3 + A_3^\bullet$ are close to equilibrium. Equations of the form of Equation (4.4) are solved for the total concentration of each species and its corresponding radical, $C_{A_2} + C_{A_2^\bullet}$ and $C_{A_3} + C_{A_3^\bullet}$. A detailed step-by-step explanation of the treatment of these equations and reactions is given in Section 3.5.

Figure 4.5 shows the concentrations of naphthalene and phenanthrene calculated using the partial-equilibrium approximation versus reference solutions calculated using the full ABF mechanism in a closed isothermal system. For comparison, data calculated using the steady-state approximation is also shown. The figure shows that the partial-equilibrium approximation performs better than the state-state approximation at low temperatures and at short times. This is because of the improved treatment of the reactions responsible for the induction period and the inclusion of process (iii) (see Section A.4 in Appendix A).

At longer times, the partial-equilibrium approximation performs less well due to neglecting the loss term in Equation (4.3). In all cases, there is a crossover point after which the steady-state approximation performs better than the partial-equilibrium approximation. (The location of this point is a strong function of temperature. It is most obvious in the cases at 1600 K.) This crossover point can be exploited in models of PAH growth.
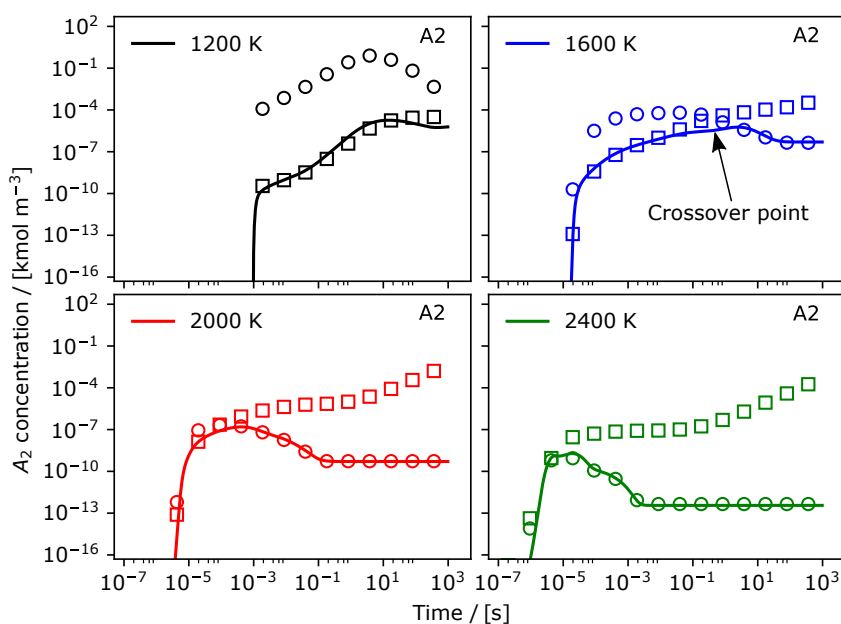
(a) Naphthalene (A_2).
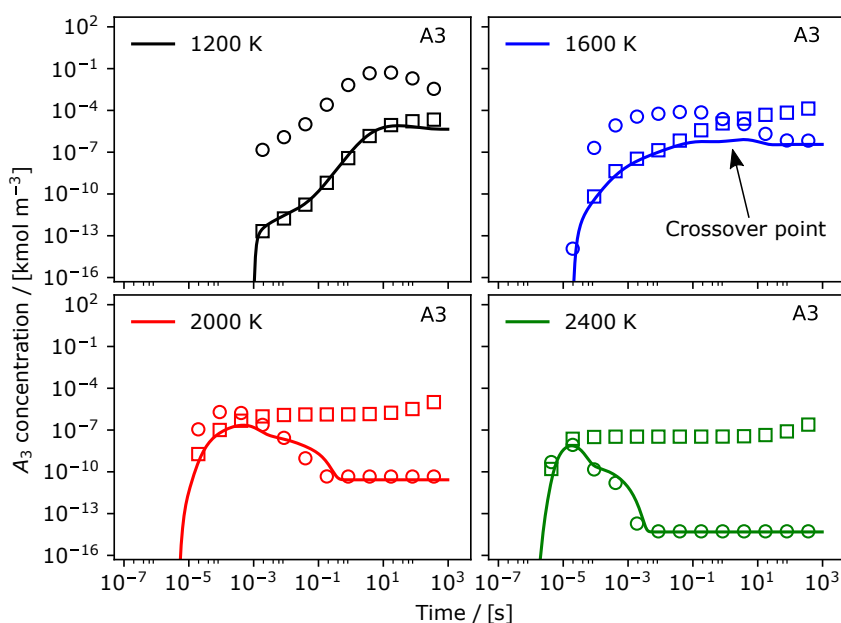
(b) Phenanthrene (A_3).

Fig. 4.5 Simulations of the reaction of ethylene in a closed isothermal system, initially at an equivalence ratio of 5.0, to form naphthalene (A_2, top panels) and phenanthrene (A_3, bottom panels). Solid lines show the results of simulations using the full ABF mechanism. Circles show the concentration of each species calculated using the steady-state approximation. Squares show the concentration of each species calculated using the partial-equilibrium approximation.

4.4.3   A combined steady-state–partial-equilibrium approximation

A new method that seeks to combine the strengths of the steady-state and partial-equilibrium approximations is proposed. The idea is to use the partial-equilibrium approximation during the induction period, before switching to use the steady-state approximation after the crossover point identified in the previous section.

The steady-state and partial-equilibrium approximations are combined as follows:

1. Use the steady-state approximation to evaluate the product concentrations, in this case $C_{A_2}^{ss}$ and $C_{A_3}^{ss}$. See Section 4.4.1.

2. Use the partial-equilibrium approximation to evaluate the product concentrations, in this case $C_{A_2}^{peq}$ and $C_{A_3}^{peq}$. See Section 4.4.2.

3. Determine the combined steady-state–partial-equilibrium product concentrations

$$C_{A_2}^{ss-peq} = \begin{cases} C_{A_2}^{peq} & \text{if } \lambda\left(\mathcal{P}_{A_2} + \mathcal{P}_{A_2\bullet}\right) > \left(\mathcal{L}_{A_2}C_{A_2} + \mathcal{L}_{A_2\bullet}C_{A_2\bullet}\right), \\ C_{A_2}^{ss} & \text{otherwise,} \end{cases} \tag{4.5}$$

and

$$C_{A_3}^{ss-peq} = \begin{cases} C_{A_3}^{peq} & \text{if } \lambda\left(\mathcal{P}_{A_3} + \mathcal{P}_{A_3\bullet}\right) > \left(\mathcal{L}_{A_3}C_{A_3} + \mathcal{L}_{A_3\bullet}C_{A_3\bullet}\right), \\ C_{A_3}^{ss} & \text{otherwise,} \end{cases} \tag{4.6}$$

where λ is a positive real number acting as a multiplier.

The rationale behind the criteria to determine the crossover point is that the production terms will be greater than the loss terms during the induction period (see the discussion in Section 4.4.2), such that the method will choose the partial-equilibrium approximation. At later times as the system stabilises, the production and loss terms will be approximately equal such that method will choose the steady-state approximation.

The multiplier λ is a parameter of the method. Its purpose is to guard against the case that the system has stabilised such that the steady-state approximation is the desired choice, but the relative values of the production and loss terms are such that the method imprudently chooses the partial-equilibrium approximation. This was not observed here, and in all cases the value of the parameter was set as $\lambda = 1$. However, it could conceivably become important in the future, so is included for completeness.

Figure 4.6 shows the concentrations of naphthalene and phenanthrene calculated using the combined steady-state–partial-equilibrium approximation versus reference solutions

calculated using the full ABF mechanism in a closed isothermal system. In contrast to
the cases when either the steady-state or partial-equilibrium approximations are applied in
isolation, the figure shows that the combined steady-state–partial-equilibrium approximation
performs well both at early times (so during the induction period) and at long time (so
when the system approaches equilibrium). Unsurprisingly, the main point at which there is
deviation from the reference solution is close to the crossover point. This is most obvious in
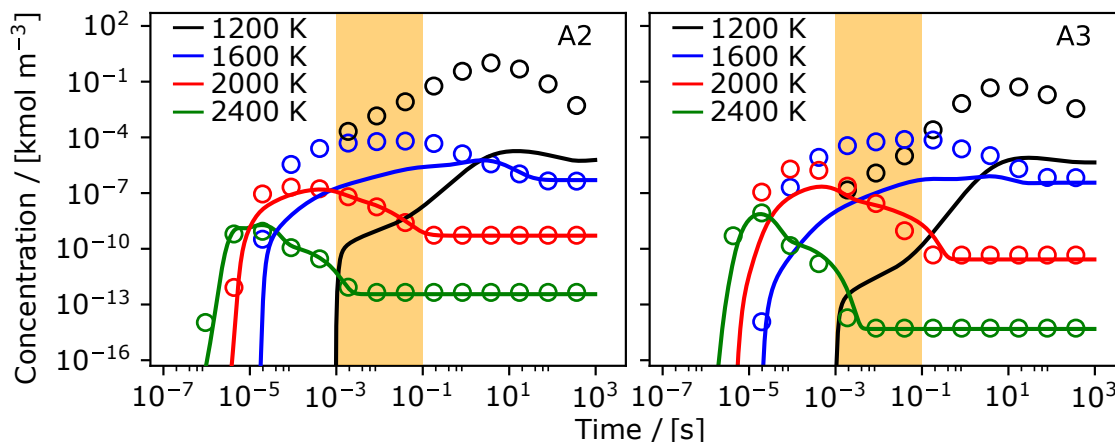the case at 1600 K and can be predicted from the data in Figure 4.5.
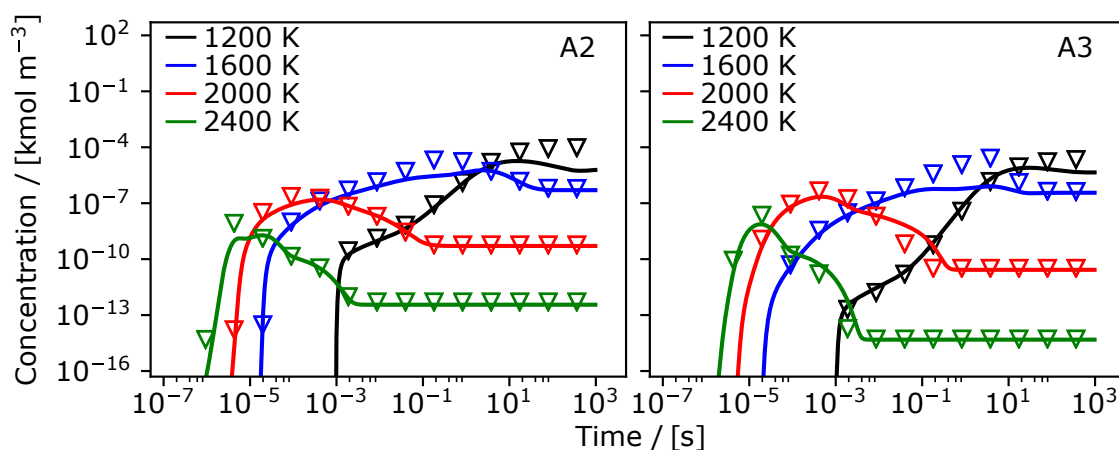
Fig. 4.6 Simulations of the reaction of ethylene in a closed isothermal system, initially at
an equivalence ratio of 5.0, to form naphthalene (A_2, left panel) and phenanthrene (A_3,
right panel). Solid lines show the results of simulations using the full ABF mechanism.
Triangles show the concentration of each species calculated using a combined steady-state
and partial-equilibrium approximations.

In order to assess the accuracy of the combined steady-state–partial-equilibrium method,
an error metric analogous to that in Equation (4.2) is defined

$$\varepsilon_{\alpha}^{\text{ss–peq}}(\tau;\phi,T) = \log\left(\frac{\int_0^\tau C_\alpha^{\text{ss–peq}}(t;\phi,T)\,\mathrm{d}t}{\int_0^\tau C_\alpha^{\text{ref}}(t;\phi,T)\,\mathrm{d}t}\right),$$

$$\hat{\varepsilon}_{\alpha}^{\text{ss–peq}}(\tau;\phi,T) = \frac{|\varepsilon_{\alpha}^{\text{ss–peq}}(\tau;\phi,T)|}{\max\limits_{\phi,T}(\varepsilon_{\alpha}^{\text{ss}})}.$$

(4.7)

$\hat{\varepsilon}_{\alpha}^{\text{ss–peq}}(\tau;\phi,T)$ is normalised by the maximum error found over the temperature-equivalence
ratio space for the *steady-state approximation*. This choice is deliberate and is intended to
enable a direct comparison between errors calculated using Equation (4.2) and Equation (4.7).

Figure 4.7 shows a map of $\hat{\varepsilon}_{\alpha}^{\text{ss–peq}}(\tau = 1.0\text{s})$ versus temperature and equivalence ratio.
A comparison with Figure 4.4 shows that the combined steady-state–partial-equilibrium
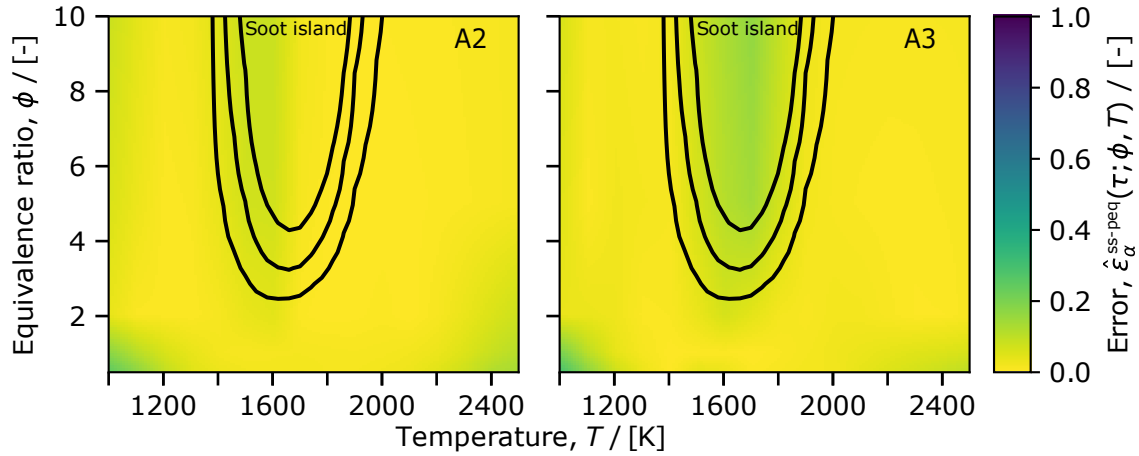
Fig. 4.7 Time-integrated steady-state–partial-equilibrium error $\hat{\varepsilon}_\alpha^{\text{ss-peq}}(\tau = 1.0s)$ for the concentration of naphthalene (A_2, left panel) and phenanthrene (A_3, right panel) calculated via simulations of the reaction of ethylene in a closed isothermal system as a function of temperature and initial equivalence ratio and the concentration of each species calculated using the combined steady-state and partial-equilibrium approximation. The black lines show the region that is most important for soot emissions (in engine applications) [299].

performs much better than the steady-state assumption applied in isolation. In particular, at low temperatures and low equivalence ratios.

4.4.4   A combined steady-state–partial-equilibrium KMC model

In this section, the application of the combined steady-state–partial-equilibrium methodology to KMC simulations of PAH growth is demonstrated in a premixed burner-stabilised ethylene-oxygen flame at an equivalence ratio of 2.4. The simulations are based on the flame studied by Ciajolo et al. [41], over a range of cold-gas flow velocities in order to vary the transition point between the steady-state and partial-equilibrium approximations.

A fully-coupled simulation of the flame using the full ABF mechanism was used to obtain reference data for the species concentrations and temperature. The KMC simulations were performed as a Lagrangian post process, where the temperature and small-molecule concentrations (up to and including benzene, A_1) from the fully-coupled simulation were imposed as boundary conditions.

The following sequence of jump processes were included in the KMC model

$$A_1 \longrightarrow A_2, \quad A_2 \longrightarrow A_3, \quad A_3 \longrightarrow A_4, \quad A_2 \longrightarrow A_2R_5, \quad A_1 \longrightarrow A_3,$$
$$A_2 \longrightarrow A_1, \quad A_3 \longrightarrow A_2, \quad A_4 \longrightarrow A_3, \quad A_2R_5 \longrightarrow A_2. \tag{4.8}$$
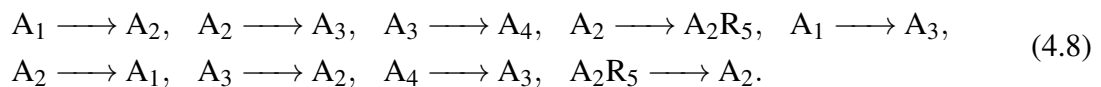
This is a superset of the processes in Sections 4.4.1–4.4.3. The sequence is truncated at A_4 to maintain consistency with the ABF mechanism for the purpose of testing. The jump processes exist in pairs (for example, $A_1 \to A_2$ and $A_2 \to A_1$. This is important to ensure consistency with the underlying chemistry, in this case the ABF mechanism. The $A_3 \to A_1$ process is an exception and is omitted because its rate was negligible. The full set of species and reactions for each jump process is given in Table A.4 in Appendix A.

The combined steady-state–partial-equilibrium approximation method is modified to accommodate the new jump processes and to reflect the fact that the KMC model requires the method to return a set of rates as opposed to a set of concentrations. The method is as follows:

1. Use the steady-state approximation to evaluate the rate of each jump process.

2. Use the partial-equilibrium approximation to evaluate the rate of each jump process.

3. Determine the combined steady-state–partial-equilibrium approximation rates

$$r_{A_1 \to A_2}^{\text{ss-peq}} = \begin{cases} r_{A_1 \to A_2}^{\text{peq}} & \text{if } \lambda\, r_{A_1 \to A_2}^{\text{peq}} > r_{A_2 \to A_1}, \\ r_{A_1 \to A_2}^{\text{ss}} & \text{otherwise,} \end{cases} \tag{4.9}$$

$$r_{A_2 \to A_3}^{\text{ss-peq}} = \begin{cases} r_{A_2 \to A_3}^{\text{peq}} & \text{if } \lambda\, r_{A_2 \to A_3}^{\text{peq}} > r_{A_3 \to A_2}, \\ r_{A_2 \to A_3}^{\text{ss}} & \text{otherwise,} \end{cases} \tag{4.10}$$

$$r_{A_3 \to A_4}^{\text{ss-peq}} = \begin{cases} r_{A_3 \to A_4}^{\text{peq}} & \text{if } \lambda\, r_{A_3 \to A_4}^{\text{peq}} > r_{A_4 \to A_3}, \\ r_{A_3 \to A_4}^{\text{ss}} & \text{otherwise,} \end{cases} \tag{4.11}$$

$$r_{A_2 \to A_2R_5}^{\text{ss-peq}} = \begin{cases} r_{A_2 \to A_2R_5}^{\text{peq}} & \text{if } \lambda\, r_{A_2 \to A_2R_5}^{\text{peq}} > r_{A_2R_5 \to A_2}, \\ r_{A_2 \to A_2R_5}^{\text{ss}} & \text{otherwise,} \end{cases} \tag{4.12}$$

and

$$r_{A_1 \to A_3}^{\text{ss-peq}} = r_{A_1 \to A_3}^{\text{peq}} \qquad \text{always,} \tag{4.13}$$

where r denotes the rate of a jump process. The calculated steady-state–partial-equilibrium rates $r^{\text{ss-peq}}$ are used to determine which processes occur in the KMC simulation, which in turn calculates the concentrations of the final products, A_2, A_3, A_4 and A_2R_5.

Note that the desorption processes (bottom row of Equation (4.8) and right-hand side of the inequalities in Equation (4.9)–(4.12)) do not carry an 'ss' or 'peq' label because the

rates of these processes are not a function of the species concentrations calculated via the steady-state or partial-equilibrium approximations. These rates are therefore calculated without either approximation. The rate of the $A_1 \rightarrow A_3$ process was taken from the partial-equilibrium approximation because the process cannot be described using the steady-state assumption (because of the non-linear reaction, Table A.3, reaction 17). The value of the multiplier was set as $\lambda = 1$ for all cases. A detailed step-by-step explanation of the treatment of the jump processes and reactions is given in Section 3.5.4. The list of reactions used in this section is shown in Appendix A.

Figure 4.8 shows the concentrations of the products A_2, A_3, A_4 and A_2R_5 calculated by the KMC model using the combined steady-state–partial-equilibrium approximation versus reference solutions calculated using the full ABF mechanism.

The KMC model shows substantial agreement with the reference data. The main deviations occur in the concentration of A_2 before the crossover point in Figure 4.8(a) (where the model uses the partial-equilibrium approximation) and in the concentrations of A_3 and A_4 after the crossover point in Figure 4.8(c) (where the model uses the steady-state approximation) and are due to the approximate treatment of the chemistry. The relationship between the differences and the cold-gas flow velocity remains to be investigated.

The use of a KMC approach provides a framework that can be applied to simulate the growth of arbitrarily-sized PAHs. The process rates can be updated to use data from more recent mechanisms as and if required. The methodology demonstrated in Figure 4.8 allows KMC simulations of PAH growth in flame environments without introducing significant additional complexity. This is achieved by approximating the contributions of key intermediate species to the main PAH growth processes. Although the intermediate species may be of interest for some applications, this combined steady-state and partial-equilibrium methodology is proposed for use in coupled simulations of PAH growth leading to soot (or other carbonaceous particle) formation, where it is necessary for the model to simulate a large ensemble of PAHs.
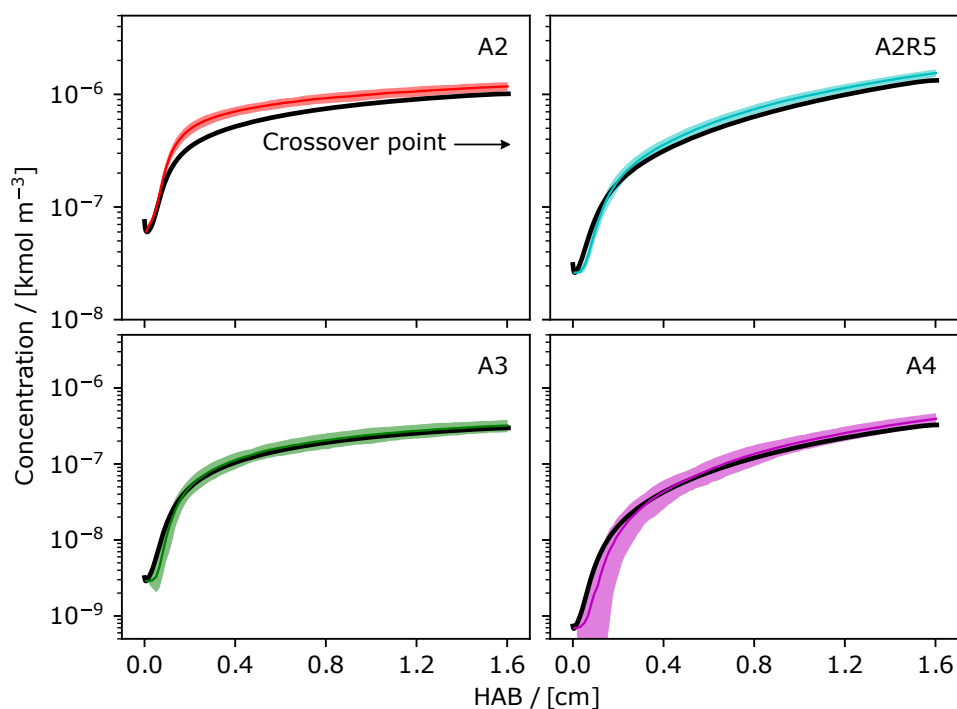
(a) Cold-gas flow velocity of 4 cm/s [as per 41].

Fig. 4.8 Simulations of a premixed burner-stabilized ethylene flame at an equivalence ratio of 2.4 [41] to form naphthalene (A_2, top left), acenaphthylene (A_2R_5, top right), phenanthrene (A_3, bottom left) and pyrene (A_4, bottom right). Solid black lines show the results of fully-coupled flame simulations using the full ABF mechanism. Coloured lines show the average result from 100 KMC simulations using a combination of the steady-state and partial-equilibrium approximations. The coloured shaded region surrounding the lines shows two standard deviations to either side of the average KMC results. Part 1.
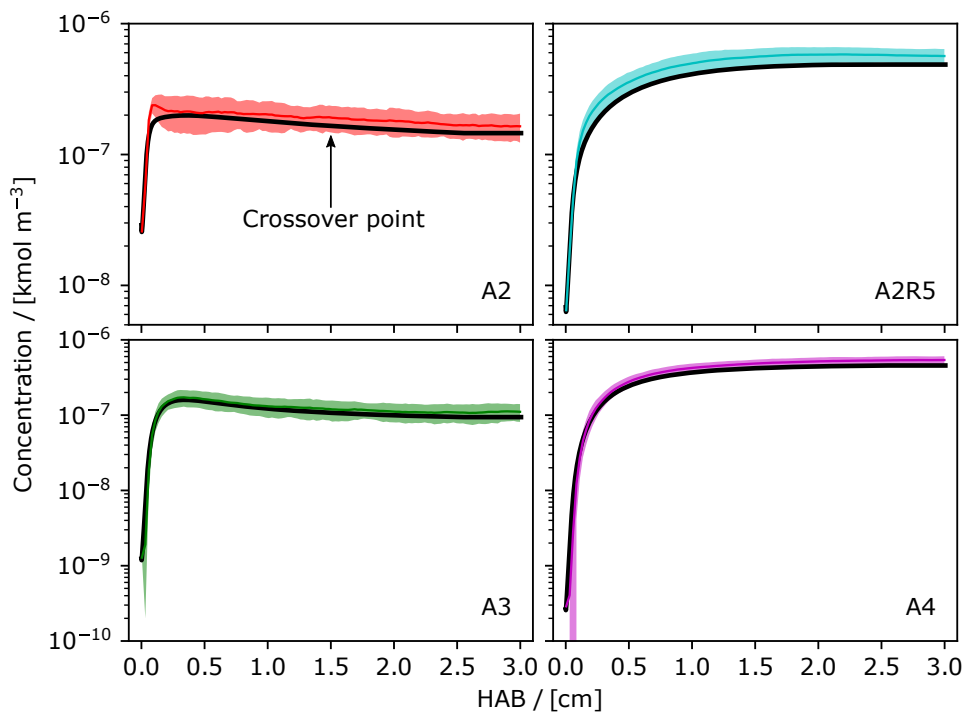
(b) Cold-gas flow velocity of 12 cm/s.
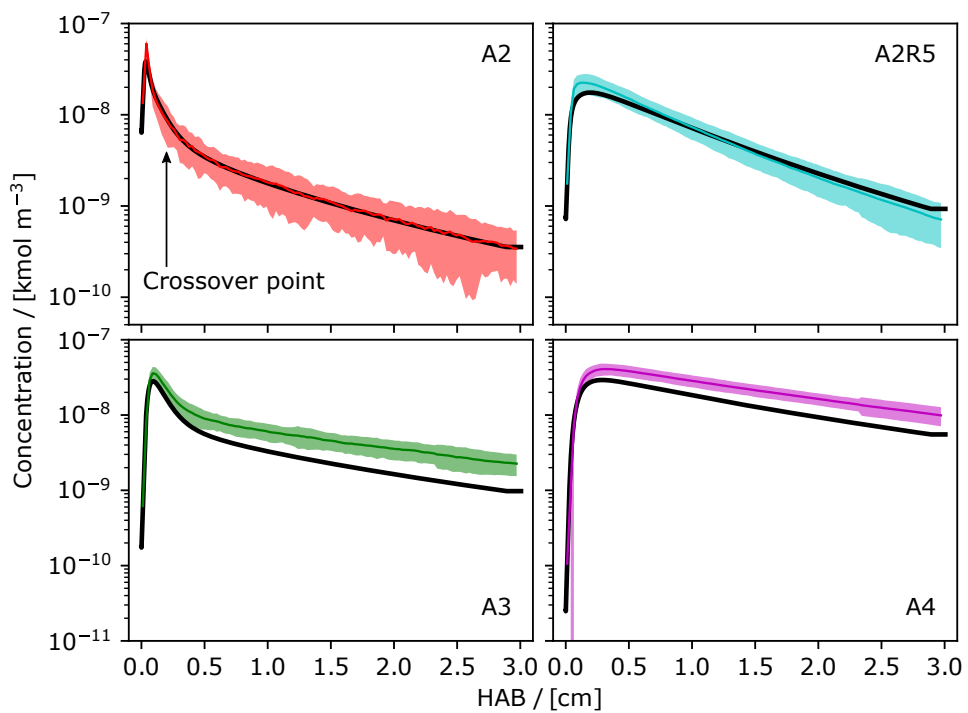
(c) Cold-gas flow velocity of 24 cm/s.

Fig. 4.8 Simulations of premixed burner-stabilized ethylene flames. Part 2.

4.5 Conclusions

This chapter has investigated the application of the steady-state and partial-equilibrium approximations for ring growth processes in the context of PAH-KMC models. These approximations were used to approximate the concentrations of intermediate species and express key growth pathways as jump processes. Simulations of closed systems showed that the steady-state approximation gave good results at high temperatures and long times, whereas the partial-equilibrium approximation gave good results at short times and low temperatures. A new methodology that combines both approximations was developed and tested in closed systems. The methodology compares the rate of partial-equilibrium growth with the rate of ring desorption to determine whether to use the steady-state or partial-equilibrium approximation. The methodology showed a substantial improvement in accuracy over the steady-state approximation across temperatures ranging from 1000 to 2500 K and equivalence ratios ranging from 0.5 to 10.

The proposed methodology was implemented in a KMC model of PAH growth to compute the growth rate of stochastic jump processes. The application of the model was demonstrated for simulations of premixed ethylene flames. The results were in close agreement with reference solutions obtained from fully-coupled simulations of the flames using the ABF mechanism. The ABF mechanism was selected because it contains well-established HACA sequences for PAH growth which are common to many later mechanisms and because it does not contain routes that are unique to small PAHs. This is an important requirement for generalising the KMC model developed in this work to describe the growth of arbitrarily-sized PAHs. The new methodology has the potential to be used to study the growth of large ensembles of PAHs, for example, in fully-coupled simulations of PAH growth and soot formation.

Chapter 5

Statistics of curvature integration in a counterflow diffusion flame

In this chapter, a Kinetic Monte Carlo (KMC) model that includes processes to integrate curvature due to the formation of five- and seven-member rings was used to simulate PAHs growing in lightly sooting ethylene and acetylene counterflow diffusion flames. The model included new processes to form seven-member rings and to embed five-member rings via hydrogen-abstraction-acetylene-addition and bay closure reactions. The mass spectra of PAHs predicted by the model were assessed against experimental data, and the distribution of embedded five-member rings and seven-member rings was studied as a function of spatial location, molecule size and frequency of events sampled in the simulation. The number of events and proportion of PAHs containing embedded five-member rings and seven-member rings were analysed at the end of the simulation domain. The simulations showed that the formation of seven-member rings and the embedding of five-member rings are competing processes. Both types of rings were observed more frequently as the simulation proceeded from the fuel outlet towards the stagnation plane.

Collaborative Contributions

The work presented in this chapter has been published in *Proceedings of the Combustion Institute* and has been presented in the *Symposium (International) on Combustion*. The work includes contributions from co-authors. Angiras Menon supplied the rate coefficients for this work. Laura Pascazio suggested improvements to the model. Eric J. Bringley helped editing the figures and writing the manuscript. Jethro Akroyd helped editing the manuscript. The model implementation, stochastic simulations, figure preparation and manuscript writing were done by the author.

5.1   Introduction

Curvature induced during the growth of polycyclic aromatic hydrocarbons (PAHs) has important consequences for carbon materials. Curved PAHs, such as coranulenne, have been detected in flame-generated carbonaceous particles [166, 354] as well as in premixed [3, 102] and non-premixed flames [190]. These PAHs have been strongly associated with the formation of fullerenes [121] and are known to possess a persisting dipole moment due to the flexoelectric effect [189, 194]. For this reason, they have been suggested as possible candidates to explain the formation of nascent carbonaceous particles [191, 22].

The curvature of carbonaceous materials arises from five- and seven-member rings that are embedded during the growth of a PAH. Five-member rings have been found in carbon nanotubes [175], graphene [267] and fullerenes [121]. In carbonaceous particles, high-resolution transmission electron microscopy (HR-TEM) has suggested they are present in curved fringes [333, 21] and different types of five-member rings have been directly observed using atomic force microscopy [45]. Seven-member rings have been observed in non-graphitising carbon [115], nanotubes [175] and graphene [253]. The Stone-Wales defect, a double pair of five- and seven-member rings has also been detected in graphene [248] as well as lines of consecutive five- and seven-member rings that constitute grain boundaries [131].

The processes that form embedded five-member rings have been studied using different methods. Frenklach and collaborators [348, 359, 349] described the embedding of five-member rings via acetylene additions and used a Kinetic Monte Carlo (KMC) model to study the growth of graphene sheets under different conditions. Yapp et al. [358] combined a KMC model with a probabilistic model to estimate the Gauss curvature of flame generated PAHs. Using density functional theory, Raj [255] calculated the process rates of curved and planar PAHs, and processes that form seven-member rings have been studied by Kislov et al. [157]. Recently, Menon et al. [206] developed rates for the formation of seven-member rings on

sites containing five-member rings. However, no KMC model has been used to study the statistics of the formation of seven-member rings and their impact on curvature.

The **purpose of this chapter** is to study the inclusion of curvature in PAHs due to HACA growth and bay closure reactions in KMC simulations of a counter-flow diffusion flame. The KMC model used the process rates calculated by Menon et al. [206], for first time enabling simulation of the growth of an ensemble of PAHs that include seven-member rings. The model results are consistent with experimental mass spectra and give insight into the relative abundance and location of PAHs containing embedded five-member rings and seven-member rings.

5.2   Curvature integration processes

The KMC model used in this chapter includes two types of process that integrate curvature: The formation of seven-member rings next to existing partially embedded five-member rings and the embedding of five-member rings. These processes are shown in Figure 5.1.

Figure 5.1(a) and (b) show new processes that form seven-member rings via HACA bay capping. The process in Figure 5.1(a) results in a seven-member ring coupled to an embedded five-member ring. The process in Figure 5.1(b) results in a seven-member ring coupled to a partially embedded five-member ring. The process rates were taken from Menon et al. [206].

Figure 5.1(c) and (d) show new processes for the closure of seven-member bays adjacent to five-member rings. The process rates were taken from Menon et al. [206].

Figure 5.1(e) shows a new process that embeds a five-member ring at a six-member bay site that includes a partially embedded five-member ring. There are many possible configurations of such a site. In this work, it was assumed that all configurations proceed at the same rate. The rate is taken by analogy with the most similar process that has been studied in the literature - the closure of a six-member bay site containing only six-member rings. The rate of this process was first calculated by Raj et al. [256]. In this work the rate calculation was repeated at the B3LYP/6-311+G(d,p) level of theory. The process was observed to proceed via bay closure following hydrogen abstraction (with a barrier in the range 30–35 kcal/mol), or via hydrogen addition, carbene formation or direct cyclisation routes (all with barriers of $\sim$100 kcal/mol). The assumption that this rate can be applied to the process in Figure 5.1(e) is made on the grounds that hydrogen abstraction is expected to be the most likely route and is expected to have similar rates in both processes, coupled with the observation [206] that the rates of the processes in Figure 5.1(a) and (b) are similar and insensitive to the location of the five-member ring, and likewise for the processes in Figure 5.1(c) and (d).

(a)

+H /-H$_2$ /+C$_2$H$_2$ /-H

(b)

+H /-H$_2$ /+C$_2$H$_2$ /-H

(c)

+H /-H$_2$ /-H

(d)

+H /-H$_2$ /-H

(e)

+H /-H$_2$ /-H

(f)

+H /-H$_2$ /+C$_2$H$_2$ /-H
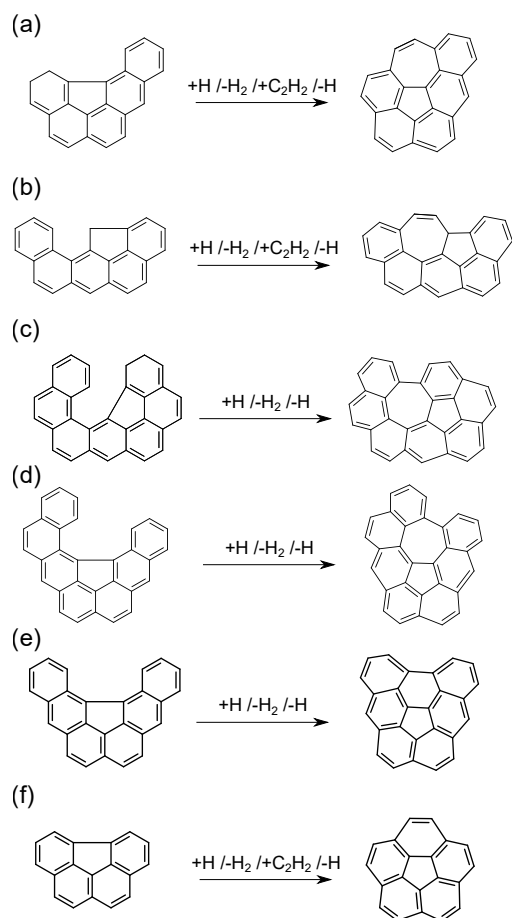
Fig. 5.1 Curvature integration jump processes.

Finally, Figure 5.1(f) shows a bay capping process that embeds a five-member ring at an armchair site centred on a partially embedded five-member ring. This process is well-known and has been included in previous KMC models. The rate of this process is taken from Raj [255].

Details of the sources for the rates of other processes are provided in Chapter 3. Processes that form seven-member rings in the absence of five-member rings are neglected. This is based on the experimental observation that seven-member rings are typically found next to five-member rings in different carbonaceous materials [104, 131].

5.3   Methodology

5.3.1   Flame model

The ethylene and acetylene counter-flow diffusion flames studied by Skeen et al. [296] were selected as targets for this study. These are lightly sooting flames with faint luminosity on the oxidiser side of the stagnation plane. Similar flames have been used for mass spectrometry studies of radical-radical reactions [140] and the spatial dependence of oxygen substituted compounds [339].

A schematic of the ethylene flame is shown in Figure 5.2 and similar to that of acetylene. The flames were simulated using Cantera [96] with the mechanism of Narayanaswamy et al. [227] to solve the one-dimensional continuity, momentum, species and energy equations. The distance from fuel outlet (DFFO) was defined as the flames spatial coordinate.
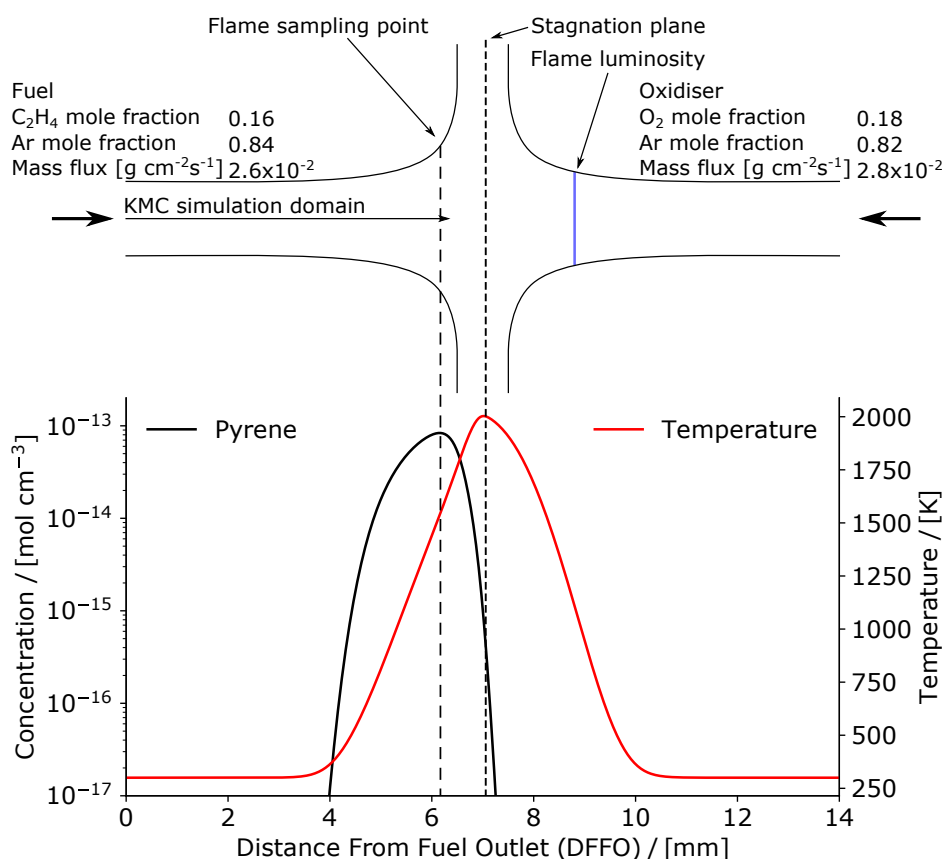
Fig. 5.2 Schematic of the ethylene flame. The concentration of pyrene and temperature show the flame structure.

5.3.2   Kinetic Monte Carlo model

A KMC model was used to simulate the growth of PAHs on the fuel side of the flame. The model tracks the spatial coordinates of the carbon atoms and corresponding reactive sites in each PAH. It uses a combination of the steady-state and partial-equilibrium approximations to estimate the rate of reaction at each site. This treatment of the rates has previously been shown to give good agreement with deterministic simulations of HACA growth, (see Chapter 4).The temperature and species concentrations from the flame simulations (Section 5.3.1) were provided as boundary conditions to the KMC model, which simulated the growth of PAHs in a Lagrangian control volume travelling from the fuel inlet (DFFO = 0 mm) to just after the sample point (DFFO = 6.17 mm). The PAH growth started from pyrene (the largest PAH in the chemcial mechanism), the concentration of which was imposed as a boundary condition from the flame simulations. Methyl additions and oxidation reactions were assumed to be insignificant on the fuel side due to the concentrations of the necessary reactants being low in this domain. Hence, they were neglected in this work. The formation of soot particles by PAH coagulation was not included in the simulation based on the assumption that the PAH growth is dominated by gas-phase reactions, consistent with the selection of lightly sooting flames with faint luminosity.

5.4   Results and discussion

5.4.1   Mass spectra

Figure 5.3 shows simulated mass spectra for the acetylene and ethylene flames versus corresponding experimental data. The peaks heights are scaled to match at m/z=202, corresponding to imposing the pyrene concentration as a boundary condition. The maximum number of PAHs in the simulations was 14,060 and 81,500 respectively.

The simulations reproduce the relative abundance of the major peaks reasonably well for the acetylene flame. The level of agreement is less certain for the ethylene flame, where the experimental data are only available up to $m/z = 310$. In both cases, and in particular the ethylene flame, the simulations underpredict the peaks for small PAHs, for example at $m/z = 226$. This highlights a potential gap in the current modelling approach, where the growth of multiple small PAHs is simulated in the gas-phase chemical mechanism, and then re-simulated rather than imposed in the KMC simulation.

A number of peaks are missing from the simulated spectra. There are several reasons for this. Firstly, some experimentally observed phenomena including methyl-addition [113], oxygenated species [339, 133], and isotopes [278] are neglected in the current model. Sec-

ondly, the model simulates the growth of PAHs from a single species - pyrene. Given that all the remaining growth processes add two carbons, the simulated spectra currently only include even-carbon-numbered species.
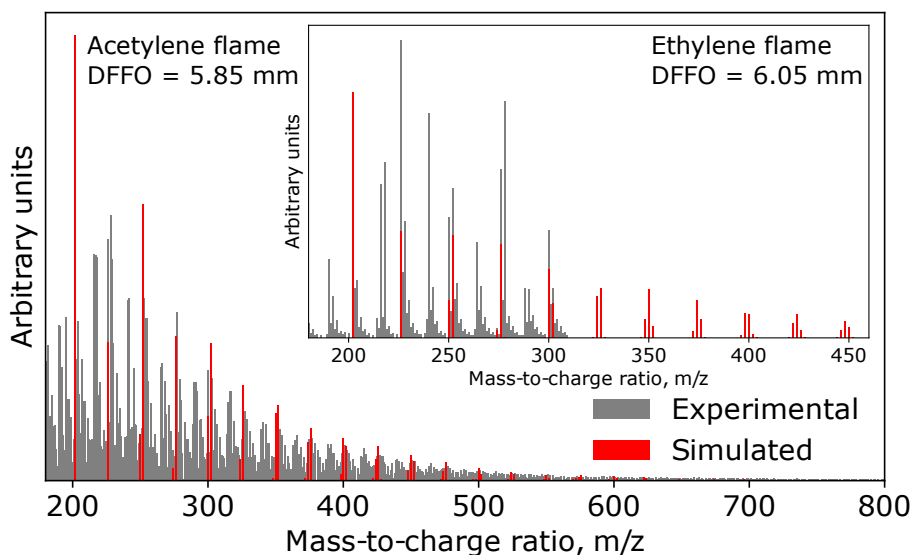
Fig. 5.3 Simulated and experimental [296] mass spectra for the acetylene (main) and ethylene (inset) flames.

5.4.2   Integration of five- and seven-member rings

Figure 5.4 shows the spatial distribution of PAHs containing five- and seven-member rings in the ethylene flame. The temperature and residence time both contribute to the observed distribution and it is not possible to separate each contribution within the current study. The first PAHs with one embedded five-member ring are observed at DFFO $\approx$ 5.7 mm. The concentration of these PAHs increases throughout the remainder of the simulation domain. The subsequent addition of five- and seven-member rings occurs via competitive processes that embed a five-member ring either by adding a six- or seven-member ring. A strong correlation is observed between the concentrations of PAHs with two-embedded five member rings and one seven-member ring. Similarly, the concentrations of PAHs with four embedded five-member rings correlate strongly with the concentrations of PAHs with two seven-member rings. By the end of the simulation domain, a few PAHs containing up to six embedded five-member rings or four seven-member rings can be observed.

Figure 5.5 presents a flux diagram showing the relative sampling frequency of the processes that integrate curvature in the ethylene flame. The most frequent processes are HACA (1(f), 47.4%) and bay closure (1(e), 37.3%) processes that embed five-member rings
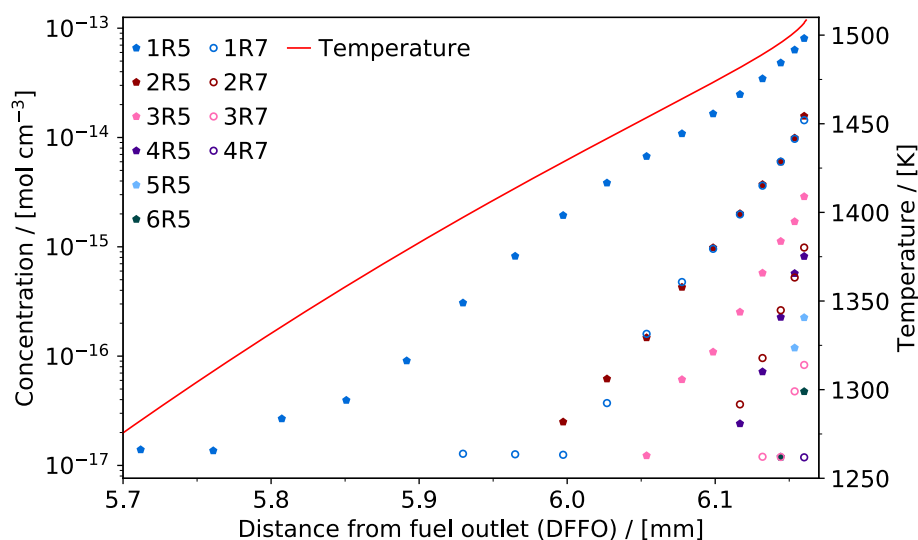
Fig. 5.4 Spatial distribution of temperature and of PAHs containing five- and seven-member rings in the ethylene flame. nR5 denotes PAHs containing exactly n embedded five-member rings; nR7 denotes exactly n seven-member rings (embedded or otherwise).

by adding six-member rings. These occur with similar frequencies. The rate of the bay closure processes is surprisingly high, but can be explained by the nature of the partially embedded five-member ring. Unlike partially embedded five-member rings in armchair
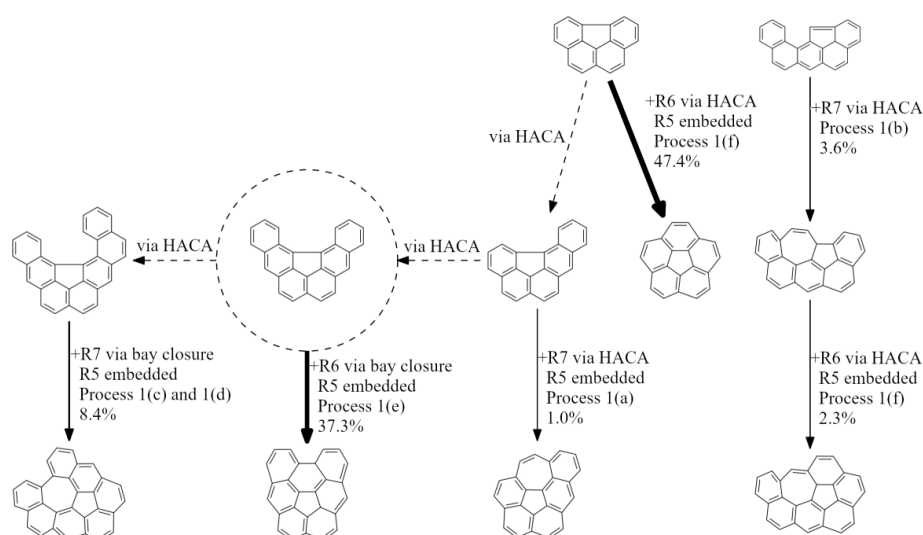
Fig. 5.5 Flux diagram showing the sampling frequency of processes that integrate curvature in the ethylene flame. The solid arrows show processes that integrate curvature. The percentages show the relative sampling frequency of each process. The dashed arrows show processes that add carbon.

sites, which may migrate and desorb [348], bay sites containing partially embedded five-member rings do not allow such migration. Once a bay site containing partially embedded five-member ring appears, it is likely to close and embed the five-member ring.

Both bay closure (1(c) and 1(d), 8.4%) and HACA (1(a), 1.0%) processes simultaneously embed five-member rings by adding seven-member rings. In this case, the rate of the bay closure is considerably higher than the HACA processes. This is attributed to the inability of a partially embedded five-member ring to migrate from a bay, as above. The remainder of the seven-member ring additions occur via HACA (1(b), 3.6%), two thirds of the time followed by the embedding of a five-member ring (1(f), 2.3%).

5.4.3 Sensitivity analysis on novel process rates

A sensitivity analysis of the model response with respect to the rates of the processes that embed five-member and form seven-member rings was performed for the ethylene-oxygen counterflow diffusion flame. In the first instance, fourteen simulations with approximately 10,000 PAHs each were performed without changing any of the rate parameters. The results of these simulations were averaged to create a base case for the sensitivity analysis. The processes sampled in the base case were dominated by HACA events (77.9%), followed by desorption reactions (9.4%), internal rearrangements (6.8%), bay closures (5.7%) and phenyl additions (0.2%). Of these, only the processes that contribute to the formation of seven-member rings and processes that embed five-member rings were selected for investigation in the sensitivity analysis. These are processes 1(a)–1(f) shown in Figure 5.1 and correspond to processes S17, S21, S22, S23, S24 and S25 from Table 3.4.

The largest uncertainty in the process rates is assumed to be due to the uncertainty in the barrier height predicted by the DFT methods used to compute the elementary rate constants. It was assumed that this corresponds to an uncertainty of ± 2 kcal/mol in the activation energy [206]. However, assessing the sensitivity of the model by varying the activation energy in each elementary rate constant one at a time is prohibitively expensive. For this reason, only the reactions that most contribute to processes 1(a)–1(f) were included in the sensitivity analysis. These reactions are listed in Table 5.1. The activation energies for each process were simultaneously perturbed by ± 2 kcal/mol in order to effect an overall change in the jump process rate. In each case, the simultaneous decrease in the activation energies resulted in the jump process rate approximately doubling at the end point conditions of the flame simulation. Similarly, the simultaneous increase in the activation energy resulted in the jump process rate approximately halving at the same conditions.

Table 5.1 Reactions selected for sensitivity analysis. The full list of reactions is shown in Table 3.3. The activation energy was varied by ± 2 kcal/mol.

No.	Reactions	$k = AT^n \exp(-E_A/R_{gas}T)$ [a]		
		A	n	E_A
	Process 1(a)			
	Seven-member ring growth on a five-carbon bay site (partially embedded five-member ring)			
72	$C_sR_6-H + H \rightarrow C_sR_6{}^{\bullet} + H_2$	5.897×10^{07}	1.847	17.120
73	$C_sR_6{}^{\bullet} + C_2H_2 \rightarrow C_sR_6-C_2H_2$	1.348×10^{03}	2.573	4.935
83	$C_sR_6H-C_sR_6{}^{\bullet} \rightarrow C_sR_6-CsR_6 + H$	3.207×10^{10}	0.958	23.130
84	$C_sR_5-H + H \rightarrow C_sR_5{}^{\bullet} + H_2$	1.479×10^{07}	1.854	17.070
85	$C_sR_5{}^{\bullet} + C_2H_2 \rightarrow C_sR_5-C_2H_2$	1.098×10^{03}	2.581	7.651
87	$C_sR_5H-C_sR_6{}^{\bullet} \rightarrow C_sR_5-CsR_6 + H$	3.590×10^{11}	0.604	30.050
	Process 1(b)			
	Seven-member ring growth on a five-carbon bay site (edge five-member ring)			
80	$C_sR_6-H + H \rightarrow C_sR_6{}^{\bullet} + H_2$	6.586×10^{07}	1.766	14.770
81	$C_sR_6{}^{\bullet} + C_2H_2 \rightarrow C_sR_6-C_2H_2$	3.886×10^{03}	2.592	4.012
83	$C_sR_6H-C_sR_6{}^{\bullet} \rightarrow C_sR_6-CsR_6 + H$	3.207×10^{10}	0.958	23.130
84	$C_sR_5-H + H \rightarrow C_sR_5{}^{\bullet} + H_2$	1.479×10^{07}	1.854	17.070
85	$C_sR_5{}^{\bullet} + C_2H_2 \rightarrow C_sR_5-C_2H_2$	1.098×10^{03}	2.581	7.651
87	$C_sR_5H-C_sR_6{}^{\bullet} \rightarrow C_sR_5-CsR_6 + H$	3.590×10^{11}	0.604	30.050
	Process 1(c)			
	Seven-member bay closure (site 1)			
88	$C_sR_6-H + H \rightarrow C_sR_6{}^{\bullet} + H_2$	3.915×10^{07}	1.876	9.421
90	$C_sR_7-C_sR_7-H \rightarrow C_sR_7-C_sR_7 + H$	2.033×10^{10}	1.067	31.600
91	$C_sR_6-H + H \rightarrow C_sR_6{}^{\bullet} + H_2$	3.091×10^{07}	1.891	9.308
93	$C_sR_7-C_sR_7-H \rightarrow C_sR_7-C_sR_7 + H$	1.861×10^{10}	1.136	29.570
	Process 1(d)			
	Seven-member bay closure (site 2)			
103	$C_sR_6-H + H \rightarrow C_sR_6{}^{\bullet} + H_2$	2.767×10^{07}	1.913	9.542
105	$C_sR_7-C_sR_7-H \rightarrow C_sR_7-C_sR_7 + H$	6.424×10^{09}	1.093	32.16
106	$C_sR_6-H + H \rightarrow C_sR_6{}^{\bullet} + H_2$	2.843×10^{07}	1.906	9.533
108	$C_sR_7-C_sR_7-H \rightarrow C_sR_7-C_sR_7 + H$	2.006×10^{10}	1.099	32.81
	Process 1(e)			
	Six-member bay closure (partially embedded five-member ring)			
37	$C_sR_6-H + H \rightarrow C_sR_6{}^{\bullet} + H_2$	9.240×10^{07}	1.500	9.646
38	$C_sR_6{}^{\bullet} \rightarrow C_sR_6-R_6{}^{\bullet}$	1.110×10^{11}	0.658	23.990
	Process 1(f)			
	Six-member ring growth on a partially embedded five-member ring armchair			
65	$C_sR_6-H + H \rightarrow C_sR_6{}^{\bullet} + H_2$	2.540×10^{11}	0.931	16.440
66	$C_sR_6{}^{\bullet} + C_2H_2 \rightarrow C_sR_6-C_2H_2$	1.630×10^{12}	0.409	5.675
69	$C_sR_6H_2-CsR_6H^{\bullet} \rightarrow C_sR_6-CsR_6 + H$	3.160×10^{12}	0.787	36.510
71	$C_sR_6H-CsR_6 \rightarrow C_sR_6-CsR_6 + H$	8.150×10^{11}	0.563	24.860

[a] *The units are mole, centimetre, second, and kilocalorie.*

Seven repeat simulations with approximately 10,000 PAHs were used for each of the positive and negative activation energy perturbations (so fourteen simulations in total) for each jump process. Normalised sensitivity coefficients were calculated and averaged across the set of repeat simulations

$$S_{ki} = \frac{x_i}{y_k} \frac{\partial y_k}{\partial x_i}, \tag{5.1}$$

where y_k is the kth model response and x_i is the ith model parameter. In this case, the model responses were the number of carbon atoms, number of hydrogen atoms, and number of five-, six-, and seven-member rings, and the model parameters were the jump process rates.

Figure 5.6 shows the normalised sensitivity coefficients for the average number of carbon and hydrogen atoms and the number of five-, six-, and seven-member rings. In general, both the ± 2 kcal/mol perturbations result in sensitivity coefficients with the same sign and similar magnitude. Figures 5.6(a)–(d) show that the number of carbon atoms, hydrogen atoms, six-member rings and edge five-member rings are insensitive to the processes included in the sensitivity analysis. These are primarily controlled by HACA additions on a free edge or a zig-zag site. Figure 5.6(e) shows that the number of seven-member rings has positive sensitivity coefficients with respect to the processes that form this kind of ring and negative sensitivity coefficients with respect to processes that embed five-member rings. As discussed in Section 5.4.2, this behaviour is due to the fact that these processes compete for similar reactive sites. Figure 5.6(f) shows that the number of embedded five-member rings shows positive sensitivity coefficients with respect to the processes analysed in this work; higher sensitivity was observed with respect to the processes that directly embed a five-member ring without forming a seven-member ring. The sensitivity analysis shows that the processes that embed five-member and form seven-member rings have a significant effect on the morphology (*i.e.* the relative abundance of five-, six- and seven-member rings), but not the mass of the soot particles. For this reason, the locations and relative heights of the computed mass spectra are relatively insensitive to these processes.

(a) Carbon atoms

(b) Hydrogen atoms

(c) Six-member rings

(d) Edge five-member rings

(e) Seven-member rings

(f) Embedded five-member rings
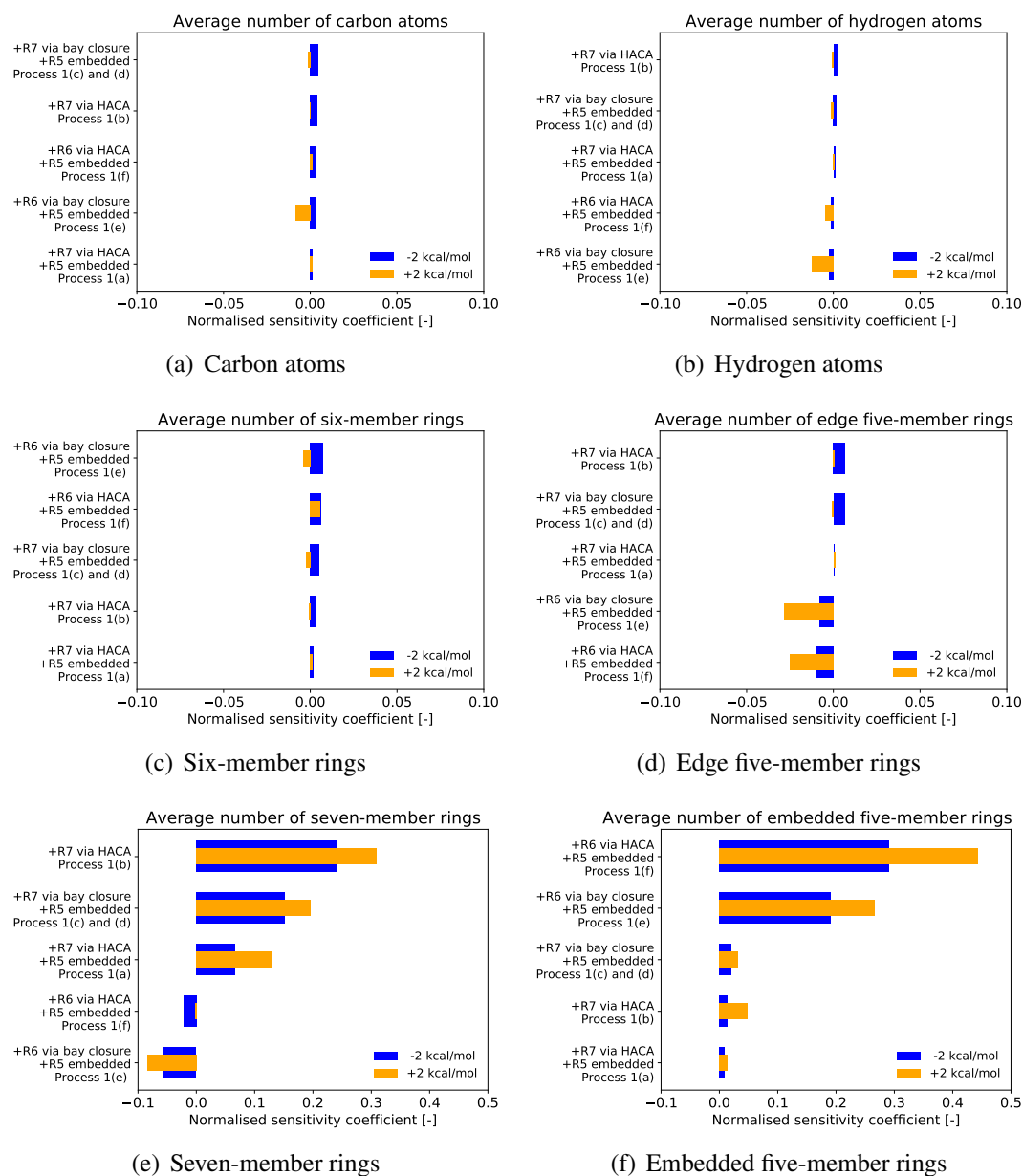
Fig. 5.6 Normalised sensitivity coefficients for the average number of rings and atoms in the simulated PAHs. Data for both a ± 2 kcal/mol change in activation energy are shown. Processes 1(a) to (f) are shown in Figure 5.1.

5.4.4   Assessing PAH curvature

The probabilistic model by Yapp et al. [358] estimated the Gauss curvature as a function of the number of embedded five-member rings and six-member rings in a PAH. However, the presence of coupled five- and seven-member rings that share a common bond result in a molecule that is nearly flat [248], violating the assumptions made in the probabilistic model.

The introduction of processes that integrate coupled five- and seven-member rings in this work allows us to assess the proportion of PAHs for which this occurs.

To assess this, Figure 5.7 shows the distributions of the number of PAHs containing different numbers rings at the end of the simulation domain in the ethylene flame. Most of the small PAHs are completely flat. This is expected because a minimum number of five six-member rings is needed to embed a five-member ring. The maximum proportion of PAHs with one embedded five-member ring occurs in PAHs with around 15 six-member rings. This maximum is accompanied by a significant growth in the proportion of PAHs with a second embedded five-member ring. This delayed increase in the number of PAHs that contain a second embedded five-member ring is due to the isolated pentagon rule [162]: adjacent five-member rings are not allowed. This reduces the degrees of freedom when trying to embed a second five-member ring. The maximum proportion of PAHs with seven-member rings occurs in PAHs with around 20 six-member rings. The reduction in the proportion of PAHs containing ether five- or seven-member rings in large PAHs follows the overall trend in the total number of PAHs.

Overlaid on Figure 5.7(b) is a scatter plot of the proportion of PAHs with at least one embedded five-member ring that also contain a seven-member ring, $\phi_{7|5}$. These PAHs violate the assumptions in the probabilistic model by Yapp et al. [358]. The data become noisy as the number of five-member rings in large species (containing more than 35 six-member rings) decreases. It is observed that the larger a PAH containing an embedded five-member ring, the more likely it is to include a seven-member ring.

The same trend is observed in the proportion of PAHs with at least one seven-member ring that also contain at least one embedded five-member ring, $\phi_{5|7}$ shown in Figure 5.7(c). The larger a PAH containing a seven-member ring, the more likely it is to include a embedded five-member ring. It is also observed that a proportion of PAHs that contain seven-member rings contain no embedded five-member rings. These result from the HACA growth of seven-member rings on partially embedded five-member rings (Figure 5.5, Process 1(b), 3.6%). These five-member rings are eventually embedded as PAHs grows, until all PAHs that contain seven-member rings also contain embedded five-member rings in PAHs with more than 30 six-member rings.
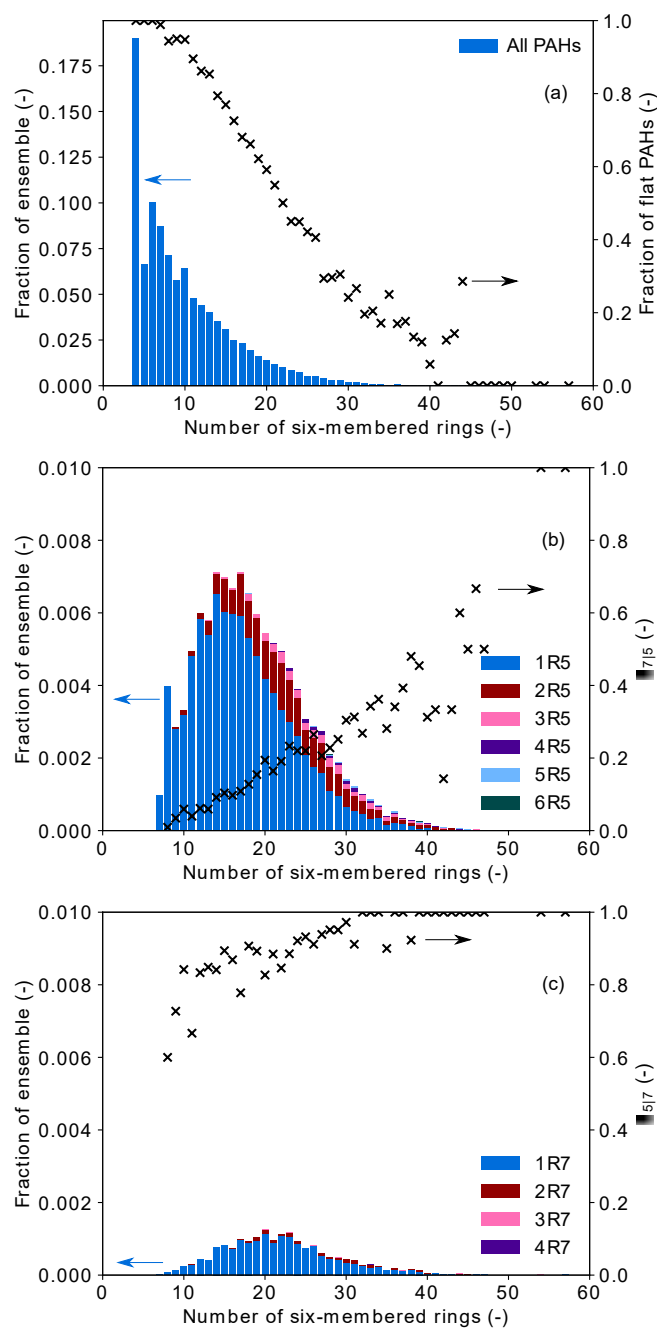
Fig. 5.7 Histograms showing the distributions of the number of five- and seven-member rings as a function of the number of six-member rings in PAHs in the ethylene flame. The proportion of PAHs with a j-member ring that also contain an i-member ring is denoted $\phi_{i|j}$. nR5 denotes PAHs containing exactly n embedded five-member rings; nR7 denotes exactly n seven-member rings (embedded or otherwise). DFFO = 6.17 mm.

5.5   Conclusions

A KMC model that, for the first time, includes processes to integrate curvature due to the formation of coupled five- and seven-member rings has been used to simulate PAHs growing in ethylene and acetylene counterflow diffusion flames. The simulation results reproduce the major peaks and relative abundances of experimental mass spectra. Including more processes and a more intimate coupling with the gas-phase would allow the simulation of peaks that are currently missing from the simulated spectra.

The addition of five- and seven-member rings occurs via competitive HACA and bay closure processes. It was observed that approximately 85% of the events that integrate curvature correspond to the embedding of five-member rings via the formation of six-member rings, with HACA and bay closures occurring in similar proportions. The remaining 15% correspond to the formation of seven-member rings coupled to five-member rings, with bay closures occurring approximately twice as often as HACA.

The proportion of PAHs at the end of the simulation domain containing embedded five-member rings and/or seven-member rings is observed to pass through a maximum for PAHs containing $\sim$20 six-member rings. The proportion that contains both five- and seven-member rings increases with PAH size. The assumption that the PAHs contain only five and six-member rings made in the probabilistic model introduced by Yapp et al. [358] is increasingly violated as the PAHs increase in size.

The development of a KMC model that includes processes to describe the formation of five- and seven-member rings by HACA and bay closure processes provides a starting point for future work to model the cross-linking of PAHs. Cross-linking has been suggested to be important for soot formation [121], including specific suggestions about the role of aryl-crosslinks [127], rim-based five-member rings [53], resonantly stabilised radicals [139] and localised π-radicals [192]. Such cross-linking is expected to create bay sites that require the growth processes implemented in this work.

Research data

The source code for the KMC model [46] used in this chapter is available on GitHub (https://github.com/ucam-ceb-como/MOpS) under an open source licence. Animations of three representative structures are available to download from the University of Cambridge data repository (doi:10.17863/CAM.51755).

Chapter 6

The role of oxygenated species in the growth of graphene, fullerenes and carbonaceous particles

In this chapter, the growth of carbonaceous materials was studied using a Kinetic Monte Carlo model that captures the growth and oxidation of six-member and partially-embedded five-member rings. A novel algorithm was used to resolve the migration of partially-embedded five-member rings around the edges of molecules. Circumcoronene molecules were grown at 1500 K and 1 atm in the presence of varying mole fractions of atomic and molecular oxygen and constant mole fractions of hydrogen and acetylene. Four regions of carbon growth associated with different carbonaceous products were identified. Graphene was formed in the presence of high mole fractions of atomic oxygen $\left(10^{-4} < X_O \leq 10^{-2}\right)$. Fullerenes were formed in the presence of low mole fractions of atomic oxygen and high mole fractions of molecular oxygen $\left(X_O \leq 10^{-4} \text{ and } 10^{-2} < X_{O_2} \leq 10^{-1}\right)$. Low mole fractions of both atomic and molecular oxygen $\left(X_O \leq 10^{-4} \text{ and } X_{O_2} \leq 10^{-2}\right)$ resulted in structures that became curved as time progressed. The highest mole fractions of atomic oxygen $\left(X_O > 10^{-2}\right)$ produced small structures. The production and consumption of partially-embedded five-member rings appear to explain the formation of the observed structures. The oxidation of partially-embedded five-member rings produces sites that grow into graphenic structures. Formation and subsequent embedding of partially-embedded five-member rings result in curved structures that resemble fullerenes. This work shows that different oxidising conditions result in the evolution of different carbonaceous materials.

Collaborative Contributions

The work presented in this chapter has been submitted for publication in *Carbon* and is primarily the work of the author. Jacob W. Martin, Eric J. Bringley and Jethro Akroyd helped define the scope of the work and editing the manuscript. The model implementation, stochastic simulations, figure preparation and manuscript writing were done by the author.

6.1   Introduction

Carbonaceous particles, fullerenes and graphene can be produced simultaneously under different conditions. Carbonaceous particles are primarily formed from polycyclic aromatic hydrocarbons (PAHs) produced in oxygen deficient environments such as flames or pyrolysis reactors. There is strong evidence that the interaction of two PAHs leads to the inception of carbonaceous particles, but the identity of these PAHs, and the nature of their interactions, remain elusive [335]. Fullerenes can be produced alongside carbonaceous particles in arc discharge reactors [40]. Fullerenes can also be produced in regions of high temperature [121] and in the presence of oxidising species [130, 118] in low pressure benzene [121] and acetylene [344] flames. Fullerenes are thought to share common intermediates with carbonaceous particles that, instead of gaining mass, embedded five-member rings until the structure becomes fully curved [121]. Graphene can also be produced alongside carbonaceous particles in the gas phase of plasma reactors among other methods [238]. In one setup, ethanol and argon are used in a microwave plasma reactor [57, 56, 55, 314, 315, 225, 13] in which the presence of oxygen in the precursor was found to be necessary [56]. In another setup, mixtures of methane, hydrogen and argon have been used to produce graphene in a microwave plasma [292, 24] or an arc-discharge plasma at different pressures [334]. In non-plasma conditions, large molecules that resemble graphene have been detected alongside carbonaceous particles in low pressure acetylene flames [344].

Partially-embedded five-member rings play an important role in the growth and oxidation of graphene, fullerenes and carbonaceous particles. Frenklach and collaborators suggested that these rings participate in the growth of graphene sheets by creating additional sites [348] and showed that these rings are able to migrate around the edge of the molecule [351]. These rings can be produced and consumed by oxygenated species [294, 85], become fully-embedded forming curved polycyclic aromatic hydrocarbons (cPAHs) [359, 358] or be consumed by neighbouring seven-member rings [206, 154]. Recently, partially-embedded five-member rings have been studied for their ability to form localised π-radicals [193]. These

radicals have been suggested to form stable bonds with other PAHs and may participate in the formation of crosslinked carbonaceous materials [193, 240, 207, 208].

The interactions between carbonaceous materials and oxygenated species have been extensively studied. Early works [332, 72, 232] showed that the oxidation of carbonaceous materials appears to be dominated by molecular oxygen (O_2), hydroxyl radical (OH) and atomic oxygen (O). The first two of these species are associated with the oxidation of six-member rings [294, 293] and appear to dominate the oxidation of carbonaceous particles [103, 91, 230, 228, 231]. Atomic oxygen has been suggested to contribute to the oxidation of resonantly stabilised radicals [85] as well as producing epoxy and ether groups on the basal planes of PAHs [168]. Those oxygenated groups possibly explain the different oxidation rates observed in recent oxidation experiments [228]. The interactions between oxygenated species and different carbonaceous materials have been studied mostly in combustion experiments. However, few studies have focused on conditions that favour the production of materials like graphene or fullerenes. A systematic study on the combined effect of surface growth in the presence of different oxygenated species is still missing.

The **purpose of this chapter** is to investigate the effect of the oxygenated species on the formation of carbonaceous particles, fullerenes and graphene. A detailed KMC model is used to simulate the oxidation and growth of molecules in the presence of constant mole fractions of hydrogen and acetylene, and varying mole fractions of atomic and molecular oxygen. Two improvements are made to the model. First, the model is expanded to include the oxidation of partially-embedded five-member rings and six-member rings with rates calculated using a steady-state approximation. Second, a new numerical algorithm is introduced for the efficient simulation of the migration of partially-embedded five-member rings whilst retaining accurate growth and oxidation rates.

6.2   Methodology

6.2.1   Kinetic Monte Carlo model

Kinetic Monte Carlo models are useful to study the growth and oxidation of carbonaceous materials because they keep track of the sites that determine the reactivity of the molecules. These sites are allowed to react based on a set of reaction rules that are assumed to be a function of the site type. This gives these models the ability explore the transformation of different structures beyond typical gas phase chemical kinetic mechanisms.

In this chapter, the detailed particle model discussed in Chapter 3 is used to track the evolution of molecules in different chemical environments. In this chapter the model

new processes were added for the oxidation of partially-embedded five-member rings and six-member rings using published rates from the literature [85, 293, 65]. The numerical performance of the model was also improved by including a new algorithm to describe the migration of partially-embedded five-member rings more efficiently (see Section 3.7.5). The algorithm was developed to be exact (*i.e.* it has no effect on the results calculated by the model), yet reduced computational times by more than an order of magnitude for all simulated cases. A complete description of the individual reactions, the process rates and the new migration algorithm is given in Chapter 3.

6.2.2   Parameter space

Most detailed models have focused on the growth and oxidation of carbonaceous materials in isolated conditions [294, 293, 85]. The few studies that have considered the competition between growth and oxidation have done so in the context of combustion [339, 340, 274, 69]. A systematic parameter sweep to investigate the competition between growth and oxidation is still missing in the literature. To begin to address this gap, the chemical conditions selected in this work have been chosen to consider a constant potential for the growth of carbonaceous materials while varying the potential for both the oxidation of six-member rings and partially-embedded five-member rings.

The oxidation of six-member rings is dominated by two species: molecular oxygen and hydroxyl radicals. However, hydroxyl radicals participate in hydrogen abstraction reactions [229, 7, 29] that promote surface growth. Molecular oxygen has a high energy barrier for the same reaction making its contribution to growth processes negligible [85]. For this reason, molecular oxygen was selected for this study. Atomic oxygen was selected as a second oxidising species because it is known to attack partially-embedded five-member rings [85].

It is desired to study conditions that are relevant to a wide range of experimental scenarios including fuel-rich flames, plasma and pyrolysis reactors. The parameter space therefore spans several orders of magnitude. The conditions used in the study are as follows: The mole fractions of species that contribute to growth were held constant at $X_\text{H} = 0.01$ and $X_{\text{H}_2} = X_{\text{C}_2\text{H}_2} = 0.1$. These conditions have been widely used to study typical growth environments [348, 206, 255]. Likewise, temperature and pressure were held constant at 1500 K and 1 atm and the simulation time held constant at 5 ms, consistent with previous studies [348, 293, 255, 206]. The mole fractions of atomic and molecular oxygen were varied in log-scaled intervals covering the ranges $10^{-8} \leq X_\text{O} \leq 10^{-1}$ and $10^{-6} \leq X_{\text{O}_2} \leq 10^{-1}$. The balance of the reaction mixture was argon.

The KMC model was used to simulate the oxidation and growth of an ensemble of 300 circumcoronene ($C_{54}H_{18}$ and 19 six-member rings) molecules at each condition. The interactions between multiple molecules was not considered.

6.3 Results and discussion

6.3.1 Regions of carbon growth

The growth of the molecules resulted in different morphologies in the different chemical environments sampled by the parameter space. However, small variations in the mole fractions of molecular and atomic oxygen resulted in similar structures. The parameter space could then be divides in four regions of carbon growth, where each region is associated with the observation of different carbonaceous structures: (1) large cPAHs, (2) small cPAHs, (3) large flat molecules, and (4) small molecules.

Figure 6.1 shows the average number of carbons observed in each molecule at the end of each simulation. The edges of the four regions of carbon growth are indicated with dashed lines. Experimental data for flames that produce carbonaceous particles [69, 231], fullerenes [197] and large flat molecules that resemble graphene [346] are shown (and are joined by continuous lines to guide the eye). Symbols are only shown for conditions that had sufficient hydrogen and acetylene to sustain the growth of carbonaceous structures. The geometry of representative molecules sampled from each region are also shown. The geometry of the full set of molecules is available in the Research Data associated with this work.

Region 1 (bottom left of Figure 6.1) encompasses the lowest mole fractions of atomic and molecular oxygen, $10^{-8} \leq X_O \leq 10^{-4}$ and $10^{-6} \leq X_{O_2} \leq 10^{-2}$. The molecules in Region 1 contained an average of 300 carbon atoms. The molecules were mostly flat at early times, but became curved as simulations progressed. This can be seen in the representative structures in Figure 6.1. Although the observed structures were large cPAHs, the main product in Region 1 will be carbonaceous particles. There is strong evidence that carbonaceous particles are formed by the interaction of two intermediate (and unknown) PAHs [335]. These interactions were not part of the scope of this study and the possibility to form carbonaceous particles was not included in the current model. However, the molecules in this region spend significant time in the reaction environment before becoming curved. During this time the molecules could form carbonaceous particles. Most premixed sooting flames lie in Region 1. The maximum concentrations of molecular and atomic oxygen appear on the upstream side of the flame front, whilst the maximum concentrations of hydrogen and acetylene appear within the
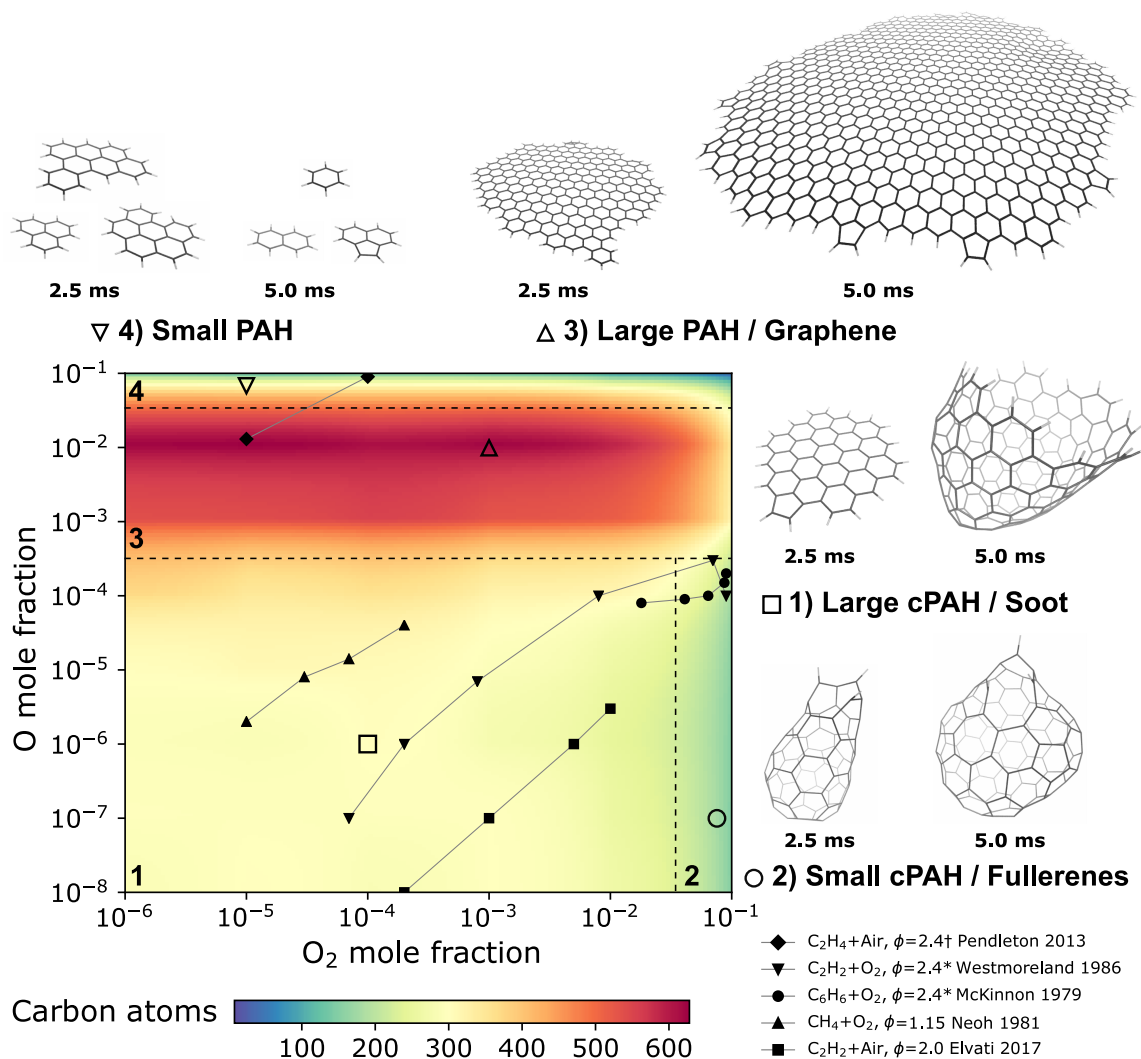
Fig. 6.1 Average number of carbons in each molecule versus mole fraction of atomic and molecular oxygen. Four regions of carbon growth (1 to 4) are indicated with dashed lines. Representative structures sampled from each region, at conditions indicated with open symbols, are shown. Experiments for which it is possible to estimate the mole fractions of atomic and molecular and oxygen are also shown. These correspond to: ($\blacklozenge$) plasma ignition experiment [246], ($\blacktriangledown$) acetylene/oxygen low pressure flame [346], ($\bullet$) benzene/oxygen low pressure flame [197], ($\blacktriangle$) methane/oxygen flame [232] and ($\blacksquare$) ethylene/air sooting flame [69]. Plasma ignition experiment is indicated with a dagger (†). Low pressure conditions (2.7kPa) are indicated with an asterisk (*).

flame. This is represented as a movement towards the bottom left of Figure 6.1. Two example flames in Figure 6.1 are fully contained in Region 1: a sooting acetylene/air flame [273, 69] and the methane/oxygen experiments by Neoh [231]. The latter is included to highlight that oxidation by hydroxyl radicals becomes significant in flames with low mole fractions

of molecular oxygen $\left(X_{O_2} < 10^{-5}\right)$. Two other experiments are partially contained in this region and will be discussed below.

Region 2 (bottom right of Figure 6.1) encompasses low mole fractions of atomic oxygen and high mole fractions of molecular oxygen, $10^{-8} \leq X_O \leq 10^{-4}$ and $10^{-2} < X_{O_2} \leq 10^{-1}$. The molecules in Region 2 contained an average of 150 carbon atoms. The structures in this region were highly curved and smaller than those in Region 1. Most of the structures became curved at short times. This can be seen in the representative structures in Figure 6.1. The structures in this region resembled open caged fulleroids. Closed caged structures could not be produced in the simulations because no process to close the molecular structure was included in the current model. The interpretation of these observations is that the main product in Region 2 will be fullerenes as the closure is widely thought to be energetically favoured [121]. These observations are consistent with the experimental evidence presented in Figure 6.1, where both carbonaceous particles and fullerenes have been reported in the low pressure acetylene/oxygen [121, 344] and benzene/oxygen flames [130, 128, 129] that straddle Region 1 and Region 2.

Region 3 (middle of Figure 6.1) encompasses high mole fractions of atomic oxygen and spans the full range of mole fractions of molecular oxygen in Figure 6.1, $10^{-4} < X_O \leq 10^{-2}$ and $10^{-6} \leq X_{O_2} \leq 10^{-1}$. Region 3 is characterised by the highest average number of carbons per molecule: the molecules in Region 3 contained an average of 500 carbon atoms at $X_O = 10^{-3}$ and 600 carbon atoms at $X_O = 10^{-2}$. At high values of molecular oxygen $\left(X_{O_2} > 10^{-2}\right)$ the molecules in Region 3 showed a lower number of carbons (approximately 300) per molecule due to oxidation. The structures in Region 3 were significantly larger than in the other regions. Most of the molecules were flat throughout the simulation. This can be seen in the representative structures in Figure 6.1. The largest molecules were sampled at the higher mole fractions of atomic oxygen $\left(X_O = 10^{-2}\right)$. To the author's knowledge this is the first time that such large structures have been obtained in a model that allows for the inclusion of curvature as a result of competing oxidation and surface growth. The preferred structure in this region is graphene. The high mole fractions of atomic oxygen that characterise this region make the synthesis of graphene in typical flame conditions unlikely. The only flame that appears to be close to this region is the low pressure acetylene/oxygen flame [344, 346] that reported the presence of large flat molecules in these conditions. However, this observation makes an argument for the production of graphene in other environments. Plasma experiments [*e.g.* 312, 313, 225, 55, 56] are known to form large numbers of oxygen radicals and ions that could perhaps explain the production of graphene. One of the challenges for these processes is to improve the prediction and detection of species formed in the plasma to explain the production of new materials.

Lastly, Region 4 (top of Figure 6.1) encompasses the highest mole fractions of atomic oxygen and spans the full range of mole fractions of molecular oxygen in Figure 6.1, $X_O > 10^{-2}$ and $10^{-6} \leq X_{O_2} \leq 10^{-1}$. This region was characterised by a reduction in size of the molecules, despite the presence of hydrogen and acetylene. The molecules in Region 4 were flat and decreased in size during the simulations. This can be seen in the representative structures in Figure 6.1.

Two opposite effects are clearly seen on the structures shown in Figure 6.1. Molecular oxygen contributes to the integration of curvature while atomic oxygen inhibits it. The mechanism by which these two species lead to one process or the other appears to be related to the production and consumption of partially-embedded five-member rings and is discussed in the following sections.

6.3.2   Size distributions

The consideration of the average number of carbons per molecule allowed a straightforward comparison between the different regions of carbon growth. However, to have a more complete picture of the predicted structures, it is necessary to analyse the evolution of the size distribution of the sampled species as a function of the chemical conditions.

Figure 6.2 shows the molecular mass distributions of the sampled molecules halfway through (2.5 ms) and at the end (5.0 ms) of each simulation. Kernel density estimates (calculated using Seaborn with a Gaussian kernel and optimal bandwidth [343]) were used to estimate the continuous distribution functions shown in Figure 6.2 from the masses of the molecules sampled by the KMC simulations.

The mass distributions sampled in Region 1 at 2.5 ms were centred around 2,000 a.m.u. with maximum values of approximately 4,000 a.m.u. By 5.0 ms the distributions were centred around 5,500 a.m.u. and presented a tail that extended up to 10,000 a.m.u. The molecules in these tails did not show any particular morphological difference in their structure other than being larger than the other molecules sampled in Region 1. They had a similar number of embedded five-member rings and similarly few hydrogen atoms.

Region 2 showed very similar mass distributions at both simulation times. The distributions were centred at 2,000 a.m.u. with a range extending from 1,000 to 3,000 a.m.u. The similarity of the mass distributions is an indication that the growth of these molecules is not significant after 2.5 ms. This effect can be explained by the decrease in the number of sites available for growth as the structure becomes highly curved.

The mass distributions sampled in Region 3 increased in width during the simulations. At 2.5 ms the distributions were centred around 2,000 a.m.u. with a range extending to approximately 4,000 a.m.u. However, at 5.0 ms the distributions showed ranges extending
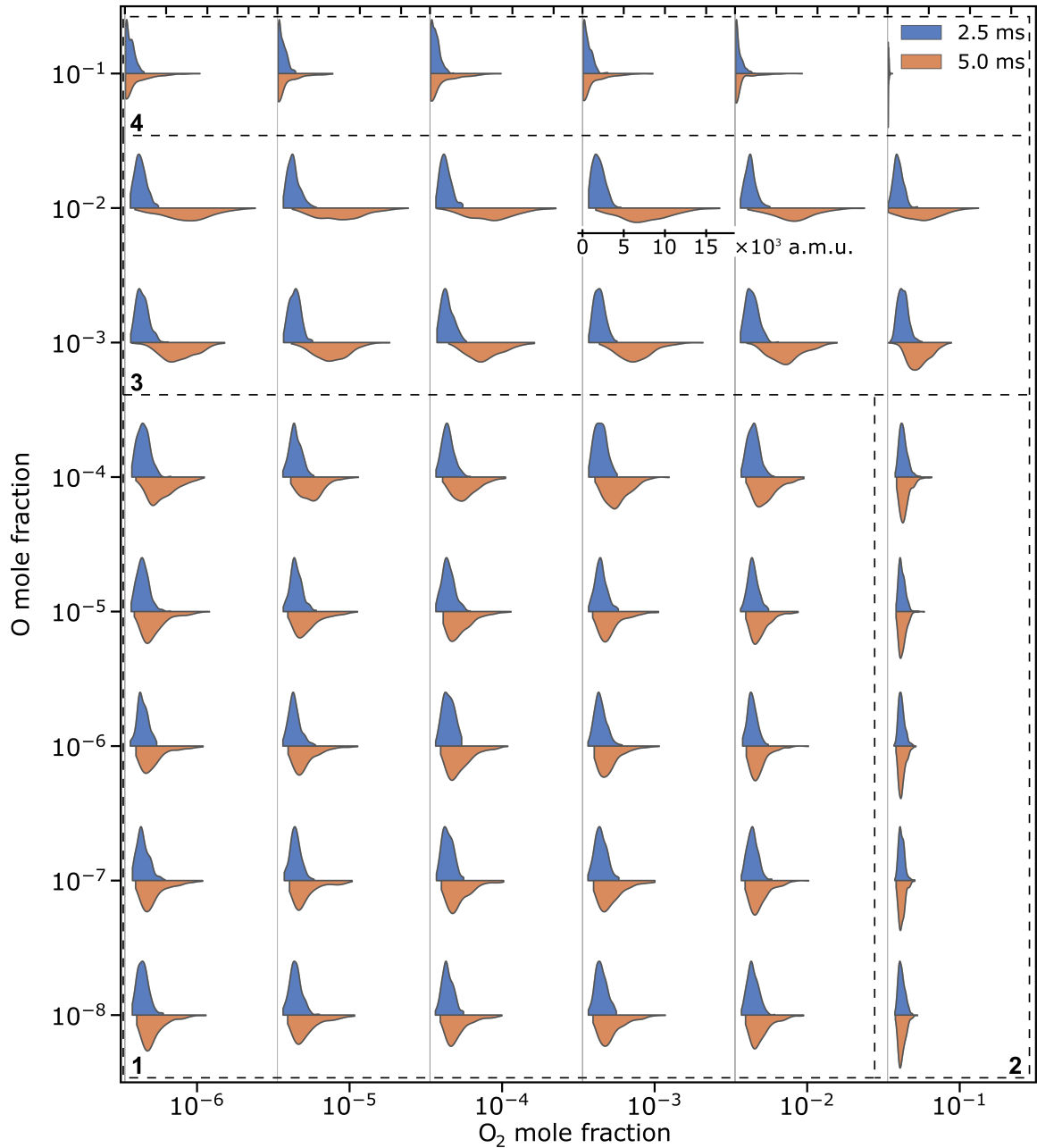
Fig. 6.2 Molecular mass distribution of molecules versus mole fraction of atomic and molecular oxygen. Simulation times of 2.5 and 5.0 ms are shown in blue and orange. Four regions of carbon growth (1 to 4) are indicated with dashed lines.

to 13,000 a.m.u. at $X_O = 10^{-3}$ and extending to more than 16,000 a.m.u. at $X_O = 10^{-2}$. The only exception to these large distributions appeared at $X_{O_2} = 10^{-1}$, $X_O = 10^{-3}$, where the distribution showed a maximum value of 6,000 a.m.u. The large maximum values are indicative of the growth of large structures. These large structures were observed to be flat or

slightly curved. Region 4 showed distributions centred at masses of less than 1,000 a.m.u. but with long tails composed of a few large molecules up to 7,000 a.m.u. in size appearing between 2.5 ms and 5.0 ms. The molecules in the tails of the distribution were smaller than, but otherwise similar to those observed in Region 3 at 5.0 ms.

The residence time has different effects on the mass distribution of the molecules in each region. This can be seen by comparing the distributions of Regions 1 and 3 in Figure 6.2. At 2.5 ms the mass distributions in each region are similar. However, the mass distributions are significantly different at 5.0 ms, with Region 3 showing significantly larger molecules. The integration of curvature appears to be crucial in controlling the surface growth of carbonaceous structures. This can be observed in the mass distributions in Region 2, which did not change after 2.5 ms.

6.3.3   Inclusion of curvature

The curvature of carbonaceous nanostructures is caused by the presence of fully-embedded five-member [348] rings and seven-member [317] rings. In the extreme case, the presence of embedded five-member rings can lead to the formation of closed caged fullerenes. In the absence of embedded five-member and seven-member rings, the molecules take the form of large sheets of six-member rings that resemble graphene.

Figure 6.3 shows the average number of fully-embedded five-member rings per molecule at 2.5 ms and 5.0 ms. The figure shows that, except at the highest mole fractions of atomic oxygen in Region 4, five-member rings are embedded in the molecules during the simulations.
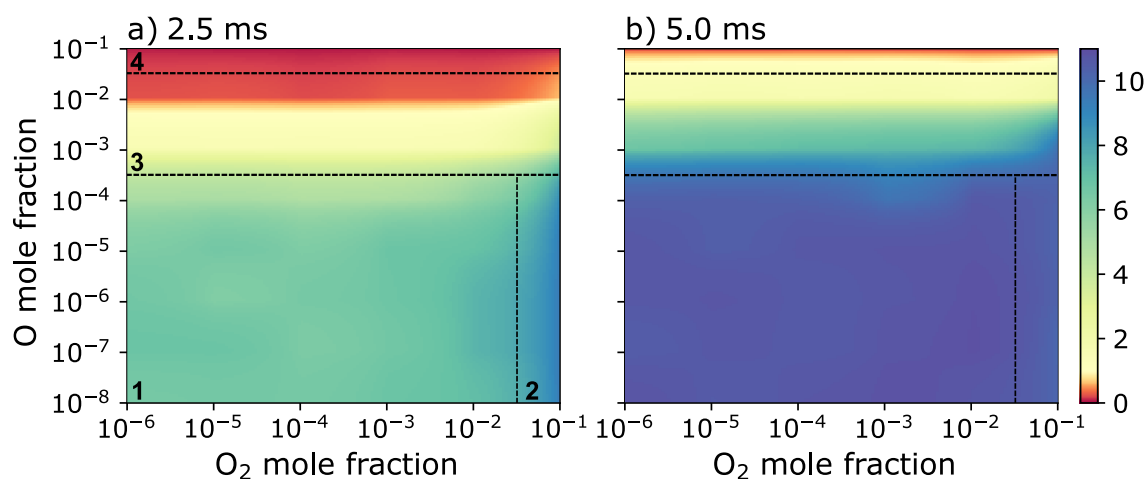
Fig. 6.3 Average number of fully-embedded five-member rings per molecule at (a) 2.5 ms and (b) 5.0 ms.

The molecules from Region 1 showed an average of 6 and 11 fully-embedded five-member rings at 2.5 ms and 5.0 ms, respectively. In this region the molecules became increasingly curved during the simulations. At low concentrations of oxygenated species, the molecules steadily embed five-member rings and gain curvature. This has also been observed in the counterflow diffusion flames discussed in Chapter 4.

At 2.5 ms, Region 2 already shows structures that contain an average of 11 embedded five-member rings per molecule, where the first molecule to reach this value was observed after only 1.1 ms. At 5.0 ms, every part of the region has an average of 11 embedded five-member rings. Molecular oxygen in the presence of favourable conditions for surface growth (hydrogen and acetylene) provides an additional pathway for the inclusion of five-member rings. This agrees with the observations of fullerenes sampled from diffusion flames [118] where it was suggested that the presence of molecular oxygen enhances the formation of curved structures.

Region 3 shows a trend similar to that in Regions 1 and 2, but with much slower inclusion of embedded five-member rings. At 2.5 ms the molecules presented an average of only 1 and 0 embedded five-member rings at $X_O = 10^{-3}$ and $X_O = 10^{-2}$ respectively. By 5.0 ms the number of embedded rings had reached 6 and 2 for the same conditions. It appears that for carbonaceous structures subject to HACA growth, the probability of embedding a partially-embedded five-member ring, and thus including curvature, increases with residence time.

The majority of the molecules in Region 4 did not appear to embed curvature at any time. The small structures that characterise this region were not large enough to fully-embed a five-member ring before being oxidised. However, a set of conditions where the molecules kept growing without at least some molecules including curvature after some time was not found in this study. This observation, although not surprising, has profound implications for the production of defect free graphene.

6.3.4   Mechanism for the formation of carbonaceous materials

Partially-embedded five-member rings play a crucial role in the formation of the different carbon structures discussed in this work. Figure 6.4 shows processes that produce, transform and consume partially-embedded five-member rings. Under different conditions these processes can explain the formation of graphene, fullerenes and carbonaceous particles. The production of these rings can happen via three processes shown in the top row of the figure: (i) bay closure, (ii) HACA growth neighbouring five-member rings occupying edge positions and (iii) the oxidation of free-edge six-member rings by molecular oxygen. These processes form two different types of partially-embedded five-member rings (second row of Figure 6.4),
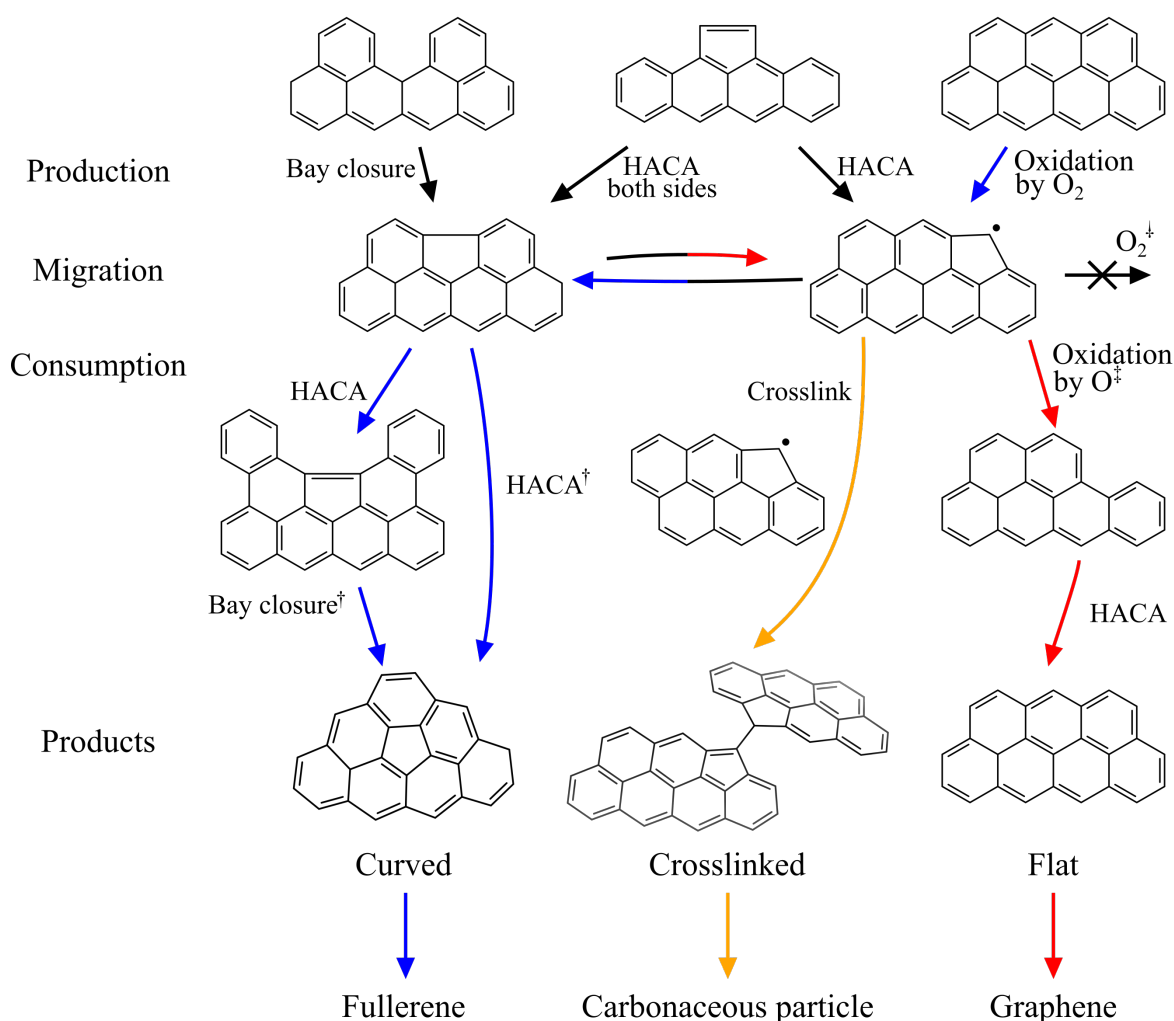
Fig. 6.4 Proposed mechanism of the formation of carbonaceous particles, fullerenes and graphene from partially-embedded five-member rings. Black arrows show processes that are present in all conditions. Blue arrows show processes that favour the production of fullerenes. Red arrows show processes that favour the production of graphene. Orange arrows show the crosslinking of partially-embedded five-member rings. Crosslinking was not studied in this work but has been suggested by other studies [193, 139].

where the partially-embedded five-member ring can occupy either an edge position (left) or a corner position (right). Once formed, these structures can interconvert via ring migration processes. Previous studies have shown that the edge position is kinetically favoured [351].

The third row of Figure 6.4 shows the processes that consume partially-embedded five-member rings. The bay closure and HACA processes (marked with a dagger, †) contribute to the inclusion of curvature via bay-capping of partially-embedded five-member rings occupying edge positions [348, 359, 255]. Oxidation by atomic oxygen (marked with a

double dagger, ‡) and the recombination of partially-embedded five-member rings next to seven-member rings (not shown) remove partially-embedded five-member rings occupying corner positions without introducing curvature. A fifth process (crosslinking, orange) is discussed later. The recombination of partially-embedded five-member rings next to seven-member rings (shown in the Chapter 3, Table 3.4, process S27) appeared to be unimportant due to the infrequent sampling of the processes (corresponding to less than 2% of the processes that removed partially-embedded five-member rings at any given point in the parameter space). The oxidation of partially-embedded five-member rings occupying corner positions by molecular oxygen is not favoured [85] (marked with a turned dagger ⸸), whereas oxidation by atomic oxygen (‡) leaves behind an armchair site that can undergo subsequent HACA growth as shown in Figure 6.4.

In KMC models, the number of times each process is sampled is proportional to the rate of that process. In this work, the contribution of the chemical environment to growth processes was held constant by maintaining fixed values of the C_2H_2, H and H_2 mole fractions, temperature and pressure, while the contribution to oxidation processes varied as a function of location in the $O-O_2$ parameter space. Figure 6.5 shows the number of sampled processes that produce (top row of Figure 6.4) and consume (third row of Figure 6.4) partially-embedded five-member rings across the $O-O_2$ parameter space. The bars have been divided to show the contribution of each process. The number of sampled processes for six-member ring growth are also shown.

The different regions of the parameter space show different behaviours. In Region 1 the formation of partially-embedded five-member rings was dominated by HACA (blue) and bay closure (green) processes. This region also showed an increase in the production of partially-embedded five-member rings via oxidation (red) of six-member rings as the mole fraction of molecular oxygen increased. The consumption of partially-embedded five-member rings in this region was dominated by HACA (blue) and bay closure (green) processes that result in curved structures. The number of six-member ring growth processes (orange) sampled in this region was the second highest, exceeded only by Region 3.

Region 2 showed increased production of partially-embedded five-member rings due to oxidation (red) by molecular oxygen. The consumption of these rings was mainly driven by HACA (blue) and bay closure (green) processes forming fully-embedded five-member rings. This increased production of partially-embedded five-member rings is consistent with previous work [293]. The low number of six-member ring growth processes (orange) sampled in this region is a consequence of the rapid embedding of curvature and the consequent reduction in the number of sites available for further HACA growth.
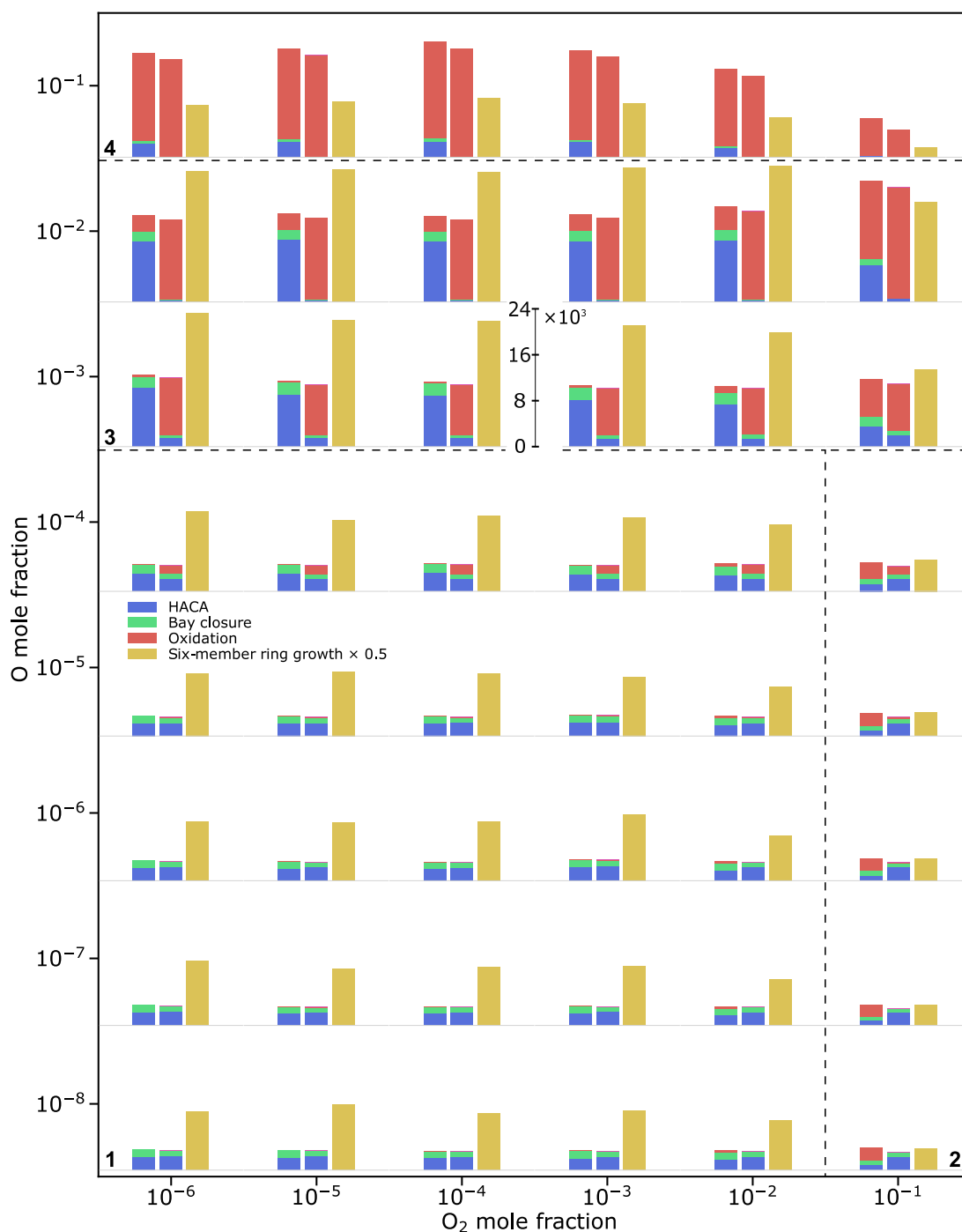
Fig. 6.5 Number of sampled processes that produce or consume partially-embedded five-member rings in each simulation of 300 molecules. The first bar in each plot shows processes that produce partially-embedded five-member rings. The second bar shows processes that consume partially-embedded five-member rings. The bars are divided to show the contributions by HACA (blue), bay closure (green) and oxidation (red). The third bar shows processes that produce six-member rings (orange). Four regions of carbon growth (1 to 4) are indicated with dashed lines.

In Region 3, partially-embedded five-member rings were produced by HACA (blue), bay closure (green) and six-member ring oxidation (red) processes. The number of sampled oxidation processes increased as the mole fraction of molecular oxygen increased. The consumption of partially-embedded five-member rings was mainly due to oxidation (red) by atomic oxygen, with this process becoming more dominant as the mole fraction of atomic oxygen increased. The armchair sites produced by the oxidation (red) of partially-embedded five-member rings by atomic oxygen allow further growth without the inclusion of curvature. This is consistent with the observation that Region 3 sampled the highest number of six-member ring growth processes (orange) of all regions, with the number of sampled processes only notably decreasing at very high mole fractions of molecular oxygen $\left(X_{O_2} > 10^{-2}\right)$. It is possible that atomic oxygen produced in plasma reactors contributes to the formation of graphene following these processes.

Region 4 sampled a large number of oxidation (red) processes that both produced and consumed partially-embedded five-member rings, alongside a significant number of six-member ring growth processes (orange) consistent with the production of armchair sites by the oxidation (red) of partially-embedded five-member rings by atomic oxygen. The net effect was a reduction in the size of the molecules during the simulations in Region 4.

The combination of processes that produce and consume partially-embedded five-member rings provides a possible explanation for the formation of fullerenes and graphene. In the absence of atomic oxygen, high mole fractions of molecular oxygen result in the production of additional partially-embedded five-member rings that can become fully-embedded after migration processes move them to edge positions. This results in curved structures, with an associated decrease in the number of sites that are available for reaction. This reduces the rate of growth and results in conditions that are favourable for the formation of fullerenes. Crosslinking with other carbonaceous molecules may be another process that contributes to the formation of fullerenes [121]. In the presence of atomic oxygen, partially-embedded five-member rings occupying a corner position can be oxidised to produce armchair sites that can subsequently grow via a HACA addition. This results in larger flat molecules that resemble graphene. These processes are indicated in Figure 6.4 with blue and red arrows showing processes discussed in connection with the formation of fullerenes and graphene respectively. There is also evidence for the formation of graphene in oxygen-free plasma reactors [292, 24]. This suggests that there must also be other mechanisms that prevent the inclusion of curvature in the molecules. A possible pathway could be the consumption of partially-embedded five-member rings due to ring enlargements caused by reactions with species that add a single carbon atom (*e.g.* methyl radicals) [8]. This process could

convert five-member rings into six-member rings as previously suggested by Whitesides and Frenklach [348].

The orange arrows on Figure 6.4 indicate crosslinking processes between (as yet unknown) structures. Although these processes are not simulated in the current KMC model, they are believed to occur during the formation of carbonaceous particles and may be related to the presence of five-member rings. Many structures containing five-member rings have been shown to be able to form localised π-radicals [193]. The structure containing the partially-embedded five-member ring occupying a corner position (right, second row of Figure 6.4) is an example of such a radical. It has been shown that the crosslinking of large localised π-radicals (from approximately 400 a.m.u.) results in stable bonded and stacked structures [193], that multiple localised π-radicals are possible within a single structure and that the concentrations of localised π-radicals are potentially significant at 1400–1500 K [207], leading to the suggestion of localised π-radicals as possible candidates to explain the inception of carbonaceous particles. Under conditions that slowly consume partially-embedded five-member rings (Region 1), as opposed to rapidly embedding the rings (Region 2) or oxidising them (Region 3), the molecules are likely to have enough time to form localised radical sites and interact with other molecules. Both of these observations are consistent with the pressure dependency of the different products: lower pressures drastically reduce the formation of carbonaceous particles, favouring the formation of fullerenes and graphene. This mechanism for the formation of carbonaceous particles via the collision of localised π-radicals needs further investigation.

6.4   Conclusions

A KMC model was used to study the growth of carbonaceous structures under different chemical conditions. The model includes processes for growth and for the oxidation of six-member rings and partially-embedded five-member rings, and uses a new algorithm for the efficient simulation of the migration of partially-embedded five-member rings around the edge of the molecules. The mole fractions of hydrogen and acetylene were held constant at $X_H = 0.01$ and $X_{H_2} = X_{C_2H_2} = 0.1$, whilst the mole fractions of atomic and molecular oxygen were varied in range $10^{-8} \leq X_O \leq 10^{-1}$ and $10^{-6} \leq X_{O_2} \leq 10^{-1}$. The balance of the reaction mixture was argon.

The model was used to simulate the change in the structure of 300 circumcoronene ($C_{54}H_{18}$ with 19 six-member rings) molecules at each set of conditions. It was observed that atomic and molecular oxygen, which preferentially oxidise five-member and six-member rings respectively, have different effects on the size and morphology of the resulting carbona-

ceous structures. Four different regions of carbon growth, each of which is associated with processes that produce and consume partially-embedded five-member rings, were observed:

- In conditions with significant mole fractions of atomic oxygen $\left(10^{-4} < X_O \leq 10^{-2}\right)$ and the full range of mole fractions of molecular oxygen $\left(X_{O_2} \leq 10^{-1}\right)$, the oxidation of partially-embedded five-member rings produces armchair sites that participate in further growth processes. This produces large and flat molecules that keep growing as time progresses. This region is associated with the production of graphene.

- In conditions with significant mole fractions of molecular oxygen $\left(X_{O_2} > 10^{-2}\right)$ and low mole fractions of atomic oxygen $\left(X_O \leq 10^{-4}\right)$, the oxidation of six-member rings produces additional partially-embedded five-member rings that become rapidly embedded and formed highly curved structures. This region is associated with the production of fullerenes.

- In conditions with high mole fractions of atomic oxygen $\left(X_O > 10^{-2}\right)$ and the full range of mole fractions of molecular oxygen $\left(X_{O_2} \leq 10^{-1}\right)$, the oxidation of both six-member rings and partially-embedded five-member rings resulted in a reduction in the size of the simulated molecules.

- In conditions with low mole fractions of both molecular and atomic oxygen $\left(X_{O_2} \leq 10^{-2}\right.$ and $X_O \leq 10^{-4}\right)$ the simulated molecules became curved and grew slowly resulting in molecules with intermediate sizes. The possibility is raised that the slow inclusion of curvature in this region allows the formation of localised π-radicals in partially-embedded five-member rings. These radicals have been suggested to participate in the formation of carbonaceous particles [193].

The regions of carbon growth with low mole fractions of atomic oxygen agree well with known observations of the appearance of carbonaceous particles and fullerenes. The other regions seem unlikely to be observed in typical flame environments. However, processes associated with an increased production of atomic oxygen such as plasma reactors may operate at such conditions. This could contribute to the production of graphene in such processes.

The production and consumption of partially-embedded five-member rings appears to be important in explaining the formation of graphene, fullerenes and carbonaceous particles. These rings have been observed experimentally [45]. Further work is necessary to understand their role with respect to the viability of crosslinking in different chemical environments.

Research data

The source code for the KMC model [46] used in this chapter is available on GitHub (https://github.com/ucam-ceb-como/MOpS) under an open source licence. All simulated structures are available to download from the University of Cambridge data repository (doi:10.17863/CAM.66055).

Chapter 7

Conclusions

7.1 Conclusions of the thesis

In this thesis, the growth of polycyclic aromatic hydrocarbons (PAHs) has been studied in different chemical environments that favour the formation of carbonaceous materials using a detailed population balance model solved with stochastic numerical methods. A Kinetic Monte Carlo (KMC) algorithm has been used to solve the transformation of the sites that constitute the edge of PAHs and is thus a Kinetic Monte Carlo-ARomatic Site (KMC-ARS) model. This work presents methodological improvements in the stochastic modelling of PAHs as well as results related to the morphology of carbonaceous structures.

Several improvements relevant to stochastic models of PAH growth have been proposed in this work. The most critical improvements are: (1) a methodology to calculate process rates using a combination of a steady-state approximation and a partial-equilibrium approximation, (2) developed processes that include curvature in PAHs via the embedding of five-member rings or via the formation of seven-member rings, (3) an algorithm to resolve the migration of partially-embedded five-member rings while deferring the update of the PAH structure, and (4) processes for the oxidation of partially-embedded five-member rings and six-member rings.

A methodology to calculate KMC process rates using a combination of a steady-state approximation and a partial-equilibrium approximation has been developed. The methodology compares the rate of partial-equilibrium growth with the rate of ring desorption to determine whether to use the steady-state or partial-equilibrium approximation. The combined methodology was compared against the steady-state approximation in atmospheric pressure closed systems at different temperatures and equivalence ratios. The combined methodology showed a substantial improvement in accuracy over the steady-state approximation across

temperatures ranging from 1000 to 2500 K and equivalence ratios ranging from 0.5 to 10.

Processes that include curvature via the embedding of five-member rings or via the formation of seven-member rings have been included. The processes that produce these rings can proceed via hydrogen-abstraction, acetylene-addition reactions or via bay closure reactions and follow the rates calculated in a recent study for the kinetics of the formation of curvature [206]. A process that removes curvature via the recombination of a coupled five- and seven-member ring has also been included.

An algorithm to resolve the migration of partially-embedded five-member rings has been implemented in the stochastic model. The algorithm resolves the sites from the molecular edge while deferring the update of the PAH structure and is referred as the *update-deferred* algorithm. The PAH structure is updated after a non-migration process is sampled. The algorithm was proved to be exact in the sense that it reproduces the same sites and waiting times as an algorithm that updates the PAH structure after every migration process is called. Numerical testing of the algorithm showed that, on average, the ratio of computational times between the algorithm that updates the structure after each process and the update-deferred algorithm was over two orders of magnitude. This represents significant computational savings.

Lastly, processes for the oxidation of six-member rings and for the oxidation of partially-embedded five-member rings have been included. These processes use the rates from recent studies [85, 65] with a steady-state approximation for the oxygenated intermediates. The processes allow the oxidation of these rings by the combined interaction of oxygenated species creating reaction intermediates.

Different aspects of the formation of carbonaceous materials have been studied in this work. The formation of small PAHs in premixed ethylene flames has been studied to analyse the performance of the combined partial-equilibrium–steady-state approximation methodology. The integration of curvature has been studied in the fuel side of counterflow diffusion flames of ethylene and acetylene. The effect of oxygenated species in the growth of PAHs has been studied to understand what species increase the production of different carbonaceous materials.

The combined partial-equilibrium–steady-state approximation has been used in KMC simulations of premixed ethylene flames in the context of small PAH growth. The results were in close agreement with reference solutions obtained from fully-coupled simulations of the flames using the ABF mechanism [4]. This demonstrates that the methodology is able to reproduce the growth rate of small PAHs and it is proposed that the methodology can be extended as a general method for any given size of PAH.

The integration of curvature in PAHs due to the formation of coupled five- and seven-member rings has been studied in the fuel side of ethylene and acetylene counterflow diffusion flames. The major peaks and relative abundances of experimental mass spectra have been reproduced. The formation of five- and seven-member rings occurred via competitive processes amongst the sites that produce these rings. It was observed that approximately 85% of the events that integrate curvature correspond to the embedding of five-member rings while the remaining 15% correspond to the formation of seven-member rings coupled to five-member rings. The proportion of PAHs that contains both five- and seven-member rings appeared to increase with the molecular size and residence time.

The impact of oxygenated species in the growth of PAHs has been studied in a parameter space that included constant mole fractions of hydrogen and acetylene and varying mole fractions of molecular and atomic oxygen in the ranges $10^{-6} \leq X_{O_2} \leq 10^{-1}$ and $10^{-8} \leq X_O \leq 10^{-1}$. Four regions of carbon growth, each of which is associated with processes that produce and consume partially-embedded five-member rings and with an specific carbonaceous product were found. Graphene was produced in the region with significant atomic oxygen ($10^{-4} < X_O \leq 10^{-2}$) under all studied molecular oxygen conditions ($X_{O_2} \leq 10^{-1}$). In this region, the oxidation of partially-embedded five-member rings produces armchair sites that participate in further growth processes. This produces large and flat molecules that keep growing as time progresses. This is the first time that a KMC model of PAH growth that has processes that include curvature reports the formation of graphene. Fullerenes were associated to the region with the highest molecular oxygen ($X_{O_2} > 10^{-2}$) and low atomic oxygen ($X_O \leq 10^{-4}$). In this region, the oxidation of six-member rings creates additional partially-embedded five-member rings that become rapidly embedded and formed small curved structures. The region with the highest atomic oxygen ($X_O > 10^{-2}$) under all studied molecular oxygen conditions ($X_{O_2} \leq 10^{-1}$) was associated with planar structures with only few rings. The oxidation of both six-member rings and partially-embedded five-member rings resulted in a reduction in the size of the simulated molecules. Lastly, in the region with the lowest molecular and atomic oxygen ($X_{O_2} \leq 10^{-2}$ and $X_O \leq 10^{-4}$) the simulated molecules became curved and grew slowly resulting in intermediate sizes. In this region the appearance of seven-member rings agrees with the observation of these rings appearing at longer residence times from the simulations of counterflow diffusion flames. The slow inclusion of curvature in this region possibly allows the formation of localised π-radicals that could participate in the formation of carbonaceous particles as suggested in [193, 139].

7.2   Suggestions for further work

Coupling detailed population balance model to gas-phase chemistry

In this thesis, the detailed population balance model is applied as a post-processing technique where the gas phase chemistry is first solved. The predicted temperature and gas phase species concentrations are supplied as input to the detailed population balance model (Chapters 4 and 5). Although this approximation has been shown to produce accurate predictions for the species contained in carbonaceous particles [37, 256, 339], it heavily relies on PAHs and carbonaceous particles being diluted (having mass fractions significantly smaller than the main gas phase products). It is not clear if this approximation is valid under all reactive conditions and it would be desirable for the gas phase and population balance equations to be solved simultaneously.

Crosslinking reactions

Previous stochastic models of PAH growth have simulated the physical interaction between the PAHs that are widely thought to constitute carbonaceous particles [358, 37, 5, 291]. In these models, the inception of particles follows the mechanism of pyrene dimerisation suggested by Frenklach and Schuetz [279, 76] that has been used in several other models [for example 269, 362, 291, 5, 4, 81, 152]. However, there is growing evidence that the dimerisation of pyrene is a reversible process that is not able to explain the nucleation of carbonaceous particles [35, 295, 61, 270]. These findings have motivated studies of other possible mechanisms that are able to explain the inception of carbonaceous particles. Two of these recent mechanisms for particle inception rely on the continuous formation of crosslinked PAHs. First, Johansson et al. [139] have suggested resonantly stabilised radicals as possible species that could lead to carbonaceous particles. These radicals gain additional stabilisation by forming resonant structures. It was suggested that these radicals could form crosslinks with σ-radicals and neutral species leading to the inception of carbonaceous particles. Second, Martin et al. [193] have suggested localised π-radicals as possible species that can produce crosslinked PAHs by interacting with other localised π-radicals and σ-radicals [208]. These radicals localise their radical behaviour around five-member rings. This mechanism, also discussed briefly in Chapter 6, needs further investigation.

Fullerene closure reactions

In this thesis several simulated carbonaceous structures became curved with increasing residence times. Some of these structures ended up being significantly curved with only a few

edge atoms and sites. Such molecules should be able to participate in cage closure reactions. These reactions suggested in different mechanisms of fullerene formation [280, 121, 93] have been suggested as the final step in the formation of closed cage structures. Other processes that can affect fullerenes, such as the closed network growth mechanism [60], have been suggested as a possible way to explain the appearance of multiple fullerenes from exposing a single one to a reactive environment. These processes appear to be important and their investigation is suggested as further work.

References

[1] E. Adkins and J. Miller. Extinction measurements for optical band gap determination of soot in a series of nitrogen-diluted ethylene/air non-premixed flames. *Phys. Chem. Chem. Phys.*, 17(4):2686–95, 2015. doi:10.1039/c4cp04452e.

[2] J. Ahrens, M. Bachmann, T. Baum, J. Griesheimer, R. Kovacs, P. Weilmünster, and K.-H. Homann. Fullerenes and their ions in hydrocarbon flames. *Int. J. Mass Spectrom. Ion Process.*, 138:133–148, 1994. doi:10.1016/0168-1176(94)04036-2.

[3] B. Apicella, P. Pré, M. Alfè, A. Ciajolo, V. Gargiulo, C. Russo, A. Tregrossi, D. Deldique, and J. Rouzaud. Soot nanostructure evolution in premixed flames by high resolution electron transmission microscopy (HRTEM). *Proc. Combust. Inst.*, 35(2):1895–1902, 2015. doi:10.1016/j.proci.2014.06.121.

[4] J. Appel, H. Bockhorn, and M. Frenklach. Kinetic modeling of soot formation with detailed chemistry and physics: Laminar premixed flames of C_2 hydrocarbons. *Combust. Flame*, 121(1-2):122–136, 2000. doi:10.1016/S0010-2180(99)00135-2.

[5] M. Balthasar and M. Kraft. A stochastic approach to calculate the particle size distribution function of soot particles in laminar premixed flames. *Combust. Flame*, 133(3):289–298, 2003. doi:10.1016/S0010-2180(03)00003-8.

[6] M. Balthasar, F. Mauss, and H. Wang. A computational study of the thermal ionization of soot particles and its effect on their growth in laminar premixed flames. *Combust. Flame*, 129(1):204–216, 2002. doi:10.1016/S0010-2180(02)00344-9.

[7] M. Baradyn and A. Ratkiewicz. Kinetics of the hydrogen abstraction PAH + •OH → PAH radical + H_2O reaction class: An application of the Reaction Class Transition State Theory (RC-TST) and Structure–Activity Relationship (SAR). *J. Phys. Chem. A*, 123(4):750–763, 2019. doi:10.1021/acs.jpca.8b10988.

[8] M. Baroncelli, Q. Mao, S. Galle, N. Hansen, and H. Pitsch. Role of ring-enlargement reactions in the formation of aromatic hydrocarbons. *Phys. Chem. Chem. Phys.*, 22: 4699–4714, 2020. doi:10.1039/C9CP05854K.

[9] T. Baum, S. Löffler, P. Löffler, P. Weilmünster, and K.-H. Homann. Fullerene ions and their relation to PAH and soot in low-pressure hydrocarbon flames. *Ber. Bunsenges. Phys. Chem.*, 96(7):841–857, 1992. doi:10.1002/bbpc.19920960702.

[10] J. E. Bennett, H. Tamura-Wicks, R. M. Parks, R. T. Burnett, C. A. Pope, III, M. J. Bechle, J. D. Marshall, G. Danaei, and M. Ezzati. Particulate matter air pollution and

national and county life expectancy loss in the USA: A spatiotemporal analysis. *PLOS Med.*, 16(7):1–18, 07 2019. doi:10.1371/journal.pmed.1002856.

[11] S. W. Benson. The induction period in chain reactions. *J. Chem. Phys.*, 20(10): 1605–1612, 1952. doi:10.1063/1.1700223.

[12] G. P. Beretta, J. C. Keck, M. Janbozorgi, and H. Metghalchi. The rate-controlled constrained-equilibrium approach to far-from-local-equilibrium thermodynamics. *Entropy*, 14(2):92–130, 2012. doi:10.3390/e14020092.

[13] E. Bertin, A. Münzer, S. Reichenberger, R. Streubel, T. Vinnay, H. Wiggers, C. Schulz, S. Barcikowski, and G. Marzun. Durability study of platinum nanoparticles supported on gas-phase synthesized graphene in oxygen reduction reaction conditions. *Appl. Surf. Sci.*, 467-468:1181–1186, 2019. doi:10.1016/j.apsusc.2018.10.061.

[14] J. Bittner and J. Howard. Composition profiles and reaction mechanisms in a near-sooting premixed benzene/oxygen/argon flame. *Symp. (Int.) Combust.*, 18(1):1105–1116, 1981. doi:10.1016/S0082-0784(81)80115-4. Eighteenth Symposium (International) on Combustion.

[15] G. Blanquart, P. Pepiot-Desjardins, and H. Pitsch. Chemical mechanism for high temperature combustion of engine relevant fuels with emphasis on soot precursors. *Combust. Flame*, 156(3):588–607, 2009. doi:10.1016/j.combustflame.2008.12.007.

[16] H. Bockhorn. *Soot formation in combustion: mechanisms and models*, volume 59. Springer Science & Business Media, 2013.

[17] A. Boje, J. Akroyd, S. Sutcliffe, and M. Kraft. Study of industrial titania synthesis using a hybrid particle-number and detailed particle model. *Chem. Eng. Sci.*, 219: 115615, 2020. doi:10.1016/j.ces.2020.115615.

[18] T. C. Bond, S. J. Doherty, D. W. Fahey, P. M. Forster, T. Berntsen, B. J. DeAngelo, M. G. Flanner, S. Ghan, B. Kärcher, D. Koch, S. Kinne, Y. Kondo, P. K. Quinn, M. C. Sarofim, M. G. Schultz, M. Schulz, C. Venkataraman, H. Zhang, S. Zhang, N. Bellouin, S. K. Guttikunda, P. K. Hopke, M. Z. Jacobson, J. W. Kaiser, Z. Klimont, U. Lohmann, J. P. Schwarz, D. Shindell, T. Storelvmo, S. G. Warren, and C. S. Zender. Bounding the role of black carbon in the climate system: A scientific assessment. *J. Geophys. Res. Atmos.*, 118(11):5380–5552, 2013. doi:10.1002/jgrd.50171.

[19] M. L. Botero, E. M. Adkins, S. González-Calera, H. Miller, and M. Kraft. PAH structure analysis of soot in a non-premixed flame using high-resolution transmission electron microscopy and optical band gap analysis. *Combust. Flame*, 164:250–258, 2016. doi:10.1016/j.combustflame.2015.11.022.

[20] M. L. Botero, D. Chen, S. González-Calera, D. Jefferson, and M. Kraft. HRTEM evaluation of soot particles produced by the non-premixed combustion of liquid fuels. *Carbon*, 96:459–473, 2016. doi:10.1016/j.carbon.2015.09.077.

[21] M. L. Botero, N. Eaves, J. A. Dreyer, Y. Sheng, J. Akroyd, W. Yang, and M. Kraft. Experimental and numerical study of the evolution of soot primary particles in a diffusion flame. *Proc. Combust. Inst.*, 37(2):2047–2055, 2019. doi:10.1016/j.proci.2018.06.185.

[22] K. Bowal, J. W. Martin, A. J. Misquitta, and M. Kraft. Ion-induced soot nucleation using a new potential for curved aromatics. *Combust. Sci. Technol.*, 191(5-6):747–765, 2019. doi:10.1080/00102202.2019.1565496.

[23] G. Brinkmalm, D. Barofsky, P. Demirev, D. Fenyö, P. Håkansson, R. E. Johnson, C. T. Reimann, and B. U. Sundqvist. Formation of fullerenes in MeV ion track plasmas. *Chem. Phys. Lett.*, 191(3):345–350, 1992. doi:10.1016/0009-2614(92)85312-X.

[24] N. Bundaleska, J. Henriques, M. Abrashev, A. M. Botelho do Rego, A. M. Ferraria, A. Almeida, F. M. Dias, E. Valcheva, B. Arnaudov, K. K. Upadhyay, M. F. Montemor, and E. Tatarova. Large-scale synthesis of free-standing N-doped graphene using microwave plasma. *Sci. Rep.*, 8(1):12595, Aug 2018. doi:10.1038/s41598-018-30870-3.

[25] N. Bundaleska, D. Tsyganov, A. Dias, E. Felizardo, J. Henriques, F. M. Dias, M. Abrashev, J. Kissovski, and E. Tatarova. Microwave plasma enabled synthesis of free standing carbon nanostructures at atmospheric pressure conditions. *Phys. Chem. Chem. Phys.*, 20:13810–13824, 2018. doi:10.1039/C8CP01896K.

[26] H. Calcote. Mechanisms of soot nucleation in flames—A critical review. *Combust. Flame*, 42:215–242, 1981. doi:10.1016/0010-2180(81)90159-0.

[27] H. F. Calcote, D. B. Olson, and D. G. Keil. Are ions important in soot formation? *Energy Fuels*, 2(4):494–504, 1988. doi:10.1021/ef00010a016.

[28] J. Camacho, Y. Tao, and H. Wang. Kinetics of nascent soot oxidation by molecular oxygen in a flow reactor. *Proc. Combust. Inst.*, 35(2):1887 – 1894, 2015. doi:10.1016/j.proci.2014.05.095.

[29] X.-M. Cao, Z.-R. Li, J.-B. Wang, and X.-Y. Li. Rate rules for hydrogen abstraction reaction kinetics of polycyclic aromatic hydrocarbons and vinyl radical. *Theor. Chem. Acc.*, 139(6):94, 2020. doi:10.1007/s00214-020-02612-0.

[30] M. J. Castaldi, N. M. Marinov, C. F. Melius, J. Huang, S. M. Senkan, W. J. Pit, and C. K. Westbrook. Experimental and modeling investigation of aromatic and polycyclic aromatic hydrocarbon formation in a premixed ethylene flame. *Symp. (Int.) Combust.*, 26(1):693–702, 1996. doi:10.1016/S0082-0784(96)80277-3.

[31] M. Celnik, R. Patterson, M. Kraft, and W. Wagner. Coupling a stochastic soot population balance to gas-phase chemistry using operator splitting. *Combust. Flame*, 148(3):158–176, 2007. doi:10.1016/j.combustflame.2006.10.007.

[32] M. Celnik, A. Raj, R. West, R. Patterson, and M. Kraft. Aromatic site description of soot particles. *Combust. Flame*, 155(1-2):161–180, 2008. doi:10.1016/j.combustflame.2008.04.011.

[33] M. Celnik, R. Patterson, M. Kraft, and W. Wagner. A predictor-corrector algorithm for the coupling of stiff ODEs to a particle population balance. *J. Comput. Phys.*, 228 (8):2758–2769, 2009. doi:10.1016/j.jcp.2008.12.030.

[34] R. K. Chakrabarty, H. Moosmüller, W. P. Arnott, M. A. Garro, G. Tian, J. G. Slowik, E. S. Cross, J.-H. Han, P. Davidovits, T. B. Onasch, and D. R. Worsnop. Low fractal dimension cluster-dilute soot aggregates from a premixed flame. *Phys. Rev. Lett.*, 102: 235504, Jun 2009. doi:10.1103/PhysRevLett.102.235504.

[35] D. Chakraborty, H. Lischka, and W. L. Hase. Dynamics of pyrene-dimer association and ensuing pyrene-dimer dissociation. *J. Phys. Chem. A*, 124(43):8907–8917, 2020. doi:10.1021/acs.jpca.0c06677.

[36] D. Chen and H. Wang. Cation$-\pi$ interactions between flame chemi-ions and aromatic compounds. *Energy Fuels*, 31(3):2345–2352, 2017. doi:10.1021/acs.energyfuels.6b02354.

[37] D. Chen, Z. Zainuddin, E. Yapp, J. Akroyd, S. Mosbach, and M. Kraft. A fully coupled simulation of PAH and soot growth with a population balance model. *Proc. Combust. Inst.*, 34(1):1827–1835, 2013. doi:10.1016/j.proci.2012.06.089.

[38] V. Chernov, M. J. Thomson, S. B. Dworkin, N. A. Slavinskaya, and U. Riedel. Soot formation with C_1 and C_2 fuels using an improved chemical mechanism for PAH growth. *Combust. Flame*, 161(2):592–601, 2014. doi:10.1016/j.combustflame.2013.09.017.

[39] W. Choi, I. Lahiri, R. Seelaboyina, and Y. S. Kang. Synthesis of graphene and its applications: A review. *Crit. Rev. Solid State Mater. Sci.*, 35(1):52–71, 2010. doi:10.1080/10408430903505036.

[40] G. Churilov, P. Novikov, V. Tarabanko, V. Lopatin, N. Vnukova, and N. Bulina. On the mechanism of fullerene formation in a carbon plasma. *Carbon*, 40(6):891–896, 2002. doi:10.1016/S0008-6223(01)00211-1.

[41] A. Ciajolo, A. D'Anna, R. Barbella, A. Tregrossi, and A. Violi. The effect of temperature on soot inception in premixed ethylene flames. *Symp. (Int.) Combust.*, 26(2): 2327–2333, 1996. doi:10.1016/S0082-0784(96)80061-0.

[42] CMCL Innovations. *K*inetics software v10.0.1, 2019.

[43] J. Cole, J. Bittner, J. Longwell, and J. Howard. Formation mechanisms of aromatic compounds in aliphatic flames. *Combust. Flame*, 56(1):51–70, 1984. doi:10.1016/0010-2180(84)90005-1.

[44] M. B. Colket and D. J. Seery. Reaction mechanisms for toluene pyrolysis. *Symp. (Int.) Combust.*, 25(1):883–891, 1994. doi:10.1016/S0082-0784(06)80723-X.

[45] M. Commodo, K. Kaiser, G. D. Falco, P. Minutolo, F. Schulz, A. D'Anna, and L. Gross. On the early stages of soot formation: Molecular structure elucidation by high-resolution atomic force microscopy. *Combust. Flame*, 205:154–164, 2019. doi:10.1016/j.combustflame.2019.03.042.

[46] Computational Modelling Group. MOpS Particle Simulator. https://github.com/ucam-ceb-como/MOpS, 2021. Commit: 404e1504c65bfb0a3f02d238bfac8be728073233.

[47] B. Connelly, M. Long, M. Smooke, R. Hall, and M. Colket. Computational and experimental investigation of the interaction of soot and NO in coflow diffusion flames. *Proc. Combust. Inst.*, 32(1):777–784, 2009. doi:10.1016/j.proci.2008.06.182.

[48] J. Coro, M. Suárez, L. S. Silva, K. I. Eguiluz, and G. R. Salazar-Banda. Fullerene applications in fuel cells: A review. *Int. J. Hydrog. Energy*, 41(40):17944–17959, 2016. doi:10.1016/j.ijhydene.2016.08.043.

[49] R. F. Curl and R. E. Smalley. Probing C$_{60}$. *Science*, 242(4881):1017–1022, 1988. doi:10.1126/science.242.4881.1017.

[50] A. D'Anna and J. Kent. A model of particulate and species formation applied to laminar, nonpremixed flames for three aliphatic-hydrocarbon fuels. *Combust. Flame*, 152(4):573–587, 2008. doi:10.1016/j.combustflame.2007.08.003.

[51] A. D'Anna and A. Violi. A kinetic model for the formation of aromatic hydrocarbons in premixed laminar flames. *Symp. (Int.) Combust.*, 27(1):425–433, 1998. doi:10.1016/S0082-0784(98)80431-1. Twenty-Seventh Sysposium (International) on Combustion Volume One.

[52] A. D'Anna and A. Violi. Detailed modeling of the molecular growth process in aromatic and aliphatic premixed flames. *Energy Fuels*, 19(1):79–86, 2005. doi:10.1021/ef0499675.

[53] A. D'Anna, A. Violi, A. D'Alessio, and A. F. Sarofim. A reaction pathway for nanoparticle formation in rich premixed flames. *Combust. Flame*, 127(1):1995–2003, 2001. doi:10.1016/S0010-2180(01)00303-0.

[54] M. Dasgupta, P. Fortugno, and H. Wiggers. Plasma-assisted gas-phase synthesis and in-line coating of silicon nanoparticles. *Plasma Process. Polym.*, 17(5):1900245, 2020. doi:10.1002/ppap.201900245.

[55] A. Dato. Graphene synthesized in atmospheric plasmas—a review. *J. Mater. Res.*, 34 (1):214–230, 2019. doi:10.1557/jmr.2018.470.

[56] A. Dato and M. Frenklach. Substrate-free microwave synthesis of graphene: experimental conditions and hydrocarbon precursors. *New J. Phys.*, 12(12):125013, 2010. doi:10.1088/1367-2630/12/12/125013.

[57] A. Dato, V. Radmilovic, Z. Lee, J. Phillips, and M. Frenklach. Substrate-free gas-phase synthesis of graphene sheets. *Nano Letters*, 8(7):2012–2016, 2008. doi:10.1021/nl8011566.

[58] A. M. Dean. Detailed kinetic modeling of autocatalysis in methane pyrolysis. *J. Phys. Chem.*, 94(4):1432–1439, 1990.

[59] F. Defoeux, V. Dias, C. Renard, P. Van Tiggelen, and J. Vandooren. Experimental investigation of the structure of a sooting premixed benzene/oxygen/argon flame burning at low pressure. *Proc. Combust. Inst.*, 30(1):1407–1415, 2005. doi:10.1016/j.proci.2004.08.014.

[60] P. W. Dunk, N. K. Kaiser, C. L. Hendrickson, J. P. Quinn, C. P. Ewels, Y. Nakanishi, Y. Sasaki, H. Shinohara, A. G. Marshall, and H. W. Kroto. Closed network growth of fullerenes. *Nat. Commun.*, 3(1):855, May 2012. doi:10.1038/ncomms1853.

[61] N. Eaves, S. Dworkin, and M. Thomson. The importance of reversibility in modeling soot nucleation and condensation processes. *Proc. Combust. Inst.*, 35(2):1787–1794, 2015. doi:10.1016/j.proci.2014.05.036.

[62] N. A. Eaves, A. Veshkini, C. Riese, Q. Zhang, S. B. Dworkin, and M. J. Thomson. A numerical study of high pressure, laminar, sooting, ethane-air coflow diffusion flames. *Combust. Flame*, 159(10):3179–3190, 2012. doi:10.1016/j.combustflame.2012.03.017.

[63] N. A. Eaves, S. B. Dworkin, and M. J. Thomson. Assessing relative contributions of pahs to soot mass by reversible heterogeneous nucleation and condensation. *Proc. Combust. Inst.*, 36(1):935–945, 2017. doi:10.1016/j.proci.2016.06.051.

[64] L. B. Ebert. Is soot composed predominantly of carbon clusters? *Science*, 247(4949): 1468–1471, 1990. doi:10.1126/science.247.4949.1468.

[65] D. E. Edwards, D. Y. Zubarev, W. A. Lester, and M. Frenklach. Pathways to soot oxidation: Reaction of OH with phenanthrene radicals. *J. Phys. Chem. A*, 118(37): 8606–8613, 2014. doi:10.1021/jp5033178.

[66] M. L. Eggersdorfer and S. E. Pratsinis. The structure of agglomerates consisting of polydisperse particles. *Aerosol Sci Tech*, 46(3):347–353, 2012. doi:10.1080/02786826.2011.631956.

[67] M. L. Eggersdorfer, D. Kadau, H. J. Herrmann, and S. E. Pratsinis. Aggregate morphology evolution by sintering: Number and diameter of primary particles. *J. Aerosol Sci.*, 46:7–19, 2012. doi:10.1016/j.jaerosci.2011.11.005.

[68] A. Eibeck and W. Wagner. An efficient stochastic algorithm for studying coagulation dynamics and gelation phenomena. *SIAM J. Sci. Comput.*, 22(3):802–821, 2000. doi:10.1137/S1064827599353488.

[69] P. Elvati, V. T. Dillstrom, and A. Violi. Oxygen driven soot formation. *Proc. Combust. Inst.*, 36(1):825–832, 2017. doi:10.1016/j.proci.2016.09.019.

[70] C. Esarte, M. Peg, M. P. Ruiz, A. Millera, R. Bilbao, and M. U. Alzueta. Pyrolysis of ethanol: Gas and soot products formed. *Ind. Eng. Chem. Res.*, 50(8):4412–4419, 2011. doi:10.1021/ie1022628.

[71] A. Fahr and S. Stein. Reactions of vinyl and phenyl radicals with ethyne, ethene and benzene. *Symp. (Int.) Combust.*, 22(1):1023–1029, 1989. doi:10.1016/S0082-0784(89)80112-2.

[72] C. P. Fenimore and G. W. Jones. Oxidation of soot by hydroxyl radicals. *J. Phys. Chem.*, 71(3):593–597, 1967. doi:10.1021/j100862a021.

[73] C. P. Fenimore and G. W. Jones. Coagulation of soot to smoke in hydrocarbon flames. *Combust. Flame*, 13(3):303–310, 1969. doi:10.1016/0010-2180(69)90008-X.

[74] M. Frenklach. On the driving force of PAH production. *Symp. (Int.) Combust.*, 22(1): 1075–1082, 1989.

[75] M. Frenklach. On surface growth mechanism of soot particles. *Symp. (Int.) Combust.*, 26(2):2285–2293, 1996. doi:10.1016/S0082-0784(96)80056-7.

[76] M. Frenklach. Reaction mechanism of soot formation in flames. *Phys. Chem. Chem. Phys.*, 4:2028–2037, 2002. doi:10.1039/B110045A.

[77] M. Frenklach. Method of moments with interpolative closure. *Chem. Eng. Sci.*, 57 (12):2229–2239, 2002. doi:10.1016/S0009-2509(02)00113-6.

[78] M. Frenklach. New form for reduced modeling of soot oxidation: Accounting for multi-site kinetics and surface reactivity. *Combust. Flame*, 201:148–159, 2019. doi:10.1016/j.combustflame.2018.12.023.

[79] M. Frenklach and L. B. Ebert. Comment on the proposed role of spheroidal carbon clusters in soot formation. *J. Phys. Chem.*, 92(2):561–563, 1988.

[80] M. Frenklach and A. M. Mebel. On the mechanism of soot nucleation. *Phys. Chem. Chem. Phys.*, 22:5314–5331, 2020. doi:10.1039/D0CP00116C.

[81] M. Frenklach and H. Wang. Detailed modeling of soot particle nucleation and growth. *Symp. (Int.) Combust.*, 23(1):1559 – 1566, 1991. doi:10.1016/S0082-0784(06)80426-1. Twenty-Third Symposium (International) on Combustion.

[82] M. Frenklach and H. Wang. Detailed mechanism and modeling of soot particle formation. In H. Bockhorn, editor, *Soot formation in combustion: Mechanisms and models*, volume 59, pages 165–192. Springer Science & Business Media, 1994.

[83] M. Frenklach, W. Gardiner, S. Stein, D. Clary, and T. Yuan. Mechanism of soot formation in acetylene-oxygen mixtures. *Combust. Sci. Technol.*, 50(1-3):79–115, 1986. doi:10.1080/00102208608923927.

[84] M. Frenklach, C. A. Schuetz, and J. Ping. Migration mechanism of aromatic-edge growth. *Proc. Combust. Inst.*, 30(1):1389–1396, 2005. doi:10.1016/j.proci.2004.07.048.

[85] M. Frenklach, Z. Liu, R. I. Singh, G. R. Galimova, V. N. Azyazov, and A. M. Mebel. Detailed, sterically-resolved modeling of soot oxidation: Role of O atoms, interplay with particle nanostructure, and emergence of inner particle burning. *Combust. Flame*, 188:284–306, 2018. doi:10.1016/j.combustflame.2017.10.012.

[86] M. Frenklach, R. I. Singh, and A. M. Mebel. On the low-temperature limit of HACA. *Proc. Combust. Inst.*, 37(1):969–976, 2019. doi:10.1016/j.proci.2018.05.068.

[87] S. K. Friedlander. *Smoke, dust, and haze: Fundamentals of Aerosol Dynamics*. Oxford university press, 2000.

[88] J. Gao, J. Zhao, and F. Ding. Transition metal surface passivation induced graphene edge reconstruction. *J. Am. Chem. Soc.*, 134(14):6204–6209, 2012. doi:10.1021/ja2104119.

[89] Y. Georgievskii, J. A. Miller, and S. J. Klippenstein. Association rate constants for reactions between resonance-stabilized radicals: $C_3H_3 + C_3H_3$, $C_3H_3 + C_3H_5$, and $C_3H_5 + C_3H_5$. *Phys. Chem. Chem. Phys.*, 9:4259–4268, 2007. doi:10.1039/B703261G.

[90] H. Ghiassi, I. C. Jaramillo, and J. S. Lighty. Kinetics of soot oxidation by molecular oxygen in a premixed flame. *Energy Fuels*, 30(4):3463–3472, 2016. doi:10.1021/acs.energyfuels.5b02942.

[91] H. Ghiassi, D. Lignell, and J. S. Lighty. Soot oxidation by OH: Theory development, model, and experimental validation. *Energy Fuels*, 31(3):2236–2245, 2017. doi:10.1021/acs.energyfuels.6b02193.

[92] D. T. Gillespie. A general method for numerically simulating the stochastic time evolution of coupled chemical reactions. *J. Comput. Phys.*, 22(4):403–434, 1976. doi:10.1016/0021-9991(76)90041-3.

[93] A. Goel, P. Hebgen, J. B. Vander Sande, and J. B. Howard. Combustion synthesis of fullerenes and fullerenic nanostructures. *Carbon*, 40(2):177 – 182, 2002. doi:10.1016/S0008-6223(01)00170-1. Third International Conference on Carbon Black.

[94] S. Goodarzi, T. Da Ros, J. Conde, F. Sefat, and M. Mozafari. Fullerene: biomedical engineers get to revisit an old friend. *Mater. Today*, 20(8):460–480, 2017. doi:10.1016/j.mattod.2017.03.017.

[95] M. Goodson and M. Kraft. An efficient stochastic algorithm for simulating nano-particle dynamics. *J. Comput. Phys.*, 183(1):210–232, 2002. doi:10.1006/jcph.2002.7192.

[96] D. G. Goodwin, R. L. Speth, H. K. Moffat, and B. W. Weber. Cantera: An object-oriented software toolkit for chemical kinetics, thermodynamics, and transport processes. https://www.cantera.org, 2018. Version 2.4.0. (accessed: 03.05.2018).

[97] A. N. Gorban. Model reduction in chemical dynamics: slow invariant manifolds, singular perturbations, thermodynamic estimates, and analysis of reaction graph. *Curr. Opin. Chem. Eng.*, 21:48–59, 2018. doi:10.1016/j.coche.2018.02.009.

[98] A. N. Gorban and I. V. Karlin. Method of invariant manifold for chemical kinetics. *Chem. Eng. Sci.*, 58(21):4751–4768, 2003. doi:10.1016/j.ces.2002.12.001.

[99] D. A. Goussis. Quasi steady state and partial equilibrium approximations: Their relation and their validity. *Combust. Theory Model.*, 16(5):869–926, 2012. doi:10.1080/13647830.2012.680502.

[100] D. A. Goussis and S.-H. Lam. A study of homogeneous methanol oxidation kinetics using CSP. *Symp. (Int.) Combust.*, 24(1):113–120, 1992. doi:10.1016/S0082-0784(06)80018-4.

[101] S. C. Graham, J. B. Homer, J. L. J. Rosenfeld, and T. M. Sugden. The formation and coagulation of soot aerosols generated by the pyrolysis of aromatic hydrocarbons. *Proc. R. Soc. Lond.*, 344(1637):259–285, 1975. doi:10.1098/rspa.1975.0101.

[102] W. J. Grieco, J. B. Howard, L. C. Rainey, and J. B. V. Sande. Fullerenic carbon in combustion-generated soot. *Carbon*, 38(4):597–614, 2000. doi:10.1016/S0008-6223(99)00149-9.

[103] H. Guo, P. M. Anderson, and P. B. Sunderland. Optimized rate expressions for soot oxidation by OH and O_2. *Fuel*, 172:248 – 252, 2016. doi:10.1016/j.fuel.2016.01.030.

[104] J. Guo, J. R. Morris, Y. Ihm, C. I. Contescu, N. C. Gallego, G. Duscher, S. J. Pennycook, and M. F. Chisholm. Topological defects: Origin of nanopores and enhanced adsorption performance in nanoporous carbon. *Small*, 8(21):3283–3288, 2012. doi:10.1002/smll.201200894.

[105] R. C. Haddon. Chemistry of the fullerenes: The manifestation of strain in a class of continuous aromatic molecules. *Science*, 261(5128):1545–1550, 1993. doi:10.1126/science.261.5128.1545.

[106] R. C. Haddon. C_{60}: sphere or polyhedron? *J. Am. Chem. Soc.*, 119(7):1797–1798, 1997. doi:10.1021/ja9637659.

[107] T. A. Halgren. Merck molecular force field. I. Basis, form, scope, parameterization, and performance of MMFF94. *J. Comput. Chem.*, 17:490–519, 1996. doi:10.1002/(SICI)1096-987X(199604)17:5/6<490::AID-JCC1>3.0.CO;2-P.

[108] V. Hall-Roberts, A. Hayhurst, D. Knight, and S. Taylor. The origin of soot in flames: is the nucleus an ion? *Combust. Flame*, 120(4):578–584, 2000. doi:10.1016/S0010-2180(99)00116-9.

[109] M. Hammad, P. Fortugno, S. Hardt, C. Kim, S. Salamon, T. C. Schmidt, H. Wende, C. Schulz, and H. Wiggers. Large-scale synthesis of iron oxide/graphene hybrid materials as highly efficient photo-fenton catalyst for water remediation. *Environ. Technol. Inno.*, 21:101239, 2021. doi:10.1016/j.eti.2020.101239.

[110] J. Hansen and L. Nazarenko. Soot climate forcing via snow and ice albedos. *Proc. Natl. Acad. Sci. U.S.A*, 101(2):423 –428, 2004. doi:10.1073/pnas.2237157100.

[111] N. Hansen, T. A. Cool, P. R. Westmoreland, and K. Kohse-Höinghaus. Recent contributions of flame-sampling molecular-beam mass spectrometry to a fundamental understanding of combustion chemistry. *Prog. Energy Combust. Sci.*, 35(2):168–191, 2009. doi:10.1016/j.pecs.2008.10.001.

[112] N. Hansen, W. Li, M. E. Law, T. Kasper, P. R. Westmoreland, B. Yang, T. A. Cool, and A. Lucassen. The importance of fuel dissociation and propargyl + allyl association for the formation of benzene in a fuel-rich 1-hexene flame. *Phys. Chem. Chem. Phys.*, 12: 12112–12122, 2010. doi:10.1039/C0CP00241K.

[113] N. Hansen, M. Schenk, K. Moshammer, and K. Kohse-Höinghaus. Investigating repetitive reaction pathways for the formation of polycyclic aromatic hydrocarbons in combustion processes. *Combust. Flame*, 180:250–261, 2017. doi:10.1016/j.combustflame.2016.09.013.

[114] L. B. Harding, Y. Georgievskii, and S. J. Klippenstein. Predictive theory for Hydrogen atom-Hydrocarbon radical association kinetics. *J. Phys. Chem. A*, 109(21):4646–4656, 2005. doi:10.1021/jp0508608.

[115] P. J. F. Harris. Fullerene-like models for microporous carbon. *J. Mater. Sci.*, 48(2): 565–577, Jan 2013. doi:10.1007/s10853-012-6788-1.

[116] S. J. Harris and I. M. Kennedy. The coagulation of soot particles with van der waals forces. *Combust. Sci. Technol.*, 59(4-6):443–454, 1988. doi:10.1080/00102208808947110.

[117] B. Haynes and H. Wagner. Soot formation. *Prog. Energy Combust. Sci.*, 7(4):229–273, 1981. doi:10.1016/0360-1285(81)90001-0.

[118] P. Hebgen, A. Goel, J. B. Howard, L. C. Rainey, and J. B. Vander Sande. Synthesis of fullerenes and fullerenic nanostructures in a low-pressure benzene/oxygen diffusion flame. *Proc. Combust. Inst.*, 28(1):1397 – 1404, 2000. doi:10.1016/S0082-0784(00)80355-0.

[119] E. Hesstvedt, Ö. Hov, and I. S. A. Isaksen. Quasi-steady-state approximations in air pollution modeling: Comparison of two numerical schemes for oxidant prediction. *Int. J. Chem. Kinet.*, 10(9):971–994, 1978. doi:10.1002/kin.550100907.

[120] K. J. Higgins, H. Jung, D. B. Kittelson, J. T. Roberts, and M. R. Zachariah. Size-selected nanoparticle chemistry: Kinetics of soot oxidation. *J. Phys. Chem. A*, 106(1): 96–103, 2002. doi:10.1021/jp004466f.

[121] K.-H. Homann. Fullerenes and soot formation— new pathways to large particles in flames. *Angew. Chem. Int. Ed. Engl.*, 37(18):2434–2451, 1998. doi:10.1002/(SICI)1521-3773(19981002)37:18<2434::AID-ANIE2434>3.0.CO;2-L.

[122] D. Hou and X. You. Reaction kinetics of hydrogen abstraction from polycyclic aromatic hydrocarbons by H atoms. *Phys. Chem. Chem. Phys.*, 19:30772–30780, 2017. doi:10.1039/C7CP04964A.

[123] D. Hou, C. S. Lindberg, M. Y. Manuputty, X. You, and M. Kraft. Modelling soot formation in a benchmark ethylene stagnation flame with a new detailed population balance model. *Combust. Flame*, 203:56–71, 2019. doi:10.1016/j.combustflame.2019.01.035.

[124] D. Hou, D. Zong, C. S. Lindberg, M. Kraft, and X. You. On the coagulation efficiency of carbonaceous nanoparticles. *J. Aerosol Sci.*, 140:105478, 2020. doi:10.1016/j.jaerosci.2019.105478.

[125] J. Houston Miller. The kinetics of polynuclear aromatic hydrocarbon agglomeration in flames. *Symp. (Int.) Combust.*, 23(1):91–98, 1991. doi:10.1016/S0082-0784(06)80246-8. Twenty-Third Symposium (International) on Combustion.

[126] J. Houston Miller, K. C. Smyth, and W. G. Mallard. Calculations of the dimerization of aromatic hydrocarbons: Implications for soot formation. *Symp. (Int.) Combust.*, 20 (1):1139–1147, 1985. doi:10.1016/S0082-0784(85)80604-4. Twentieth Symposium (International) on Combustion.

[127] J. B. Howard. Carbon addition and oxidation reactions in heterogeneous combustion and soot formation. *Proc. Combust. Inst.*, 23(1):1107–1127, 1991.

[128] J. B. Howard. Fullerenes formation in flames. *Symp. (Int.) Combust.*, 24(1):933 – 946, 1992. doi:10.1016/S0082-0784(06)80111-6. Twenty-Fourth Symposium on Combustion.

[129] J. B. Howard, A. L. Lafleur, Y. Makarovsky, S. Mitra, C. J. Pope, and T. K. Yadav. Fullerenes synthesis in combustion. *Carbon*, 30(8):1183 – 1201, 1992. doi:10.1016/0008-6223(92)90061-Z. Special Issue on Fullerenes.

[130] J. B. Howard, J. T. McKinnon, M. E. Johnson, Y. Makarovsky, and A. L. Lafleur. Production of C_{60} and C_{70} fullerenes in benzene-oxygen flames. *J. Phys. Chem.*, 96 (16):6657–6662, 1992. doi:10.1021/j100195a026.

[131] P. Y. Huang, C. S. Ruiz-Vargas, A. M. van der Zande, W. S. Whitney, M. P. Levendorf, J. W. Kevek, S. Garg, J. S. Alden, C. J. Hustedt, Y. Zhu, J. Park, P. L. McEuen, and D. A. Muller. Grains and grain boundaries in single-layer graphene atomic patchwork quilts. *Nature*, 469(7330):389–392, 2011. doi:10.1038/nature09718.

[132] M. Iriarte, A. Hernanz, J. M. Gavira-Vallejo, J. Alcolea-González, and R. de Balbín-Behrmann. μ-Raman spectroscopy of prehistoric paintings from the El Reno cave (Valdesotos, Guadalajara, Spain). *J. Archaeol. Sci. Rep.*, 14:454–460, 2017. doi:10.1016/j.jasrep.2017.06.008.

[133] C. Irimiea, A. Faccinetto, X. Mercier, I.-K. Ortega, N. Nuns, E. Therssen, P. Desgroux, and C. Focsa. Unveiling trends in soot nucleation and growth: When secondary ion mass spectrometry meets statistical analysis. *Carbon*, 144:815–830, 2019. doi:10.1016/j.carbon.2018.12.015.

[134] S. Irle, G. Zheng, Z. Wang, and K. Morokuma. The C_{60} formation puzzle "solved": QM/MD simulations reveal the shrinking hot giant road of the dynamic fullerene self-assembly mechanism. *J. Phys. Chem. B*, 110(30):14531–14545, 2006. doi:10.1021/jp061173z.

[135] N. A. H. Janssen, G. Hoek, M. Simic-Lawson, P. Fischer, L. van Bree, H. ten Brink, M. Keuken, R. W. Atkinson, H. R. Anderson, B. Brunekreef, and F. R. Cassee. Black carbon as an additional indicator of the adverse health effects of airborne particles compared with PM10 and PM2.5. *Environ. Health Perspect.*, 119(12):1691–1699, 2011. doi:10.1289/ehp.1003369.

[136] L. Jay, A. Sandu, F. Potra, and G. Carmichael. Improved quasi-steady-state-approximation methods for atmospheric chemistry integration. *SIAM J. Sci. Comput.*, 18(1):182–202, 1997. doi:10.1137/S1064827595283033.

[137] K.-J. Jeon and Z. Lee. Size-dependent interaction of au nanoparticles and graphene sheet. *Chem. Commun.*, 47:3610–3612, 2011. doi:10.1039/C0CC05167E.

[138] M. Jiménez, R. Rincón, A. Marinas, and M. Calzada. Hydrogen production from ethanol decomposition by a microwave plasma: Influence of the plasma gas flow. *Int. J. Hydrog. Energy*, 38(21):8708 – 8719, 2013. doi:10.1016/j.ijhydene.2013.05.004.

[139] K. Johansson, M. Head-Gordon, P. Schrader, K. Wilson, and H. Michelsen. Resonance-stabilized hydrocarbon-radical chain reactions may explain soot inception and growth. *Science*, 361(6406):997–1000, 2018.

[140] K. O. Johansson, T. Dillstrom, P. Elvati, M. F. Campbell, P. E. Schrader, D. M. Popolan-Vaida, N. K. Richards-Henderson, K. R. Wilson, A. Violi, and H. A. Michelsen. Radical-radical reactions, pyrene nucleation, and incipient soot formation in combustion. *Proc. Combust. Inst.*, 36(1):799–806, 2017. doi:10.1016/j.proci.2016.07.130.

[141] B. M. Jones, F. Zhang, R. I. Kaiser, A. Jamal, A. M. Mebel, M. A. Cordiner, and S. B. Charnley. Formation of benzene in the interstellar medium. *Proc. Natl. Acad. Sci. U.S.A*, 108(2):452–457, 2011. doi:10.1073/pnas.1012468108.

[142] W. P. Jones and S. Rigopoulos. Rate-controlled constrained equilibrium: Formulation and application to nonpremixed laminar flames. *Combust. Flame*, 142(3):223–234, 2005. doi:10.1016/j.combustflame.2005.03.008.

[143] Y. Ju and W. Sun. Plasma assisted combustion: Dynamics and chemistry. *Prog. Energy Combust. Sci.*, 48:21–83, 2015. doi:10.1016/j.pecs.2014.12.002.

[144] R. Jullien and M. Kolb. Hierarchical model for chemically limited cluster-cluster aggregation. *J. Phys. A Math. Theor.*, 17(12):L639–L643, aug 1984. doi:10.1088/0305-4470/17/12/003.

[145] K. H. Jung, J. K. Kim, J. H. Noh, J. W. Eun, H. J. Bae, M. G. Kim, Y. G. Chang, Q. Shen, S. J. Kim, S. H. Kwon, W. S. Park, J. Y. Lee, and S. W. Nam. Characteristic molecular signature for the early detection and prediction of polycyclic aromatic hydrocarbons in rat liver. *Toxicol. Lett.*, 216(1):1–8, 2013. doi:10.1016/j.toxlet.2012.11.001.

[146] A. Kazakov and M. Frenklach. Dynamic modeling of soot particle coagulation and aggregation: Implementation with the method of moments and application to high-pressure laminar premixed flames. *Combust. Flame*, 114(3–4):484–501, 1998. doi:10.1016/S0010-2180(97)00322-2.

[147] J. C. Keck and D. Gillespie. Rate-controlled partial-equilibrium method for treating reacting gas mixtures. *Combust. Flame*, 17(2):237–241, 1971. doi:10.1016/S0010-2180(71)80166-9.

[148] G. A. Kelesidis, E. Goudeli, and S. E. Pratsinis. Flame synthesis of functional nanostructured materials and devices: Surface growth and aggregation. *Proc. Combust. Inst.*, 36(1):29–50, 2017. ISSN 1540-7489. doi:10.1016/j.proci.2016.08.078.

[149] H. Kellerer, R. Koch, and S. Wittig. Measurements of the growth and coagulation of soot particles in a high-pressure shock tube. *Combust. Flame*, 120(1-2):188–199, 2000. doi:10.1016/S0010-2180(99)00067-X.

[150] C. T. Kelley. *Iterative Methods for Optimization*. Society for Industrial and Applied Mathematics, 1999. doi:10.1137/1.9781611970920.

[151] A. Khosousi and S. B. Dworkin. Soot surface reactivity during surface growth and oxidation in laminar diffusion flames. *Combust. Flame*, 162(12):4523–4532, 2015. doi:10.1016/j.combustflame.2015.09.005.

[152] C. Kim, A. El-Leathy, F. Xu, and G. Faeth. Soot surface growth and oxidation in laminar diffusion flames at pressures of 0.1–1.0 atm. *Combust. Flame*, 136(1):191 – 207, 2004. doi:10.1016/j.combustflame.2003.09.017.

[153] K.-H. Kim, S. A. Jahan, E. Kabir, and R. J. Brown. A review of airborne polycyclic aromatic hydrocarbons (PAHs) and their human health effects. *Environ. Int.*, 60:71–80, 2013. doi:10.1016/j.envint.2013.07.019.

[154] V. V. Kislov and A. M. Mebel. The formation of naphthalene, azulene, and fulvalene from cyclic C_5 species in combustion: An *Ab Initio*/RRKM study of 9-H-Fulvalenyl (C_5H_5–C_5H_4) radical rearrangements. *J. Phys. Chem. A*, 111(38):9532–9543, 2007. doi:10.1021/jp0732099.

[155] V. V. Kislov, A. M. Mebel, and S. H. Lin. *Ab Initio* and DFT study of the formation mechanisms of polycyclic aromatic hydrocarbons: The phenanthrene synthesis from biphenyl and naphthalene. *J. Phys. Chem. A*, 106(25):6171–6182, 2002. doi:10.1021/jp020406t.

[156] V. V. Kislov, N. I. Islamova, A. M. Kolker, S. H. Lin, and A. M. Mebel. Hydrogen abstraction acetylene addition and Diels-Alder mechanisms of PAH formation: A detailed study using first principles calculations. *J. Chem. Theory Comput.*, 1(5): 908–924, 2005. doi:10.1021/ct0500491.

[157] V. V. Kislov, A. I. Sadovnikov, and A. M. Mebel. Formation Mechanism of Polycyclic Aromatic Hydrocarbons beyond the Second Aromatic Ring. *J. Phys. Chem. A*, 117 (23):4794–4816, 2013. doi:10.1021/jp402481y.

[158] D. Koch and J. Hansen. Distant origins of Arctic black carbon: A Goddard Institute for Space Studies ModelE experiment. *J. Geophys. Res. Atmos.*, 110(4):1–14, 2005. doi:10.1029/2004JD005296.

[159] M. Kolb and H. J. Herrmann. Surface fractals in irreversible aggregation. *Phys. Rev. Lett.*, 59:454–457, Jul 1987. doi:10.1103/PhysRevLett.59.454.

[160] W. Krätschmer, L. D. Lamb, K. Fostiropoulos, and D. R. Huffman. Solid C_{60}: a new form of carbon. *Nature*, 347(6291):354–358, Sep 1990. doi:10.1038/347354a0.

[161] H. Kroto. C_{60}^B buckminsterfullerene, other fullerenes and the icospiral shell. *Comput. Math. Appl.*, 17(1):417–423, 1989. doi:10.1016/0898-1221(89)90171-5.

[162] H. W. Kroto. The stability of the fullerenes C_n, with n = 24, 28, 32, 36, 50, 60 and 70. *Nature*, 329(6139):529–531, 1987. doi:10.1038/329529a0.

[163] H. W. Kroto and K. McKay. The formation of quasi-icosahedral spiral shell carbon particles. *Nature*, 331(6154):328–331, Jan 1988. doi:10.1038/331328a0.

[164] H. W. Kroto, J. R. Heath, S. C. O'Brien, R. F. Curl, and R. E. Smalley. C_{60}: Buckminsterfullerene. *Nature*, 318(6042):162–163, Nov 1985. doi:10.1038/318162a0.

[165] A. L. Lafleur, J. B. Howard, J. A. Marr, and T. Yadav. Proposed fullerene precursor corannulene identified in flames both in the presence and absence of fullerene production. *J. Phys. Chem.*, 97(51):13539–13543, 1993. doi:10.1021/j100153a020.

[166] A. L. Lafleur, J. B. Howard, K. Taghizadeh, E. F. Plummer, L. T. Scott, A. Necula, and K. C. Swallow. Identification of $C_{20}H_{10}$ dicyclopentapyrenes in flames: Correlation with corannulene and fullerene formation. *J. Phys. Chem.*, 100(43):17421–17428, 1996. doi:10.1021/jp9605313.

[167] J. Y. W. Lai, P. Elvati, and A. Violi. Stochastic atomistic simulation of polycyclic aromatic hydrocarbon growth in combustion. *Phys. Chem. Chem. Phys.*, 16:7969–7979, 2014. doi:10.1039/C4CP00112E.

[168] R. Larciprete, P. Lacovig, S. Gardonio, A. Baraldi, and S. Lizzit. Atomic oxygen on graphite: Chemical characterization and thermal reduction. *J. Phys. Chem. C*, 116 (18):9900–9908, 2012. doi:10.1021/jp2098153.

[169] C. K. Law. *Combustion Physics*. Cambridge University Press, 2006. doi:10.1017/CBO9780511754517.

[170] A. T. Lawal. Graphene-based nano composites and their applications. a review. *Biosens. Bioelectron.*, 141:111384, 2019. doi:10.1016/j.bios.2019.111384.

[171] C. Lee, X. Wei, J. W. Kysar, and J. Hone. Measurement of the elastic properties and intrinsic strength of monolayer graphene. *Science*, 321(5887):385–388, 2008. doi:10.1126/science.1157996.

[172] H. C. Lee, W.-W. Liu, S.-P. Chai, A. R. Mohamed, A. Aziz, C.-S. Khe, N. S. Hidayah, and U. Hashim. Review of the synthesis, transfer, characterization and growth mechanisms of single and multilayer graphene. *RSC Adv.*, 7:15644–15693, 2017. doi:10.1039/C7RA00392G.

[173] K. Lee, M. Thring, and J. Beér. On the rate of combustion of soot in a laminar soot flame. *Combust. Flame*, 6:137–145, 1962. doi:10.1016/0010-2180(62)90082-2.

[174] Y. A. Levendis and R. C. Flagan. Combustion of uniformly sized glassy carbon particles. *Combust. Sci. Technol.*, 53(2-3):117–136, 1987. doi:10.1080/00102208708947023.

[175] S. Iijima, T. Ichihashi, and Y. Ando. Pentagons, heptagons and negative curvature in graphite microtubule growth. *Nature*, 356(6372):776–778, 1997. doi:10.1038/356776a0.

[176] H. Lin, P. Liu, Z. He, Y. Zhang, B. Guan, and Z. Huang. Formation of the first aromatic ring through the self-recombination of but-1-ene-3-yne with H-assistance in combustion. *Int. J. Hydrog. Energy*, 41(31):13736–13746, 2016. doi:10.1016/j.ijhydene.2016.06.123.

[177] L. Lin, H. Peng, and Z. Liu. Synthesis challenges for graphene industry. *Nat. Mater.*, 18(6):520–524, Jun 2019. doi:10.1038/s41563-019-0341-4.

[178] C. S. Lindberg, M. Y. Manuputty, E. K. Yapp, J. Akroyd, R. Xu, and M. Kraft. A detailed particle model for polydisperse aggregate particles. *J. Comput. Phys.*, 397: 108799, 2019. doi:10.1016/j.jcp.2019.06.074.

[179] P. Liu, H. Lin, Y. Yang, C. Shao, C. Gu, and Z. Huang. New insights into thermal decomposition of polycyclic aromatic hydrocarbon oxyradicals. *J. Phys. Chem. A*, 118(48):11337–11345, 2014. doi:10.1021/jp510498j.

[180] P. Liu, Z. Li, A. Bennett, H. Lin, S. M. Sarathy, and W. L. Roberts. The site effect on PAHs formation in HACA-based mass growth process. *Combust. Flame*, 199:54–68, 2019. doi:10.1016/j.combustflame.2018.10.010.

[181] T. Løvas, D. Nilsson, and F. Mauss. Automatic reduction procedure for chemical mechanisms applied to premixed methane/air flames. *Proc. Combust. Inst.*, 28(2): 1809–1815, 2000. doi:10.1016/S0082-0784(00)80583-4.

[182] T. Løvas, E. Houshfar, M. Bugge, and Ø. Skreiberg. Automatic generation of kinetic skeletal mechanisms for biomass combustion. *Energy Fuels*, 27(11):6979–6991, 2013. doi:10.1021/ef400949h.

[183] P. J. Lupo, P. H. Langlois, J. Reefhuis, C. C. Lawson, E. Symanski, T. A. Desrosiers, Z. G. Khodr, A. J. Agopian, M. A. Waters, K. N. Duwe, R. H. Finnell, L. E. Mitchell, C. A. Moore, P. A. Romitti, and G. M. Shaw. Maternal occupational exposure to polycyclic aromatic hydrocarbons: Effects on gastroschisis among offspring in the national birth defects prevention study. *Environ. Health Perspect.*, 120(6):910–915, 2012. doi:10.1289/ehp.1104305.

[184] U. Maas and S. Pope. Simplifying chemical kinetics: Intrinsic low-dimensional manifolds in composition space. *Combust. Flame*, 88(3):239–264, 1992. doi:10.1016/0010-2180(92)90034-M.

[185] M. Y. Manuputty, C. S. Lindberg, J. A. Dreyer, J. Akroyd, J. Edwards, and M. Kraft. Understanding the anatase-rutile stability in flame-made TiO_2. *Combust. Flame*, 226: 347–361, 2021. doi:10.1016/j.combustflame.2020.12.017.

[186] N. M. Marinov. A detailed chemical kinetic model for high temperature ethanol oxidation. *Int. J. Chem. Kinet.*, 31(3):183–220, 1999. doi:10.1002/(SICI)1097-4601(1999)31:3<183::AID-KIN3>3.0.CO;2-X.

[187] N. M. Marinov and P. C. Malte. Ethylene oxidation in a well-stirred reactor. *Int. J. Chem. Kinet.*, 27(10):957–986, 1995. doi:10.1002/kin.550271003.

[188] N. M. Marinov, W. J. Pitz, C. K. Westbrook, M. J. Castaldi, and S. M. Senkan. *Modeling of aromatic and polycyclic aromatic hydrocarbon formation in premixed methane and ethane flames*, volume 116-117. 1996. ISBN 0010220960893. doi:10.1080/00102209608935550.

[189] J. W. Martin, R. I. Slavchov, E. K. Y. Yapp, J. Akroyd, S. Mosbach, and M. Kraft. The polarization of polycyclic aromatic hydrocarbons curved by pentagon incorporation: The role of the flexoelectric dipole. *J. Phys. Chem. C*, 121(48):27154–27163, 2017. doi:10.1021/acs.jpcc.7b09044.

[190] J. W. Martin, M. Botero, R. I. Slavchov, K. Bowal, J. Akroyd, S. Mosbach, and M. Kraft. Flexoelectricity and the formation of carbon nanoparticles in flames. *J. Phys. Chem. C*, 122(38):22210–22215, 2018. doi:10.1021/acs.jpcc.8b08264.

[191] J. W. Martin, K. Bowal, A. Menon, R. I. Slavchov, J. Akroyd, S. Mosbach, and M. Kraft. Polar curved polycyclic aromatic hydrocarbons in soot formation. *Proc. Combust. Inst.*, 37(1):1117–1123, 2019. doi:10.1016/j.proci.2018.05.046.

[192] J. W. Martin, D. Hou, A. Menon, J. Akroyd, X. You, and M. Kraft. Reactivity of polycyclic aromatic hydrocarbon radicals: Implications for soot formation. *J. Phys. Chem. C*, 123(43):26673, 2019.

[193] J. W. Martin, D. Hou, A. Menon, L. Pascazio, J. Akroyd, X. You, and M. Kraft. Reactivity of polycyclic aromatic hydrocarbon soot precursors: Implications of localized π-radicals on rim-based pentagonal rings. *J. Phys. Chem. C*, 123(43):26673–26682, 2019. doi:10.1021/acs.jpcc.9b07558.

[194] J. W. Martin, A. Menon, C. T. Lao, J. Akroyd, and M. Kraft. Dynamic polarity of curved aromatic soot precursors. *Combust. Flame*, 206:150–157, 2019. doi:10.1016/j.combustflame.2019.04.046.

[195] J. R. McConnell, R. Edwards, G. L. Kok, M. G. Flanner, C. S. Zender, E. S. Saltzman, J. R. Banta, D. R. Pasteris, M. M. Carter, and J. D. W. Kahl. 20th-century industrial black carbon emissions altered arctic climate forcing. *Science*, 317(5843):1381–1384, 2007. doi:10.1126/science.1144856.

[196] B. A. McGuire, R. A. Loomis, A. M. Burkhardt, K. L. K. Lee, C. N. Shingledecker, S. B. Charnley, I. R. Cooke, M. A. Cordiner, E. Herbst, S. Kalenskii, M. A. Siebert, E. R. Willis, C. Xue, A. J. Remijan, and M. C. McCarthy. Detection of two interstellar polycyclic aromatic hydrocarbons via spectral matched filtering. *Science*, 371(6535): 1265–1269, 2021. doi:10.1126/science.abb7535.

[197] J. T. McKinnon. *Chemical and physical mechanisms of soot formation*. PhD thesis, Massachusetts Institute of Technology, 1989.

[198] A. M. Mebel and V. V. Kislov. Can the $C_5H_5 + C_5H_5 \rightarrow C_{10}H_{10} \rightarrow C_{10}H_9 + H$ / $C_{10}H_8 + H_2$ reaction produce naphthalene? An *ab initio*/RRKM Study. *J. Phys. Chem. A*, 5(113):9825–9833, 2009.

[199] A. M. Mebel, Y. Georgievskii, A. W. Jasper, and S. J. Klippenstein. Temperature- and pressure-dependent rate coefficients for the HACA pathways from benzene to naphthalene. *Proc. Combust. Inst.*, 000:1–8, 2016. doi:10.1016/j.proci.2016.07.013.

[200] A. M. Mebel, Y. Georgievskii, A. W. Jasper, and S. J. Klippenstein. Pressure-dependent rate constants for PAH growth: formation of indene and its conversion to naphthalene. *Faraday Discuss.*, 195:637–670, 2016. doi:10.1039/C6FD00111D.

[201] A. M. Mebel, Y. Georgievskii, A. W. Jasper, and S. J. Klippenstein. Temperature- and pressure-dependent rate coefficients for the HACA pathways from benzene to naphthalene. *Proc. Combust. Inst.*, 36(1):919–926, 2017. doi:10.1016/j.proci.2016.07.013.

[202] A. M. Mebel, A. Landera, and R. I. Kaiser. Formation mechanisms of naphthalene and indene: From the interstellar medium to combustion flames. *J. Phys. Chem. A*, 121(5):901–926, 2017. doi:10.1021/acs.jpca.6b09735.

[203] R. S. Mehta, D. C. Haworth, and M. F. Modest. An assessment of gas-phase reaction mechanisms and soot models for laminar atmospheric-pressure ethylene-air flames. *Proc. Combust. Inst.*, 32(1):1327–1334, 2009. doi:10.1016/j.proci.2008.06.149.

[204] C. F. Melius, J. A. Miller, and E. M. Evleth. Unimolecular reaction mechanisms involving C_3H_4, C_4H_4, and C_6H_6 hydrocarbon species. *Symp. (Int.) Combust.*, 24(1): 621–628, 1992. doi:10.1016/S0082-0784(06)80076-7. Twenty-Fourth Symposium on Combustion.

[205] C. F. Melius, M. E. Colvin, N. M. Marinov, W. J. Pit, and S. M. Senkan. Reaction mechanisms in aromatic hydrocarbon formation involving the C_5H_5 cyclopentadienyl moiety. *Symp. (Int.) Combust.*, 26(1):685–692, 1996. doi:10.1016/S0082-0784(96)80276-1.

[206] A. Menon, G. Leon, J. Akroyd, and M. Kraft. A density functional theory study on the kinetics of seven-member ring formation in polyaromatic hydrocarbons. *Combust. Flame*, 217:152–174, 2020. doi:10.1016/j.combustflame.2020.03.032.

[207] A. Menon, J. Martin, G. Leon, D. Hou, L. Pascazio, X. You, and M. Kraft. Reactive localized π-radicals on rim-based pentagonal rings: Properties and concentration in flames. *Proc. Combust. Inst.*, 2020. doi:10.1016/j.proci.2020.07.042.

[208] A. Menon, J. W. Martin, J. Akroyd, and M. Kraft. Reactivity of polycyclic aromatic hydrocarbon soot precursors: Kinetics and equilibria. *J. Phys. Chem. A*, 124(48): 10040–10052, 2020. doi:10.1021/acs.jpca.0c07811.

[209] H. A. Michelsen, M. B. Colket, P.-E. Bengtsson, A. D'Anna, P. Desgroux, B. S. Haynes, J. H. Miller, G. J. Nathan, H. Pitsch, and H. Wang. A review of terminology used to describe soot formation and evolution under combustion and pyrolytic conditions. *ACS Nano*, 14(10):12470–12490, 2020. doi:10.1021/acsnano.0c06226.

[210] J. A. Miller and S. J. Klippenstein. The recombination of propargyl radicals: Solving the master equation. *J. Phys. Chem. A*, 105(30):7254–7266, 2001. doi:10.1021/jp0102973.

[211] J. A. Miller and S. J. Klippenstein. The recombination of propargyl radicals and other reactions on a C_6H_6 potential. *J. Phys. Chem. A*, 107(39):7783–7799, 2003. doi:10.1021/jp030375h.

[212] J. A. Miller and C. F. Melius. Kinetic and thermodynamic issues in the formation of aromatic compounds in flames of aliphatic fuels. *Combust. Flame*, 91(1):21–39, 1992. doi:10.1016/0010-2180(92)90124-8.

[213] J. H. Miller, J. D. Herdman, C. D. Green, and E. M. Webster. Experimental and computational determinations of optical band gaps for PAH and soot in a N2-diluted, ethylene/air non-premixed flame. *Proc. Combust. Inst.*, 34(2):3669–3675, 2013. doi:10.1016/j.proci.2012.05.054.

[214] P. Mitchell and M. Frenklach. Monte Carlo simulation of soot aggregation with simultaneous surface growth-why primary particles appear spherical. *Symp. (Int.) Combust.*, 27(1):1507–1514, 1998. doi:10.1016/S0082-0784(98)80558-4. Twenty-Seventh Sysposium (International) on Combustion Volume One.

[215] P. Mitchell and M. Frenklach. Particle aggregation with simultaneous surface growth. *Phys. Rev. E*, 67:061407, Jun 2003. doi:10.1103/PhysRevE.67.061407.

[216] T. Mitra, T. Zhang, A. D. Sediako, and M. J. Thomson. Understanding the formation and growth of polycyclic aromatic hydrocarbons (PAHs) and young soot from n-dodecane in a sooting laminar coflow diffusion flame. *Combust. Flame*, 202:33–42, 2019. doi:10.1016/j.combustflame.2018.12.010.

[217] V. B. Mohan, K. tak Lau, D. Hui, and D. Bhattacharyya. Graphene-based materials and their composites: A review on production, applications and product limitations. *Compos. B. Eng*, 142:200–220, 2018. doi:10.1016/j.compositesb.2018.01.013.

[218] M. Mojica, J. A. Alonso, and F. Méndez. Synthesis of fullerenes. *J. Phys. Org. Chem.*, 26(7):526–539, 2013. doi:10.1002/poc.3121.

[219] J. Molina. Graphene-based fabrics and their applications: a review. *RSC Adv.*, 6: 68261–68291, 2016. doi:10.1039/C6RA12365A.

[220] N. Morgan, M. Kraft, M. Balthasar, D. Wong, M. Frenklach, and P. Mitchell. Numerical simulations of soot aggregation in premixed laminar flames. *Proc. Combust. Inst.*, 31(1):693–700, 2007. doi:10.1016/j.proci.2006.08.021.

[221] N. W. Moriarty and M. Frenklach. *Ab initio* study of naphthalene formation by addition of vinylacetylene to phenyl. *Proc. Combust. Inst.*, 28(2):2563–2568, 2000. doi:10.1016/S0082-0784(00)80673-6.

[222] N. W. Moriarty, N. J. Brown, and M. Frenklach. Hydrogen migration in the phenylethen-2-yl radical. *J. Phys. Chem. A*, 103(35):7127–7135, 1999. doi:Doi 10.1021/Jp991481f.

[223] Z. Mou and M. Kertesz. Pancake bond orders of a series of π-stacked triangulene radicals. *Angew. Chem. Int. Ed. Engl.*, 56(34):10188–10191, 2017. doi:10.1002/anie.201704941.

[224] R. Muñoz and C. Gómez-Aleixandre. Review of CVD synthesis of graphene. *Chem. Vap. Deposition*, 19(10-11-12):297–322, 2013. doi:10.1002/cvde.201300051.

[225] A. Münzer, L. Xiao, Y. H. Sehlleier, C. Schulz, and H. Wiggers. All gas-phase synthesis of graphene: Characterization and its utilization for silicon-based lithium-ion batteries. *Electrochim. Acta*, 272:52–59, 2018. doi:10.1016/j.electacta.2018.03.137.

[226] A. Nag, A. Mitra, and S. C. Mukhopadhyay. Graphene and its sensor-based applications: A review. *Sens. Actuators A: Phys.*, 270:177–194, 2018. doi:10.1016/j.sna.2017.12.028.

[227] K. Narayanaswamy, G. Blanquart, and H. Pitsch. A consistent chemical mechanism for oxidation of substituted aromatic species. *Combust. Flame*, 157(10):1879–1898, 2010. doi:10.1016/j.combustflame.2010.07.009.

[228] A. Naseri, A. D. Sediako, F. Liu, M. Barati, R. D. Baker, and M. J. Thomson. In-situ studies of O_2 and O radical oxidation of carbon black using thermogravimetric analysis and environmental transmission electron microscopy. *Carbon*, 156:299–308, 2020. doi:10.1016/j.carbon.2019.09.039.

[229] M. Nayebzadeh, M. Vahedpour, A. Shiroudi, and J. M. Rius-Bartra. Kinetics and oxidation mechanism of pyrene initiated by hydroxyl radical. A theoretical investigation. *Chem. Phys.*, 528:110522, 2020. doi:10.1016/j.chemphys.2019.110522.

[230] K. Neoh, J. Howard, and A. Sarofim. Effect of oxidation on the physical structure of soot. *Symp. (Int.) Combust.*, 20(1):951–957, 1985. doi:10.1016/S0082-0784(85)80584-1. Twentieth Symposium (International) on Combustion.

[231] K. G. Neoh. *Soot burnout in flames*. PhD thesis, Massachusetts Institute of Technology, 1981.

[232] K. G. Neoh, J. B. Howard, and A. F. Sarofim. *Soot Oxidation in Flames*. Springer US, Boston, MA, 1981. doi:10.1007/978-1-4757-6137-5_9.

[233] K. S. Novoselov, A. K. Geim, S. V. Morozov, D. Jiang, Y. Zhang, S. V. Dubonos, I. V. Grigorieva, and A. A. Firsov. Electric field effect in atomically thin carbon films. *Science*, 306(5696):666–669, 2004. doi:10.1126/science.1102896.

[234] N. M. O'Boyle, M. Banck, C. A. James, C. Morley, T. Vandermeersch, and G. R. Hutchison. Open babel: An open chemical toolbox. *J. Cheminformatics*, 3(1):33, Oct 2011. doi:10.1186/1758-2946-3-33.

[235] N. M. O'Boyle, M. Banck, C. A. James, C. Morley, T. Vandermeersch, and G. R. Hutchison. The Open Babel package. http://openbabel.org, 2011. Version 2.3.1. (accessed: 17.04.2019).

[236] K. Ono, K. Dewa, Y. Matsukawa, Y. Saito, Y. Matsushita, H. Aoki, K. Era, T. Aoki, and T. Yamaguchi. Experimental evidence for the sintering of primary soot particles. *J. Aerosol Sci.*, 105:1–9, 2017. doi:10.1016/j.jaerosci.2016.11.013.

[237] R. Ono. Optical diagnostics of reactive species in atmospheric-pressure nonthermal plasma. *J. Phys. D: Appl. Phys.*, 49(8):083001, 2016. doi:10.1088/0022-3727/49/8/083001.

[238] S. Park and R. S. Ruoff. Chemical methods for the production of graphenes. *Nature Nanotech.*, 4(4):217–224, Apr 2009. doi:10.1038/nnano.2009.58.

[239] D. S. N. Parker, F. Zhang, Y. S. Kim, R. I. Kaiser, A. Landera, V. V. Kislov, A. M. Mebel, and A. G. G. M. Tielens. Low temperature formation of naphthalene and its role in the synthesis of PAHs (Polycyclic Aromatic Hydrocarbons) in the interstellar medium. *Proc. Natl. Acad. Sci. U.S.A*, 109(1):53–58, 2012. doi:10.1073/pnas.1113827108.

[240] L. Pascazio, J. W. Martin, A. Menon, D. Hou, X. You, and M. Kraft. Aromatic penta-linked hydrocarbons in soot nanoparticle formation. *Proc. Combust. Inst.*, 2020. doi:10.1016/j.proci.2020.09.029.

[241] R. I. Patterson, J. Singh, M. Balthasar, M. Kraft, and W. Wagner. Extending stochastic soot simulation to higher pressures. *Combust. Flame*, 145(3):638–642, 2006. doi:10.1016/j.combustflame.2006.02.005.

[242] R. I. A. Patterson and M. Kraft. Models for the aggregate structure of soot particles. *Combust. Flame*, 151(1-2):160–172, 2007. doi:10.1016/j.combustflame.2007.04.012.

[243] R. I. A. Patterson, J. Singh, M. Balthasar, M. Kraft, and J. R. Norris. The linear process deferment algorithm: A new technique for solving population balance equations. *SIAM J. Sci. Comput.*, 28(1):303–320, 2006. doi:10.1137/040618953.

[244] F. Pedregosa, G. Varoquaux, A. Gramfort, V. Michel, B. Thirion, O. Grisel, M. Blondel, P. Prettenhofer, R. Weiss, V. Dubourg, J. Vanderplas, A. Passos, D. Cournapeau, M. Brucher, M. Perrot, and E. Duchesnay. Scikit-learn: Machine learning in Python. *J. Mac. Learn. Res.*, 12:2825–2830, 2011.

[245] S. J. Pendleton, A. Montello, C. Carter, W. Lempert, and M. A. Gundersen. Vibrational and rotational CARS measurements of nitrogen in afterglow of streamer discharge in atmospheric pressure fuel/air mixtures. *J. Phys. D: Appl. Phys.*, 45(49):495401, 2012. doi:10.1088/0022-3727/45/49/495401.

[246] S. J. Pendleton, S. Bowman, C. Carter, M. A. Gundersen, and W. Lempert. The production and evolution of atomic oxygen in the afterglow of streamer discharge in atmospheric pressure fuel/air mixtures. *J. Phys. D: Appl. Phys.*, 46(30):305202, 2013. doi:10.1088/0022-3727/46/30/305202.

[247] N. Peters and B. Rogg. *Reduced Kinetic Mechanisms for Applications in Combustion Systems*. Springer-Verlag Berlin Heidelberg, 1993. doi:10.1007/978-3-540-47543-9.

[248] A. I. Podlivaev and L. A. Openov. Dynamics of the Stone-Wales defect in graphene. *Phys. Solid State*, 57(4):820–824, Apr 2015. doi:10.1134/S1063783415040265.

[249] C. J. Pope, J. A. Marr, and J. B. Howard. Chemistry of fullerenes C_{60} and C_{70} formation in flames. *J. Phys. Chem.*, 97(42):11001–11013, 1993. doi:10.1021/j100144a018.

[250] S. B. Pope. Small scales, many species and the manifold challenges of turbulent combustion. *Proc. Combust. Inst.*, 34(1):1–31, 2013. doi:10.1016/j.proci.2012.09.009.

[251] J. Prager, H. N. Najm, M. Valorani, and D. A. Goussis. Skeletal mechanism generation with CSP and validation for premixed n-heptane flames. *Proc. Combust. Inst.*, 32 I(1):509–517, 2009. doi:10.1016/j.proci.2008.06.074.

[252] S. E. Pratsinis. Simultaneous nucleation, condensation, and coagulation in aerosol reactors. *J. Colloid Interface Sci.*, 124(2):416–427, 1988. doi:10.1016/0021-9797(88)90180-4.

[253] S. H. Pun and Q. Miao. Toward negatively curved carbons. *Acc. Chem. Res.*, 51(7):1630–1642, 2018. doi:10.1021/acs.accounts.8b00140.

[254] J. Quaas, Y. Ming, S. Menon, T. Takemura, M. Wang, J. E. Penner, A. Gettelman, U. Lohmann, N. Bellouin, O. Boucher, A. M. Sayer, G. E. Thomas, A. McComiskey, G. Feingold, C. Hoose, J. E. Kristjánsson, X. Liu, Y. Balkanski, L. J. Donner, P. A. Ginoux, P. Stier, B. Grandey, J. Feichter, I. Sednev, S. E. Bauer, D. Koch, R. G. Grainger, A. Kirkevg, T. Iversen, Ø. Seland, R. Easter, S. J. Ghan, P. J. Rasch, H. Morrison, J.-F. Lamarque, M. J. Iacono, S. Kinne, and M. Schulz. Aerosol indirect

effects – general circulation model intercomparison and evaluation with satellite data. *Atmos. Chem. Phys.*, 9(22):8697–8717, 2009. doi:10.5194/acp-9-8697-2009.

[255] A. Raj. Structural effects on the growth of large polycyclic aromatic hydrocarbons by C_2H_2. *Combust. Flame*, 204:331–340, 2019. doi:10.1016/j.combustflame.2019.03.027.

[256] A. Raj, M. Celnik, R. Shirley, M. Sander, R. Patterson, R. West, and M. Kraft. A statistical approach to develop a detailed soot growth model using PAH characteristics. *Combust. Flame*, 156(4):896–913, 2009. doi:10.1016/j.combustflame.2009.01.005.

[257] A. Raj, P. L. W. Man, T. S. Totton, M. Sander, R. A. Shirley, and M. Kraft. New polycyclic aromatic hydrocarbon (PAH) surface processes to improve the model prediction of the composition of combustion-generated PAHs and soot. *Carbon*, 48 (2):319–332, 2010. doi:10.1016/j.carbon.2009.09.030.

[258] A. Raj, M. Sander, V. Janardhanan, and M. Kraft. A study on the coagulation of polycyclic aromatic hydrocarbon clusters to determine their collision efficiency. *Combust. Flame*, 157(3):523–534, 2010. doi:10.1016/j.combustflame.2009.10.003.

[259] A. Raj, I. D. C. Prada, A. A. Amer, and S. H. Chung. A reaction mechanism for gasoline surrogate fuels for large polycyclic aromatic hydrocarbons. *Combust. Flame*, 159(2):500–515, 2012. doi:10.1016/j.combustflame.2011.08.011.

[260] V. Ramanathan and G. Carmichael. Global and regional climate changes due to black carbon. *Nat. Geosci.*, 1:221 – 227, 2008. doi:10.1038/ngeo156.

[261] E. Ranzi and T. Faravelli. CRECK Modeling Group, 2015. Accessed 01 March 2019.

[262] E. Ranzi, A. Frassoldati, R. Grana, A. Cuoci, T. Faravelli, A. P. Kelley, and C. K. Law. Hierarchical and comparative kinetic modeling of laminar flame speeds of hydrocarbon and oxygenated fuels. *Prog. Energy Combust. Sci.*, 38(4):468–501, 2012. doi:10.1016/j.pecs.2012.03.004.

[263] H. Richter and J. Howard. *Formation of polycyclic aromatic hydrocarbons and their growth to soot - a review of chemical reaction pathways*, volume 26. 2000. ISBN 0360-1285. doi:10.1016/S0360-1285(00)00009-5.

[264] H. Richter and J. B. Howard. Formation and consumption of single-ring aromatic hydrocarbons and their precursors in premixed acetylene, ethylene and benzene flames. *Phys. Chem. Chem. Phys.*, 4:2038–2055, 2002. doi:10.1039/B110089K.

[265] H. Richter, W. J. Grieco, and J. B. Howard. Formation mechanism of polycyclic aromatic hydrocarbons and fullerenes in premixed benzene flames. *Combust. Flame*, 119(1-2):1–22, 1999. doi:10.1016/S0010-2180(99)00032-2.

[266] H. Richter, S. Granata, W. H. Green, and J. B. Howard. Detailed modeling of PAH and soot formation in a laminar premixed benzene/oxygen/argon low-pressure flame. *Proc. Combust. Inst.*, 30(1):1397–1405, 2005. doi:j.proci.2004.08.088.

[267] A. W. Robertson and J. H. Warner. Atomic resolution imaging of graphene by transmission electron microscopy. *Nanoscale*, 5:4079–4093, 2013. doi:10.1039/C3NR00934C.

[268] D. E. Rosner and H. D. Allendorf. High-temperature kinetics of graphite oxidation by dissociated oxygen. *AIAA J.*, 3(8):1522–1523, 1965. doi:10.2514/3.3186.

[269] S. P. Roy and D. C. Haworth. A systematic comparison of detailed soot models and gas-phase chemical mechanisms in laminar premixed flames. *Combust. Sci. Technol.*, 188(7):1021–1053, 2016. doi:10.1080/00102202.2016.1145117.

[270] H. Sabbah, L. Biennier, S. J. Klippenstein, I. R. Sims, and B. R. Rowe. Exploring the role of PAHs in the formation of soot: Pyrene dimerization. *J. Phys. Chem. A*, 1(19):2962–2967, 2010. doi:10.1021/jz101033t.

[271] K. Sabelfeld, S. Rogasinsky, A. Kolodko, and A. Levykin. Stochastic algorithms for solving Smolouchovsky coagulation equation and applications to aerosol growth simulation. *Monte Carlo Methods Appl.*, 2(1):41–88, 1996. doi:10.1515/mcma.1996.2.1.41.

[272] B. Saha, S. Irle, and K. Morokuma. Hot giant fullerenes eject and capture C_2 molecules: QM/MD simulations with constant density. *J. Phys. Chem. C*, 115(46):22707–22716, 2011. doi:10.1021/jp203614e.

[273] M. Salamanca, M. Sirignano, M. Commodo, P. Minutolo, and A. D'Anna. The effect of ethanol on the particle size distributions in ethylene premixed flames. *Exp. Therm. Fluid Sci.*, 43:71–75, 2012. doi:10.1016/j.expthermflusci.2012.04.006. Seventh Mediterranean Combustion Symposium.

[274] J. C. Saldinger, Q. Wang, P. Elvati, and A. Violi. Characterizing the diversity of aromatics in a coflow diffusion Jet A-1 surrogate flame. *Fuel*, 268:117198, 2020. doi:10.1016/j.fuel.2020.117198.

[275] M. Sander, R. H. West, M. S. Celnik, and M. Kraft. A detailed model for the sintering of polydispersed nanoparticle agglomerates. *Aerosol Sci Tech*, 43(10):978–989, 2009. doi:10.1080/02786820903092416.

[276] M. Sander, R. I. A. Patterson, A. Braumann, A. Raj, and M. Kraft. Developing the PAH-PP soot particle model using process informatics and uncertainty propagation. *Proc. Combust. Inst.*, 33(1):675–683, 2011. doi:10.1016/j.proci.2010.06.156.

[277] K. Sasaki, T. Wakasaki, S. Matsui, and K. Kadota. Distributions of C_2 and C_3 radical densities in laser-ablation carbon plumes measured by laser-induced fluorescence imaging spectroscopy. *J. Appl. Phys.*, 91(7):4033–4039, 2002. doi:10.1063/1.1455151.

[278] M. Schenk, L. Leon, K. Moshammer, P. Oßwald, T. Zeuch, L. Seidel, F. Mauss, and K. Kohse-Höinghaus. Detailed mass spectrometric and modeling study of isomeric butene flames. *Combust. Flame*, 160(3):487–503, 2013. doi:10.1016/j.combustflame.2012.10.023.

[279] C. A. Schuetz and M. Frenklach. Nucleation of soot: Molecular dynamics simulations of pyrene dimerization. *Proc. Combust. Inst.*, 29(2):2307–2314, 2002. doi:10.1016/S1540-7489(02)80281-4.

[280] P. Schwerdtfeger, L. N. Wirz, and J. Avery. The topology of fullerenes. *Wiley Interdiscip. Rev. Comput. Mol. Sci.*, 5(1):96–145, 2015. doi:10.1002/wcms.1207.

[281] L. T. Scott. Methods for the chemical synthesis of fullerenes. *Angew. Chem. Int. Ed. Engl.*, 43(38):4994–5007, 2004. doi:10.1002/anie.200400661.

[282] A. S. Semenikhin, A. S. Savchenkova, I. V. Chechet, S. G. Matveev, Z. Liu, M. Frenklach, and A. M. Mebel. Rate constants for H abstraction from benzo(a)pyrene and chrysene: A theoretical study. *Phys. Chem. Chem. Phys.*, 19:25401–25413, 2017. doi:10.1039/C7CP05560A.

[283] A. S. Semenikhin, A. S. Savchenkova, I. V. Chechet, S. G. Matveev, M. Frenklach, and A. M. Mebel. Transformation of an embedded five-membered ring in polycyclic aromatic hydrocarbons via the Hydrogen-Abstraction–Acetylene-Addition mechanism: A theoretical study. *J. Phys. Chem. A*, 125(16):3341–3354, 2021. doi:10.1021/acs.jpca.1c00900.

[284] R. F. Service. Study fingers soot as a major player in global warming. *Science*, 319 (March):2008, 2008. doi:10.1126/science.319.5871.1745.

[285] S. Shekar, W. J. Menz, A. J. Smith, M. Kraft, and W. Wagner. On a multivariate population balance model to describe the structure and composition of silica nanoparticles. *Comput. Chem. Eng.*, 43:130–147, 2012. doi:10.1016/j.compchemeng.2012.04.010.

[286] H. Shen, L. Zhang, M. Liu, and Z. Zhang. Biomedical applications of graphene. *Theranostics*, 2(3):283–294, 2012. doi:10.7150/thno.3642.

[287] Y. Shen and C.-F. Chen. Helicenes: Synthesis and applications. *Chem. Rev.*, 112(3): 1463–1535, 2012. doi:10.1021/cr200087r.

[288] B. S. Sherigara, W. Kutner, and F. D'Souza. Electrocatalytic properties and sensor applications of fullerenes and carbon nanotubes. *Electroanalysis*, 15(9):753–772, 2003. doi:10.1002/elan.200390094.

[289] R. Siddall. Mineral pigments in archaeology: Their analysis and the range of available materials. *Minerals*, 8(5), 2018. doi:10.3390/min8050201.

[290] K. Siegmann, H. Hepp, and K. Sattler. Reactive dimerization: A new PAH growth mechanism in flames. *Combust. Sci. Technol.*, 109(1-6):165–181, 1995. doi:10.1080/00102209508951900.

[291] J. Singh, M. Balthasar, M. Kraft, and W. Wagner. Stochastic modeling of soot particle size and age distributions in laminar premixed flames. *Proc. Combust. Inst.*, 30(1): 1457–1464, 2005. doi:10.1016/j.proci.2004.08.120.

[292] M. Singh, A. Sengupta, K. Zeller, G. Skoptsov, and R. L. Vander Wal. Effect of hydrogen concentration on graphene synthesis using microwave-driven plasma-mediated methane cracking. *Carbon*, 143:802–813, 2019. doi:10.1016/j.carbon.2018.11.082.

[293] R. Singh and M. Frenklach. A mechanistic study of the influence of graphene curvature on the rate of high-temperature oxidation by molecular oxygen. *Carbon*, 101:203–212, 2016. doi:10.1016/j.carbon.2016.01.090.

[294] R. I. Singh, A. M. Mebel, and M. Frenklach. Oxidation of graphene-edge six- and five-member rings by molecular oxygen. *J. Phys. Chem. A*, 119(28):7528–7547, 2015. doi:10.1021/acs.jpca.5b00868.

[295] M. Sirignano and C. Russo. Pyrene dimerization in controlled temperature environment: An experimental study. *Proc. Combust. Inst.*, 38(1):1173–1180, 2021. doi:https://doi.org/10.1016/j.proci.2020.06.367.

[296] S. A. Skeen, H. A. Michelsen, K. R. Wilson, D. M. Popolan, A. Violi, and N. Hansen. Near-threshold photoionization mass spectra of combustion-generated high-molecular-weight soot precursors. *J. Aerosol Sci.*, 58:86–102, 2013. doi:10.1016/j.jaerosci.2012.12.008.

[297] N. A. Slavinskaya and P. Frank. A modelling study of aromatic soot precursors formation in laminar methane and ethene flames. *Combust. Flame*, 156(9):1705–1722, 2009. doi:10.1016/j.combustflame.2009.04.013.

[298] N. A. Slavinskaya, U. Riedel, S. B. Dworkin, and M. J. Thomson. Detailed numerical modeling of PAH formation and growth in non-premixed ethylene and ethane flames. *Combust. Flame*, 159(3):979–995, 2012. doi:10.1016/j.combustflame.2011.10.005.

[299] A. Smallbone, A. Bhave, A. R. Coble, S. Mosbach, M. Kraft, and R. McDavid. *Identifying Optimal Operating Points in Terms of Engineering Constraints and Regulated Emissions in Modern Diesel Engines*. SAE International, 2011-01-1388. doi:10.4271/2011-01-1388.

[300] G. P. Smith, D. M. Golden, M. Frenklach, N. W. Moriarty, B. Eiteneer, M. Goldenberg, C. T. Bowman, R. K. Hanson, S. Song, W. C. Gardiner, Jr., V. V. Lissianski, and Z. Qin. GRI-MECH 3.0. http://www.me.berkeley.edu/gri_mech/, 1999. Version 3.0. (accessed: 01.04.2017).

[301] G. P. Smith, C. Park, J. Schneiderman, and J. Luque. C_2 Swan band laser-induced fluorescence and chemiluminescence in low-pressure hydrocarbon flames. *Combust. Flame*, 141(1):66–77, 2005. doi:10.1016/j.combustflame.2004.12.010.

[302] M. V. Smoluchowski. Versuch einer mathematischen theorie der koagulationskinetik kolloider lösungen. *Z. Phys. Chem.*, 92U(1):129–168, 1918. doi:doi:10.1515/zpch-1918-9209.

[303] M. Smooke, C. McEnally, L. Pfefferle, R. Hall, and M. Colket. Computational and experimental study of soot formation in a coflow, laminar diffusion flame. *Combust. Flame*, 117(1):117–139, 1999. doi:10.1016/S0010-2180(98)00096-0.

[304] M. D. Smooke, R. J. Hall, M. B. Colket, J. Fielding, M. B. Long, C. S. McEnally, and L. D. Pfefferle. Investigation of the transition from lightly sooting towards heavily sooting co-flow ethylene diffusion flames. *Combust. Theory Model.*, 8(3):593–606, 2004. doi:10.1088/1364-7830/8/3/009.

[305] M. Sola. Forty years of Clar's aromatic π-sextet rule. *Front. Chem.*, 1(October):4–11, 2013. doi:10.3389/fchem.2013.00022.

[306] S. E. Stein and A. Fahr. High-temperature stabilities of hydrocarbons. *J. Phys. Chem.*, 89(17):3714–3725, 1985. doi:10.1021/j100263a027.

[307] S. E. Stein, J. A. Walker, M. M. Suryan, and A. Fahr. A new path to benzene in flames. *Symp. (Int.) Combust.*, 23(1):85–90, 1991. doi:10.1016/S0082-0784(06)80245-6. Twenty-Third Symposium (International) on Combustion.

[308] Z. Sun and J. Wu. Open-shell polycyclic aromatic hydrocarbons. *J. Mater. Chem.*, 22:4151–4160, 2012. doi:10.1039/C1JM14786B.

[309] H. Takehara, M. Fujiwara, M. Arikawa, M. D. Diener, and J. M. Alford. Experimental study of industrial scale fullerene production by combustion synthesis. *Carbon*, 43(2):311–319, 2005. doi:10.1016/j.carbon.2004.09.017.

[310] Y. Tan and P. Frank. A detailed comprehensive kinetic model for benene oxidation using the recent kinetic results. *Symp. (Int.) Combust.*, 26(1):677–684, 1996. doi:10.1016/S0082-0784(96)80275-X.

[311] W. Tang, R. S. Tranter, and K. Brezinsky. An optimized semidetailed submechanism of benzene formation from propargyl recombination. *J. Phys. Chem. A*, 110(6):2165–2175, 2006. doi:10.1021/jp052797s.

[312] E. Tatarova, F. M. Dias, E. Felizardo, J. Henriques, C. M. Ferreira, and B. Gordiets. Microwave plasma torches driven by surface waves. *Plasma Sources Sci. Technol.*, 17(2):024004, 2008. doi:10.1088/0963-0252/17/2/024004.

[313] E. Tatarova, J. P. Henriques, E. Felizardo, M. Lino da Silva, C. M. Ferreira, and B. Gordiets. Microwave plasma source operating with atmospheric pressure air-water mixtures. *J. Appl. Phys.*, 112(9):093301, 2012. doi:10.1063/1.4762015.

[314] E. Tatarova, J. Henriques, C. C. Luhrs, A. Dias, J. Phillips, M. V. Abrashev, and C. M. Ferreira. Microwave plasma based single step method for free standing graphene synthesis at atmospheric conditions. *Appl. Phys. Lett.*, 103(13):134101, 2013. doi:10.1063/1.4822178.

[315] E. Tatarova, A. Dias, J. Henriques, A. M. B. do Rego, A. M. Ferraria, M. V. Abrashev, C. C. Luhrs, J. Phillips, F. M. Dias, and C. M. Ferreira. Microwave plasmas applied for the synthesis of free standing graphene sheets. *J. Phys. D: Appl. Phys.*, 47(38):385501, 2014. doi:10.1088/0022-3727/47/38/385501.

[316] E. Tatarova, A. Dias, J. Henriques, M. Abrashev, N. Bundaleska, E. Kovacevic, N. Bundaleski, U. Cvelbar, E. Valcheva, B. Arnaudov, A. M. B. do Rego, A. M. Ferraria, J. Berndt, E. Felizardo, O. M. N. D. Teodoro, T. Strunskus, L. L. Alves, and B. Gonçalves. Towards large-scale in free-standing graphene and n-graphene sheets. *Sci. Rep.*, 7(1):10175, Aug 2017. doi:10.1038/s41598-017-10810-3.

[317] H. Terrones and M. Terrones. Curved nanostructured materials. *New J. Phys.*, 5:126–126, Oct 2003. doi:10.1088/1367-2630/5/1/126.

[318] H.-R. Tian, M.-M. Chen, K. Wang, Z.-C. Chen, C.-Y. Fu, Q. Zhang, S.-H. Li, S.-L. Deng, Y.-R. Yao, S.-Y. Xie, R.-B. Huang, and L.-S. Zheng. An unconventional hydrofullerene $C_{66}H_4$ with symmetric heptagons retrieved in low-pressure combustion. *J. Am. Chem. Soc.*, 141(16):6651–6657, 2019. doi:10.1021/jacs.9b01638.

[319] A. Tielens. Interstellar polycyclic aromatic hydrocarbon molecules. *Annu. Rev. Astron. Astrophys.*, 46(1):289–337, 2008. doi:10.1146/annurev.astro.46.060407.145211.

[320] A. Tikhonov. Systems of differential equations containing small parameters for derivatives. *Mat. Sb.*, 31 (73)(3):575–586, 1952. In Russian.

[321] W. Tsang and R. F. Hampson. Chemical kinetic data base for combustion chemistry. Part I. Methane and related compounds. *J. Phys. Chem. Ref. Data*, 15(3):1087–1279, 1986. doi:10.1063/1.555759.

[322] S. Tsantilis and S. E. Pratsinis. Soft- and hard-agglomerate aerosols made at high temperatures. *Langmuir*, 20(14):5933–5939, 2004. doi:10.1021/la036389w.

[323] D. Tsyganov, N. Bundaleska, E. Tatarova, A. Dias, J. Henriques, A. Rego, A. Ferraria, M. Abrashev, F. Dias, C. C. Luhrs, et al. On the plasma-based growth of 'flowing' graphene sheets at atmospheric pressure conditions. *Plasma Sources Sci. Technol.*, 25(1):015013, 2015. doi:10.1088/0963-0252/25/1/015013.

[324] T. Turányi and A. S. Tomlin. *Analysis of Kinetic Reaction Mechanisms*. Springer, Berlin, Heidelberg, 2015. doi:10.1007/978-3-662-44562-4.

[325] T. Turányi, A. S. Tomlin, and M. J. Pilling. On the error of the quasi-steady-state approximation. *J. Phys. Chem.*, 97(1):163–172, 1993. doi:10.1021/j100103a028.

[326] B. V. Unterreiner, M. Sierka, and R. Ahlrichs. Reaction pathways for growth of polycyclic aromatic hydrocarbons under combustion conditions, a DFT study. *Phys. Chem. Chem. Phys.*, 6(18):4377–4384, 2004. doi:10.1039/b407279k.

[327] M. J. Vallius, J. Ruuskanen, A. Mirme, and J. Pekkanen. Concentrations and estimated soot content of PM1, PM2.5, and PM10 in a subarctic urban atmosphere. *Environ. Sci. Technol.*, 34(10):1919–1925, 2000. doi:10.1021/es990603e.

[328] S. Vemury and S. E. Pratsinis. Self-preserving size distributions of agglomerates. *J. Aerosol Sci.*, 26(2):175–185, 1995. doi:10.1016/0021-8502(94)00103-6.

[329] A. Veshkini, S. B. Dworkin, and M. J. Thomson. A soot particle surface reactivity model applied to a wide range of laminar ethylene/air flames. *Combust. Flame*, 161 (12):3191–3200, 2015. doi:10.1016/j.combustflame.2014.05.024.

[330] A. Violi. Cyclodehydrogenation reactions to cyclopentafused polycyclic aromatic hydrocarbons. *J. Phys. Chem. A*, 109(34):7781–7787, 2005. doi:10.1021/jp052384r.

[331] A. Violi, A. Kubota, T. Truong, W. Pitz, C. Westbrook, and A. Sarofim. A fully integrated kinetic Monte Carlo/molecular dynamics approach for the simulation of soot precursor growth. *Proc. Combust. Inst.*, 29(2):2343–2349, 2002. doi:10.1016/S1540-7489(02)80285-1.

[332] J. Walls and R. Strickland-Constable. Oxidation of carbon between 1000–2400°C. *Carbon*, 1(3):333 – 338, 1964. doi:10.1016/0008-6223(64)90288-X.

[333] C. Wang, T. Huddle, C.-H. Huang, W. Zhu, R. L. V. Wal, E. H. Lester, and J. P. Mathews. Improved quantification of curvature in high-resolution transmission electron microscopy lattice fringe micrographs of soots. *Carbon*, 117:174–181, 2017. doi:10.1016/j.carbon.2017.02.059.

[334] C. Wang, Z. Lu, J. Ma, X. Chen, C. Yang, and W. Xia. Pressure-dependent synthesis of graphene nanoflakes using $Ar/H_2/CH_4$ non-thermal plasma based on rotating arc discharge. *Diam. Relat. Mater.*, 111:108176, 2021. doi:10.1016/j.diamond.2020.108176.

[335] H. Wang. Formation of nascent soot and other condensed-phase materials in flames. *Proc. Combust. Inst.*, 33(1):41–67, 2011. doi:10.1016/j.proci.2010.09.009.

[336] H. Wang and M. Frenklach. Calculations of rate coefficients for the chemically activated reactions of acetylene with vinylic and aromatic radicals. *J. Phys. Chem.*, 98 (44):11465–11489, 1994. doi:10.1021/j100095a033.

[337] H. Wang and M. Frenklach. A detailed kinetic modeling study of aromatics formation in laminar premixed acetylene and ethylene flames. *Combust. Flame*, 110(1-2): 173–221, 1997. doi:10.1016/S0010-2180(97)00068-0.

[338] M.-J. Wang, C. A. Gray, S. A. Reznek, K. Mahmud, and Y. Kutsovsky. *Carbon Black*. American Cancer Society, 2003. doi:10.1002/0471238961.0301180204011414.a01.pub2.

[339] Q. Wang, P. Elvati, D. Kim, K. O. Johansson, P. E. Schrader, H. A. Michelsen, and A. Violi. Spatial dependence of the growth of polycyclic aromatic compounds in an ethylene counterflow flame. *Carbon*, 149:328–335, 2019. doi:10.1016/j.carbon.2019.03.017.

[340] Q. Wang, J. C. Saldinger, P. Elvati, and A. Violi. Insights on the effect of ethanol on the formation of aromatics. *Fuel*, 264:116773, 2020. doi:10.1016/j.fuel.2019.116773.

[341] Y. Wang, A. Raj, and S. H. Chung. A PAH growth mechanism and synergistic effect on PAH formation in counterflow diffusion flames. *Combust. Flame*, 160(9):1667–1676, 2013. doi:10.1016/j.combustflame.2013.03.013.

[342] Y. Wang, A. Raj, and S. H. Chung. Soot modeling of counterflow diffusion flames of ethylene-based binary mixture fuels. *Combust. Flame*, 162(3):586–596, 2015. doi:10.1016/j.combustflame.2014.08.016.

[343] M. L. Waskom. Seaborn: statistical data visualization. *J. Open Source Softw.*, 6(60): 3021, 2021. doi:10.21105/joss.03021.

[344] P. Weilmünster, A. Keller, and K.-H. Homann. Large molecules, radicals, ions, and small soot particles in fuel-rich hydrocarbon flames: Part I: positive ions of polycyclic aromatic hydrocarbons (PAH) in low-pressure premixed flames of acetylene and oxygen. *Combust. Flame*, 116(1):62 – 83, 1999. doi:10.1016/S0010-2180(98)00049-2.

[345] C.-s. Wen. *The fundamentals of aerosol dynamics*. World Scientific, 1996.

[346] P. R. Westmoreland. *Experimental and theoretical analysis of oxidation and growth chemistry in a fuel-rich acetylene flame*. PhD thesis, Massachusetts Institute of Technology, 1986.

[347] P. R. Westmoreland, A. M. Dean, J. B. Howard, and J. P. Longwell. Forming benzene in flames by chemically activated isomerization. *J. Phys. Chem.*, 93(25):8171–8180, 1989. doi:10.1021/j100362a008.

[348] R. Whitesides and M. Frenklach. Detailed Kinetic Monte Carlo simulations of graphene-edge growth. *J. Phys. Chem. A*, 114(2):689–703, 2010. doi:10.1021/jp906541a.

[349] R. Whitesides and M. Frenklach. Effect of reaction kinetics on graphene-edge morphology and composition. *Z. fur Phys. Chem.*, 229(4):597–614, 2015. doi:10.1515/zpch-2014-0633.

[350] R. Whitesides, D. Domin, R. Salomón-Ferrer, W. A. Lester, and M. Frenklach. Graphene layer growth chemistry: Five- and six-member ring flip reaction. *J. Phys. Chem. A*, 112(10):2125–2130, 2008. doi:10.1021/jp075785a.

[351] R. Whitesides, D. Domin, R. Salomón-Ferrer, W. A. Lester, and M. Frenklach. Embedded-ring migration on graphene zigzag edge. *Proc. Combust. Inst.*, 32(1): 577 – 583, 2009. doi:10.1016/j.proci.2008.06.096.

[352] T. Wigmans. Industrial aspects of production and use of activated carbons. *Carbon*, 27 (1):13–22, 1989. doi:10.1016/0008-6223(89)90152-8. Proceedings of the Conference on Porosity and Carbon materials: Measurements and applications.

[353] F. J. Wright. The oxidation of soot by O atoms. *Symp. (Int.) Combust.*, 15(1): 1449 – 1460, 1975. doi:10.1016/S0082-0784(75)80403-6. Fifteenth Symposium (International) on Combustion.

[354] X. Z. Wu, Y. R. Yao, M. M. Chen, H. R. Tian, J. Xiao, Y. Y. Xu, M. S. Lin, L. Abella, C. B. Tian, C. L. Gao, Q. Zhang, S. Y. Xie, R. B. Huang, and L. S. Zheng. Formation of Curvature Subunit of Carbon in Combustion. *J. Am. Chem. Soc.*, 138(30):9629–9633, 2016. doi:10.1021/jacs.6b04898.

[355] T. Yang, T. P. Troy, B. Xu, O. Kostko, M. Ahmed, A. M. Mebel, and R. I. Kaiser. Hydrogen-abstraction/acetylene-addition exposed. *Angew. Chem. Int. Ed. Engl.*, 55 (48):14983–14987, 2016. doi:10.1002/anie.201607509.

[356] E. K. Yapp, D. Chen, J. Akroyd, S. Mosbach, M. Kraft, J. Camacho, and H. Wang. Numerical simulation and parametric sensitivity study of particle size distributions in a burner-stabilised stagnation flame. *Combust. Flame*, 162(6):2569–2581, 2015. doi:10.1016/j.combustflame.2015.03.006.

[357] E. K. Yapp, R. I. Patterson, J. Akroyd, S. Mosbach, E. M. Adkins, J. Houston Miller, and M. Kraft. Numerical simulation and parametric sensitivity study of optical band gap in a laminar co-flow ethylene diffusion flame. *Combust. Flame*, 167:320–334, 2016. doi:10.1016/j.combustflame.2016.01.033.

[358] E. K. Yapp, C. G. Wells, J. Akroyd, S. Mosbach, R. Xu, and M. Kraft. Modelling PAH curvature in laminar premixed flames using a detailed population balance model. *Combust. Flame*, 176:172–180, 2017. doi:10.1016/j.combustflame.2016.10.004.

[359] X. You, R. Whitesides, D. Zubarev, W. A. Lester, and M. Frenklach. Bay-capping reactions: Kinetics and influence on graphene-edge growth. *Proc. Combust. Inst.*, 33 (1):685–692, 2011. doi:10.1016/j.proci.2010.05.110.

[360] H.-B. Zhang, X. You, H. Wang, and C. K. Law. Dimerization of polycyclic aromatic hydrocarbons in soot nucleation. *J. Phys. Chem. A*, 118(8):1287–1292, 2014. doi:10.1021/jp411806q.

[361] Q. L. Zhang, S. C. O'Brien, J. R. Heath, Y. Liu, R. F. Curl, H. W. Kroto, and R. E. Smalley. Reactivity of large carbon clusters: spheroidal carbon shells and their possible relevance to the formation and morphology of soot. *J. Phys. Chem.*, 90(4):525–528, 1986. doi:10.1021/j100276a001.

[362] B. Zhao, Z. Yang, M. V. Johnston, H. Wang, A. S. Wexler, M. Balthasar, and M. Kraft. Measurement and numerical simulation of soot particle size distribution functions in a laminar premixed ethylene-oxygen-argon flame. *Combust. Flame*, 133(1):173–188, 2003. doi:10.1016/S0010-2180(02)00574-6.

[363] L. Zhao, R. I. Kaiser, B. Xu, U. Ablikim, W. Lu, M. Ahmed, M. M. Evseev, E. K. Bashkirov, V. N. Azyazov, M. V. Zagidullin, A. N. Morozov, A. H. Howlader, S. F. Wnuk, A. M. Mebel, D. Joshi, G. Veber, and F. R. Fischer. Gas phase synthesis of [4]-helicene. *Nat. Commun.*, 10(1):1510, Apr 2019. doi:10.1038/s41467-019-09224-8.

Appendix A

Additional data for Chapter 4

Tables A.1, A.2 and A.3 show the reactions and species used for the steady-state approximation and the partial-equilibrium approximation used in Sections 4.4.1–4.4.3. The treatment of non-partial-equilibrium reactions is discussed in Section A.1. The treatment of product species and their radicals is discussed in Section A.2. Table A.4 shows the jump processes used in the KMC model discussed in Section 4.4.4. Section A.4 discusses the effect of removing the ring condensation reactions in the concentrations of products.

Table A.1 Reactions used for the steady-state and partial-equilibrium approximations of naphthalene (A_2) growing from benzene (A_1). Reactions above the midline (1–20) are used in the partial-equilibrium approximation. All reactions (1–28) are used in the steady-state approximation. The treatment of reactions 21–28 in the partial-equilibrium approximation is explained in Section 3.5.3. Rates taken from ABF mechanism [4].

No.	Reaction				
1	A_1	$+ H$	$\rightleftharpoons$	$A_1^\bullet$	$+ H_2$
2	A_1	$+ OH$	$\rightleftharpoons$	$A_1^\bullet$	$+ H_2O$
3	$A_1^\bullet$	$+ H + (M)$	$\rightleftharpoons$	A_1	$+ (M)$
4	$A_1^\bullet$	$+ C_2H_2$	$\rightleftharpoons$	A_1C_2H	$+ H$
5	$A_1^\bullet$	$+ C_2H_2$	$\rightleftharpoons$	$A_1C_2H_2$	
6	A_1C_2H	$+ H$	$\rightleftharpoons$	$A_1C_2H_2$	
7	A_1C_2H	$+ C_2H$	$\rightleftharpoons$	$A_1(C_2H)C_2H_2$	$+ H$
8	A_1C_2H	$+ H$	$\rightleftharpoons$	$A_1C_2H^\bullet$	$+ H_2$
9	A_1C_2H	$+ OH$	$\rightleftharpoons$	$A_1C_2H^\bullet$	$+ H_2O$
10	$A_1C_2H^\bullet$	$+ H + (M)$	$\rightleftharpoons$	A_1C_2H	$+ (M)$
11	A_1	$+ C_2H$	$\rightleftharpoons$	A_1C_2H	$+ H$
12	$A_1C_2H_3$	$+ H$	$\rightleftharpoons$	$A_1C_2H_3^\bullet$	$+ H_2$
13	$A_1C_2H_3$	$+ OH$	$\rightleftharpoons$	$A_1C_2H_3^\bullet$	$+ H_2O$
14	$A_1C_2H_3^\bullet$	$+ H + (M)$	$\rightleftharpoons$	$A_1C_2H_3$	$+ (M)$
15	$A_1^\bullet$	$+ C_2H_4$	$\rightleftharpoons$	$A_1C_2H_3$	$+ H$
16	$A_1^\bullet$	$+ C_2H_3$	$\rightleftharpoons$	$A_1C_2H_3$	
17	A_1	$+ C_2H_3$	$\rightleftharpoons$	$A_1C_2H_3$	$+ H$
18	$A_1C_2H_3$	$+ H$	$\rightleftharpoons$	$A_1C_2H_2$	$+ H_2$
19	$A_1C_2H_3$	$+ OH$	$\rightleftharpoons$	$A_1C_2H_2$	$+ H_2O$
20	$A_1C_2H^\bullet$	$+ C_2H_2$	$\rightleftharpoons$	$A_1(C_2H)C_2H_2$	$+ H$
21[†]	$A_1C_2H_2$	$+ C_2H_2$	$\rightleftharpoons$	A_2	$+ H$
22[†]	$A_1C_2H_3^\bullet$	$+ C_2H_2$	$\rightleftharpoons$	A_2	$+ H$
23[†]	$A_1^\bullet$	$+ C_4H_4$	$\rightleftharpoons$	A_2	$+ H$
24[†]	$A_1C_2H^\bullet$	$+ C_2H_2$	$\rightleftharpoons$	$A_2^\bullet$	
25[†]	$A_1(C_2H)C_2H_2^\bullet$	$+ H$	$\rightleftharpoons$	$A_2^\bullet$	
26	A_2	$+ H$	$\rightleftharpoons$	$A_2^\bullet$	$+ H_2$
27	A_2	$+ OH$	$\rightleftharpoons$	$A_2^\bullet$	$+ H_2O$
28	$A_2^\bullet$	$+ H + (M)$	$\rightleftharpoons$	A_2	$+ (M)$

[†] Indicates reactions contributing to Equation (A.5). See Section 3.5.3.

Species sets:

$S_{ss} = \{A_1^\bullet, A_1C_2H_2, A_1C_2H, A_1C_2H^\bullet, A_1C_2H_3, A_1C_2H_3^\bullet, A_1(C_2H)C_2H_2^\bullet, A_2^\bullet, A_2\}$.

$S_{peq} = \{A_1^\bullet, A_1C_2H_2, A_1C_2H, A_1C_2H^\bullet, A_1C_2H_3, A_1C_2H_3^\bullet, A_1(C_2H)C_2H_2^\bullet\}$.

$S_{ss} \setminus S_{peq} = \{A_2^\bullet, A_2\}$.

Table A.2 Reactions used for the steady-state and partial-equilibrium approximations of phenanthrene (A_3) growing from naphthalene (A_2). Reactions above the midline (1–14) are used in the partial-equilibrium approximation. All reactions (1–19) are used in the steady-state approximation. The treatment of reactions 15–19 in the partial-equilibrium approximation is explained in Section 3.5.3. Rates taken from ABF mechanism [4].

No.	Reaction				
1	A_2	$+ H$	$\rightleftharpoons$	$A_2^\bullet$	$+ H_2$
2	A_2	$+ OH$	$\rightleftharpoons$	$A_2^\bullet$	$+ H_2O$
3	$A_2^\bullet$	$+ H + (M)$	$\rightleftharpoons$	A_2	$+ (M)$
4	$A_2^\bullet$	$+ C_2H_2$	$\rightleftharpoons$	$A_2C_2H_2$	
5	$A_2^\bullet$	$+ C_2H_2$	$\rightleftharpoons$	A_2C_2H	$+ H$
6	A_2	$+ C_2H$	$\rightleftharpoons$	A_2C_2H	$+ H$
7	A_2C_2H	$+ H$	$\rightleftharpoons$	$A_2C_2H_2$	
8	$A_2C_2H_2$	$+ H$	$\rightleftharpoons$	A_2C_2H	$+ H_2$
9	$A_2C_2H_2$	$+ OH$	$\rightleftharpoons$	A_2C_2H	$+ H_2O$
10	A_2C_2H	$+ H$	$\rightleftharpoons$	$A_2C_2H^\bullet$	$+ H_2$
11	A_2C_2H	$+ OH$	$\rightleftharpoons$	$A_2C_2H^\bullet$	$+ H_2O$
12	$A_2C_2H^\bullet$	$+ H + (M)$	$\rightleftharpoons$	A_2C_2H	$+ (M)$
13	A_2C_2H	$+ C_2H$	$\rightleftharpoons$	$A_2(C_2H)C_2H_2$	$+ H$
14	$A_2C_2H^\bullet$	$+ C_2H_2$	$\rightleftharpoons$	$A_2(C_2H)C_2H_2$	$+ H$
$15^\dagger$	$A_2C_2H^\bullet$	$+ C_2H_2$	$\rightleftharpoons$	$A_3^\bullet$	
$16^\dagger$	$A_2(C_2H)C_2H_2^\bullet$	$+ H$	$\rightleftharpoons$	$A_3^\bullet$	
17	A_3	$+ H$	$\rightleftharpoons$	$A_3^\bullet$	$+ H_2$
18	A_3	$+ OH$	$\rightleftharpoons$	$A_3^\bullet$	$+ H_2O$
19	$A_3^\bullet$	$+ H + (M)$	$\rightleftharpoons$	A_3	$+ (M)$

† Indicates reactions contributing to Equation (A.5). See Section 3.5.3.

Species sets:

$S_{ss} = \{A_2^\bullet, A_2C_2H_2, A_2C_2H, A_2C_2H^\bullet, A_2(C_2H)C_2H_2^\bullet, A_3^\bullet, A_3\}$.

$S_{peq} = \{A_2^\bullet, A_2C_2H_2, A_2C_2H, A_2C_2H^\bullet, A_2(C_2H)C_2H_2^\bullet\}$.

$S_{ss} \setminus S_{peq} = \{A_3^\bullet, A_3\}$.

Table A.3 Reactions used for partial-equilibrium approximation of phenanthrene (A_3) growing from benzene (A_1). Reactions above the midline (1–12) are used in the partial-equilibrium approximation. The treatment of reactions 13–17 is explained in Section 3.5.3. Rates taken from ABF mechanism [4].

No.		Reaction			
1	A_1	$+ H$	$\rightleftharpoons$	$A_1^\bullet$	$+ H_2$
2	A_1	$+ OH$	$\rightleftharpoons$	$A_1^\bullet$	$+ H_2O$
3	$A_1^\bullet$	$+ H + (M)$	$\rightleftharpoons$	A_1	$+ (M)$
4	$A_1^\bullet$	$+ C_2H_2$	$\rightleftharpoons$	A_1C_2H	$+ H$
5	$A_1^\bullet$	$+ C_2H_2$	$\rightleftharpoons$	$A_1C_2H_2$	
6	A_1C_2H	$+ H$	$\rightleftharpoons$	$A_1C_2H_2$	
7	A_1C_2H	$+ C_2H$	$\rightleftharpoons$	$A_1(C_2H)C_2H_2$	$+ H$
8	A_1C_2H	$+ H$	$\rightleftharpoons$	$A_1C_2H^\bullet$	$+ H_2$
9	A_1C_2H	$+ OH$	$\rightleftharpoons$	$A_1C_2H^\bullet$	$+ H_2O$
10	$A_1C_2H^\bullet$	$+ H + (M)$	$\rightleftharpoons$	A_1C_2H	$+ (M)$
11	A_1	$+ C_2H$	$\rightleftharpoons$	A_1C_2H	$+ H$
12	$A_1C_2H^\bullet$	$+ C_2H_2$	$\rightleftharpoons$	$A_1(C_2H)C_2H_2$	$+ H$
13	A_1	$+ A_1^\bullet$	$\rightleftharpoons$	P_2	$+ H$
14	P_2	$+ H$	$\rightleftharpoons$	$P_2^\bullet$	$+ H_2$
15[†]	$P_2^\bullet$	$+ C_2H_2$	$\rightleftharpoons$	A_3	$+ H$
16[†]	A_1	$+ A_1C_2H^\bullet$	$\rightleftharpoons$	A_3	$+ H$
17[†]	$A_1^\bullet$	$+ A_1C_2H$	$\rightleftharpoons$	A_3	$+ H$

[†] Indicates reactions contributing to Equation (A.5). See Section 3.5.3.

Species sets:

$S_{peq} = \{A_1^\bullet, A_1C_2H_2, A_1C_2H, A_1C_2H^\bullet, A_1(C_2H)C_2H_2^\bullet\}$.

This process is only treated using the partial-equilibrium approximation.

Table A.4 Jump processes, reactions and species for the KMC model. For each process, reactions above the midline are used in the partial-equilibrium approximation; all reactions (above and below the line) are used in the steady-state approximation. Reactions below the midline are used to calculate the overall rate of the process. Rates from ABF mechanism [4].

Jump process		Intermediate reactions				
	1	A_1	$+ H$	$\rightleftharpoons$	$A_1{}^\bullet$	$+ H_2$
	2	A_1	$+ OH$	$\rightleftharpoons$	$A_1{}^\bullet$	$+ H_2O$
	3	$A_1{}^\bullet$	$+ H + (M)$	$\rightleftharpoons$	A_1	$+ (M)$
	4	$A_1{}^\bullet$	$+ C_2H_2$	$\rightleftharpoons$	A_1C_2H	$+ H$
	5	$A_1{}^\bullet$	$+ C_2H_2$	$\rightleftharpoons$	$A_1C_2H_2$	
	6	A_1C_2H	$+ H$	$\rightleftharpoons$	$A_1C_2H_2$	
	7	A_1C_2H	$+ C_2H$	$\rightleftharpoons$	$A_1(C_2H)C_2H_2$	$+ H$
	8	A_1C_2H	$+ H$	$\rightleftharpoons$	$A_1C_2H^\bullet$	$+ H_2$
	9	A_1C_2H	$+ OH$	$\rightleftharpoons$	$A_1C_2H^\bullet$	$+ H_2O$
	10	$A_1C_2H^\bullet$	$+ H + (M)$	$\rightleftharpoons$	A_1C_2H	$+ (M)$
	11	A_1	$+ C_2H$	$\rightleftharpoons$	A_1C_2H	$+ H$
	12	$A_1C_2H_3$	$+ H$	$\rightleftharpoons$	$A_1C_2H_3{}^\bullet$	$+ H_2$
	13	$A_1C_2H_3$	$+ OH$	$\rightleftharpoons$	$A_1C_2H_3{}^\bullet$	$+ H_2O$
Free-edge	14	$A_1C_2H_3{}^\bullet$	$+ H + (M)$	$\rightleftharpoons$	$A_1C_2H_3$	$+ (M)$
ring growth	15	$A_1{}^\bullet$	$+ C_2H_4$	$\rightleftharpoons$	$A_1C_2H_3$	$+ H$
$A_1 \longrightarrow A_2$	16	$A_1{}^\bullet$	$+ C_2H_3$	$\rightleftharpoons$	$A_1C_2H_3$	
	17	A_1	$+ C_2H_3$	$\rightleftharpoons$	$A_1C_2H_3$	$+ H$
	18	$A_1C_2H_3$	$+ H$	$\rightleftharpoons$	$A_1C_2H_2$	$+ H_2$
	19	$A_1C_2H_3$	$+ OH$	$\rightleftharpoons$	$A_1C_2H_2$	$+ H_2O$
	20	$A_1C_2H^\bullet$	$+ C_2H_2$	$\rightleftharpoons$	$A_1(C_2H)C_2H_2$	$+ H$
	$21^\dagger$	$A_1C_2H_2$	$+ C_2H_2$	$\longrightarrow$	A_2	$+ H$
	$22^\dagger$	$A_1C_2H_3{}^\bullet$	$+ C_2H_2$	$\longrightarrow$	A_2	$+ H$
	$23^\dagger$	$A_1{}^\bullet$	$+ C_4H_4$	$\longrightarrow$	A_2	$+ H$
	$24^\dagger$	$A_1C_2H^\bullet$	$+ C_2H_2$	$\longrightarrow$	$A_2{}^\bullet$	
	$25^\dagger$	$A_1(C_2H)C_2H_2{}^\bullet$	$+ H$	$\longrightarrow$	$A_2{}^\bullet$	

$S_{ss} = \{A_1{}^\bullet, A_1C_2H_2, A_1C_2H, A_1C_2H^\bullet, A_1C_2H_3, A_1C_2H_3{}^\bullet, A_1(C_2H)C_2H_2{}^\bullet, A_2{}^\bullet, A_2\}$.

$S_{peq} = \{A_1{}^\bullet, A_1C_2H_2, A_1C_2H, A_1C_2H^\bullet, A_1C_2H_3, A_1C_2H_3{}^\bullet, A_1(C_2H)C_2H_2{}^\bullet\}$.

$S_{ss} \setminus S_{peq} = \{A_2{}^\bullet, A_2\}$.

Table A.4 – continued from previous page

Jump process		Intermediate reactions				
	1	A_2	$+ H$	$\rightleftharpoons$	$A_2^\bullet$	$+ H_2$
	2	A_2	$+ OH$	$\rightleftharpoons$	$A_2^\bullet$	$+ H_2O$
	3	$A_2^\bullet$	$+ H + (M)$	$\rightleftharpoons$	A_2	$+ (M)$
Free-edge ring desorption [1] $A_2 \longrightarrow A_1$	$4^\ddagger$	A_2	$+ H$	$\longrightarrow$	$A_1C_2H_2$	$+ C_2H_2$
	$5^\ddagger$	A_2	$+ H$	$\longrightarrow$	$A_1C_2H_3^\bullet$	$+ C_2H_2$
	$6^\ddagger$	A_2	$+ H$	$\longrightarrow$	$A_1^\bullet$	$+ C_4H_4$
	$7^\ddagger$	$A_2^\bullet$		$\longrightarrow$	$A_1C_2H^\bullet$	$+ C_2H_2$
	$8^\ddagger$	$A_2^\bullet$		$\longrightarrow$	$A_1(C_2H)C_2H_2$	$+ H$
	1	A_2	$+ H$	$\rightleftharpoons$	$A_2^\bullet + H_2$	
	2	A_2	$+ OH$	$\rightleftharpoons$	$A_2^\bullet$	$+ H_2O$
	3	$A_2^\bullet$	$+ H + (M)$	$\rightleftharpoons$	A_2	$+ (M)$
	4	$A_2^\bullet$	$+ C_2H_2$	$\rightleftharpoons$	$A_2C_2H_2$	
	5	$A_2^\bullet$	$+ C_2H_2$	$\rightleftharpoons$	A_2C_2H	$+ H$
	6	A_2	$+ C_2H$	$\rightleftharpoons$	A_2C_2H	$+ H$
	7	A_2C_2H	$+ H$	$\rightleftharpoons$	$A_2C_2H_2$	
	8	$A_2C_2H_2$	$+ H$	$\rightleftharpoons$	A_2C_2H	$+ H_2$
Free-edge ring growth $A_2 \longrightarrow A_3$	9	$A_2C_2H_2$	$+ OH$	$\rightleftharpoons$	A_2C_2H	$+ H_2O$
	10	A_2C_2H	$+ H$	$\rightleftharpoons$	$A_2C_2H^\bullet$	$+ H_2$
	11	A_2C_2H	$+ OH$	$\rightleftharpoons$	$A_2C_2H^\bullet$	$+ H_2O$
	12	$A_2C_2H^\bullet$	$+ H + (M)$	$\rightleftharpoons$	A_2C_2H	$+ (M)$
	13	A_2C_2H	$+ C_2H$	$\rightleftharpoons$	$A_2(C_2H)C_2H_2$	$+ H$
	14	$A_2C_2H^\bullet$	$+ C_2H_2$	$\rightleftharpoons$	$A_2(C_2H)C_2H_2$	$+ H$
	$15^\dagger$	$A_2C_2H^\bullet$	$+ C_2H_2$	$\longrightarrow$	$A_3^\bullet$	
	$16^\dagger$	$A_2(C_2H)C_2H_2^\bullet$	$+ H$	$\longrightarrow$	$A_3^\bullet$	

$S_{ss} = \{A_2^\bullet, A_2C_2H_2, A_2C_2H, A_2C_2H^\bullet, A_2(C_2H)C_2H_2^\bullet, A_3^\bullet, A_3\}$.

$S_{peq} = \{A_2^\bullet, A_2C_2H_2, A_2C_2H, A_2C_2H^\bullet, A_2(C_2H)C_2H_2^\bullet\}$.

$S_{ss} \setminus S_{peq} = \{A_3^\bullet, A_3\}$.

Table A.4 – continued from previous page

Jump process	Intermediate reactions					
Free-edge ring desorption [1] $A_3 \longrightarrow A_2$	1	A_3	$+ H$	$\rightleftharpoons$	$A_3{}^\bullet$	$+ H_2$
	2	A_3	$+ OH$	$\rightleftharpoons$	$A_3{}^\bullet$	$+ H_2O$
	3	$A_3{}^\bullet$	$+ H + (M)$	$\rightleftharpoons$	A_3	$+ (M)$
	$4^\ddagger$	$A_3{}^\bullet$		$\longrightarrow$	$A_2C_2H^\bullet$	$+ C_2H_2$
	$5^\ddagger$	$A_3{}^\bullet$		$\longrightarrow$	$A_2(C_2H)C_2H_2$	$+ H$
Armchair ring growth $A_3 \longrightarrow A_4$	1	A_3	$+ H$	$\rightleftharpoons$	$A_3{}^\bullet$	$+ H_2$
	2	A_3	$+ OH$	$\rightleftharpoons$	$A_3{}^\bullet$	$+ H_2O$
	3	$A_3{}^\bullet$	$+ H + (M)$	$\rightleftharpoons$	A_3	$+ (M)$
	4	$A_3{}^\bullet$	$+ C_2H_2$	$\rightleftharpoons$	$A_3C_2H_2$	
	5	$A_3{}^\bullet$	$+ C_2H_2$	$\rightleftharpoons$	A_3C_2H	$+ H$
	6	A_3	$+ C_2H$	$\rightleftharpoons$	A_3C_2H	$+ H$
	7	A_3C_2H	$+ H$	$\rightleftharpoons$	$A_3C_2H_2$	
	$8^\dagger$	$A_3{}^\bullet$	$+ C_2H_2$	$\longrightarrow$	A_4	$+ H$
	$9^\dagger$	A_3C_2H	$+ H$	$\longrightarrow$	A_4	$+ H$
	$10^\dagger$	$A_3C_2H_2$		$\longrightarrow$	A_4	$+ H$

$S_{ss} = \{A_3{}^\bullet, A_3C_2H_2, A_3C_2H, A_4\}$.

$S_{peq} = \{A_3{}^\bullet, A_3C_2H_2, A_3C_2H\}$.

$S_{ss} \setminus S_{peq} = \{A_4\}$.

Jump process	Intermediate reactions					
Armchair desorption $A_4 \longrightarrow A_3$	$1^\ddagger$	A_4	$+ H$	$\longrightarrow$	$A_3{}^\bullet$	$+ C_2H_2$
	$2^\ddagger$	A_4	$+ H$	$\longrightarrow$	A_3C_2H	$+ H$
	$3^\ddagger$	A_4	$+ H$	$\longrightarrow$	$A_3C_2H_2$	

Table A.4 – continued from previous page

Jump process	Intermediate reactions					
	1	A_1	$+ H$	$\rightleftharpoons$	$A_1^\bullet$	$+ H_2$
	2	A_1	$+ OH$	$\rightleftharpoons$	$A_1^\bullet$	$+ H_2O$
	3	$A_1^\bullet$	$+ H + (M)$	$\rightleftharpoons$	A_1	$+ (M)$
	4	$A_1^\bullet$	$+ C_2H_2$	$\rightleftharpoons$	A_1C_2H	$+ H$
	5	$A_1^\bullet$	$+ C_2H_2$	$\rightleftharpoons$	$A_1C_2H_2$	
	6	A_1C_2H	$+ H$	$\rightleftharpoons$	$A_1C_2H_2$	
	7	A_1C_2H	$+ C_2H$	$\rightleftharpoons$	$A_1(C_2H)C_2H_2$	$+ H$
	8	A_1C_2H	$+ H$	$\rightleftharpoons$	$A_1C_2H^\bullet$	$+ H_2$
Ring	9	A_1C_2H	$+ OH$	$\rightleftharpoons$	$A_1C_2H^\bullet$	$+ H_2O$
condensation	10	$A_1C_2H^\bullet$	$+ H + (M)$	$\rightleftharpoons$	A_1C_2H	$+ (M)$
$A_1 \longrightarrow A_3$	11	A_1	$+ C_2H$	$\rightleftharpoons$	A_1C_2H	$+ H$
	12	$A_1C_2H^\bullet$	$+ C_2H_2$	$\rightleftharpoons$	$A_1(C_2H)C_2H_2$	$+ H$
	13	A_1	$+ A_1^\bullet$	$\rightleftharpoons$	P_2	$+ H$
	14	P_2	$+ H$	$\rightleftharpoons$	$P_2^\bullet$	$+ H_2$
	15*	$P_2^\bullet$	$+ C_2H_2$	$\longrightarrow$	A_3	$+ H$
	16*	A_1	$+ A_1C_2H^\bullet$	$\longrightarrow$	A_3	$+ H$
	17*	$A_1^\bullet$	$+ A_1C_2H$	$\longrightarrow$	A_3	$+ H$

$S_{peq} = \{A_1^\bullet, A_1C_2H_2, A_1C_2H, A_1C_2H^\bullet, A_1(C_2H)C_2H_2^\bullet\}$.

This process is only treated using the partial-equilibrium approximation.

Table A.4 – continued from previous page

Jump process		Intermediate reactions				
	1	A_2	$+ H$	$\rightleftharpoons$	$A_2^\bullet + H_2$	
	2	A_2	$+ OH$	$\rightleftharpoons$	$A_2^\bullet$	$+ H_2O$
	3	$A_2^\bullet$	$+ H + (M)$	$\rightleftharpoons$	A_2	$+ (M)$
	4	$A_2^\bullet$	$+ C_2H_2$	$\rightleftharpoons$	$A_2C_2H_2$	
	5	$A_2^\bullet$	$+ C_2H_2$	$\rightleftharpoons$	A_2C_2H	$+ H$
	6	A_2	$+ C_2H$	$\rightleftharpoons$	A_2C_2H	$+ H$
	7	A_2C_2H	$+ H$	$\rightleftharpoons$	$A_2C_2H_2$	
	8	$A_2C_2H_2$	$+ H$	$\rightleftharpoons$	A_2C_2H	$+ H_2$
Five-member	9	$A_2C_2H_2$	$+ OH$	$\rightleftharpoons$	A_2C_2H	$+ H_2O$
ring growth at	10	A_2C_2H	$+ H$	$\rightleftharpoons$	$A_2C_2H^\bullet$	$+ H_2$
zig-zag	11	A_2C_2H	$+ OH$	$\rightleftharpoons$	$A_2C_2H^\bullet$	$+ H_2O$
$A_2 \longrightarrow A_2R_5$	12	$A_2C_2H^\bullet$	$+ H + (M)$	$\rightleftharpoons$	A_2C_2H	$+ (M)$
	13	A_2C_2H	$+ C_2H$	$\rightleftharpoons$	$A_2(C_2H)C_2H_2$	$+ H$
	14	$A_2C_2H^\bullet$	$+ C_2H_2$	$\rightleftharpoons$	$A_2(C_2H)C_2H_2$	$+ H$
	$15^\dagger$	$A_2^\bullet$	$+ C_2H_2$	$\longrightarrow$	A_2R_5	$+ H$
	$16^\dagger$	A_2C_2H	$+ H$	$\longrightarrow$	A_2R_5	$+ H$
	$17^\dagger$	$A_2C_2H_2$		$\longrightarrow$	A_2R_5	$+ H$

$S_{ss} = \{A_2^\bullet, A_2C_2H_2, A_2C_2H, A_2C_2H^\bullet, A_2(C_2H)C_2H_2^\bullet, A_2R_5\}$.

$S_{peq} = \{A_2^\bullet, A_2C_2H_2, A_2C_2H, A_2C_2H^\bullet, A_2(C_2H)C_2H_2^\bullet\}$.

$S_{ss} \setminus S_{peq} = \{A_2R_5\}$.

Jump process		Intermediate reactions				
Five-member	$1^\ddagger$	A_2R_5	$+ H$	$\longrightarrow$	$A_2^\bullet$	$+ C_2H_2$
ring desorption [1]	$2^\ddagger$	A_2R_5	$+ H$	$\longrightarrow$	A_2C_2H	$+ H$
$A_2R_5 \longrightarrow A_2$	$3^\ddagger$	A_2R_5	$+ H$	$\longrightarrow$	$A_2C_2H_2$	

[1] The rates of the desorption processes are independent of the concentration of intermediate PAH species, and can therefore be evaluated without a steady-state or partial-equilibrium approximation.

$^{\dagger/\ddagger}$ Reversible reactions whose forward and reverse contributions are split between jump processes. The reactions are still treated as reversible for the purpose of solving Equation (3.60) for c_{ss}.
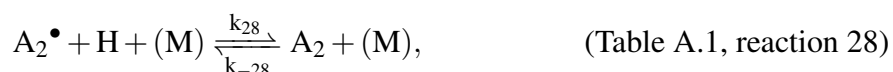
* Reactions treated as irreversible. The reverse rates were observed to be negligible.

$^{\dagger/\ddagger/*}$ Reactions used to calculate the overall rate of each jump process. See Section A.3.
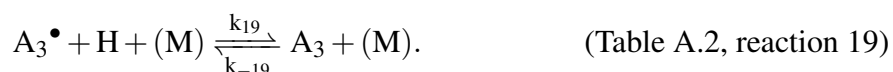
A.1 Treatment of non-partial-equilibrium reactions

The partial-equilibrium approximations used in Chapter 4 operate on a subset of reactions that exclude the formation of naphthalene (A_2, Table A.1) and phenanthrene (A_3, Tables A.2 and A.3). The concentrations of A_2 and A_3 must be calculated separately.

The concentrations of A_2 and A_3 are controlled by the final reactions in Tables A.1 and A.2

$$A_2 + H \underset{k_{-26}}{\overset{k_{26}}{\rightleftharpoons}} A_2{}^{\bullet} + H_2, \qquad \text{(Table A.1, reaction 26)}$$

$$A_2 + OH \underset{k_{-27}}{\overset{k_{27}}{\rightleftharpoons}} A_2{}^{\bullet} + H_2O, \qquad \text{(Table A.1, reaction 27)}$$

$$A_2{}^{\bullet} + H + (M) \underset{k_{-28}}{\overset{k_{28}}{\rightleftharpoons}} A_2 + (M), \qquad \text{(Table A.1, reaction 28)}$$

and

$$A_3 + H \underset{k_{-17}}{\overset{k_{17}}{\rightleftharpoons}} A_3{}^{\bullet} + H_2, \qquad \text{(Table A.2, reaction 17)}$$

$$A_3 + OH \underset{k_{-18}}{\overset{k_{18}}{\rightleftharpoons}} A_3{}^{\bullet} + H_2O, \qquad \text{(Table A.2, reaction 18)}$$

$$A_3{}^{\bullet} + H + (M) \underset{k_{-19}}{\overset{k_{19}}{\rightleftharpoons}} A_3 + (M). \qquad \text{(Table A.2, reaction 19)}$$

An algebraic relationship between the concentrations c_{A_2} and $c_{A_2{}^{\bullet}}$, and c_{A_3} and $c_{A_3{}^{\bullet}}$ can be derived by applying a steady-state or partial-equilibrium approximation to each of these sets of reactions [see for example 75]. In Chapter 4, a partial-equilibrium approximation is used to derive the following relationships

$$c_{A_2{}^{\bullet}} = c_{A_2} \left(\frac{k_{26}c_H + k_{27}c_{OH} + k_{-28}}{k_{-26}c_{H_2} + k_{-27}c_{H_2O} + k_{28}c_H} \right), \qquad \text{(A.1)}$$

$$c_{A_3{}^{\bullet}} = c_{A_3} \left(\frac{k_{17}c_H + k_{18}c_{OH} + k_{-19}}{k_{-17}c_{H_2} + k_{-18}c_{H_2O} + k_{19}c_H} \right). \qquad \text{(A.2)}$$

A.2 ODE-based simulations

In the case of the ODE-based simulations (Sections 4.4.2 and 4.4.3), the concentrations of species in the set $\alpha \notin S_{peq}$ are calculated by solving Equation (3.65). The concentrations of the main PAH products, A_2 and A_3, are treated as a special case and are calculated using Equations (A.1) and (A.2) in conjunction with solving equations of the same form as

Equation (4.4) to find the total concentration of each species and its corresponding radical

$$c_{A_2} + c_{A_2^\bullet} \approx \int_0^t P_{A_2}^{neq} + P_{A_2^\bullet}^{neq} \, dt, \tag{A.3}$$

$$c_{A_3} + c_{A_3^\bullet} \approx \int_0^t P_{A_3}^{neq} + P_{A_3^\bullet}^{neq} \, dt, \tag{A.4}$$

where

$$P_\alpha^{neq} = \sum_{i \in R_{neq}} P_\alpha^{(i)}, \tag{A.5}$$

is the production of species α due to the reactions in the set R_{neq} and $P_\alpha^{(i)}$ is defined as per Equation (3.53). The reactions in R_{neq} contributing to Equations (A.3) and (A.4) are marked with a dagger (†) in Tables A.1–A.3. Note that Table A.3, reaction 17 has a dependency on the concentration of $P_2^\bullet$. This is evaluated using the relationship

$$c_{P_2} = \frac{k_{13} c_{A_1} c_{A_1^\bullet} + k_{-14} c_{P_2^\bullet} c_{H_2}}{k_{-13} c_H + k_{14} c_H} \tag{A.6}$$

$$c_{P_2^\bullet} = \frac{k_{14} c_{P_2} c_H}{k_{-14} c_{H_2} + k_{15} c_{C_2H_2}} \tag{A.7}$$

arising from the application of a steady-state approximation to Table A.3, reactions 13–15.

The rationale behind the special treatment of A_2 and A_3 is that it avoids the need to solve tightly coupled ODEs for the non-partial-equilibrium PAH species. This reduces the computational complexity of the method, so is desirable in the context of the objective to develop a computationally efficient model.

A.3   Calculation of KMC jump process rates

The KMC model calculates the concentrations of A_2, A_2R_5, A_3 and A_4 by performing a Kinetic Monte Carlo simulation using the jump processes in Table A.4. The temperature and small-molecule concentrations (up to and including benzene, A_1) are imposed as boundary conditions. For each jump process, the concentrations of the (PAH) species in either S_{ss} or S_{peq} are calculated by solving Equation (3.61) for c_{ss} or Equation (3.68) for c_{peq}, depending on the choice of method. In both cases, the rates of the jump processes are calculated by evaluating the rates of the reactions marked †, ‡ and ∗ in Table A.4.

Similar to the treatment of the non-partial-equilibrium reactions in the ODE-based simulations (see Section 3.5.3), the KMC model uses Equations (A.1) and (A.2) to calculate

A_2 and A_3 in conjunction with tracking the total concentrations $c_{A_2} + c_{A_2^\bullet}$ and $c_{A_3} + c_{A_3^\bullet}$. Likewise, equations (A.6) and (A.7) are used to calculate the concentration of $P_2^\bullet$ in order to evaluate the rate of the phenyl addition (Table A.4, reaction 15).

The mechanism in Table A.4 can be generalised (not shown here) to describe the growth of arbitrarily-sized PAHs. See for example the work by Frenklach and co-workers [75, 84] and Celnik et al. [32].

A.4   Effect of ring condensation reactions

Figure A.1 shows the concentrations of A_2 and A_3 calculated using the partial-equilibrium approximation without the inclusion of ring condensation reactions (Figure 4.2 process (iii) in Chapter 4) versus reference solutions calculated using the full ABF mechanism in a closed isothermal system. For comparison, the data calculated using the steady-state approximation is also shown. The figure shows that given long enough, good agreement is seen between the steady-state approximation and the reference solutions. Comparison with Figure 4.5 (in Chapter 4) shows that both the improved treatment of reactions during the induction period and the inclusion of process (iii) in the partial-equilibrium approximation are important to achieve agreement with the reference data for A_3 at early times.
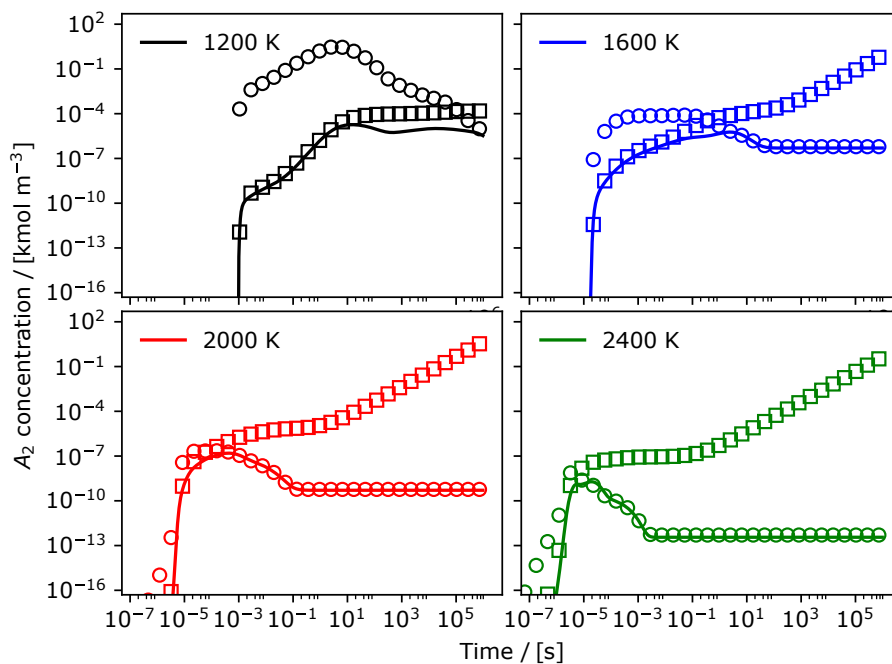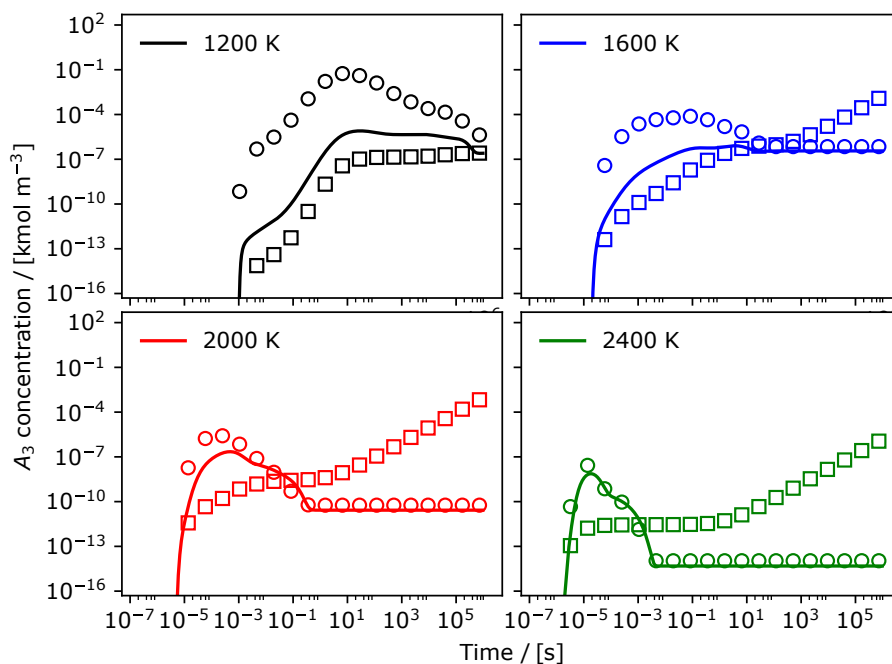
(a) Naphthalene (A_2).

(b) Phenanthrene (A_3).

Fig. A.1 Simulations of the reaction of ethylene in a closed isothermal system, initially at an equivalence ratio of 5.0, to form naphthalene (A_2, top panels) and phenanthrene (A_3, bottom panels). Solid lines show the results of simulations using the full ABF mechanism. Circles show the concentration of each species calculated using the steady-state approximation. Squares show the concentration of each species calculated using the partial-equilibrium approximation. Neither approximation includes process (iii).

Appendix B

Additional data for Chapter 6

Section B.1 gives the details for the experimental data points showed in Fig. 6.1. Section B.2 gives additional ensemble statistics.

B.1   Reported experimental conditions

This section explains the origin of the experimental data reported in Figure 6.1 in the main text.

Low pressure benzene/oxygen flame

Low pressure benzene/oxygen/argon flames have been used to study the formation of fullerenes for several decades [14, 118, 130, 128, 129]. However, the detection of atomic oxygen in these flames has been difficult due to the abundance of methane [14, 59], which has the same molecular weight as atomic oxygen. Modelling studies [*e.g.* 266, 59] have also not focused on reporting this species.

The closest data available have been taken from McKinnon [197], who studied this flame for pressures ranging between 20 and 40 torr, equivalence ratios (ϕ) ranging between 2.0 and 2.5, and dilutions between 0 and 45%. McKinnon [197] reported molecular oxygen measurements at 40 torr, $\phi = 2.4$ and 10% dilution. Temperatures between 2000 and 2030 K were reported in the regions of the flames that contained mole fractions of molecular oxygen in the range $\left(X_{O_2} \leq 10^{-1}\right)$. Atomic oxygen was not reported for these conditions but equilibrium calculations as a function of temperature and equivalence ratio were reported for a system at 20 torr and 30% dilution. Assuming that these conditions are similar to those reported above ($\phi = 2.4$, $2000 < T < 2030$ K) the equilibrium atomic oxygen mole fractions correspond to $8 \times 10^{-5} < X_O < 2 \times 10^{-4}$.

Low pressure acetylene/oxygen flame

Several low pressure acetylene/oxygen/argon flames have been used to study the formation of carbonaceous particles. Of particular interest is that of Homann and collaborators [344], who used undiluted flames at 20 torr with equivalence ratios between 1.75 and 2.65. They reported the presence of fullerene ions of different sizes as well as large PAHs with more than 400 carbon atoms at an equivalence ratio $\phi = 2.5$ and a laminar flame speed of 42 cm/s. The C/H ratio of the largest PAH molecules was reported to be between 6.0 and 7.0, which suggests the presence of large edges and few fully-embedded five-member rings.

The mole fractions of the gas phase species in these flames were taken from Westmoreland [346], who studied a flame at 20 torr with an equivalence ratio of 2.4 with 5.0% dilution by argon. Westmoreland [346] reported mole fractions for molecular oxygen as a function of height above the burner and estimated mole fractions for atomic oxygen using five different mechanisms that show similar trends and reasonable agreement with each other. Values were taken from those reported from the mechanism by Warnatz (WZ).

Atmospheric ethylene/air plasma ignition

Measuring species generated in plasma conditions is a complicated task that becomes even more difficult in the presence of carbonaceous materials. Most plasma experiments associated with carbonaceous fuels have focused on determining the concentrations of atomic oxygen during the ignition of the flame in the context of plasma assisted combustion. However, even in this case only a few experiments have attempted to measure the concentration of atomic oxygen in fuel rich conditions [237, 143]. In this work the results from ignition experiments by Pendleton et al. [246] are used to estimate the concentration of atomic oxygen in plasma environments. Further work is needed to determine better estimates.

Pendleton et al. [246] used a streamer discharge to create a Gaussian-like voltage waveform lasting for 40 ns. Two-photon absorption laser-induced fluorescence (TALIF) was used to measure the number density of atomic oxygen 8 mm above an atmospheric pressure McKenna burner at the point of igniting the flame. Using premixed ethylene and air at an equivalence ratio of 2.4 and a flame speed of 10 cm/s they reported an oxygen atom number density of 4.5×10^{17} cm^{-3} that decayed to 7.0×10^{16} cm^{-3} as the atomic oxygen was consumed. In a previous work [245] they reported temperatures between 1350 and 1540 K measured using coherent anti-Stokes Raman spectroscopy (CARS). These values imply that the mole fraction of atomic oxygen lies in the range $1.3 \times 10^{-2} < X_O < 9.3 \times 10^{-2}$.

Methane/oxygen burnout experiments

The experiments by Neoh and collaborators [232, 231, 230] used a two-flame system. A premixed methane/oxygen flame (equivalence ratio, $\phi = 2.10$) was used to generate carbonaceous particles (soot). The gases and carbonaceous particles (soot) produced in this flame were introduced into a second flame that operated under oxidising conditions with equivalence ratios between 0.85 and 1.15.

The values reported in Chapter 6 are from the second flame with an equivalence ratio of 1.15 [232]. Although Neoh et al. [232] do not report the mole fraction of acetylene, the mole fraction of hydrogen for this case was reported to be between 2 and 3%, which is high enough to result in mole fractions of acetylene and hydrogen that are relevant to the current work. The mole fractions for molecular oxygen, atomic oxygen and hydroxyl radical are reported in more detail in [231] for these conditions. These experiments show values as high as $X_{O_2} = 10^{-2}$, $X_O = 10^{-3}$ in oxidising conditions. The values reported in the main text correspond to values where enough acetylene and hydrogen could be assumed to be present in the burnout experiments.

Atmospheric ethylene/air flame

The atmospheric pressure ethylene/air flame investigated by Salamanca et al. [273] (equivalence ratio, $\phi = 2.01$) was modelled by Elvati et al. [69] using a combination of two mechanisms [50, 186]. The mole fractions of both atomic and molecular oxygen are reported in the supplemental material provided by Elvati et al. [69, Figure S2(a) and (f)]. The concentration of hydrogen and acetylene in the reported domain appear to be sufficient to sustain the growth of carbonaceous materials ($X_{C_2H_2} > 0.01$ and $X_{H_2} > 0.01$).

B.2   Additional ensemble statistics

In this section additional ensemble statistics are reported. The number of six-member rings, embedded five-member rings, seven-member rings, number of carbon atoms, number of hydrogen atoms and fraction of the ensemble that was oxidised (reduced the number of carbon atoms) were computed for 2.5 ms and 5.0 ms of simulation time.

Radar plots are used to present the changes in the means of the tracked variables; a representative example with the legend is shown in Figure B.1, while the average values for each point of the molecular and atomic oxygen mole fraction parameter space are shown in Figure B.2. The figures show results at two times: at half the simulation time (2.5 ms) in red and the end of the simulation time (5.0 ms) in blue.
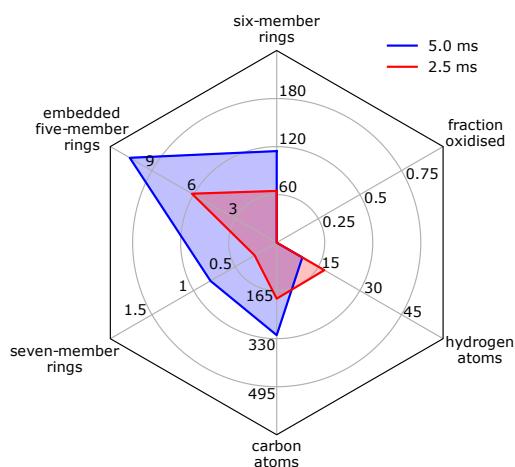

Fig. B.1 Radar plots showing the observed range of values for the selected response variables (see text). The two radars shown correspond to values observed at half the simulation time (2.5 ms) in red and values at the end of the simulation time (5.0 ms) in blue. The ranges shown in this figure correspond to values used in Fig. B.2.
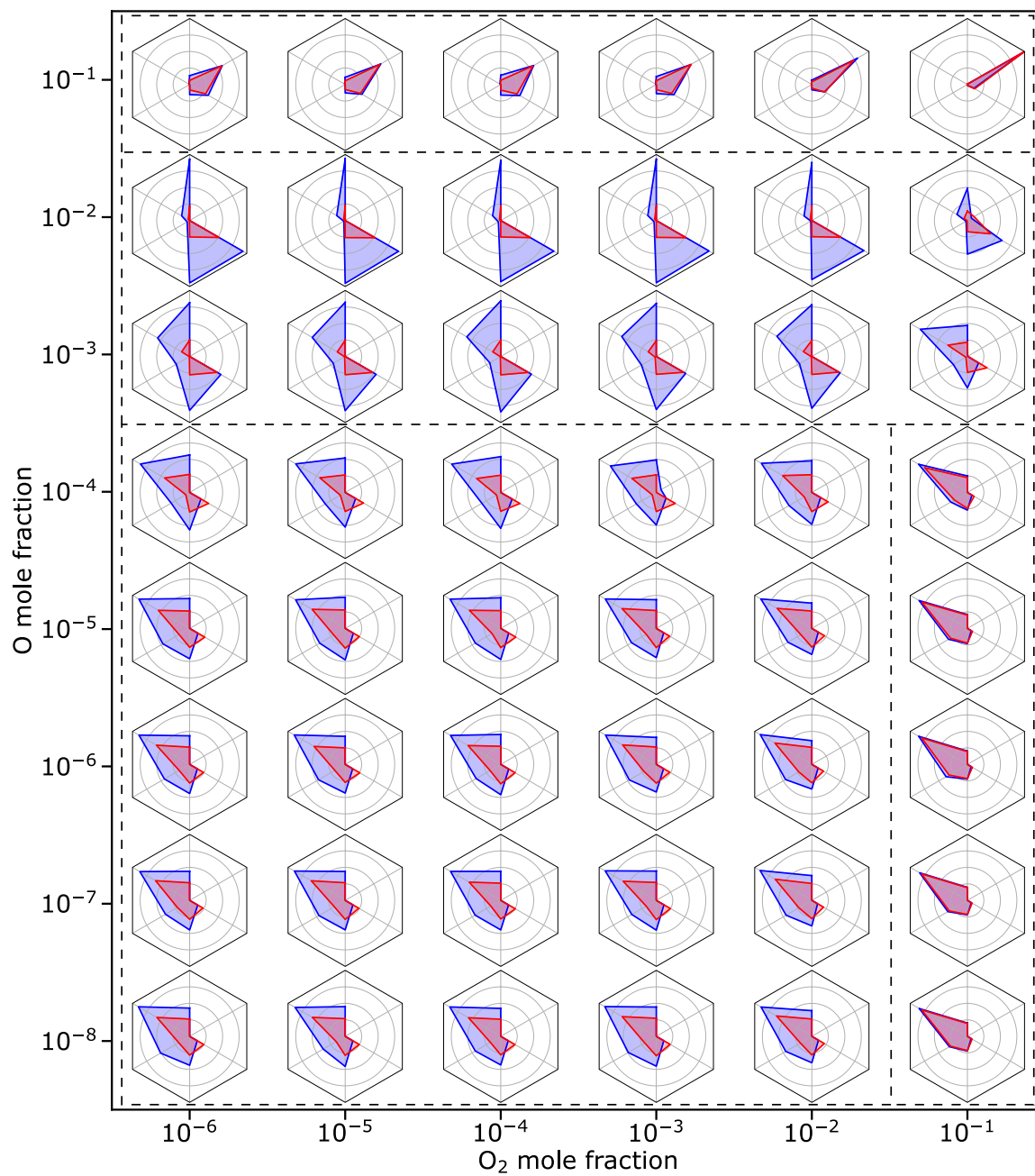
Fig. B.2 Observed average values of the selected response variables (see Fig. B.1) as a function of molecular and atomic oxygen mole fractions. The two radars shown correspond to values observed at half the simulation time (2.5 ms) in red and values at the end of the simulation time (5.0 ms) in blue. The ranges used in this figure are shown in Fig. B.1. Regions of carbon growth are shown with a dashed line.